![Université de Toulouse]

THÈSE

En vue de l'obtention du

DOCTORAT DE L'UNIVERSITÉ DE TOULOUSE

Délivré par l'université Toulouse III – Paul Sabatier
Discipline ou spécialité : Sciences et Génie des Matériaux

Présentée et soutenue par Rongying LIN
Le 5 Juin 2012

FORMULATION OF ELECTROLYTES BASED ON IONIC LIQUIDS FOR SUPERCAPACITOR APPLICATIONS

JURY

F. FAVIER	Chargé de recherche	Laboratoire ICG – Montpellier	Rapporteur
J. LE-BIDEAU	Professeur	IMN – Université de Nantes	Rapporteur
C. CACHET-VIVIER	Maitre de conférences	ICMPE – Paris	Examinateur
F. ALLOIN	Directeur de recherche	LEPMI – Grenoble	Examinateur
P-L. TABERNA	Chargé de Recherche	CIRIMAT, Université de Toulouse	Examinateur
P-L. FABRE	Professeur	LGC – Université de Toulouse	Examinateur
S. FANTINI	Directeur Scientifique	SOLVIONIC, Toulouse	Examinateur
P. SIMON	Professeur	CIRIMAT Université de Toulouse	Directeur de thèse

Ecole doctorale : Sciences de la Matière
Unité de recherche : Institut Carnot CIRIMAT
Directeurs de Thèse : Pr. Patrice SIMON et Dr. Sébastien FANTINI

Dedicated to my parents. . .

Acknowledgements

I am also grateful to research enginners, Ph.D students, post-doctoral reseachers whom our pathways have crossed during these years in CIRIMAT, Romain, Adriana and Pascale. Yann, thank you for your support, encouragement throughout these years. Thank you for being there always, even for my defence despite having a flight to catch almost immediately after.

To the Ph.D. students and post-docs in my team in CIRIMAT, Céline, Laurent, Emilie, Penny, Etsuro, Julie, Jérémy, Cyrille, Eider, Wan-Yu, Lorie…, Céline, thank you for the detailed and professional training that you have provided me during my first year. Etsuro san, thank you for your support and your humour! Julie, thank you for good times we had together, for your kindness and valuable friendship. Eider, getting to know you is one of the most magical thing! Although our paths crossed for some time, it was too short! Thank you for the marvellous and fabulous moments spent together in Toulouse as well as in the Basque country and especially being there always even at hundreds of kilometres away! Wan-Yu, knowing you is one of the best comfort, like having a sister. Thank you for your presence and the good times we have had together and I look forward to the many more ones to come! Thank you all for the great team spirit!

Apart from my team, I would like to especially acknowledge the help and motivation I have gotten in one way or another in the final leg. Aude, being always energetic and enthusiastic, thank you for the company at work. Congcong and Aneesha, I am grateful to have met you ladies with such pleasant dispositions, and am thankful for all the fantastic moments shared together! Claire, although we shared the office not for too long, I really appreciate the time together and the humour we shared! Thank you for brightening the office and your support!! Leila, thank you for the daily smiles, bisous, concern and all the administrative support you provided, I would have been so lost without all these information! Laurent and Pauline, thank you very much for the French translations! Pauline, thank you for being such a sweet and lovely friend! Thank you for opening my eyes to the artistic world, and sharing the therapeutic handcraft activities! Thank you for being there and the daily company at work!

For the engineers, Ph.D. students, master students and post-docs whom I have not mentioned, thank you for smiles and bisous that filled the corridors.

For these three years, I had experienced wonderful working relations with great and fantastic colleagues in Solvionic: Sandrine, Delphine, Angélique, Mélanie, Sébastien, David, Aratz, Fleurine, Nicolas, Virginie, Frederic and François. Thank you all for the memorable moments and warm company! Special thanks to Sandrine, Delphine and Angélique, thank you for your kindness, help and advices not only for work matters, but also for my personal matters such as

dealing with complicated procedures like paying for tax, buying a car and renting a flat in France. Thank you for the French lessons from time to time during lunch, and the funny French expressions that we do not usually get from textbooks. Most importantly, I treasure the friendship that we share! Sébastien, apart from being my co-supervisor, thank you also for your lifts to the industrial site before I have my own transport. Thank you for your humour and kindness once again. François, our C.E.O., thank you for the support and understanding throughout these 3 years.

Also, special thanks to Professor Chen Ping, Professor Jaenicke, Professor Chuah and Professor Loh Kian Ping for their guidance and valuable advices throughout my academic pathway. Thank you Professor Chen, for encouraging me to further my studies, looking back, I am grateful for your time and valuable advices. Thank you, Professor Jaenicke, for your constant concern about the alumni students, and support all these years.

The group of Singaporeans and Malaysians in Toulouse, Vivian, Yean Ling, Yue Siang, Sindie, Jasmine, Denise, Jamie, Gwendolyn, See Bin and families, thank you for filling my years in France with delicious asian delicacies and wonderful company, festive celebrations and mahjong sessions!!

Great thanks to my galfriends, Liling, Huimin, Shuxian, Yiting, Peijing, and good friend, Gerald for being always there and especially for their motivation and support that can be felt all the way from Singapore. Thanks to whatsapp application for making this possible too!!

Also, thanks to my uncles, aunties and cousins who keep me connected virtually all the time, their well wishes and encouragements from Singapore. Especially Uncle Jeffrey, thank you for your messages of concern from time to time and for bringing me around to new places in Singapore each time I return.

Alexandre, thank you for your unlimited patience, love, warmth, humour and support in every possible way to see the completion of this work. Thank you for being there always. I would also like thank your lovely family, Patrick, Régine, Aurélie, Papi, Mamie, Tonton, Papé and Tatie for their unconditional support and company.

Lastly, I owe a lot to my family, I would like to thank my parents, grandmother and brother, Ray, who longed to see this achievement come true, for their unconditional support and love during these distant years. Thanks bro, for looking after the needs of our family while I am away from home.

Contents

Table of Contents

General Introduction

General Introduction

Energy is the foundation pillar of our society, without which, life on earth is unsustainable. As of 2010 reports from the Europe's Energy Portal (EEP) [1], energy related emissions account for almost 80 % of the EU's total greenhouse gas emissions and nearly 45 % of European electricity generation is based on low-carbon energy sources, mainly nuclear and hydropower [2]. Current target for the EU are set at increasing the share of renewable energy to 20 %. Following the aftermath of the earthquake and tsunami stricken Fukushima, which have posed profound implications for the future of world nuclear power, there is an urgent call to up the share of renewable energies even more to replace and if not liberate the strain on nuclear means of carbon-free generation of energy.

Amongst several directives drawn up by the Department of Energy (DOE) of the USA [3] and the EEP, exhaustive efforts have been committed over the last decades and ongoing towards the development and deployment of renewable energies in view to curb the increasing damages to the environment and climate due to intensifying industrialization and globalization amidst our growing population and vastly developing nations. Low carbon emission renewable alternatives, such as solar, wind, and tidal waves, have been sought to address the challenges of today's energy concerns on increasing emission of greenhouse gases, that is worsening the extent of global warming. However, such alternatives though clean, are intermittent sources, that could not be dispensable in times of need. This then leads to the question of sustainability of such means of harnessing energy generated from natural earth elements. In order to support these renewable alternatives, strong complimentary storage systems or networks ought to be established alongside to realize the eventual deployment and accessibility of these harvested energy [4], answering to the central goals for energy policy which currently includes the security of supply, competitiveness and sustainability of energy which had been listed in the Lisbon Treaty [5].

Following the directives set out from the DOE and the EEP, storage systems play an important role in the management of such sporadic production of energy. With good establishment of energy storage systems, a wide range of distributed and centralized renewable energy can be exploited in view of increasing energy efficiency. Furthermore, energy storage provides for better electro-mobility, keeping the carbon emissions low, while maintaining inevitable activities of globalization and development (transport, heating and industries).

Electrochemical energy storage (EES) systems serve as one of the distributed energy technologies and are drawing attention in research to address today's industrial and societal challenges for security and sustainability of energy that they can provide. EES plays an important role in electro-mobility owing to their easy integration in autonomous systems such as transportation and electronics. EES are traditionally divided into energy devices (batteries) and power devices (electrochemical capacitors: ECs). Batteries are characterized by charge/discharge times from minutes to hours, while ECs are high-power devices (~10 kW.kg^{-1}) with medium energy density (~5 Wh.kg^{-1}) that can be fully charged/discharged in a matter of seconds [6, 7]. Progress in battery research has been improving, particularly in the development of Li-ion batteries [8]. Despite these improvements, implementation of these Li-ion batteries in energy storage and electro-mobility has been impeded by safety concerns on lithium's reactivity, together with conventional organic electrolytes, could lead to fire and/or explosions.

Electrochemical capacitors, also known as supercapacitors are emerging to be prospective energy storage devices that are complement in energy management to batteries, and a possible replacement of batteries in the near future. Amongst the different types of supercapacitors, symmetric ones which have carbon-based electrodes are of great interest due to the versatility of carbon which enables a wide variety of nano-textured electrodes, offering a vast range of physical properties to custom for different types of applications [9]. In view of answering to today's objectives of energy storage and efficiency, there is a need to formulate greener and safer electrolytes and concurrently improving the performances of these carbon-based ECs. Ionic liquids have been attracting a lot of attention as safe electrolytes for EES due to their interesting electrochemical as well as physical properties (ionic conductivity, melting points, electrochemical stability, etc.). In this context, this thesis has been effectuated and financed by SOLVIONIC, a company which specialized in the research and development of ionic liquids and formulation of electrolytes, in collaboration with CIRIMAT. The main interest of this collaboration is to formulate electrolytes based on ionic liquids for supercapacitor applications, in view to improve energy storage performances as well as safety.

In order to realize this, the project was kick started first by the molecular-scale study and conceptualization of the electrochemical double layer through (1) effects of solvent on the capacitive behaviour conventional electrolytes, (2) corroboration of the pore-size relationship in using a neat IL, a solvated IL and followed by the optimization of electrode/electrolyte interface at the EDL through (3) effects of architected electrodes in electrolytes consisting of pure ILs on capacitive behaviour and capacitance.

The first chapter presents a concise bibliography in the three main subjects of this research; Supercapacitors, liquid electrolytes and the current EDL investigations closely related to the research path taken by this work. These include firstly, new carbon materials with different nanostructures obtained through different synthesis routes for improving the performances of supercapacitors. Secondly, electrolytes of different nature and their properties which have been extensively studied to extend the current supercapacitor limits for different applications are also discussed in this chapter. Finally the understanding of the EDL (through different electrodes, categories of electrolytes and complementary modelling and experimental techniques) that has earned their important role in towards the advancement of the energy storage technology will be presented.

The second chapter consolidates the experimental conditions, physical and electrochemical characterization techniques applied in this project.

The third chapter studies the effects of solvent on the capacitive behaviour in conventional electrolytes using the same salt, NEt_4BF_4 in two different solvents; propylene carbonate (PC) and acetonitrile (AN). The objective is to understand the solvation effects of the same salt in different solvent during adsoption/desorption of the ions.

The forth chapter investigates the electrical double layer through corroborating between optimized capacitance and ion-pore size relationship using titanium carbide derived carbons (CDCs) in neat IL (EMI-TFSI) and solvated IL (EMI-TFSI dissolved in AN). The use of ILs first allows the understanding of ion-pore size relationship for increasing capacitance in the absence of solvent. The subsequent introduction of AN into neat IL enables a systematic study of the solvent effect on capacitance.

The fifth chapter follows through the synthesis and formulation of electrolytes purely based on ILs and the implementation of the designed electrolyte in supercapacitor application through electrolyte/electrode interface optimization.

Lastly, a short general conclusion describes the results obtained from this work, followed by the perspectives inspired by this research work.

References

[1]   http://www.energy.eu/
[2]   http://energy.gov/
[3]   Communication from the commission to the European parliament, the council, the European economic and social committee and the committee of the regions (COM(2010) 639 of 10 November 2010)
[4]   http://energy.gov/articles/energy-matters-clean-energy-technology-markets
[5]   Article 194 of the treaty on the functioning of the European Union (TFUE)
[6]   Miller, J. R.; Simon, P. *Science* **321** (2008) 651.
[7]   Conway, B. E. *Electrochemical Supercapacitors: Scientific Fundamentals and Technological Applications* (Kluwer, 1999).
[8]   Armand, M.; Tarascon, J. M. *Nature* **451** (2008) 652.
[9]   Béguin, F., Frackowiak, E. *Carbon Materials for Electrochemical Energy Storage Systems; Béguin, F., Frackowiak, E., Eds*.; *CRC Press/Taylor and Francis:* Boca Raton, FL (2009).

Chapter I : Bibliography

I. The electrochemical double layer capacitors (EDLCs)

I-1. Humble inception of charge storage

I-1.1. Capacitor

The demonstration of the first capacitor was mostly dated back to a german scientist named Ewald Georg von Kleist in late 1745. He found that electrical charge could be stored by connecting a high-voltage electrostatic generator by a wire to a volume of water in a hand-held glass jar. After having disconnected the wire from the generator, he received a painful spark upon contact with the conducting wire. In a letter describing the experiment, he said "I would not take a second shock for the kingdom of France."[1]. In 1746, Pieter van Musschenbroek, a physicist and mathematician in Leiden, Netherlands invented a similar capacitor called the *Leyden jar*. It was a simple glass jar coated inside and outside with metal foil as shown in Figure I- 1 [2]:
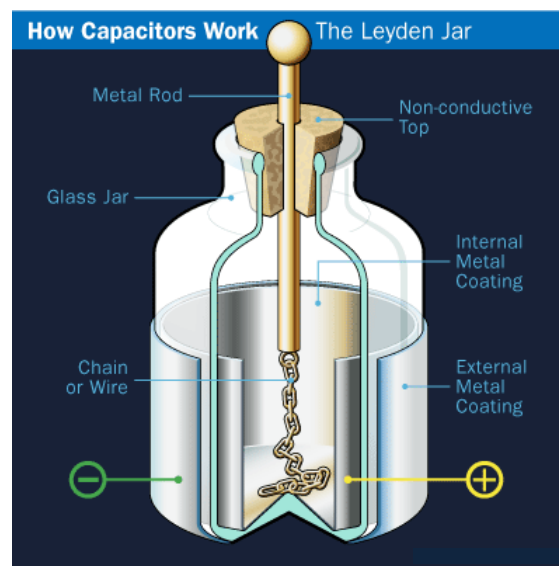
Figure I- 1: Schematic of the *Leyden Jar* [2].

Although it was thought for a time that water was the key ingredient, the glass acted as a dielectric. There was usually a metal wire or chain driven through a cork in the top of the jar. The chain was then hooked to a hand-cranked static generator. Once charges are delivered, the jar would hold two equal but opposite charges in equilibrium until they were connected with a wire, producing a slight spark or shock.

Using this *Leyden jar* capacitor, Benjamin Franklin then performed many electricity/charge-related experiments. Upon modification of the capacitor by replacing the

glass jar by a flat glass plate, he found out that the same charge can be produced; this gave rise to the flat plate capacitors or Franklin square.

English scientist and chemist Michael Faraday also conducted several experiments on the *Leyden jar* in attempts to store the electrons produced during his experiment into the capacitor. His experiment led to the development of first usable capacitors, which were constructed by using large oil barrels. Faraday's earlier contribution to this field led to the attribution of *farad* as the unit of capacitance today.

I-1.2. The electrochemical double layer (EDL)

The study of the electrochemical double layer concept by chemists started in the late 1800s, by von Helmholtz who developed and modelled the postulates from investigations on colloidal suspensions [3]. Further research was then done on surface of metal electrodes in the late 19th and early mid-20th centuries by Gouy, Chapman, Stern and Grahame [4,5,6,7]. EDL concept is thus developed by using conducting electrolytes, instead of insulating dielectric materials in capacitors.

In 1957, General Electric then first patented the demonstration of practical use of a double layer capacitor for electrical charge storage with the use of crude porous carbon electrodes in an aqueous electrolyte [8]. It was only nine years later, in 1966 that this hypothesis of charge storage occurs in the electric double layer at the electrolyte/electrode interface, was accepted when SOHIO was granted a patent that was achieved by chemist Robert A. Rightmire [9]. SOHIO produced the first commercial Electrochemical Double Layer Capacitors (EDLCs) and subsequently patented a disc-shaped device that consisted of carbon paste electrodes, formed by soaking porous carbon in an electrolyte separated by ion-permeable separator [10]: this same format is currently and commonly being used. Non aqueous electrolytes were also used in the early days of EDLCs development by SOHIO, but the poor sales led to the licensing of their technology to NEC in 1971. NEC then further developed and marketed the EDLCs successfully, that are primarily for CMOS memory back-up applications, providing back-up power for consumer electronic goods [11]. Such devices typically had a lower voltage and higher internal resistance as compared to current EDLCs [12]. The most powerful ECs which were larger than devices available in Japan and the U.S. were reported to start a 3000 horsepower diesel locomotive by Russian Alexander Ivanov who owns ECOND company. The coin cell design and wounded configuration of today's ECs, was then developed by Panasonic. By the 1980s, the improvement of EDLCs moved from

increasing voltage per cell (6 cells in series for 5.5 V in NEC versus 3 cells in series for 5.4 V in Panasonic), to increasing voltage of capacitor sets to 1500 V by ELIT in Russia. At the same time, ELNA company from Japan produced their own double-layer capacitor under the name "Dynacap". Pinnacle Research Institute developed the first high-power double-layer capacitors (PRI ultracapacitor) in 1982, by incorporating metal-oxide electrodes and was designed for military applications such as laser weaponry and missile guidance systems. An ultracapacitor development program was initiated in 1989 by the DOE, and contracted to Maxwell technologies to develop advanced ECs with both short and long term goals defined for 1998–2003 and thereafter [13]. This includes a technology suitable for levelling a battery or fuel cell storage systems in electric vehicles (EVs) to provide the necessary power for acceleration, and additionally allow for recuperation of brake energy. Since then (only in the 21st century) electrochemical capacitors became famous in the context of hybrid electric vehicles. ECs gained popularity in research and other EC companies from all around the world such as ELTON (Russia), CAP-XX (Australia), Nesscap (Korea) and Nippon Chemi-con, NCC (Japan) emerged with a variety of ECs that offers energy densities ranging from 1-10 Wh.kg^{-1} and power densities up to 20 kW.kg^{-1}.

Table 1 shows the current manufacturers and distributors of a wide range of EDLCs in the world.

Table I- 1: Commercial supercapacitors [14]; Data obtained from [15] (*).

Manufacturer	Cell/ module voltage (V)	Electrolyte	Capacitance (F)	Specific energy (Wh.kg^{-1})	Specific power (kW.kg^{-1})	ESR (mΩ)	Mass (kg)
Maxwell Technologies (cell)	2.7	AN	3000	5.5	11.4	0.29	0.55
NessCap (cell)	2.7	PC	3500	5.2	9.7	0.28	0.67
Nippon Chemi-Con (cell)	2.5	PC	2400	4	4.3	0.7	0.52
Batscap	2.7	AN	2600	5.3	20	0.3	0.5
***Panasonic**	2.5	PC	1200	**2.3	*514	1.0	0.34

* Power based on P = 9/16*(1-EF)*V^2/R, EF = efficiency of discharge
** Energy density at 400 W/kg constant power, V$_{rated}$ - 1/2 V$_{rated}$

To date, many other types of supercapacitors have been developed, consisting of different charge storing mechanism, to custom for the different demands of energy utilisations. Current companies that are investing in electrochemical capacitor development include NEC, ELNA, VYNA, YUNASKO and more.

I-2. Supercapacitors: Interest and Applications

Interests – Similar to tailors customizing clothing to fit their customers of different body builds, energy systems need to be customized for the wide ranging applications to cater to respective specific power and energy demands. Ragone plots allow the comparison of electrical energy storage devices showing both specific power density (speed of charge and discharge) and specific energy density (storage capacity). The EES are thus categorized according to their charge storage mechanism and plotted on the Ragone plot according to their respective specific power (W.kg^{-1}) and the specific energy (Wh.kg^{-1}) as shown in Figure I- 2 [16], which show the significantly large area covered by the ECs, bridging demands between conventional dielectric capacitors and batteries.
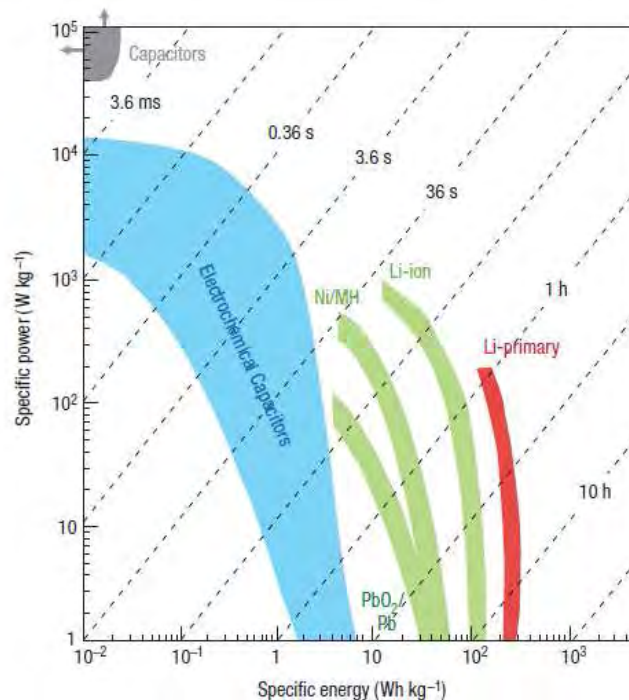
Figure I- 2: Ragone plot - Specific power against specific energy, for various electrical energy storage devices [16].

ECs, also known as supercapacitors, ultracapacitors or electrochemical double layer capacitors (EDLCs) have attracted considerable attention as evidenced on the ragone plot whereby they can rapidly store and release energy, catering to both power and energy needs.

Diagonal lines depict the time constants of the devices, obtained by dividing the energy density by the power [16]. Supercapacitors emerge as a very promising candidate for EES owing to the vast variety and combination of materials eligible for EDLCs, allowing them to cover an expansive region on the Ragone plot. The characteristics offered by the supercapacitors distinct from those of batteries due to their different charge storage mechanisms, resulting in different placement on the Ragone plot. Table below lists the distinctive functions and characteristics between the dielectric capacitors, supercapacitors and batteries.

Table I- 2: Comparison of typical capacitor, supercapacitor and battery characteristics [17].

Characteristics	Capacitor	Supercapacitor	Battery
Charge storage mechanism	Surface adsorption of electrical charges at electrodes	Surface adsorption of ions at electrodes	Faradic reactions in bulk of electrode
Specific energy (Wh.kg^{-1})	< 0.1	1 to10	10 to 400
Specific power (kW.kg^{-1})	>> 50	≤ 20	≤ 2
Discharge Time	10^{-6} to 10^{-3} s	1-10 s	0.3 to3 h
Charging Time			1 to 5 h
Charge/Discharge Efficiency (%)	~100	85 to 98	70 to 85
Cycle Life (Cycles)	Infinite	≥ 1000 000	≤ 1000 (@ 100% DOD)
Max Voltage determinants	Dielectric thickness and strength	Electrode/Electrolyte stability	-
Charge storage	Electrostatic	Electrostatic; Surface	Bulk

Although batteries have been the popular forms of energy storage for the past decades, the less familiar capacitors are gradually finding their way into the energy storage field with the abilities to offer equal, if not, better performances than batteries. Advantages of current developed EDLCs include high power, 98% delivery/uptake, cost competitiveness of materials, high charge/discharge efficiency, low self-discharge, adequate operating voltage and high cyclability. Furthermore, EDLCs using activated carbon have no intrinsic open-

circuit voltage and yet have symmetric charge/discharge power capability over the complete range of potential operation (maximum rated voltage to near zero). Thus carbon/carbon capacitors can be utilized over the complete voltage range without damage for at least 1000000 cycles. Batteries operate in a relatively narrow range having a well-defined open-circuit voltage and a minimum discharge voltage below which the cell will be damaged. The chemistry of high power batteries is faradic with reactions occurring primarily in the bulk of the electrode materials. However, the power is limited by diffusion of the reactants even when the electrodes are thin and the particle size of the electrode material is nano-scaled [18].

Applications - Supercapacitors have had its debut mainly in CMOS memory back-up and are now widely used in power electronics for peak power saving and back-up supplies (as support for power disruption (see Figure I- 3c)). Today, one of the most promising applications is their use in the transportation field, that is, in hybrid-electric vehicles (HEVs) in particular, energy harvesting, recovery of braking energy and faster start-up for the engine [19,20,21]. Examples include their usage as backup power in the Toyota Prius when braking and as power assists in some BMW models. More recent implementations in HEVs are made by Peugeot SA in e-HDi micro-hybrid technology featuring the new generation 'stop/start' technology based on the combination of a 1.6 litre HDi Euro 5 diesel engine and a reversible alternator in the Peugeot 308 model (Figure I- 3a) [22]. It relies on an alternator control system (Volt Control) to recover energy during deceleration and a supercapacitor to store and deliver additional energy on startup (e-booster), allowing a 15% reduction in fuel consumption in urban traffic and a 5 $g.km^{-1}$ reduction in CO_2 emissions for approved cycle fuel consumption. Supercapacitor equipped buses have also been used in relatively small numbers in California and China is deploying 13000 electric buses.

The ease and speed of charging and longer cycling life in supercapacitors make them important participants in energy storage. One example is the Rhein-Neckar regional transport operator, RNV (Germany) using Variobahn trams fitted with Bombardier's Mitrac Energy Saver technology. Trials in Mannheim have demonstrated a reduction in energy consumption of up to 30 % using Energy Saver, which is currently fitted in 19 RNV trams (Figure I- 3b)

In 2006, implementation of supercapacitors was successfully achieved in emergency doors (16 per plane) on Airbus A380 (Figure I- 3c). Such examples affirmed the accountability of the EDLC technology in their performance, safety and reliability. ECs are definitely ready for large-scale implementation.

Figure I- 3: Supercapacitor applications. Peugeot 308 with e-HDI hybrid technology **(a)**, and Rhein-Neckar regional transport operator, RNV (Germany) using Variobahn trams fitted with Bombardier's Mitrac Energy Saver technology **(b)**, and EC installed in emergency doors of the Airbus 380 **(c)**.

I-3. Chemistry

I-3.1. Dielectric Capacitors

Starting with the basic term of "capacitors", they were first developed with two simple conductive plates (positively and negatively charged) sandwiching a dielectric material in between. Charge separation at the plates is achieved by the application of an external bias and the charges are then said to be "stored" by residing on the surfaces of the plates by the external driving force as shown in the Figure I- 4.
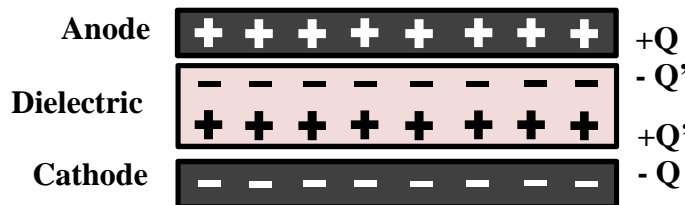
Figure I- 4: Schematic of charge distribution and storage of a conventional capacitor.

In order to keep the charges separate, the medium between the anode and cathode, called the dielectric, must be non-conductive – an electrical insulator. As the stored charge increases, the electric field across the dielectric increases. This situation gives rise to a voltage which increases proportionally with the charge. Capacitance, is then the ratio of the charge magnitude on each plate to the electric potential (voltage) between the plates, and can be quantified using the following equation:

$$C = \frac{\varepsilon_0 \varepsilon_r A}{d} \quad \text{(Eq I- 1)}$$

where C is the capacitance in Farads, ε_0 and ε_r are the permittivity in vacuum and relative permittivity of the dielectric material respectively in F.m^{-1}; A, the area of the plates in m^2, and d, the distance of separation between the two parallel plates in m.

I.3.2. Electrochemical Double Layer (EDL) – In a supercapacitor.

The Electrochemical Double Layer (EDL) defers from Figure I- 4 through two main modifications in the former set-up; (1) charge separation at the dielectric/electrode interface is established at the electrode/solution interface instead and (2) a large capacitance is developed using high specific area carbon powder or porous carbon materials, on the order of 1000 to 2000 $m^2.g^{-1}$. An overall capacitance of about 250 $F.g^{-1}$ is attainable from such elaborated surface area, given a nominal specific capacitance of 25 $\mu F.cm^{-2}$ [23].

The EDL occurs across the interfacial region, paved by electrolyte ions and the residing surface charges of the active material (metal, semiconductor, oxide, or carbon surface). The thin EDL of 5-6 angstroms corresponds to the diameters of the solvent molecules and ions. Moreover, the ions as compared to the dielectric material, can conform to the high rugosity and porosity of carbonaceous electrodes, leading to an increase in pairing of charge per unit surface area and hence the escalated capacitance (with increase *A* and small *d* in Eq I-1). EDLCs, super- and ultra- capacitors, hence earned that superlative in their names from the fact that the amount of charge that can be stored is in the tens or hundreds of Farads per gram of active material as compared to conventional capacitors which offer charge storage in the magnitude of microfarads.

Early models of the EDL started first with von Helmholtz, called the Helmholtz model, which is described to comprise of two array layers of opposite charges, separated by a small distance of atomic dimensions, paved along the interfacial axis. Illustration of this perception of charge distributions at the electrode/electrolyte interface is shown in Figure I-5a, it is assumed that the surface charge is exactly compensated by a layer of strongly adsorbed ions of opposite valence, the counter-ions. Gouy and Chapman then came up with the model with a diffuse layer between the electrode and the bulk solution as shown in Figure I-5b, accounting for the Brownian movement of the ions which are considered as point charges. In this model, the ions which counterbalance the surface charge are dispersed in the solution, creating a diffuse layer [24]. Grahame defined the Helmholtz compact layer into the internal and external layers [25] and further studies by Stern produced a model (Figure I-5) which combines both the Helmholtz and Gouy-Chapman models and takes into account the finite size of the ions. These models hence sum up to the modern electrochemical double layer as shown in Figure I-5.
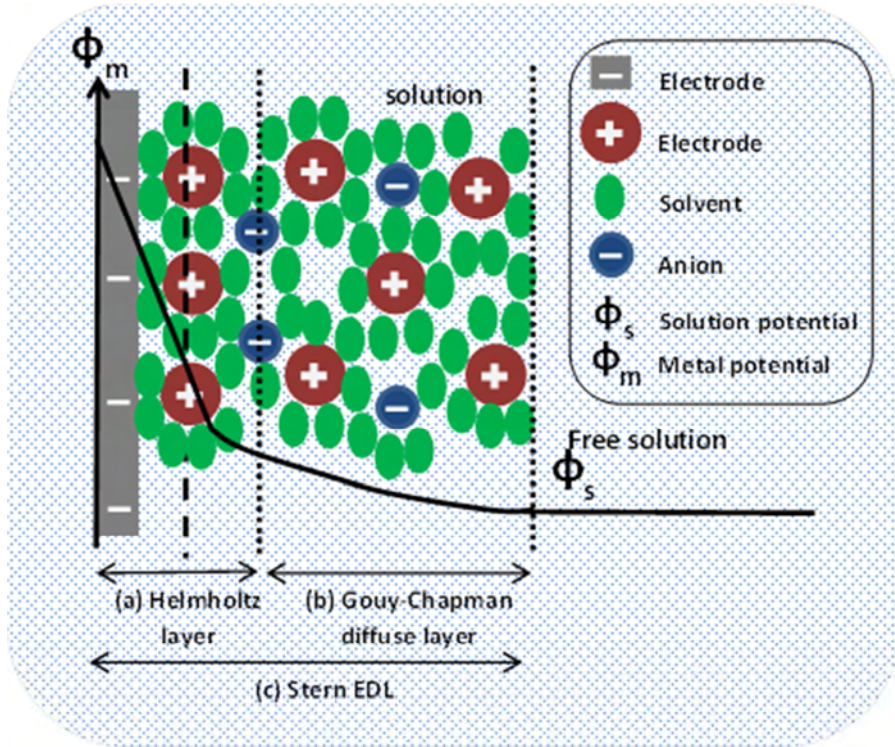
Figure I- 5: Modern Electrochemical double layer based on the Helmholtz model **(a)**, the Gouy-Chapman diffuse layer model **(b)**, and the Stern model **(c)**.

In this model (Figure I-5), three domains can be distinguished: (1) The Helmholtz layer composed of strongly bound ions close to the surface; (2) The diffuse layer composed by more dispersed ions, and; (3) The free solution, when it exists.

The overall EDL capacitance, C_{EDL} can hence be represented by an equivalent circuit of a series combination of the capacitance of the compact Helmholtz layer, C_H and that of the Gouy-Chapman diffuse layer, C_{diff} as shown in Figure:

$$C_H \qquad C_{diff}$$
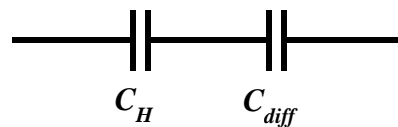
Thereby obtaining the related equation:

$$\frac{1}{C_{EDL}} = \frac{1}{C_H} + \frac{1}{C_{diff}} \qquad \text{(Eq I- 2)}$$

For highly concentrated electrolyte, $C_{EDL} \approx C_H$, the energy, E_{max}, and the power, $P_{max,}$ of supercapacitors are calculated according to the following equations:

$$E_{max} = \frac{1}{2} C V_{max}^{2} \qquad \text{(Eq I- 3)}$$

13

$$P_{max} = \frac{V_{max}^2}{4R} \quad \text{(Eq I- 4)}$$

Where V is the voltage established between the two plates and R is the equivalent series resistance of the cell.

For charge storage in an EDLC, the capacitance concept is the same except that the metallic plates are now replaced by the active materials, usually non-metallic conductive substance coated on metallic current collectors, and the dielectric material is replaced by a polymeric separator fully submerged in a sea of electrolyte ions as shown in Figure I- 6a. However, ionic current is required to bring ions to the active material interface; hence the separator must not only be ion-conductive but also an electronic insulator. The electrochemical capacitor contains one positive electrode with electron deficiency and the other one with an excess of electrons, with the electrodes of the same material, that is, a symmetrical cell. The maximal charge density is accumulated at the Helmholtz layer, formed between the charged carbon particle surface and the corresponding opposite charge of the electrolyte ions as shown in Figure I- 6b.
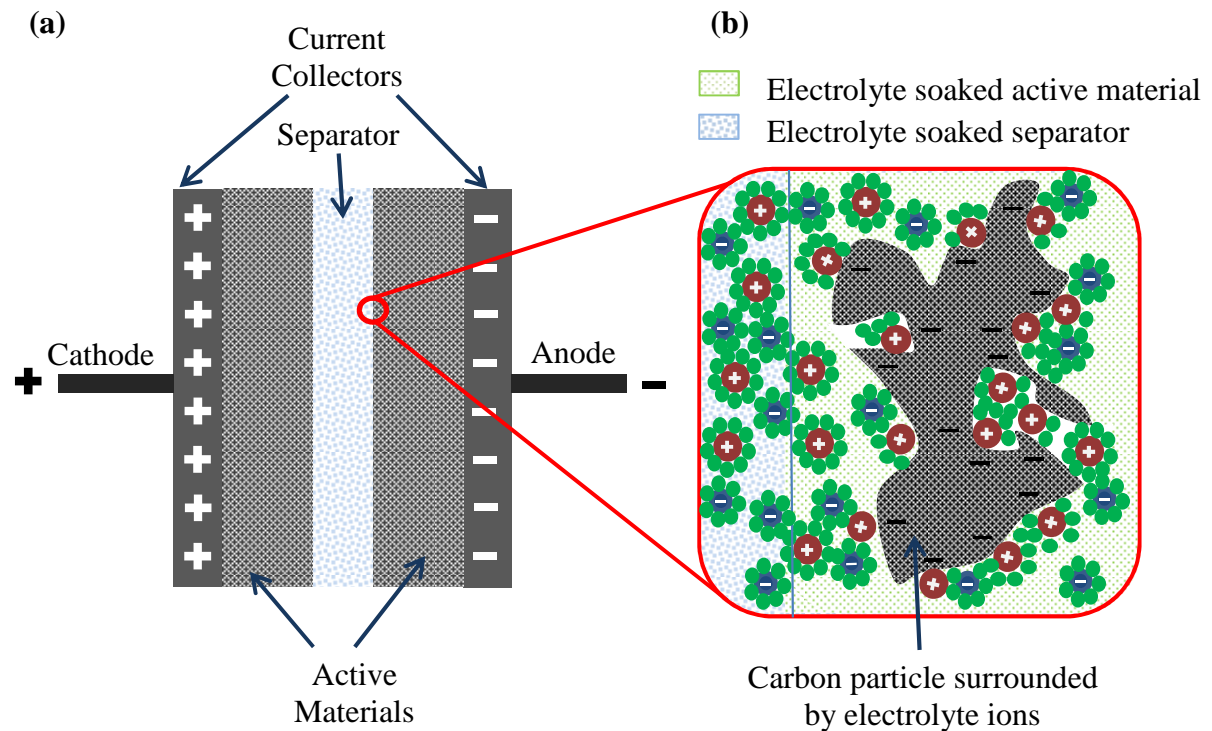
Figure I- 6: Schematic of a symmetric supercapacitor cell set-up (a) a schematic of EDL formed between a carbon particle and electrolyte ions.

14

Charge storage in a real symmetrical supercapacitor hence takes place at surfaces of both electrodes in contact with the electrolyte ions (Figure I- 6a), resulting in an equivalent circuit as shown below:
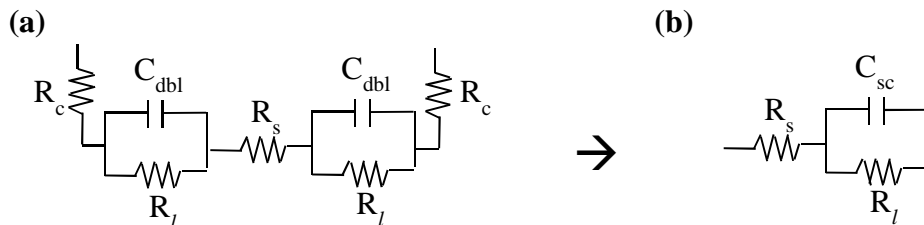
Figure I- 7 : Equivalent circuit of a supercapacitor consisting of resistance components from contacts between electrodes and current collectors, R_c, electrolyte resistance, R_s, leakage current, R_l and the double layer capacitance, C_{dbl} **(a)** and the simplified equivalent circuit **(b).**

The equivalent circuit (Figure I- 7) of an EDLC comprises of a capacitance C_{sc}, a parallel resistance R_l responsible for self-discharge (in the presence of surface functional groups or other impurities), and an equivalent series resistance (internal resistance of the capacitor), R_s or ESR. The key factors in determining the power and energy of an EDLC other than its capacitance, are a maximum value of C_{sc} and a minimum value of R_s. The time constant of the charging and discharging circuits is equal to $R_s C_{sc}$, while the time constant for self-discharge is equal to $R_l C_{sc}$. Hence R_l should be at its possible maximum value. The series resistance is mainly determined by the choice of the electrolyte and the current collector/active material film contact.

The capacity stated on an EDLC device includes the weight of the cell as a whole including the aluminium housing. Hence it is important that the design is optimized to achieve the maximum capacity. As illustrated in Figure I- 8, current technology of packing the entire cell involves the rolling of a long running tape of the stack with separators in between every sheet of current collector laminated with active carbon. This design not only keeps the stack compact, but also makes full use of every available space and every side of the active material. Aluminium tabs of contacts are then welded to the current collectors as electrode terminals for external connection.
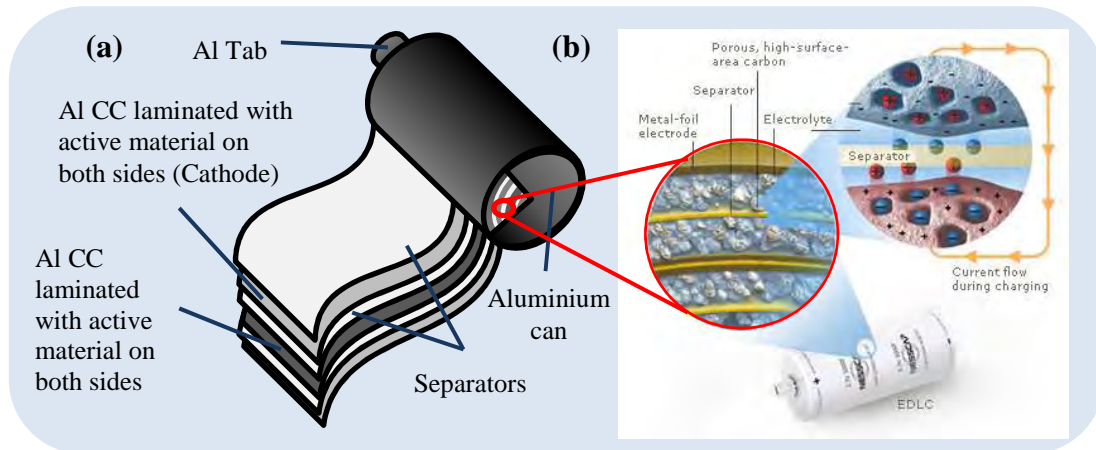
Figure I- 8: Schematic of a commercial spirally wound double layer capacitor and the layers that constitute the wounded stack **(a)** and the cross-sectional schematic of the EDLC in a Nesscap supercapacitor [26] **(b)**.

Although various types of supercapacitors exist, according to their charge storage mechanisms, like pseudo-capacitors and hybrid capacitors, we will focus on the elaboration of EDLCs.

EDLCs only store the charges based on simple electrostatic attraction between the surface charges of the polarized electrode and the corresponding oppositely charged electrolyte ions that formed the EDL as shown in Figure I- 8b. The amount of energy stored is very large compared to a traditional capacitor due to the enormous surface area that is available on the porous carbon electrodes and the small distance provided by the Helmholtz layer thickness. Though EDLCs are considered electrochemical devices, no chemical reactions are involved in the energy storage mechanism. The energy storage mechanism is a physical phenomenon (non-faradaic) and is thus highly reversible; this gives EDLCs their extremely long cycle life. Since the rates of charge and discharge are dependent only upon the physical movement of ions, the supercapacitor can store and release energy much faster (meaning more power) than a battery that relies on slower chemical reactions. EDLCs will be the focus of this thesis and will be further elaborated in the following chapters.

II. State-of-the-art of constituent materials of a symmetrical carbon/carbon supercapacitor

II-1. Electrodes

Carbon is the main material for electrodes used in symmetric EDLCs. Carbon-based electrodes are of great interest as they are light-weight, of moderate cost, abundant, easy to process, possess high electronic conductivity and high specific surface area (high charge storage). Tremendous surface area can be obtained owing to their versatility which enables the different nanostructures to be produced, bringing about a wide variety of physical properties, to tailor for different types of applications. Templated carbons [27], carbide-derived carbons (CDCs) [28,29,30], onions-like carbons (OLCs) [31], carbon fabrics (cloth, fibres) [32], nanotubes [33], activated graphene [34] and nanohorns [35] have been used as electrodes for EDLC applications [36].
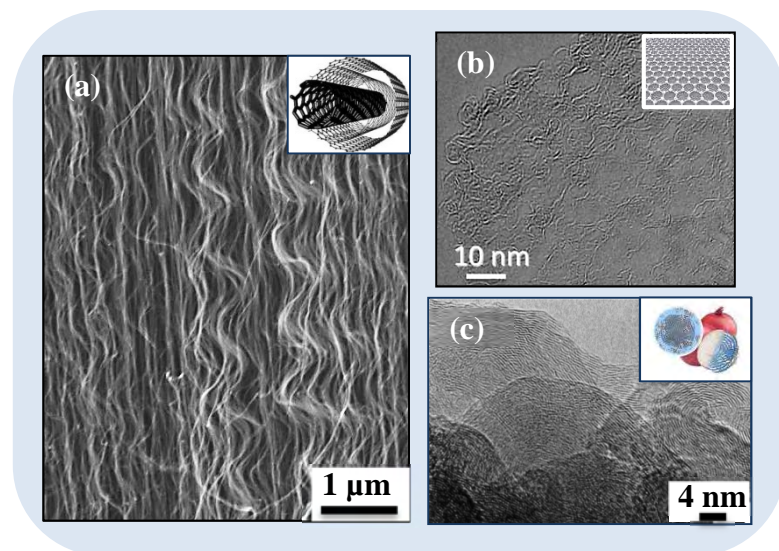
Figure I- 9: Electron microscope images and their schematic representations - CNT brush [37] **(a)**, activated graphene [38] **(b)** and onion-like structured carbon [39] **(c)**.

Figure I- 9 shows the microscopic images of some of the carbons mentioned. Sp^2-hybridized graphitic carbon is especially interesting in terms of high conductivity, electrochemical stability, open porosity, versatility in different architectural forms [40]. The main carbon materials used in this work can be categorized into their dimension of ionic conductivity; 0-dimensional (0-D), 1-D, 2-D and 3-D in the OLCs, CNTs, graphene, and activated carbons and the CDCs respectively.

0-D: Onion-like carbons (OLCs)

OLCs are 0-D quasi-spherical nanoparticles consisting of concentric graphitic shells [41]. Despite having layers that resemble that of the layers in an onion, the surface within the inter-layers are not exploitable and only the outer-surface of the onion-like carbon particles contribute to the EDL formation for charge storage. One of the most widely used and inexpensive methods of producing OLCs is annealing of detonation nanodiamond powders which allows large amount to be synthesized [42]. OLCs are also found after chlorination of carbides [43,44]. SSA measured ranges from 200-980 $m^2.g^{-1}$ depending on the synthesis conditions [45,46]. Carbon onion cells are able to deliver the stored energy under a high current density [47] and when thin electrodes of carbon onions are used in microsupercapacitors, they offer high power (~1 kW cm^{-3} and ability to cycle at a high scan rate of 200 $V.s^{-1}$) and high energy densities [48]. However, reported capacitance values are low around 30 $F.g^{-1}$[31,47].

1-D: Carbon Nanotubes (CNTs)

CNTs are often referred to '1-D' owing to the electronic transport uniquely along the tube axis and they exist as either single- or multi-layers of carbon and have diameters ranging from 1 to 50 nm. Several synthesis routes of CNTs include using arc discharge in helium atmosphere [49,50], laser ablation [51], chemical vapour deposition [52,53]. Specific surface area of CNTs spans over a very broad range from 50 to 1300 $m^2.g^{-1}$. [54,55]. The SSA value mostly depends on the number of walls on the CNTs. The use of CNTs [56] provide a good model system with improved surface accessibility and high conductivity, leading to impressive power densities but low energy density. However, the use of onions and CNTs can lead to a two-fold decrease in the specific capacitance due to graphitization. CNTs as electrode materials for supercapacitors have been reported with specific capacitances of 15-130 $F.g^{-1}$, depending on a specific electrolyte system [57].

2-D: Graphene

Graphene is made up of one-atom-thick planar sheets of sp^2-bonded carbon atoms that are densely packed in a 2-dimensional (2D) honeycomb crystal lattice as shown in Figure I-9b [38] and its inset [58]. The planar graphene sheet exists as basic structural element of some carbon allotropes including graphite, charcoal, carbon nanotubes and fullerenes and when stacked together, constitutes the crystalline form of graphite with an inter-planar spacing of 0.335 nm. Occurrence of graphene formation can be from quite a number processes: epitaxial

growth on silicon carbides [59,44] and metal substrates [60], graphite oxide reduction [61], growth from metal-carbon melts [62], pyrolysis of sodium ethoxide [63], from NTs [64], sugar, graphite by sonication (exfoliation) [65], dry ice method and laser scribing method. Graphene has more utilisable surface area as both sides of the graphene sheet can contribute to the EDL as compared only side in graphite, with remarkably high electron mobility at room temperature in excess of 15000 $cm^2.V^{-1}.s^{-1}$ [58], as well as high mechanical strength and chemical stability, with a high theoretical SSA of 2630 $m^2.g^{-1}$ [66]. Supercapacitors based on reduced graphene oxide (KOH activation) have been tested in different electrolytes yielding capacitance values from 130 $F.g^{-1}$[67] to 200 $F.g^{-1}$ [34,68,69] in aqueous electrolytes, 100 to 160 $F.g^{-1}$ in organic electrolytes [70,38] and ~75 $F.g^{-1}$ [71] in an ionic liquid. Application of graphene sheets in micro-supercapacitors rendered short response time [72].

3-D: Carbide-derived Carbons (CDC)s and Activated carbons (ACs)

CDCs are attractive in the way that their syntheses permit a tight control on the pore sizes, allowing a narrow pore size distribution with most of the pore dimension accessible to the electrolyte ions, thereby decreasing dead pore volume that do not contribute to the formation of the EDL. CDCs are obtained through high temperature extraction of metals and metalloids from carbide precursors, by using vacuum deposition [73], etching in supercritical water [74] or halogenation [75,76]. The carbide structure is transformed into pure carbon through this reaction with the retention of the original shape and volume of the carbide precursor. SSA measured for CDCs is generally more than 2000 $m^2.g^{-1}$ with a bulk porosity of more than 50 vol% depending on the carbide structure [16,40,77] .

ACs are derived from carbon-rich organic precursors by carbonization (heat treatment) in inert atmosphere. Coconut shells, wood, pitch and coke are some of the carbon-rich organic natural sources of precursors for deriving activated carbon, and they can be also synthetically made from selected polymeric precursors [78,79]. AC is then obtained by two processes: (1) a carbonization process which involves thermal treatment in an inert atmosphere and (2) an activation process to create a porous network in the bulk of the carbon particles. Such activation process is carried out by a partial, controlled oxidation of the carbon precursor grains; physical (high temperature treatment in oxidizing atmosphere) or chemical (hot acidic or alkaline oxidation, $ZnCl_2$ process) routes can be used. Figure I- 10a shows an activated carbon grain with pit-holes of about 100 microns. Besides these large pits, there is tremendous surface area from the pores that tunnel into the actual charcoal particles (Figure I- 10b). Most AC materials produced from traditional methods mentioned above do not offer sufficient

control over porosity [80], resulting in having a wide pore size distribution spanning from micropores of less than 2 nm, mesopores of between 2 and 50 nm, to macropores of larger than 50 nm (according to the IUPAC) in a grain (Figure I- 10c) due to the poor control of pore size in the activation process.
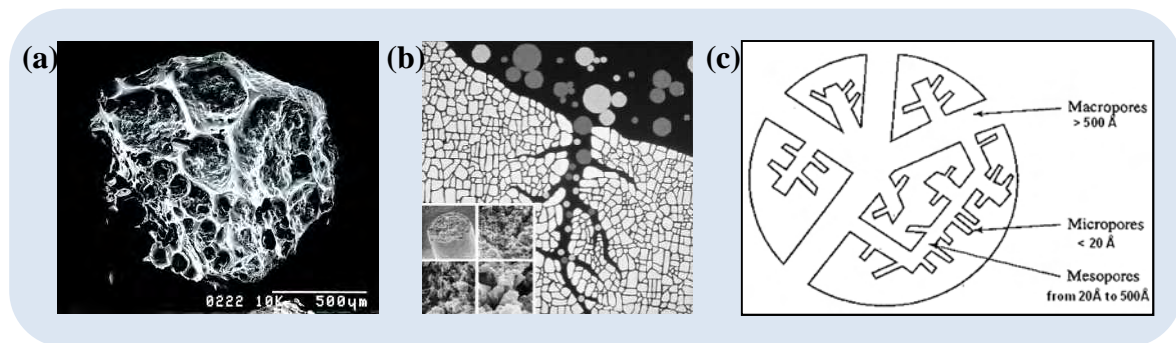
Figure I- 10: A granule of activated carbon **(a)**, cross-sectional view of a pore channel **(b)** and schematic of the pore size network of an activated carbon grain **(c)**.

Although specific surface area measured can be as high as 3000 $m^2.g^{-1}$, the actual accessible pores to ions are only in the range from 1000 to 2000 $m^2.g^{-1}$. Capacitance values achieved in AC-based electrodes largely depends on the type of electrolytes used (explained in later sections); about 100 $F.g^{-1}$ and 50 $F.cm^{-3}$ in organic electrolytes to 200 $F.g^{-1}$ in aqueous systems [81].

Carbon powders are mixed with ***binder*** to prepare the electrodes. Binders commonly used in the formation of carbon films are PolyTetraFluoroEthylene (PTFE) and PolyVinyldiFluoride (PVdF).

The active material slurry (carbon + binder) is coated onto ***current collectors***. Aluminium current collectors can be used for both the positive and negative electrodes for supercapacitors operating in organic electrolytes.

Separators are made up of porous and non-conducting material. They serve as electrolyte reservoirs and maintain ionic integrity. Properties such as thickness, porosity and stability of the separators are vital in maintaining a low ESR (large enough for ions to pass) and durability of the supercapacitor. Polymeric separators are one of the common materials such as polypropylene, polytetrafluoroethylene (PTFE). Materials that offer better mechanical integrity such as porous alumina and glass fibres can be useful in devices that undergo cycling at extreme temperatures.

II-2. Electrolytes

Energy storage has a direct relationship with the electrochemical stability potential, *V* of the electrolyte according to:

$$E = \frac{1}{2}CV^2 \quad \text{(Eq I- 5)}$$

Macroscopically, the physical properties are also equally important for improving the efficiency of energy storage in terms of wettability of the carbon by the electrolyte, low ionic conductivities for low ESR values and consequently power delivery. The transition temperatures (boiling, melting, glass transition, flash points) play a crucial role in the range of temperatures they can operate and the safety of the supercapacitors depends largely on the flash points (the lowest temperature at which a volatile material can vaporize to form an ignitable mixture in air) of the electrolyte.

Microscopically among the entities of the electrolyte, conductance and dissociation of the ions determine the performance of the supercapacitor and ultimately depends on the following factors:

- Solubility of the salt or acid
- Degree of dissociation or extent of cation and anion pairing in solution
- Dielectric constant of the bulk solvent
- Electron pair donicity of the solvent molecules
- Mobility of the free, dissociated ions
- Viscosity of the solvent
- Solvation of the free ions and the radii of the solvated ions
- Temperature coefficient of viscosity and of ion-pairing equilibira
- Dielectric relaxation time of the solvent

III. State-of-the-art of liquid electrolytes

The criteria today for an ideal EDLC electrolyte have been set close to have the following characteristics [82]:

- A wide electrochemical window (> 4 V) in EDLC device
- A specific conductance of > 75 mS.cm^{-1} at room temperature
- A thermal stability up to 300 °C
- A freezing point or glass transition temperature below -40 °C
- Low toxicity and affordable

Today, much accomplishments have taken place, drawing us nearer to fulfill at least one of the criteria but not yet one electrolyte that fits all the above mentioned. These accomplishments have been achieved through different starting points with different materials, giving us a whole range of different electrolytes that are better designed and customized for specific applications rather than one 'magic' electrolyte.
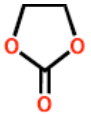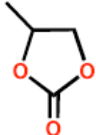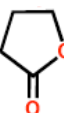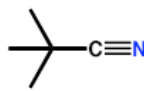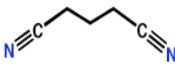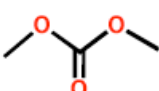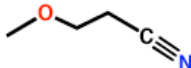
III-1. Conventional electrolytes for ECs

Conventional electrolytes that are available in commercial supercapacitors can clearly be classified into two general groups, namely aqueous and organic-based electrolytes.

Aqueous electrolytes – serve as a common and convenient conducting medium in EDLC applications and are solutions of either acids, alkali or neutral salts such as KOH and H_2SO_4 [23,81]. Aqueous electrolytes are commonly used in metal-oxide (such as ruthenium oxide and manganese oxides) pseudocapacitors and are preferred due to their low cost, high ionic conductivity, high electrolyte solubility, and less rigorous cell-packaging requirements. Relatively high concentrations of aqueous solutions can thus be prepared in view of increasing conductivity (up to 700 mS.cm^{-1} for H_2SO_4) and lowering the ESR, maximising the power capability. However, corrosion is an important factor to consider in choosing the electrolyte and its concentration with regard to the consequences of self-discharge of the supercapacitor. Despite high capacitance values of up to 200 F.g^{-1} and 1100 F.g^{-1} that can be achieved with activated carbon-based electrodes and metal-oxide based pseudocapacitors respectively in aqueous systems, such systems still suffer from low energy densities due to the limitation of the operating voltage to that of electrochemical stability of water, that is, at 1.23 V. This restriction is however mitigated by the high overpotential of the carbon anode for the hydrogen-evolution reaction that allows cell voltages of 1.5-2.2 V to be tolerated with such asymmetric cell configuration, extending the potential window further by 1 V. On the other hand, owing to possible surface functional-groups that can be present in some carbon materials, the operating voltage in aqueous systems is limited to 0.9 V, before the decomposition of the electrolyte occurs with the surface groups of the electrode through faradaic reactions.

Organic-based (non-aqueous) electrolytes – generally constitute quaternary ammonium salts solubilized in oxidatively stable organic solvents. Table I- 3 shows some solvents that are currently being studied extensively.

Table I- 3: Properties of solvents.

Solvent name	Formula	T_m / °C	T_b (fp) / °C	ε
Ethylene Carbonate (EC)		36	248 (160)	90
Propylene Carbonate (PC)		-49	242 (123)	65
γ-butyrolactone (γ-BL)		-44	204 (60)	39
Acetonitrile (AN)		-46	81 (6)	37.5
Glutaronitrile (GL)		-29	286 (>110)	-
Dimethyl Carbonate (DMC)		5	95 (18)	3.1
Tetrahydrofuran (THF)		-108	66 (-17)	7.2
Methoxypropionitrile (MPN)		-57	165 (61)	36

The use of non-aqueous electrolytes for electrochemical capacitors is generally more preferred since higher operating voltages, *V,* can be utilized due to the wider decomposition potential limits of this group of electrolyte solutions (up to 2.7 V). Since the stored energy increases with the square of *V* (Eq I-5), this is an obvious advantage over aqueous systems. Aprotic solvents (that do not have any dissociable hydrogen), typically acetonitrile (AN) or carbonate-based solvents (propylene carbonate, ethylene carbonate, etc.) are the most common solvents used in commercial activated carbon supercapacitors, currently offering a wide operation temperature range of -30 °C to +80 °C with a cell voltage of 2.5-2.7 V. The research trends are veered towards mixing of these solvents and understanding the evolution that could offer new physical properties physical properties upon mixing in different proportions and among different solvents. Janes and Lust *et al.* have done extensive research

on the mixtures of ester-based organic solvents with 1 M $(C_2H_5)_3CH_3NBF_4$ (TEMA) salt in binary, ternary and quaternary solvent systems of namely, EC, DMC, ethyl methyl carbonate (EMC), diethyl carbonate (DEC), methyl formate (MF), methyl acetate (MA) and ethyl acetate (EA) [83]. Other high permittivity solvents or their mixtures of PC [84,85,86,87], γ-BL [87,88], N,N-dimethylformamide [84,88,89], sulfolane [90,91], 3-methylsulfolane [90,92] and MPN [93] have also been reported in the literature.

Despite the enlargement in the electrochemical stability window prior to that of aqueous systems, such solvents are generally volatile (hence flammable) which then require careful and expensive thermal control to curb the risk of explosion due to pressure build-up at high temperatures, threatening the safety of the devices.

III-2. Non-conventional electrolytes for ECs

There exists another class of non-aqueous and non-conventional electrolytes, called 'Ionic Liquids' which are emerging as greener and safer electrolytes, bringing us closer to the criteria asked of for today's electrolytes in EDLC applications. The *raison d'être* for moving to this non-aqueous and non-conventional neoteric genre of electrolytes will be further explained by their compelling physical and electrochemical properties in the later sections.

IV. Room Temperature Ionic Liquids (RTILs)

IV-1. Brief historic evolution of molten salts to ILs

Molten salts are salts in the liquid phase but exist normally in the solid phase at standard temperature and pressure (STP). Elemental liquid aluminium can be obtained from the electrochemical reduction of aluminium (III) in molten cryolite (Na_3AlF_6), through the Hall process at 980 °C. Despite the wide liquidus range allowed by the combination of thermal stability and non-volatility, this is not practical in molecular media. Efforts in concocting halide eutectic mixture LiCl–KCl has a 355 °C melting point, but such operating temperatures are still high, posing several problems such as serious materials incompatibilities for reactions to be carried out at any scale, and incurring high energy costs to maintain the high temperature.

Ethylammonium nitrate ($EtNH_3[NO_3]$) dawned as the first reasonable low-melting salt (Ionic liquid) with a melting point of 12 °C in 1914 [94]. Triethylammonium nitrate later emerged with a patent application which described cellulose dissolution using a molten

pyridinium salt above 130 °C in 1930s [95]. It was first discovered (Graenacher, 1934) in 1930s that cellulose could be dissolved in molten *N*-ethylpyridinium chloride. However, little attention was paid to this finding at that time. The first documented observation of ionic liquids by chemists in the mid-19th century described the so-called 'red oil' formed during Friedel–Crafts reactions, typically the reaction of the aromatic substrate benzene with chloromethane to form toluene, in the presence of a Lewis acid catalyst such as AlCl$_3$ [96].

N-alkylpyridinium chloroaluminates were then studied as electrolytes for electroplating aluminium by Hurley and Weir at Rice University in the late 1940s [97]. Further research was substantiated by Hussey, Osteryoung and Wilkes in the late 1970s [98]. By the early 1980s, Wilkes and co-workers reported one of the first 1,3-dialkylimidazolium room temperature ionic liquids (RTILs) which was obtained through the mixing of 1-ethyl-3-methylimidazolium chloride ([EMI]Cl) and aluminum trichloride [98]. However, applications for this organo-aluminate IL are limited due to the hydrophilic nature of chloroaluminate anion and its high reactivity towards water [99].

More new imadazolium-based ionic liquids with varied anions were further reported in the 1990s, such as 1-ethyl-3-methylimidazolium tetrafluoroborate (EMI-BF$_4$) by Wilkes *et al.* [100] and 1-ethyl-3-methylimidazolium hexafluorophosphate (EMI-PF$_6$) by Fuller *et al.* [101]. The rediscovery of molten salts had since begun, with the EMI$^+$ cation sprouting into the quest for many applications. Until 2001, the halogenoaluminate (III) (in particular EMI-AlCl$_4$) and the closely related alkylhalogenoaluminate (III) IL have been by far the most widely studied [102]. Imidazolium salts continue to be one of the popular classes of RTIL being investigated [5,6] including the finding of dissolving cellulose efficiently at low temperature ($\leq$ 100 °C) (Swatloski *et al.*, 2002) in a range of imidazolium-based ILs. Other cations that are gaining popularity include the classes of non-aromatic cyclic cations such as pyrrolidinium and piperidinium.

IV-2. Properties

RTILs are molten salts that conduct at room temperature, without the presence of solvents. They comprise solely of ions at room temperature and are considered as green solvents due to the following physical properties [102]: (1) good solvents for wide selection of both inorganic and organic materials with the possibility of putting usual combinations into the same phase, (2) highly polar yet non-coordinating due to poor coordinated cation-anion, (3) immiscibility with some organic solvents to provide polar and non-aqueous selectivity for

two-phase systems, (4) non-volatility for high vacuum systems, (5) can be gelled with polymers. As such, they find their applications in synthesis of materials [103,104], catalysis and sensors [105,106], extraction and separation [107,108], and electrochemical processes [109,110]. Especially in the field of electrochemistry, they possess many novel specialties. Besides their high thermal (up to 350 °C) stability as a liquid (up to ~200 °C) at room temperature, they also possess excellent electrochemical stability, high heat capacity and cohesive energy density, as well as negligible vapour pressure at elevated temperatures which render them as non-flammables. One property that stands out above all others is the huge liquidus range (the span of temperatures between the freezing point and boiling point of a liquid: -80 °C to ≥ 250 °C). They are also less toxic relative to organic electrolytes.

IV-3. Chemistry

First requirement of classifying a product as an ionic liquid is having a melting point that is not much above room temperature which has been suggested to be 100 °C [111]. Cations size and symmetry make an important impact on the melting points of ionic liquids. Large cations and increased asymmetric substitution results in a melting point reduction. Usually one of the two pairing ions (usually the cations) is particularly large and possesses a low degree of symmetry, leading to the problem of efficiently packing the large irregular cations with small charge-delocalized anions. These factors result in ionic liquids having reduced lattice energy and hence lower melting points [112].

The low-temperature liquidus behaviour has been related to a simple Arrhenius law at all temperatures down to their melting point [113]:

$$\sigma = \sigma_0 \exp(\frac{E_a}{k_B T}) \qquad \text{(Eq I- 6)}$$

where E_a is the activation energy for electrical conduction, σ_0 is the maximum electrical conductivity (that it would have at infinite temperature), T is the temperature and k_B is the Boltzman constant. Usually RTILs obeys the Arrhenius behaviour given by Eq I-6) in a linear relation as shown in Figure I- 11a in the liquidus range. Beyond this point that often corresponds to their respective melting temperatures and transitions temperatures, RTILs undergoes a phase transition (gel formation or freezing), defying the linearity of the Arrhenius law. This deviation as shown in Figure I- 11b is accounted for by Vogel-Tamman-Fulcher (VTF) theory by the equation [114]:

$$\sigma = \frac{A}{\sqrt{T}} \exp \frac{B}{(T - T_g)} \qquad \text{(Eq I- 7)}$$

Where *A* and *B* are constants and T_0 is ideal glass transition temperature (usually 30-50 °C lower than that of T_g obtained by DSC measurement).
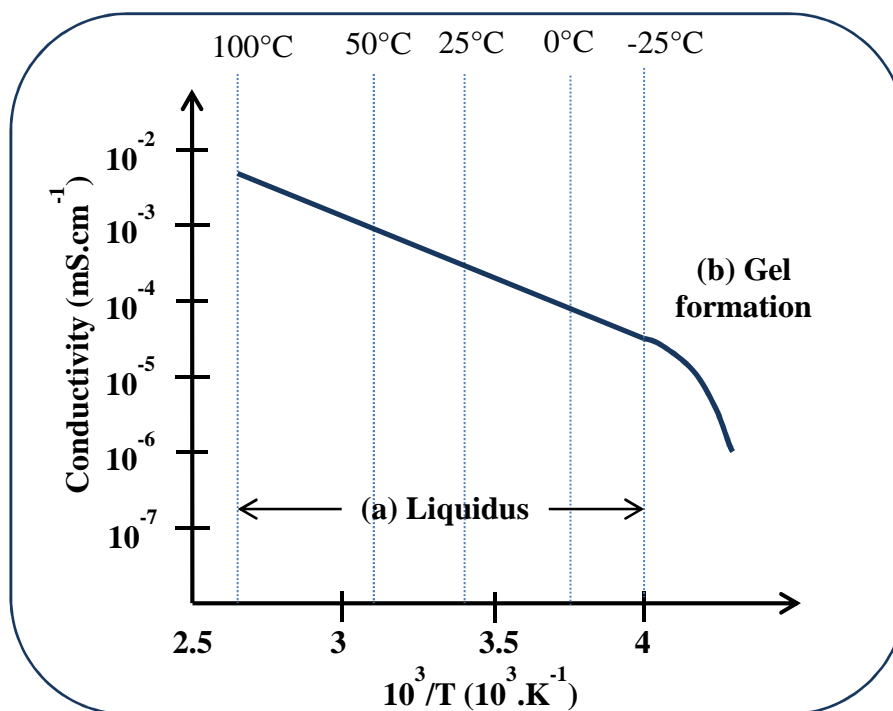
Figure I- 11: Arrhenius plots of conductivity against the inverse of temperature in a liquidus range **(a)** and gel formation range **(b)**.

Both Arrhenius and VTF equations are also used to explain the temperature behaviour of other physical magnitudes, including viscosity, diffusion constant and electrical conductivity [115].

As ionic liquids are made up solely of ion pairs, conductivity is lowered due to the ability to diffuse through fluidic flow without ionic current flow. Hence in order to describe the notion of dissociation, three classical equations have been considered in understanding and defining the properties of ILs [112]:

(1) The Nernst-Einstein equation connecting diffusion and partial equivalent ionic conductivity, λ_i,

$$\lambda_i = \frac{RT z_i D_i}{F^2} \qquad \text{(Eq I- 8)}$$

Where F is the Faraday (charge per equivalent)

(2) The Stokes-Einstein equation relating diffusivity D_i, of the ionic species *i*, of charge z_i and radius r_i, with viscosity η of the medium in which the diffusion is taking place,

27

$$D_i = \frac{k_B T}{6\pi\eta r_i} \quad \text{(Eq I- 9)}$$

(3) The Walden rule relating viscosity and equivalent conductivity, $\Lambda = \Sigma\lambda_i$,

$$\Lambda\eta = const \quad \text{(Eq I- 10)}$$

Both the Stokes-Einstein relation and the Walden rule are being interpreted the same way such that the hindering force against the motion of ions is attributed to the viscous force of the solvent/counter ions through which the co-ions move. While the Stokes-Einstein relation (Eq I-9) correlates well to most pure non-viscous liquids [116], the Walden rule relates well for the slightly more viscous (10 to 600 centipoise) ILs [112], presented by Xu *et. al.* [117] (see Figure I- 12).
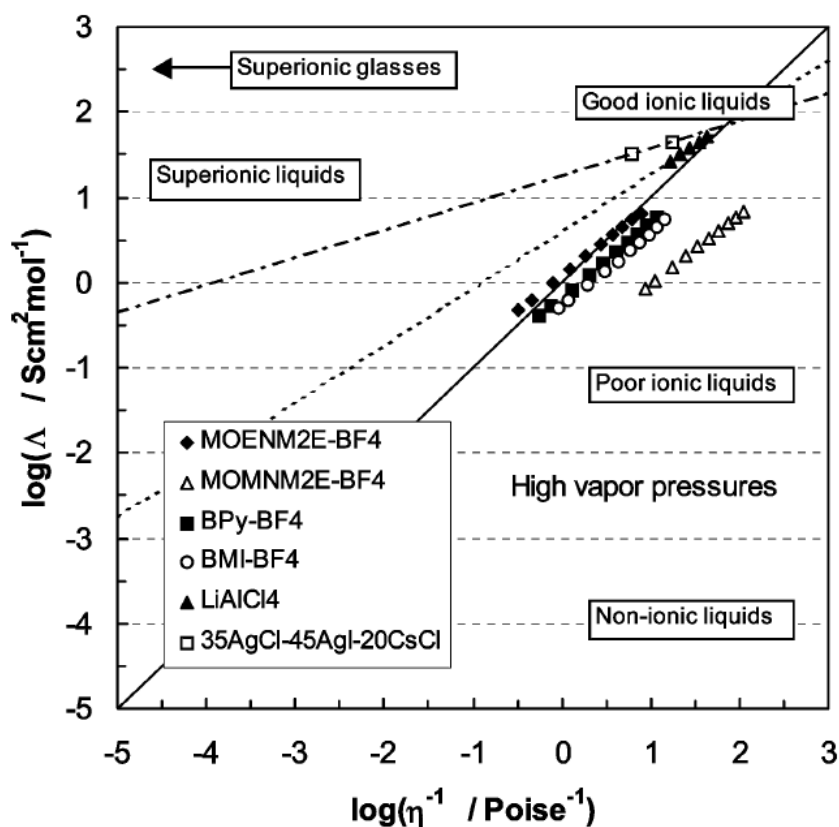
Figure I- 12 : **Walden plot as a classification for ILs and other electrolytes** - for various salts of tetrafluoroborate, BF_4^- and chloride, Cl^- from [117].

Walden plot – Walden plot is often presented with axes of equivalent conductivity in $Scm^2.mol^{-1}$ against fluidity in $Poise^{-1}$ (reciprocal of viscosity) for simplicity sake, with a diagonal line that link the opposite corners of the plot. This diagonal represents the 'ideal' Walden line in the situation where ions are fully dissociated and have equal mobility [118]. Slope deviation from this ideal line provides information on the decoupling extent of the

electrolyte ions. Hence, the Walden plot gives a direct first hand classification of ILs and electrolytes by the regions marked out in Figure I- 12, with top right region giving good ILs and the left, superionic liquids and glasses (upper side of the ideal line) being the more desirable electrolytes.

The composition and associated properties of IL depend on the cation and anion combinations: there are literally millions of different structures that may form an IL, the number of cation-anion combinations is estimated to be as high as 10^{18} [119]. ILs can thus be strategically designed by alternation of anions or the alkyl groups of cations for each particular application. There are three basic main classes that are specific to different types of applications: (1) Aprotic, (2) Protic and (3) Zwitterionic as shown in Figure I- 13.
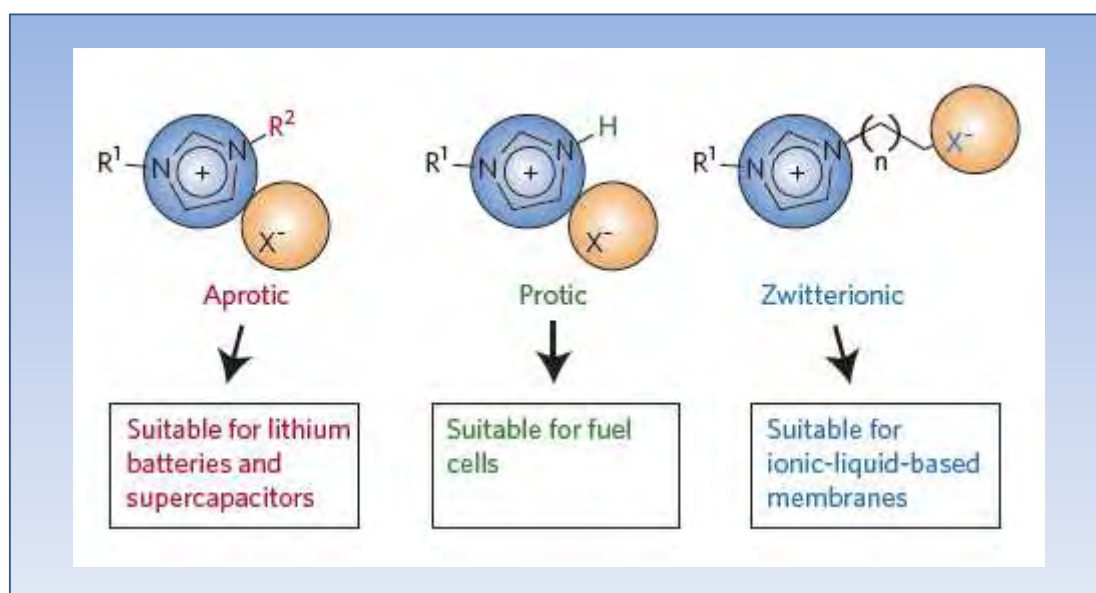
Figure I- 13: Design of Ils for specific applications [95].

Protic ILs offer aqueous like conductivities and serve as good electrolytes for fuel cells. The cation has been formed by transfer of a proton from a Brønsted acid to a Brønsted base, in a reversible process. This proton transfer process is incomplete, leaving an equilibrium fraction of the neutral acid and base as independent species present in the liquid [120]:

$$HA + B \Leftrightarrow [BH]^{+} + A^{-} \qquad \text{(Eq I- 11)}$$
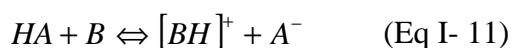
The conductivity hence depends on the gap for the protons to jump for reformation of the original molecular liquids. The gaps have to be optimized as too small a gap will cause low conductivity and too large will result in proton residing more on the cations, thereby

lowering the conductivity too. However, protic ILs are generally more fluid than aprotic ones [121].

Zwitterionic ILs consist of both anion and cation tethered in an intra-molecular form, so that the migration of IL component ions is inhibited [122]. There is an increase in melting temperature as compared to other classes as degree of freedoms decrease due to intermolecular bonding between cationic and anionic moieties. These compounds were first pioneered by Ohno and co-workers and they have reported that the addition of other salts such as LiTFSI, results in only a glass transition temperature and this observation is attributed to the shielding effect of the TFSI⁻ anion [123]. In a complementary way, zwitterionic ILs serve as ion-dissociators as well such as in anionic polymerization of styrene where the addition of buytl imidazolium butane sulfonate zwitterion provides better dissociation of the metal cation based initiators in an aprotic IL as solvent, increasing the yield by more than 50% compared to synthesis carried out in the absence of zwitterions IL and an aprotic IL solvent [124]. It was also reported that the use of zwitterionic *N*-methyl-*N*-(butyl sulfonate) pyrrolidinium largely enhanced lithium-ion diffusivity in polyelectrolyte gels [125]. The mechanism behind the enhancement of lithium-ion transport by the zwitterionic liquid is clear and it has been suggested that it may occur by shielding ion–ion interactions, thereby increasing dissociation.

Aprotic ILs is one of the most heavily researched class among the three classes especially on the cations [100,102, 111,117,126,127, 128] and are the subjects used extensively in this work.

IV-4. Aprotic ILs

There is a huge interest in increasing the cell voltage above 3 V. Under such conditions, EDLCs would not be able to keep up with its cyclability reputation because the electrochemical stability window of organic solvents decreases with increasing temperatures and also, the increase in maximum cell voltage significantly reduces the cycle life. Hence ILs, being reputed for wide electrochemical stability and high thermal stability, are immensely studied for the above mentioned interest.

The key point about ILs is that they are liquid salts, which means they consist of a salt that exists in the liquid phase. They have to be manufactured and are not simply salts dissolved in solvent. The common building blocks of ILs that bring more variety (different properties) to existing electrolytes are shown in Figure I- 14.
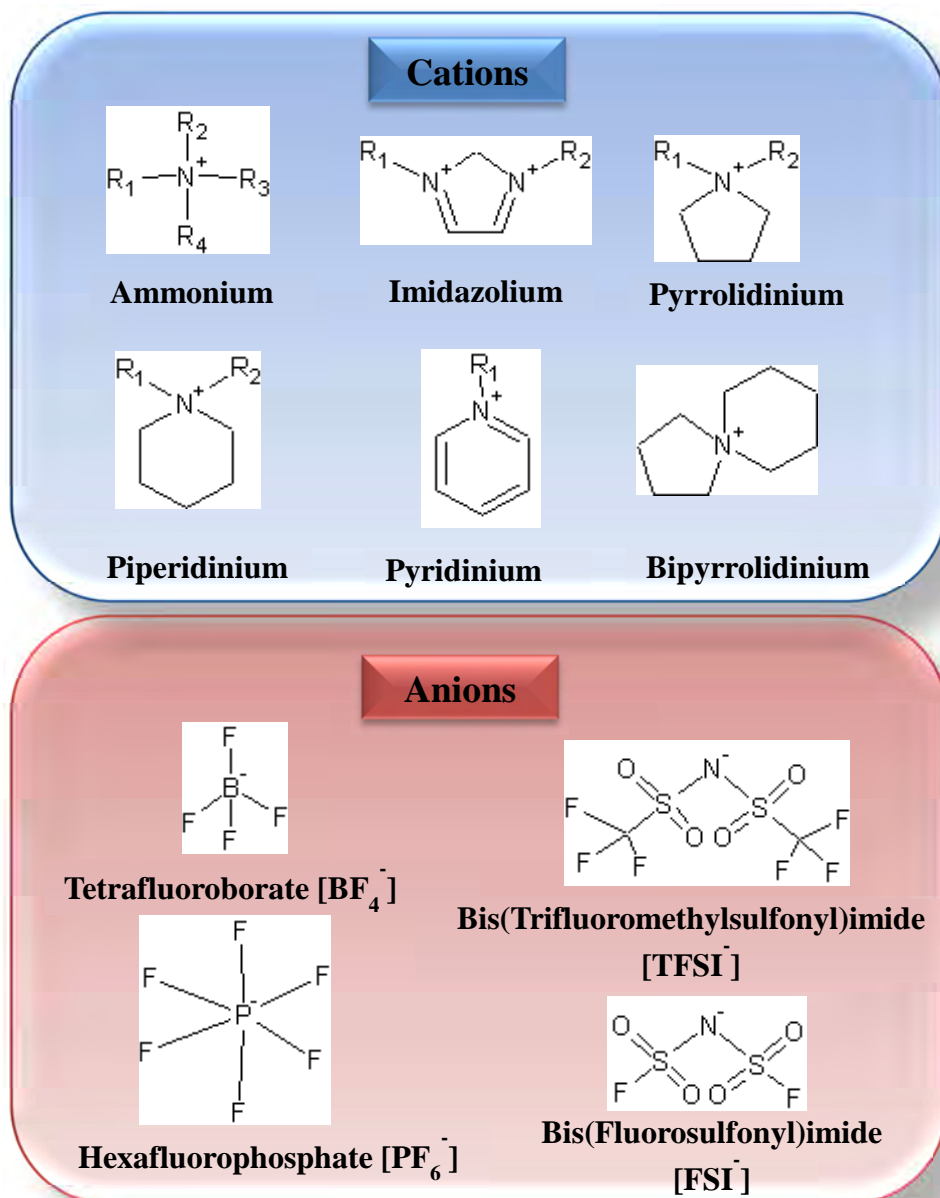
Figure I- 14 : Common building blocks of ILs – Cations (Upper panel) and anions (Lower panel). R groups may take on hydrogen atom or different alkyl groups such as methyl, ethyl, propyl, butyl etc.

Figure I- 14 showcases some cations and anions that have been attracting a lot of attention due to the ease of producing and designing them to the required standards for electrochemical processes.

Cations - For a given anion with a range of cations, conductivity generally decreases in the order: imidazolium > pyrrolidinium > ammonium > pyridinium [129,130], and this has been reported to be attributed to the planarity of the cationic core of the imidazolium ring rendering a higher conductivity as compared to the more bulky tetrahedral arrangement of

alkyl groups in the ammonium salts while the pyrrolidinium-based cations adopt an intermediate geometry and hence conductivity [131]. In electrochemical aspects, the overall trend in electrochemical stability of ILs with respect to the cations follows the order: ammonium ≈ piperidinium ≥ pyrrolidinium > imidazolium [129].

Anions - Little variation in properties might be expected between common cation salts of PF_6^- and BF_4^-; except for their miscibility: for example, BMI-PF_6 is immiscible with water, whereas BMI-BF_4 is miscible with water. Such difference allows a variety of solvents to be designed [132]. For EDLC applications, water contamination in electrolytes can cause detrimental consequences to the cycle life and performance of the devices. While ILs based on PF_6^- are generally less hydrophilic than that based on BF_4^-, it has been reported that the presence of water traces produces HF at elevated temperatures [133]. This drawback has been overcome by the use of $TFSI^-$ and FSI^- anions. Despite the presence of fluorine like in PF_6^- and BF_4^-, the fluorine atoms of the $TFSI^-$ and FSI^- anions are bonded to carbon and C-F bonds are inert against hydrolysis to form HF. Thus, IL based upon these imide and related anions are being marketed [134]. However, fluorinated anions such as these tend to be expensive, especially for use on larger scales.
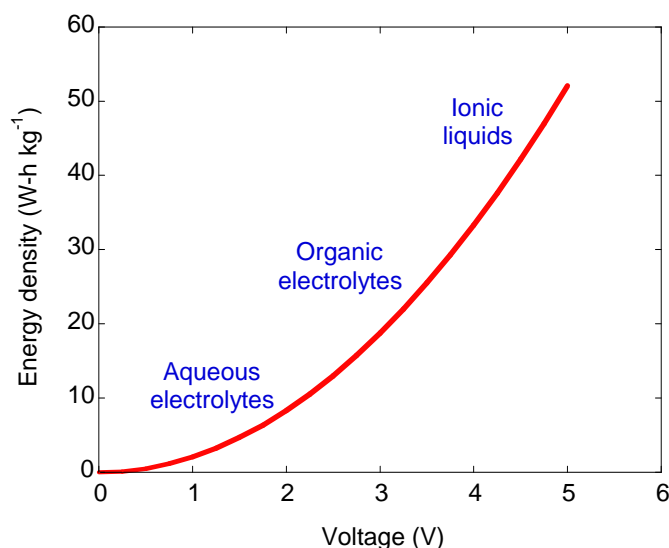
Figure I- 15: Graph depicting the increase of energy density with ILs compared to other electrolytes.

The advantages of these electrolytes are manifold, they are non-corrosive, the typical conductance is ranges from few to around 20 mS.cm^{-1}, and the electrolytes can be used up to high temperatures of about 150 °C. Especially important in light of upping device capabilities, ionic liquids themselves possess large intrinsic capacitance and wide voltage windows (up to

6.0 V) [135], which makes them the potential electrolytes for devising high-energy electrochemical capacitors compared to other existing electrolytes as depicted in Figure I- 15.

The implementation of ILs in supercapacitors have been extensively investigated and studied in both activated carbon double layer capacitors as well as in hybrid polymer supercapacitors [136]. Some examples include reports by (1) Balducci *et al.* [136] on the use of microporous activated carbon and *N*-butyl-*N*-methylpyrrolidinium bis(trifluoromethanesulfonyl)imide (PYR$_{14}$-TFSI) ionic liquid as the electrolyte, yielding a specific capacitance of 60 F.g^{-1} at a typical scan rate for EDLC at 20 mV.s^{-1}, with a maximum operating potential range of 4.5 V at 60 °C. (2) Lewandowski *et al.* [137] where 1-Ethyl-3-MethylImidazolium Tetrafluoroborate (EMI-BF$_4$), PYR$_{14}$-TFSI and 1-Butyl-3-MethylImidazolium hexafluorophosphate (BMI-PF$_6$) were used in hybrid supercapacitors as polymer dissolved in IL electrolytes. Specific capacitance was in the range of 4.2-7.7 μF.cm^{-2}, expressed in terms of total surface of the carbon materials, and up to 200 F.g^{-1} expressed in terms of carbon material mass at room temperature. (3) Zhu *et al.* [38] with the use of neat RTILs namely EMI-TFSI and BMI-BF$_4$ in carbon electrodes produced by activation of graphene, measured 200 F.g^{-1} at 3.5 V at room temperature when EMI-TFSI was used as the electrolyte. In general, the electrochemical stability of ILs measured using glassy carbon electrode is reduced by almost 1 V when used in carbon electrodes of high SSA, however other properties of the ILs are usually preserved as shown by Le bideau *et al.* [138] when ionic liquids are confined in monolithic silica.

Despite the high energy densities offered by the wide electrochemical stability of the ILs, there is always a compromise in power capability of the EDLCs due to the high resistance incurred owing to the high viscosities and lower conductivities of ILs in general. Attempts have been made [139] by adding solvents such as propylene carbonate (PC) or Acetonitrile (AN) to ILs to improve conductivity (60 mS.cm^{-1} for AN) and eventually power, but it is noteworthy that the electrochemical window which can be accommodated has to be kept within that of AN or PC which in turn limits the energy density capacity (see Figure I-15). Hence, to fully benefit from the maximum electrochemical stability of RTILs, most reported use of RTILs in EDLCs with porous electrodes are usually at elevated temperatures of ≥ 60°C [140] to reduce the electrolyte viscosity, enhance ionic mobility and thereby keeping ESR values low [141].

IV-5. Eutectic IL mixtures as electrolytes

In view to widen the operating temperature range (decreasing melting and/or glass transition temperatures) similar to that of organic electrolytes, while retaining the interesting electrochemical properties of RTILs, attempts of mixing ILs have been carried out. Binary eutectic systems first surfaced with the discovery by Wilkes et al. in 1982 [98] of a molten salt which was liquid over a wide range of compositions and to temperatures as low as −95 °C. Interest in this field of research has increased since with reported studies of *binary and ternary* eutectic systems based on the different functional groups of ILs, in search of better combined and new properties that these eutectic mixtures stand to offer.

Binary systems have been investigated by Hou *et al.* [142] using imidazolium-based ILs with organic salts. Every *et al.* [143] reported a eutectic mixture of pure ILs (mixing EMI-TFSI and EMI-Tf (triflate)) with no evidence of a melting point, only with a glass transition observed. Pyrrolidinium-based mixtures with TFSI-FSI-based ILs (see Figure I- 16), were also found to form eutectic mixtures [144] by performing differential scanning calorimetry. Deeper eutectics (-95 °C) were however observed to be mainly in mixtures of common cation with two different anions (Figure I- 16B) compared to eutectics (-25°C) in mixtures of common anion with two different cations (Figure I- 16A).
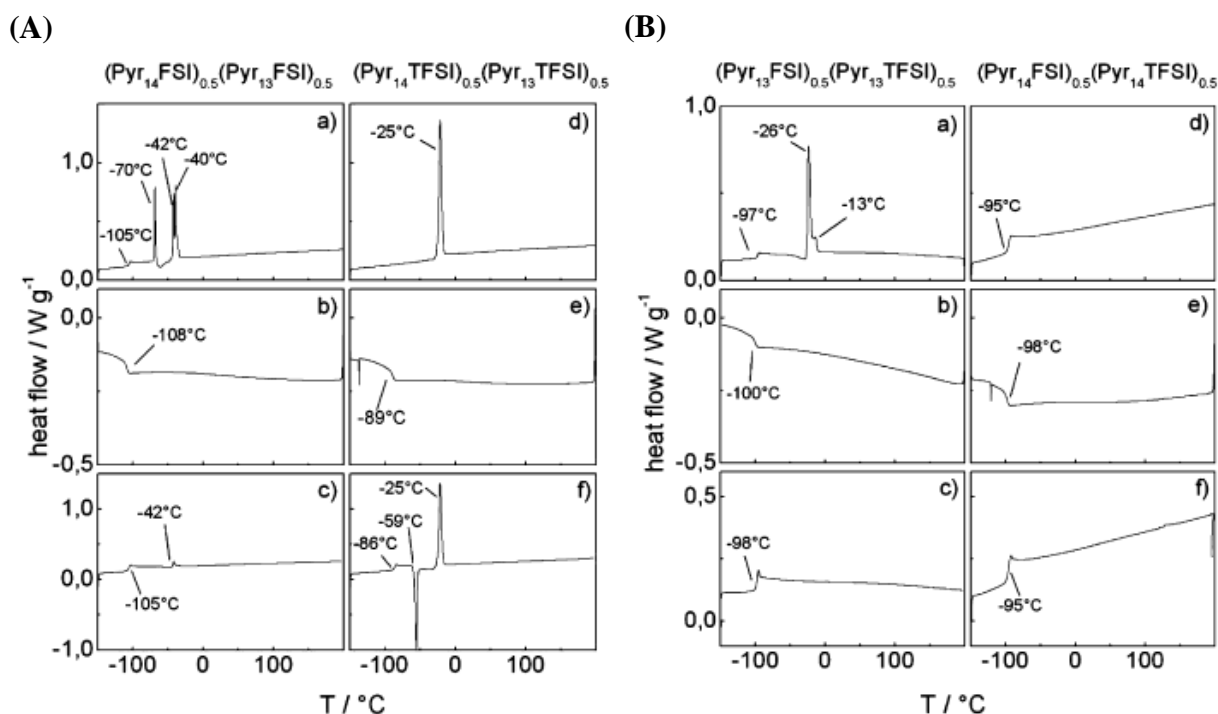
Figure I- 16 : DSC Heating and cooling cycle of the mixtures based only on one anion and two different cations (A) - $(Pyr_{14}FSI)_{0.5}(Pyr_{13}FSI)_{0.5}$ (a-c), $(Pyr_{14}TFSI)_{0.5}(Pyr_{13}TFSI)_{0.5}$ (d-f) and based only on one cation and two different

The three columnar panels (vertical down), in Figure I- 16A and B report the slow cooling (a and d) at 2 °C.min^{-1}, fast cooling (b and e) at 10 °C.min^{-1} profiles from 40 °C and heating profiles (c and f) at 10 °C.min^{-1} from -150°C of each mixture. From the slow cooling and fast heating of the four mixtures in panels a,c,d and f, melting transitions for are all lower than that of the pure ILs (PYR_{13}-FSI at -9 °C, PYR_{13}-TFSI at 10 °C, PYR_{14}-FSI at -18 °C and PYR_{14}-TFSI at -7 °C) . Reduction of melting and glass transition is seen to be more prominent in fast heating/cooling of common cation mixture – two anions system (Figure I-16B(b,c,e,f)). In the mixture of different cations and anions, only one glass transition has been observed, with the glass transition temperatures (~ -95°C) in agreement with mixtures with only one cationic species [144].

Other binary systems include IL-LiX mixtures as electrolytes for batteries applications [145,146,147]. Figure I- 17 shows the phase diagrams of pyrrolidinium-based ILs with different side chain lengths and Li salt concentrations.
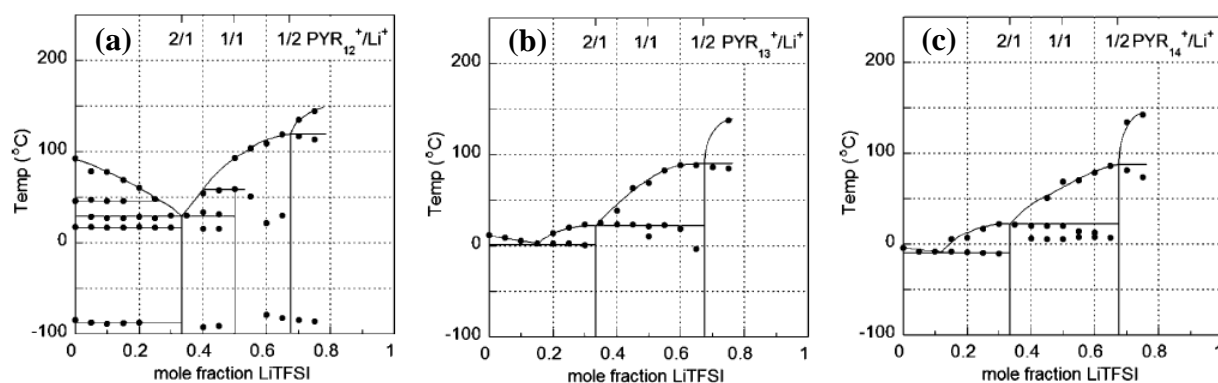
Figure I- 17 : $(1 - x)PYR_{1R}TFSI$-$(x)LiTFSI$ phase diagrams. R= 2**(a)**, R=3 **(b)** and R=4 **(c)** [145].

In this figure, eutectic temperature decreases with increasing alkyl chain on the pyrrolidinium-based cations. It was explained to be due to the prevalent Van der Waals force influencing the viscosity of these binary eutectic mixtures as the linear alkyl chain length on the N atom of the cations increases [142]. Furthermore, steric shielding of the cations increases with the alkyl chain length, anions are thus weakly attracted to the cations, hence decreasing the tendency to crystal structure formation [148]. All or some of the TFSI$^-$ anions may be coordinated to the Li$^+$ cations [145].

Ternary systems using Li salts are also explored [149,150].
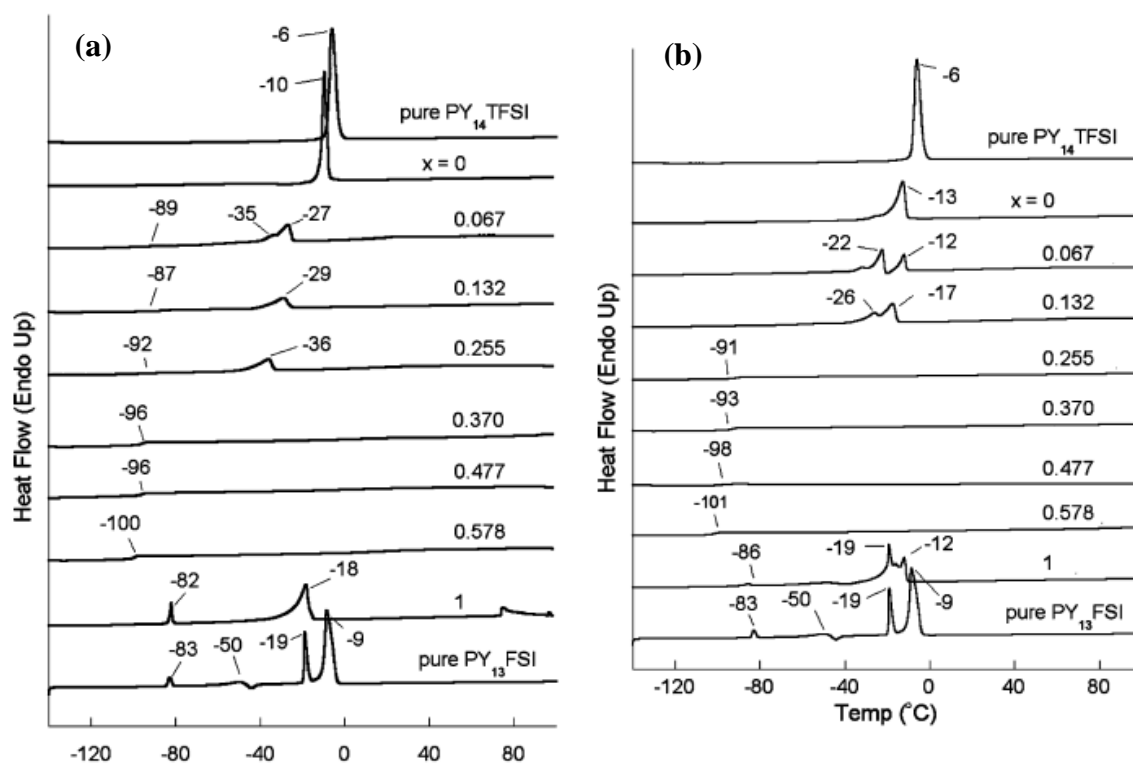
Figure I- 18: DSC heating traces (5 °C min^{-1}) of (1-x) PY$_{14}$TFSI-(x) PY$_{13}$FSI - 0.3 M LiX mixtures: (a) X = TFSI$^-$ and (b) X = PF$_6$ [150].

As shown in Figure I- 18 reported by Zhou *et al.*, the addition of small amounts of *N*-methyl-*N*-propylpyrrolidinium bis(fluorosulfonyl)imide (PY$_{13}$FSI) to *N*-butyl-*N*-methylpyrrolidinium bis(trifluoromethanesulfonyl)imide (PY$_{14}$TFSI)-lithium salt (LiTFSI or LiPF$_6$) binary mixtures increased the discrepancies of cationic forms and hence hinders their the ability to pack and crystallize. This results in a much improved conductivity at sub-ambient temperature for the mixtures relative to that the binary IL-LiX electrolytes at low temperatures.

Eutectic mixtures based on ILs increase further the combinations from just one cation and one anion as mentioned in building blocks of an IL. They allow the combination of all the desired electrochemical properties with a gain in the range of the operating temperatures.

V. State-of-the-art of EDL studies: Pore-ion size relationship

V-1. Solvated environment

The initial interest in mesoporous carbons lies in the belief that pores substantially larger than the size of the electrolyte ion and its solvation shell are required for high

capacitance. Mesoporous carbons can be synthesized with controllable pores in the range of 2 to 4 nm by template techniques [151]. Despite the fine-tuning of mesopores in carbon in view to increase power capability and energy density, mediocre improvement have been achieved with gravimetric capacitance in the range of 100–120 $F.g^{-1}$ in organic and 150–200 $F.g^{-1}$ in aqueous electrolytes [152,153]. As diameters of the mesopores are usually larger than that of the electrolyte ions, this improvement was accredited to improvement in ionic mass transport inside mesopores [16]. Moreover, the micropores of an electrode were deemed as voids that do not participate in the formation of EDL due to the inaccessibility of the microporous walls to the large solvated ions.

However, Ti-CDCs has stormed a breakthrough with enhanced specific capacitance of 50% more than AC-based EDLCs, at pore sizes less than 1 nm (in the microporous regime) [154] as shown in Figure I- 19.
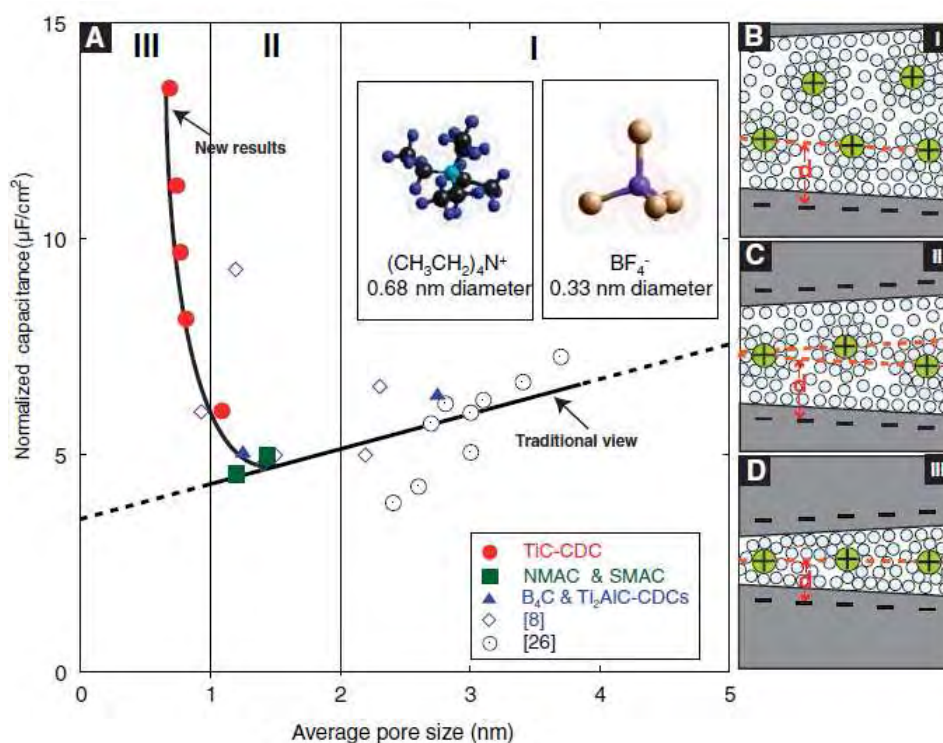
Figure I- 19: Plot of specific capacitance normalized by BET SSA for Ti-CDCs **(A)**. **(B to C)** Drawings of solvated ions residing in pores with distance between adjacent pore walls greater than 2 nm **(B)**, between 1 and 2 nm **(C)**, and less than 1 nm **(D)** [154].

It was not until this discovery of capacitance increase using micropores of sizes smaller than 1 nm that the traditional belief that carbon pore sizes ought to be larger than the size of the solvated ion for improved capacitance was overturned. The reported maximal capacitance (140 $F.g^{-1}$ in organic electrolyte) for Ti-CDCs (1000-1600 $m^2.g^{-1}$) greatly surpassed that obtained by most of today's commercial devices which use microporous

activated carbon-based electrodes in conventional non-aqueous electrolytes with cell voltage up to 2.7 V (100 F.g^{-1} and 50 F.cm^{-3}). This improvement in capacitance is due to the ability to tune the Ti-CDCs to a narrow pore size distribution as compared to the commercial microporous activated carbon. In spite of the high surface area measured (3000 m^2.g^{-1} for AC versus 1600 m^2.g^{-1} for Ti-CDCs), improvement on capacitance in the commercial microporous AC was little because not all of the area of the carbon can be fully accessible due to their diversified pore size distributions. These findings then drew suggestions that these adsorbing electrolyte ions might be partially desolvated in order to gain access to the Ti-CDCs micropores as illustrated in Figure I- 19D, resulting in the escalated capacitance values for pore sizes below 1 nm. Following studies by Raymundo-Pinero *et al.* [155], observed similar escalated capacitance, confirming that there are important surfacial contributions from micropores to the overall capacitance.

Further understanding of this observation was then carried out in a 3-electrode cell configuration in view to obtain more specific values with respect to the anode and cathode capacitances.
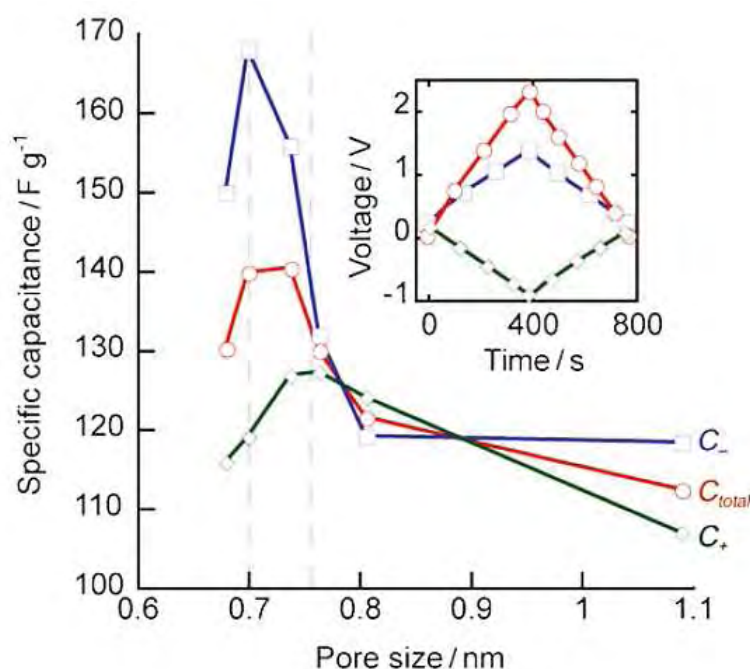
Figure I- 20 : Dependence of the capacitance on the pore size. The specific capacitances calculated from a constant current discharge (inset, colours as for main plot) for the anion/positive electrode (C_), cation/negative electrode (C_+) and the cell [156]; Electrolyte = 1.5 M NEt4BF4 in AN

By using the Ti-CDCs as model (with the ability to tune the pore sizes with good accuracy) for sieving out the effective ion sizes of adsorbing electrolyte ions, Chmiola *et al.* reported and confirmed that ions are partially stripped off of their solvation shell when

entering the pores of the electrodes and that the adaption of pore size to effective ion size does has an effect on the capacitance [156].
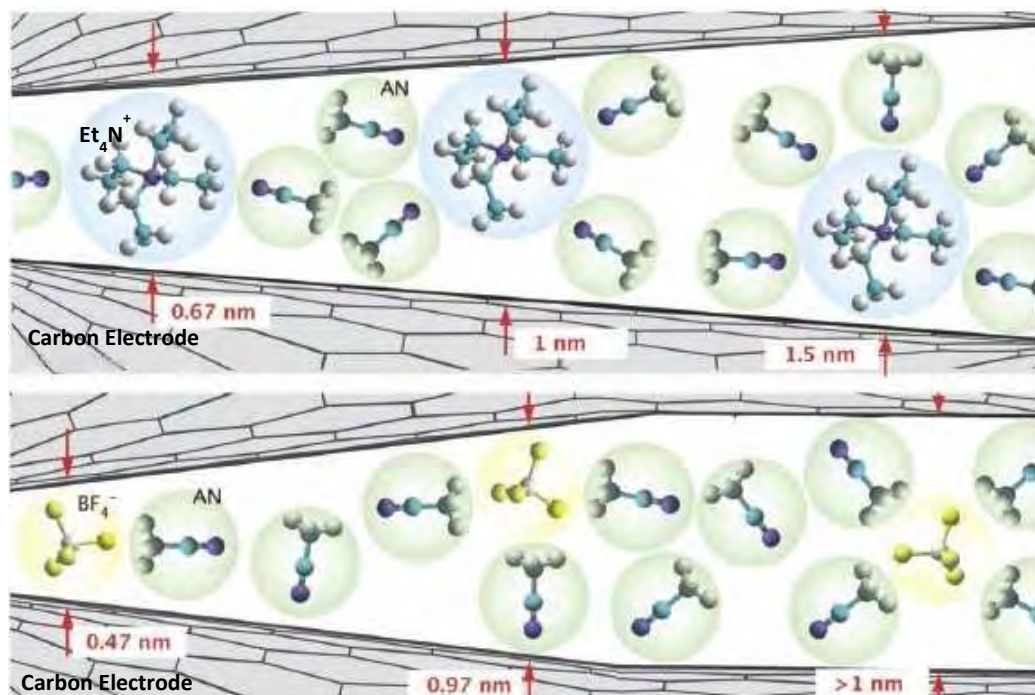
Figure I- 21 : Geometric confinement of ions in extremely small pores. Both anions and cations enter the pores with no solvent-molecule screening charge at pore sizes below 1.5 and 1 nm, respectively. Therefore, it can be asserted that in all our experiments, the ions enter the pores either bare or with partial solvent shells (NEt_4^+ = tetraethylammonium, AN = acetonitrile [156]

In this paper, the capacitance discrimination from the individual electrodes allows the identification of the pore size that enhanced capacitance for the respective cations (NEt_4^+) and anions (BF_4^-) dissolved in AN as a solvent. Optimum pore size for the ions has been deduced to be: $NEt_4^+ > BF_4^-$ (see Figure I- 20).

Computer simulations have been geared up into the study of enhanced capacitance observed by Chmiola and Largeot *et al.*, sprouting a significant number of publications on the quest for fundamental understanding of pore-ion size relationship. In the sequel of understanding the electrolyte/carbon interaction, Tanaka *et al.*[157] demonstrated that the effective size of ions could be estimated through Reverse Monte Carlo (RMC) simulations fitted from XRD experimental data using NEt_4^+ and BF_4^- ions in PC solvent as electrolyte in pitch-based activated carbon fiber. Simulation results are in compliance with those based on random sampling by Tanaka *et al.* [157]. Such molecular dynamics modelling could help to increase the comprehension of the effect of salt concentration in an electrolyte and the effective ion size based on experimental data.
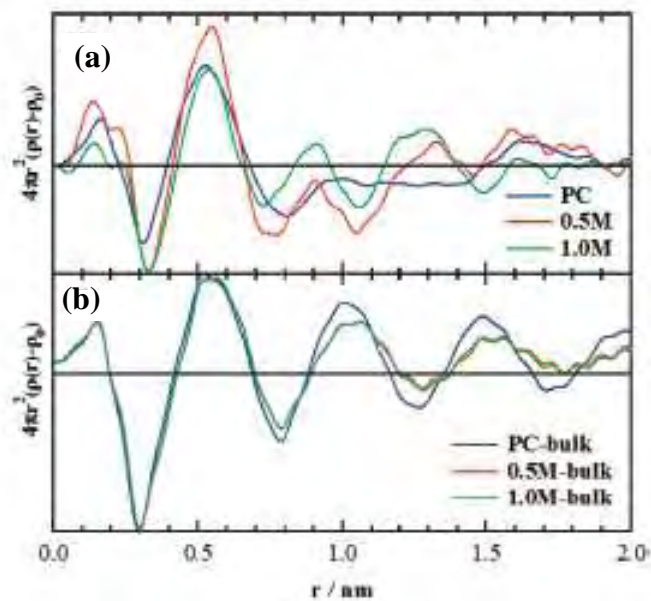
Figure I- 22: ERDFs of confined (a) and bulk (b) NEt$_4$BF$_4$/PC solutions at 303K [157].

Figure I- 22a shows the electron radial distribution functions for PC molecules in confined pores. Upon the addition of the salt, apparent peaks are observed between 0.7 to 1.3 nm due to induced ordering of PC molecules by the salt.
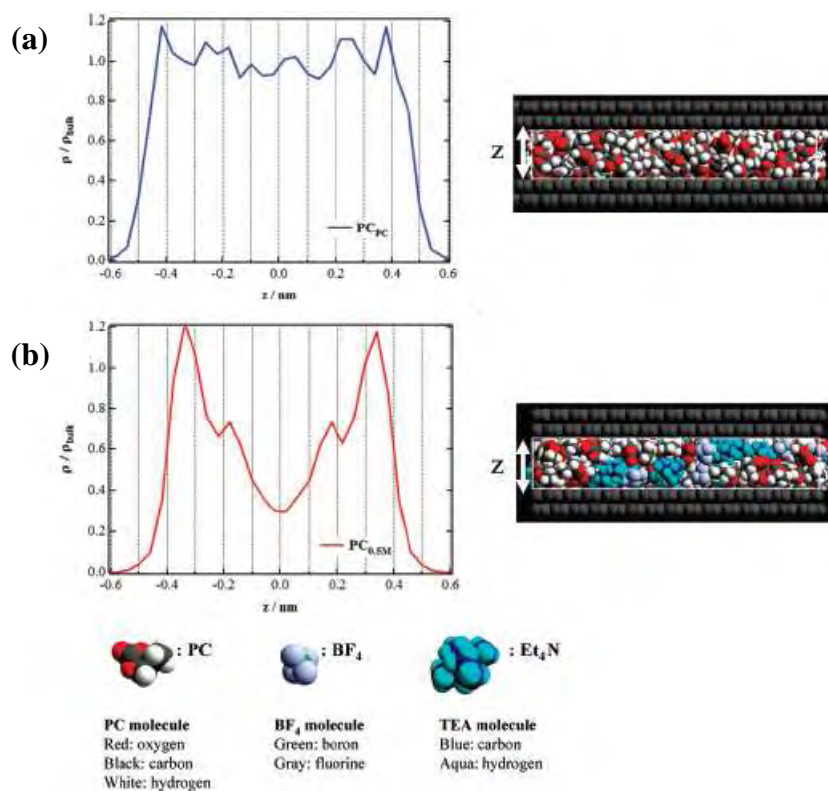
Figure I- 23: Snapshots and distribution of PC molecules and electrolytes along the pore width. Pure PC (a); NEt$_4$BF$_4$/PC solution corresponding to 0.5 M (b). The coordinate z along the pore width is shown by an arrow [157].

Once the fitting of the model and experimental data has been optimized, the RMC simulation proposes structural images as shown in Figure I- 23. Through this demonstration of the RMC, information attained from such fitting and modelling could allow more concrete estimation of the effective ion size (z-value) and is in agreement with the results obtained by the fast and efficient CME technique, with the effective ion size to be more than 1 nm [158]. Profound peaks depicted in Figure I- 23b suggest that in with the presence of the salt in the solvent, the PC molecules are located closer to the carbon pore wall which infers that a solvent structure (in the presence of a salt) different from that of the bulk exists. These results, published in 2010, was one of the first explanation of the effective confinement of ions, providing for better understanding of the adsorption phenomenon and situation given a specific type of carbon (for example a slit-shaped pore in this case) and the effect of salt in a solvent (NEt_4BF_4 in PC).

V-1.1 Electrochemical Quartz Crystal Microbalance (EQCM) studies

Adsorption/desorption mechanism and solvation situations have been intensively investigated using the Electrochemical Quartz Crystal Microbalance (EQCM) technique which probes the mass change arising from compositional changes in micropores of the electrodes such as solvation. Several conventional electrolytes such as NEt_4BF_4 dissolved in PC and aqueous tetra-ammonium salts for supercapacitors have been studied using EQCM, through the direct monitoring of the fluxes of ionic carriers in the electrodes during the charge/discharge cycles in microporous carbons [159, 160].

Whilst CVs are being collected (Figure I- 24a), the EQCM tracks the minute frequency response (Hz) concurrently throughout adsorption and desorption cycles under the application of external voltage. The CVs account for the theoretical mass change in $\mu g.cm^{-2}$ (calculated from Faraday's law) due to the ion fluxes since current response is directly registered from the migration of point charges. Simultaneously, the frequency response from EQCM is translated into experimental mass change and adsorbed ions. These measurements holds information on the solvation environment through different regimes of applied potential, that is, near the OCV, or at the extremes of the electrochemical stability window of the electrolyte.

(a)

(b)
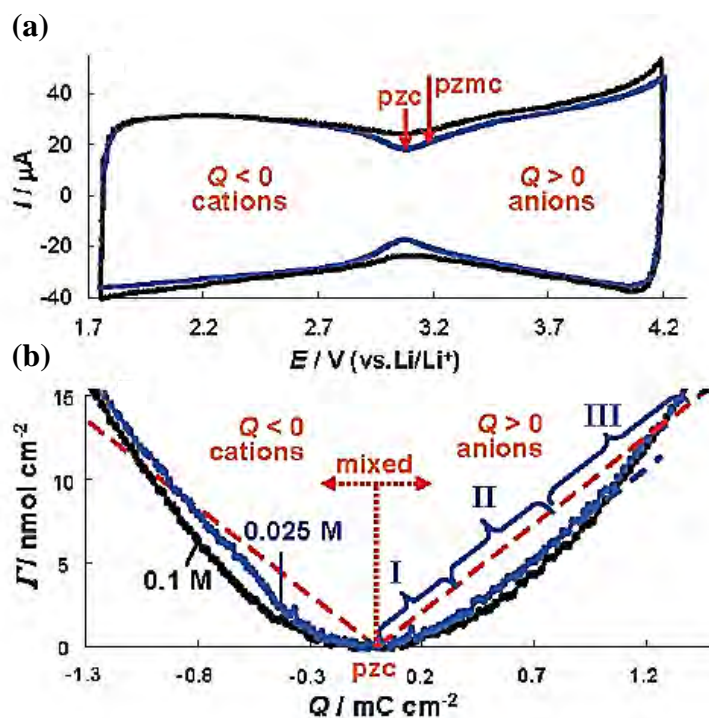
Figure I- 24: CVs of a carbon-coated quartz crystal electrode in 0.1 and 0.025 M NEt$_4$BF$_4$/PC solutions (A), and the related treated EQCM responses, Γ vs Q (B). Three domains with the characteristic different Γ/Q slopes for the 0.025 M solution are indicated. The slope within domain II (the broken blue line) is equal to the theoretical slope of the broken red straight line calculated from the Faraday law [160].

Figure I- 24 shows EQCM measurements reported by Levi *et al.* [160], with frequency response that is translated into the amount of adsorbed ions, Γ, as shown in Figure I- 24b in an electrolyte of NEt$_4$BF$_4$ in PC at different concentrations. The theoretical mass change is obtained from calculation by faraday's law from the recorded CV in Figure I- 24a. The three domains labeled I, II and III mark the different slope deviation from that of the theoretical one (dotted red line). In domain I, the slope of Γ/Q_{exp} < Γ/Q_{theo} , Γ/Q_{exp} increases gradually when the electrode is gradually positively polarized. As the BF$_4^-$ anions entering the pores are in a 'mixture region' with the NEt$_4^+$ cations exiting, this results in the slope deviation from the theoretical value. In domain II, Γ/Q_{exp} ≈ Γ/Q_{theo} indicating partial desolvation of the BF$_4^-$ ions in micropores of less than 1 nm, as observed in previous findings by our team on [154,156] for the same salt in AN as solvent. In domain III, increase of Γ/Q_{exp} > Γ/Q_{theo} suggests the breathing effect of carbon due to C-C elongation, that allows the entry of solvent molecules into the electrode at high potentials.

V-1.2 Nuclear Magnetic Resonance (NMR) Studies

Real time observation of ion migration and binding towards porous carbon surfaces was achieved through the *in-situ* NMR technique using [11]B [161]. In this work, Wang *et al.* overcome the hassle of disassembling the supercapacitor cell, risking the loss of accuracy of the analysis due to the several possible processes that can likely occur (discharging, evaporation of solvent) in *ex-situ* magic angle spinning (MAS) NMR investigations [162,163]. The system of study was carried out using commercial activated carbon YP 17 soaked in different amounts of 1.5 M NEt_4BF_4 dissolved in AN electrolyte. The cell is then subjected to gradual electrode polarizations for real time *in-situ* analysis of migration of ions during the charge/discharge process. Investigations through the analysis of chemical shifts and relaxation times have been reported (see Figure I- 25).
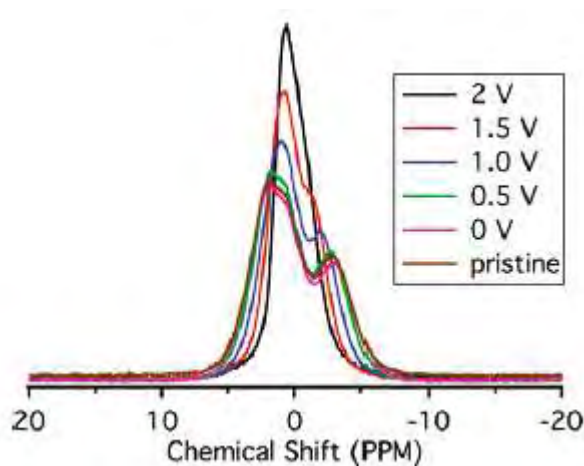
Figure I- 25: In situ ^{11}B static NMR spectra of a normal YP-17 supercapacitor held at different voltages [161].

The peaks at higher frequencies in Figure I- 25 have been ascribed to loosely bound electrolyte entities and peaks at lower frequencies to strongly bound entities of the electrolytes. During the charging of the electrode from 0 V to 2 V, the lower frequency peak attenuated gradually and shifted towards higher frequency to that of a narrow and distinctive peak attributed to weakly bound anions. This work showed that changes occur not only in the local environments, nature and the binding strength of the adsorbing anions at the surface of the electrode, but also considerable effects on weakly bound ions away from the surface. This method allows the *in-situ* study of EDL charging/discharging process by understanding the migration of ions in other systems whereby the effect of architected non-porous electrodes and/or effect of different types of electrolytes on EDLs can be unravelled.

V-2. Solventless environment

The controversy then continues to question about the degree of solvation which added on to the uncertainty if the anomalous gain in capacitance was indeed due to the proximity of both ion and pore diameters. Are the ions in the micropores partially or totally stripped off of their solvation shell? If they are not, then what is the coordination number of the ions? Do these residual solvent molecules also contribute to the elevated capacitance? What is the effective size of the ions? The implications involved in using salts in solvent in order to answer these doubts are too huge. ILs thus play an important role as solventless electrolytes for the study of the EDL in a "non-ion-associative" environment by Largeot *et al.* using EMI-TFSI ionic liquid as an electrolyte probe and Ti-CDCs [164]. This helped to provide a clearer picture of the influence of size compatibility between ions and pores on the capacitance.
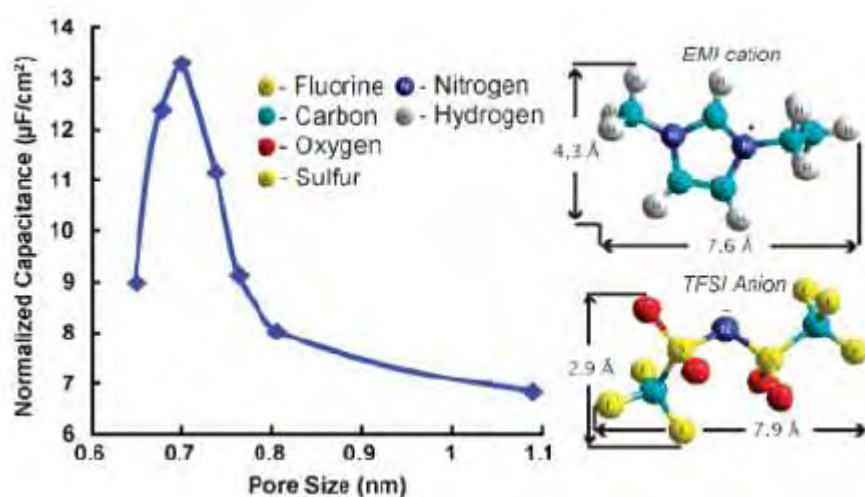
Figure I- 26: Normalized capacitance change vs the pore size of the CDC samples prepared at different temperatures; normalized capacitance is obtained by dividing the specific capacitance by the SSA. HyperChem models of the structure of EMI and TFSI ions show a size correlation [164].

An optimized capacitance value of about 160 F.g^{-1} was reported using EMI-TFSI (3 V cells) in Ti-CDCs at 60 °C as shown in Figure I- 26. The peak capacitance was measured with Ti-CDC of pore size ~0.7 nm, which corresponds to the average of the largest dimensions of both the EMI$^+$ and TFSI$^-$ ions, showing that the pore size leading to the maximum double-layer capacitance is very close to the ion size.

V-2.1. Modelling the carbon pore/geometry-ion size relationship

The extensive use of RTILs as trial electrolytes in supercapacitors triggered the study of the first few adsorbed layers on the electrode surface within the EDL. In the absence of solvents, and consisting solely of ions, the short-range coulombic correlations are strong in

RTILs. By using the Landau-Ginzburg-type continuum theory of solvent-free ionic liquids, Fedorov *et al.* [165] have investigated that two phenomenal theories apply to the adsorbing of RTIL ions to electrode surfaces owing to the strong coulombic correlations: overscreening and crowding as shown in Figure I- 27a and b respectively. Overscreening occurs when the first adsorbed monolayer has excess of charges with respect to the surface charges due to some that are counter-balanced by the second monolayer adjacent to the first at low voltages. On the other hand, overcrowding describes an excess of adsorbing ions the first two adsorbing layers and has been reported to be pronounced at higher voltages. Such a demonstration provided insights in the nonlinear polarization of ionic liquids.
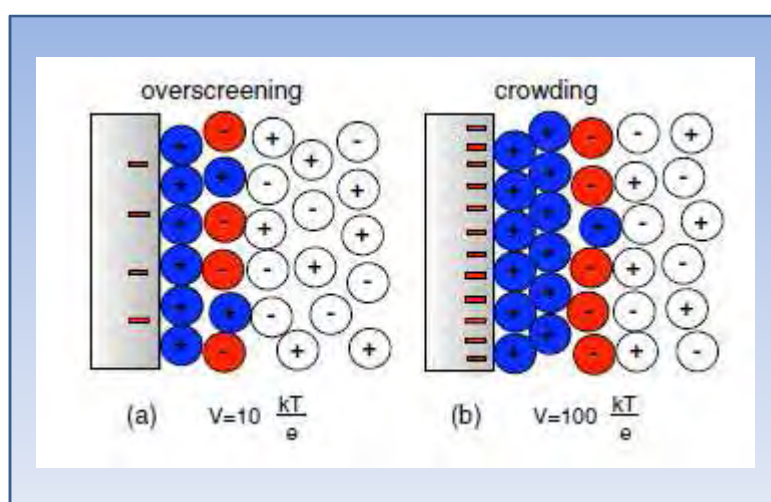
Figure I- 27 : Structure of the ionic-liquid double layer (in color) predicted by Fedorov and Korneyshev's theory and molecular dynamics simulations [165]. (a) At a moderate voltage, $V = 10k_BT/e$ (0.26 V), the surface charge is overscreened by a monolayer of counterions, which is corrected by an excess of co-ions in the second monolayer. (b) At a high voltage, $V = 100k_BT/e$ (2.6 V), the crowding of counter-ions extends across two monolayers and dominates overscreening, which now leads to a co-ion excess in the third monolayer. Because of electrostriction, the diffuse double layer (coloured ions) is more dense than the quasi-neutral bulk liquid (white ions) [166].

Following this, Merlet *et al.* [167] showed in April 2012 that by selecting correct pore size and structure, overscreening effects in IL (BMI-PF$_6$) electrolyte can be controlled by tuning carbon pore size and architecture. The study reports the local situation of the adsorbing ions from the carbon pore walls, in different architected carbons, such as graphite and porous carbons. A movie reports the charging mechanism showing exchange of ions between the bulk electrolyte and the porous electrode as shown in Figure I- 28a and b at different electrode potential.
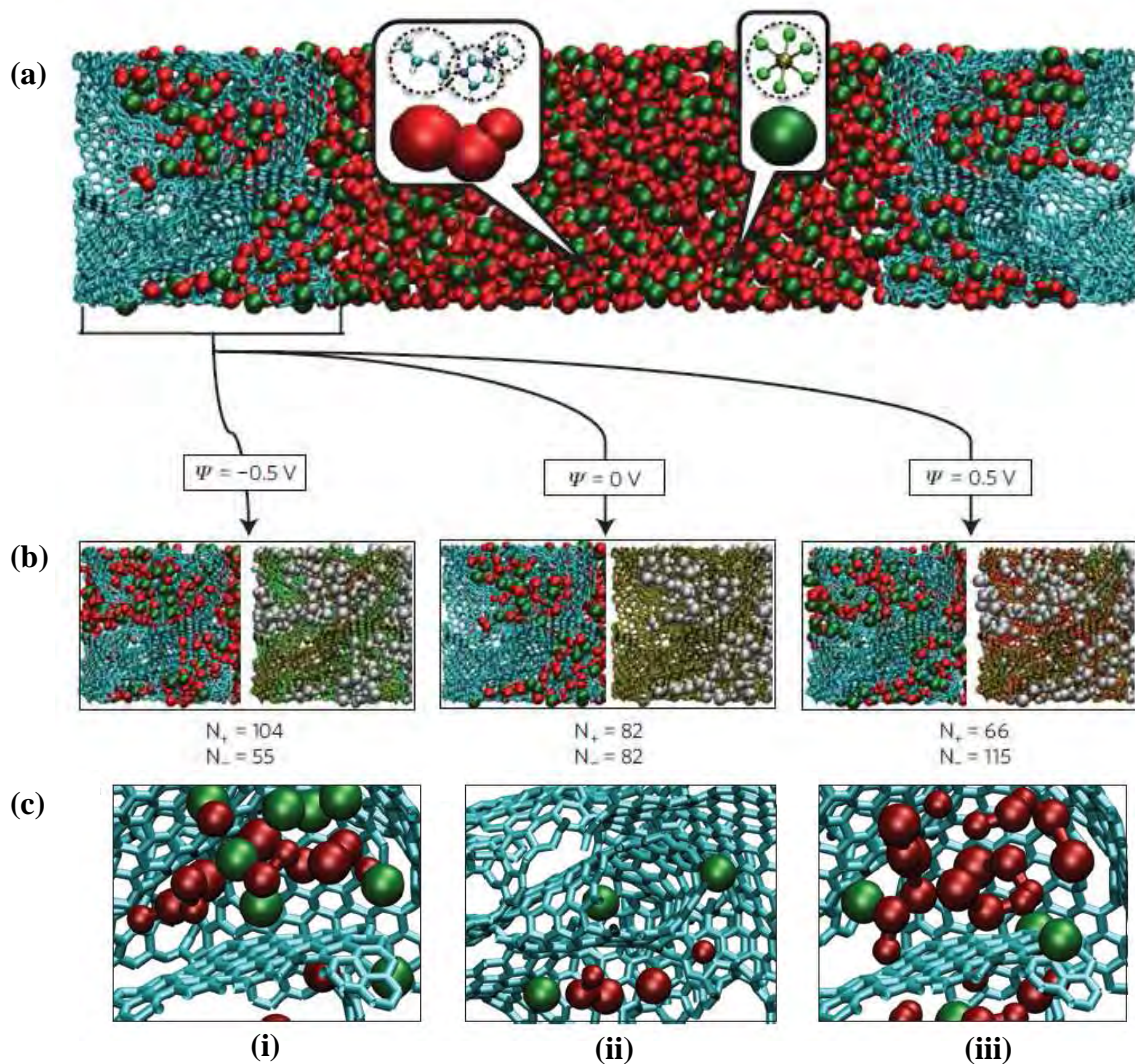
Figure I- 28: The EDLC simulation cell. The simulation cell consists of a BMI-PF$_6$ ionic liquid electrolyte surrounded by two porous electrodes (CDC-1200) held at constant electrical potentials (blue: C atoms, red: the three sites of BMI$^+$ and green: PF$_6^-$ ions) **(a)**. **Structure of the electrode for various voltages.** For each value, the same snapshot is shown twice: The ionic distribution is shown on the left. The degree of charging of the electrode atoms is shown on the right, where the carbon atoms are coloured according to the charge q they carry (green: $q < 0$, red: $q > 0$ and yellow: $q \approx 0$) **(b)**. **Typical structure of the ionic liquid inside electrified pores of the CDC-1200 material.** Blue: C–C bonds, red: BMI$^+$ and green: PF$_6^-$: Local structure near a positive surface (+0.5 V), the anionic density is enhanced **(i)**. A single anion in a nanotube-like pore positively polarized (+0.5 V) **(ii)**. same as **(i)** but near a negative surface (-0.5 V) **(iii)**. [167].

Owing to prevailing confinement effects in the narrow pores, the ionic liquid cannot adopt the same multi-layered structure as in non-porous materials like graphite, thereby storing as much charges at the electrode surface as a single chain of electrolyte counter-ions lined along a single pore wall, resulting in a much better efficiency. This clearly confirms the

results obtained earlier by Chmiola and Largeot *et al.* that when effective ion-pore sizes are in proximity, maximum capacitance can be achieved. On the other hand in graphitic carbon, depicted in Figure I- 29, overscreening was suggested to dominate at the EDL, leading to adsorbed ion (both BMI^+ and PF_6^-) densities peaking at further average distance (to the electrode surface) as compared to the depressed but nearer average adsorbed ion density in porous carbon where overscreening is less likely to happen in such confined pores of size of an ionic diameter.
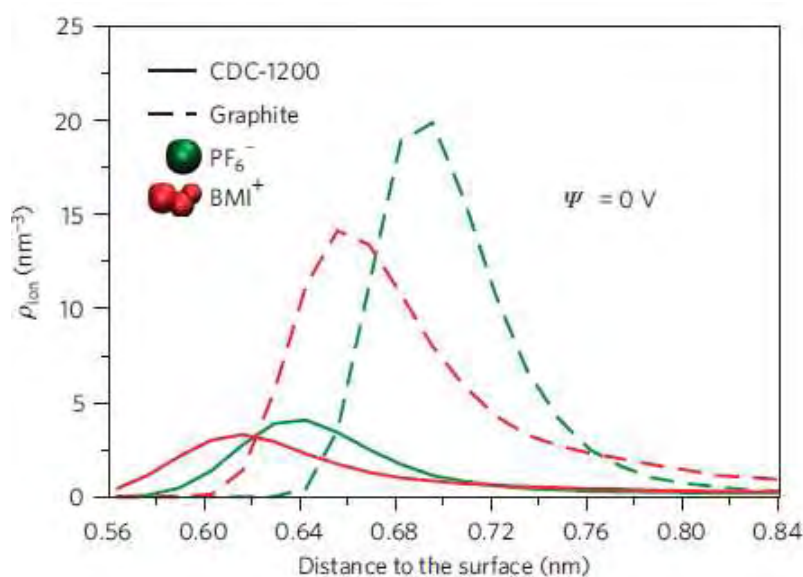
Figure I- 29: Density profiles normal to the electrode surface for graphite and CDC materials. Ionic density profiles (ρ_{ion}) for the two types of ions and $\Psi = 0$ V; the distances are given with respect to the surface accessible to an argon atom probe, with the origin set to the position of the carbon atoms [167].

Such an investigation contributes largely to the understanding of ILs adsorption in more openly structures in the case of graphite because in most graphitic carbons, graphene sheets are inevitable and results displayed could explain the differences in capacitance values obtained in openly architected carbons.

Recent reports of ILs in pore approaching 1 nm, Wu *et al.* demonstrated by using MD simulations displayed in Figure I- 30, that the use of slit-shaped nanopores with room-temperature ionic liquids exhibits a U-shaped capacitance scaling behaviour in pores widths from 0.75 to 1.26 nm [168]. This simulation gives the visualisation of the position of adsorbing ions, surrounded by counter ions, away from the pore walls due to common charges residing on the pore walls.
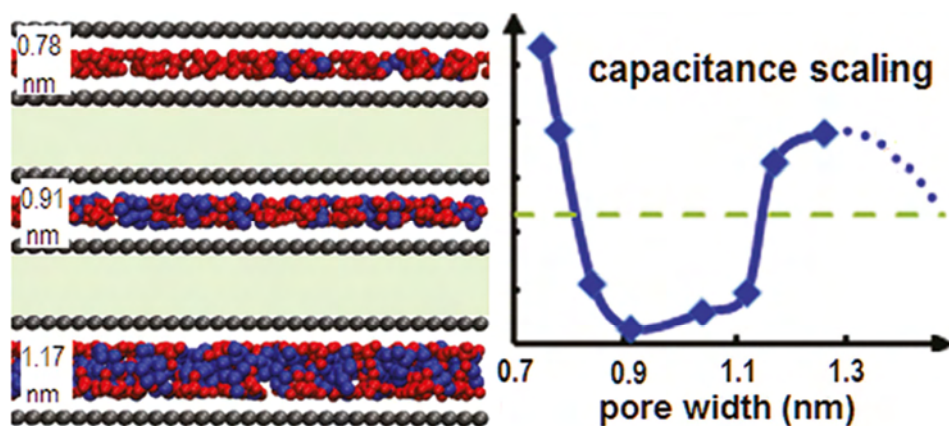
Figure I- 30: U-shaped scaling behaviour in slit-shaped pores with widths from 0.75 to 1.26 nm [168].

VI. Objectives of thesis

This project has been effectuated and financed by SOLVIONIC, a company which specialized in the research and development of ionic liquids and formulation of electrolytes, in collaboration with CIRIMAT. The main interest of this collaboration is to formulate electrolytes based on ionic liquids for supercapacitor applications, in view to improve energy storage performances as well as safety through two main directions:

VI-1. Studying the influence of solvent effects on capacitance and on charge/discharge behaviour of microporous carbons for electrochemical double layer capacitors

The importance of pore-size relationship between the electrolyte/electrode has been shown earlier for the increase in capacitance in electrodes with pore sizes less than 1 nm. In order to understand the influence of solvents on the capacitance, cavity microelectrode is used as a fast probe in understanding the solvation effects of the electrolyte in conventional electrolytes. The understanding of pure ILs and the influence of solvent on the respective electrolyte ions was attained by using both conventional 3-electrode cell set-up and a cavity microelectrode. Results obtained are presented in Chapters III and IV of this manuscript.

VI-2. Formulation of solventless ionic liquid-based electrolytes for supercapacitor applications in wide temperature range

Ionic liquids have emerged to be a promising candidate as electrolytes in wide temperature range energy storage systems due to their outstanding electrochemical properties and negligible vapour pressures. This work is therefore dedicated to formulate a solventless

electrolyte based on ionic liquids and to optimize electrolyte/electrode interface by carefully selecting appropriate electrode architecture for improving charge storage specifications in supercapacitors. Results obtained are presented in Chapter V of this manuscript.

VII. References

[1]   Houston, E. J. Electricity in Every-day Life. P.F. Collier & Son. (1905).
[2]   http://electronics.howstuffworks.com/capacitor3.htm
[3]   Helmoltz, H. V. *Annals of Physics.* **89** (1853) 211.
[4]   Gouy, G. *Comptes Rendus* **149** (1910) 654.
[5]   Chapman, D. L. *Philosophical Magazine* **25** (1913) 475.
[6]   Stern, O. *Z. elektrochem* **30** (1924) 508.
[7]   Grahame, D. C. *Chemistry Review* **41** (1947) 441.
[8]   Becker, H. I. *Low voltage electrolytic capacitor* (1957) U.S. Patent 2800616.
[9]   Rightmire, R. A. *Electrical energy storage apparatus* (1966) U.S Patent 3288641.
[10]   Boos, D. L. *Electrolytic capacitor having carbon paste electrodes* (1970) 3536963.
[11]   Endo, M.; Takeda, T.; Kim, Y. J.; Koshiba, K.; Ishii, K. *Carbon Science* **1** (2001) 117.
[12]   Rose, M. F. *Proceedings of the 33rd International Power Sources Symposium , Pennington, NJ* (1988) 572.
[13]   Murphy, T.C.; Wright, R.B.; Sutula, R.A. In Electrochemical Capacitors II, Proceedings (Delnick, F.M.; Ingersoll, D.; Andrieu, X.; Naoi, K. Eds.) *The Electrochemical Society* Pennington, NJ **vols. 96–25** (1997) 258.
[14]   Energy, Basic Research needs for Electrical Energy Storage – Report of the basic Energy Sciences *Workshop on Electrical Energy storage* (April 2007).
[15]   Burke, A. *International Journal of Energy Research* **34** (2009) 133.
[16]   Simon, P.; Gogotsi, Y. *Nature Materials* **7** (2008) 845.
[17]   Burke, A. F.; Murphy T.C. In Materials for electrochemical energy storage and conversion - Batteries, Capacitors, and Fuel Cells: Symposium Held, April 17-20 (1995) San Francisco, CA, *Materials Research Society, Pittsburg, PA*, (1995) 375.
[18]   Burke, A. *Electrochimica Acta* **53** (2007**)** 1083.
[19]   Kotz, R.; Carlen, M. *Electrochimica Acta* **45** (2000) 2483.
[20]   Burke, A. *Journal of Power Sources* **91** (2000) 37.
[21]   Broddd, R. J.; Bullock, K. R.; Leising, R. A.; Middaugh, R. L.; Miller, J. R.; Takeuchi, E. *Journal of the Electrochemical Society* **151** (2004) K1.
[22]   http://www.environment.peugeot.co.uk/e-hdi-micro-hybrid-technology/
[23]   Conway, B. E. *Electrochemical Supercapacitors: Scientific Fundamentals and Technological Applications* (Kluwer, 1999).
[24]   Van Olphen, H. An Introduction to Clay Colloid Chemistry. Interscience Publishers (1963)
[25]   Grahame, D.C. *Journal of Chemistry Physics* **16** (1948) 1117.
[26]   www.nesscap.com
[27]   Kajdos, A., Kvit, A., Jones, F., Jagiello, J. & Yushin, G. J. Am. Chem. Soc. 132, 3252–3253 (2010).
[28]   Janes, A.; Lust, E. *Journal of the Electrochemical Society* **153**, (2006) A113.
[29]   Shanina B.D.; Konchits, A.A.; Kolesnik, S.P.; Veynger, A.I.; Danishevskii, A.M.; Popov, V.V.; Gordeev, S.K.; Grechinskaya, A.V. *Carbon* **41** (2003) 3027.

[30] Dash, R.; Chmiola, J.; Yushin, G.; Gogotsi, Y.; Laudisio, G.; Singer, J.; Fischer, J.; Kucheyev, S. *Carbon* 44 (2006) 2489.

[31] Portet, C.; Chmiola, J.; Gogotsi, Y.; Park, S; Lian, K. *Electrochimica Acta* **53** (2008) 7675.

[32] Okajima, K.; Ohta, K.; Sudoh, M. Electrochimica Acta 50 (2005) 2227.

[33] Futaba, D. N.; Hata, K.; Yamada, T.; Hiraoka, T.; Hayamizu, Y.; Kakudate, Y.; Tanaike, O.; Hatori, H.; Yumura, M.; Iijima, S.; *Nature Materials* **5** (2006) 987.

[34] Stoller, M.D.; Park, S.; Zhu, Y.; An, J.; Ruoff, R.S. *Nano Letters* **8** (2008) 3498.

[35] Yang, C.-M.; Kim, Y-J. ; Endo, M.; Kanoh, H.; Yudasaka, M.; Iijima, S.; Kaneko, K. *Journal of the American Chemical Society* **129** (2007) 20.

[36] Pandolfo, A.G.; Hollenkamp, A.F. *Journal of Power Sources* **157** (2006) 11.

[37] Lin, R.; Taberna, P-L.; Fantini, S.; Presser, V.; Pérez, C.R. Malbosc, F.; Rupesinghe, N.L.; Teo, K.B. K.; Gogotsi, Y.; Simon, P. *Journal of Physical Chemistry Letters* **2** (2011) 2396.

[38] Zhu, Y.; Murali, S.; Stoller, M. D.; Ganesh, K. J.; Cai, W. ; Ferreira, P. J. Pirkle, A. ; Wallace, R. M.; Cychosz, K.A. ; Thommes, M. ; Su, D. ; Stach, E.A.; Ruoff, R. S. *Science* **332** (2011) 1537.

[39] Zheng, J.; Ekstrom, T. C.; Gordeev, S. K.; Jacob; M. *Journal of Materials Chemistry* **10** (2000) 1039.

[40] Gogotsi, Y. (ed.) <u>Carbon Nanomaterials</u> (2006) CRC.

[41] Ugarte, D. *Nature* **359**, (1992) 707.

[42] Kuznetsov, V. L.; Chuvilin, A.L.; Moroz, E.M.; Kolomiichuk, V.N.; Shaikhutdinov, Sh.K.; Butenko, Yu.V. *Carbon* **32** (1994) 873.

[43] McNallan, M.; Ersoy, D.; Zhu, R.; Lee, A.; White, C.; Welz, S.; Gogotsi, Y.; Erdemir, A.; Kovalchenko, A. *Tsinghua Science & Technology* **10** (2005) 699.

[44] Presser, V.; Heon, M.; Gogotsi, Y. *Advanced Functional Materials* **21** (2011) 810.

[45] Yushin, G.N.; Osswald, S.; Padalko, V.I.; Bogatyreva, G.P.; Gogotsi, Y. *Diamond & Related Materials* **14** (2005) 1721.

[46] Sano, N.; Wang, H.; Alexandrou, I.; Chhowalla, M.; Teo, K. B. K.; Amaratunga, G. A. J.; Iimura, K. *Journal of Applied Physics* **92** (2002) 2783.

[47] Portet, C.; Yushin, G.; Gogotsi, Y. *Carbon* **45** (2007) 2511.

[48] Pech, D.; Brunet, ; Durou, H.; Huang, P.; Mochalin, V.; Gogotsi, Y.; Taberna, P-L. Simon, P. *Nature Nanotechnology* **5** (2010) 651.

[49] Iijima, S. *Nature* **354** (1991) 56.

[50] Ebbesen, T.W.; Ajayan, P.M. *Nature* **358** (1992) 220.

[51] Guo, T.; Nikolaev, P.; Rinzler, A.G.; Tomanek, D.; Colbert, D.T.; Smalley,R.E. *Journal of Physical Chemistry* **99** (1995) 10694.

[52] José-Yacamán, M.; Miki-Yoshida, M.; Rendón, L.; Santiesteban, J. G. *Applied Physics Letters* **62** (1993) 657.

[53] Beckman, Wendy (2007-04-27). <u>"UC Researchers Shatter World Records with Length of Carbon Nanotube Arrays"</u>. University of Cincinnati.

[54] Peigney, A.; Laurent, Ch. ; Flahaut, E. ; Bacsa, R.R. ; Rousset, A. *Carbon* **39** (2001) 507.

[55] Izadi-Najafabadi, A. ; Yasuda, S. ; Kobashi, K. ; Yamada, T.; Futaba, D. N.; Hatori, H.; Yumura, M.; Iijima, S.; Hata, K. *Advanced Materials* **22**, (2010) E235.

[56] Baughman, R. H.;. Zakhidov, A. A.; de Heer, W. A. *Science* **297** (2002) 787.

[57] (a) Niu, C.; Sichel, E. K.; Hoch, R.; Moy, D.; Tennent, H. *Applied Physical Letters* **70** (1997) 1480.

(b) Pico, F.; Rojo, J. M.; Sanjuan, M. L.; Anson, A.; Benito, A. M.; Callejas, M. A.; Maser, W. K.; Martinez, M. T. *Journal of the Electrochemical Society* **151** (2004) A831.

(c) Pandolfo, A. G.; Hollenkamp, A. F. *Journal of Power Sources* **157** (2006) 11.

[58] Geim, A. K.; Novoselov, K. S. *Nature Materials* **6** (2007) 183–191.

[59] Sutter, P. *Nature Materials* **8** (2009) 171.

[60] Bae, S.; Kim, H.; Lee, Y.; Xu, X.; Park, J-S.; Zheng, Y.; Balakrishnan, J.; Lei, T.; Kim, H. R.; Song, Y. Il.; Kim, Y-J.; Kim, K.S.; Özyilmaz, B.; Ahn, J-H.; Hong, B. H.; Iijima, S. *Nature nanotechnology* **5** (2010). 574.

[61] Boehm's 1961 isolation of graphene. Graphene Times (2009-12-07).

[62] Amini, S.; Garay, J.; Liu, G.; Balandin, A. A.; Abbaschian, R. *Journal of Applied Physics* **108** (2010) 094321.

[63] Choucair, M.; Thordarson, P; Stride, J.A. *Nature Nanotechnology* **4** (2008) 30.

[64] Jiao, L.; Zhang, L.; Wang, X.; Diankov, G.; Dai, H. *Nature* **458** (2009) 877.

[65] Hernandez, Y.; Nicolosi, V.; Lotya, M.; Blighe, F.M.; Sun, Z.; De, S.; McGovern, I. T.; Holland, B.; Byrne, M.; Gun'Ko, Y.K.; Boland, J.J.; Niraj, P.; Duesberg, G.; Krishnamurthy, S.; Goodhue, R.; Hutchison, J.; Scardaci, V.; Ferrari, A.C.; Coleman, J.N. *Nature Nanotechnology* **3** (2008) 563.

[66] Zhu Y.; Murali, S.; Cai, W.; Li, X.; Suk, J.W.; Potts, J.R.; Ruoff, R.S. *Advanced Materials* **22** (2010) 3906.

[67] Stoller, M. D.; Park, S. J.; Zhu, Y. W.;. An, J. H.; Ruoff, R. S. *Nano Letters* **8** (2008) 3498.

[68] Wang, Y.; Shi, Z.; Huang, Y.; Ma, Y.; Wang, C.; Chen, M.; Chen, Y. *The Journal of Physical Chemistry C* **113** (2009) 13103.

[69] Lv, W.; Tang, D-M.; He, Y-B.; You, C-H.; Shi, Z-Q.; Chen, X-C.; Chen, C-M.; Hou, P-X.; Liu, C.; Yang, Q-H. *ACS Nano* **3** (2009) 3730.

[70] Zhu, Y.; Stoller, M.D.; Cai, W.; Velamakanni, A.; Piner, R.D.; Chen, D.; Ruoff, R.S. *.ACS Nano* **4** (2010)1227.

[71] Vivekchand, S. R. C.; Rout, C. S.; Subrahmanyam, K. S.; Govindaraj, A.; Rao, C. N. R. *Journal of Chemical Sciences* **120** (2008) 9.

[72] Miller, J. R.; Outlaw, R. A.; Holloway, B. C. *Science* **329** (2010) 1637.

[73] Cambaz, Z.G.; Yushin, G.N.; Vyshnyakova, K.L.; Pereselentseva, L.N.; Gogotsi, Y. *Journal of the American Ceramic Society* **89** (2006) 509.

[74] Jacobson, N.S.; Gogotsi, Y. ; Yoshimura, M. *Journal of Applied Chemistry* **5** (1995) 595.

[75] Ersoy, D.A.; McNallan, M.J.; Gogotsi, Y. Materials Research Innovations 5 (2001) 55.

[76] Gogotsi, Y.; Jeon, I-D.; McNalan, M.J. Journal of Materials Chemistry 7 (1997) 1841.

[77] Boehm, H.P.; Warnecke, H.H.; In *Proceedings 12th Biennial Conference on Carbon Pergamon Oxford* (1975) 149

[78] Raymundo-Pinero, E.; Kierzek, K.; Machnikowski, J.; Beguin, F. *Carbon* **44** (2006) 2498.

[79] Qu, D. *Journal of Power Sources* **109** (2002) 403.

[80] Beguin, F.; Frackowiak, E. In *Nanomaterials Handbook, Y. Gogotsi, Ed.* (CRC Press, Boca Raton, FL, (2006) 713.

[81] Simon, P.; Burk, A. *The Electrochemical Society Interface Spring* (2008).

[82] Koch, V.R. Covalent Associates Inc,

[83] Janes, A.; Lust, E. *Journal of Electroanalytical Chemistry* **588** (2006) 285.

[84] Sekido, S.; Yoshino, Y.; Muranaka, T.; Mort, M. *Denki Kagaku* **48** (1980) 40.

[85] Yashima, H.; Nogami, T.; Mikawa, H. *Synthetic Metals* **10** (1985) 229.

[86] Tanahashi, I.; Yoshida, A.; Nishino, A. *Denki Kagaku* **56** (1988) 892.

[87] Lust, E.; Janes, A.; Arulepp, M. *Journal of Electroanalytical Chemistry* **562** (2004) 33.

[88] Kanbara, T.; Yamamoto, T.; Tokuda, K.; Aoki, K. *Chemistry Letters* (1987) 217.

[89] Maletin, Y.; Strizhakova, N.; Izotov, V.; Mironova, A.; Danilin, V.; Kozachov, S. *Patent number: 6491841* (2002).

[90] Nanba, Y.; Mori, T. *Patent application number: 20090154061*(2009*)*.

[91] Naoi, K. *Fuel Cells* **10** (2010**)** 825.

[92] Sanada, Y.; Hiratsuka, K.; Morimoto, T.; Kurihara, K. *Denki Kagaku,* **51** (1993) 448.

[93] Bae, J.; Park, Y. J.; Lee, M.; Cha , S. N.; Choi , Y.J.; Lee , C.S.; Kim, J.M.; Wang, Z. L. *Advanced Materials***23** *(*2011) 3446.

[94] (a) Walden, P. *Bulletin of Imperial Academy* of *Sciences (St. Petersburg)* (1914) 1800. (b) Sugden, S.; Wilkins, H. *Journal of Chemical Society* (1929) 1291.

[95] Armand, M.; Endres, F.; macFarlane, D.R.; ohno, H.; Scrosati, B. *Nature Materials* **8** (2009) 621.

[96] Wilkes, J. S. *Green Chemistry* **4 (**2002) 73.

[97] (a) Hurley, F. H. U.S. Patent 2446331, (1948); and *Chemical Abstracts* **43** P7645b (1949). (b) Hurley F. H.; Wier, T. P. Jr. *Journal of the Electrochemical Society* **98** (1951) 207.

[98] Wilkes, J. S.; Levisky, J. A.; Wilson R. A.; Hussey, C. L. *Inorganic Chemistry* **21** (1982) 1263

[99] Dupont, J. *Journal of the Brazilian Chemical Society* **15** (2004) 341.

[100] Wilkes, J.S.; Zaworotko, M.J. *Journal of the Chemical Society: Chemical Communications* (1992) 965.

[101] Fuller, J.; Carlin, R.T.; de Long, H.C.; Haworth, D. *Journal of the Chemical Society: Chemical Communications* (1994) 299.

[102] Welton, T. *Chemical Reviews* **99** (1999) 2071.

[103] Zhou, Y.; Antonietti, M. *Journal of the American Chemical Society* **125** (2003) 14960.

[104] Zhu, H. G.; Huang, J. F.; Pan, Z.W.; Dai, S. *Chemistry of Materials* **18** (2006) 4473.

[105] Li, Z.Y.; Zhang, Q.; Liu, H.T.; He, P.; Xu, X.D; Li, J.H. *Journal of Power Sources* **158** (2006) 103-109.

[106] Wei, D.; Ivaska, A. *Analytica Chimica Acta* **607** (2008) 126.

[107] Nakashima, T.; Kawai, T. *Chemical Communications* **12** (2005), 1643.

[108] Huddleston, J.G.. Willauer., H. D.; Swatloski, R.P.; Visser, A.E.; Rogers, R.D. *Chemical Communications* (1998) 1765.

[109] Liu, H.T.; He, P.; Li, Z.Y.; Liu, Y.; Li, J. H. *Electrochimica Acta*, **51** (2006) 1925.

[110] Li, Z.Y.; Liu, H. T.; Liu, Y.; P.He,. Li, J.H. *Journal of Physical Chemistry B* **108** (2004) 17512.

[111] Seddon, K.R. *Nature Materials* **2** (2003) 363.

[112] Angell, C.A.; Xu, W.; Yoshizawa, M.; Hayashi, A.; Belieres, J-P.; Lucas, P.; Videa, M. *In Electrochemical Aspects of Ionic Liquids (Ohno, H. ed)* **Ch 2** ((2005) 6.

[113] Bockris, J.O'M.; Reddy, A.K.N. in *Modern Electrochemistry, Plenum Press, New York* (1998) Ch 4 & 5.

[114] Ohno, H. (ed.); Yoshizawa, M.; Mizumo, T. In *Electrochemical Aspects of Ionic Liquids* **Ch 6** (2005) 78.

[115] Vila, J.; Franjo, C.; Pico, J.M.; Varela, L.M.; Cabeza, O. *Portugaliae Electrochimica Acta* **25** (2007) 163.

[116] (a) Chang, I. ; Sillescu, H. *Journal of Physical Chemistry B* **101** (1997) 8794. (b) Cicerone, M.T.; Ediger, M.D. *Journal of Chemical Physics* **103** (1995) 5684.

[117] Xu, W.; Cooper, E.I.; Angell, C.A. *Journal of Physical Chemistry B* **107** (2003) 6170.

[118] Robinson, R.A.; Stokes, R.H. *Electrolyte Solutions 2ⁿᵈ Ed. Butterworths* (1959) 465.

[119] Visser, A. E.; Swatloski, R. P.; Reichert, W. M.; Mayton, R.; Sheff, S.; Wierzbicki, A.; Davis, J. H.; Rogers, R. D. *Environmental Science and Technology* **36** (2002) 2523.

[120] MacFarlane, D. R.; Seddon, K. R. *Australian Journal of Chemistry* **60** (2007) 3.

[121] Xu, W.; Angell, CA. *Science* **302** (2003) 422.

[122] Yoshizawa, M.; Narita, A.; Ohno, H. In *In Electrochemical Aspects of Ionic Liquids (Ohno, H. ed)* **Ch 20** ((2005) 245.

[123] Yoshizawa, M.; Hirao, M.; Akita, K. I.; Ohno, H.; *Journal of Materials Chemistry* **11** (2001) 1057.

[124] Vijayaraghavan, R.; Pringle, J.M.; MacFarlane, D.R. *European Polymer Journal* **44** (2008) 1758.

[125] Tiyapiboonchaiya, C.; Pringle, J. M.; Sun, J.; Byrne, N.; Howlett, P. C.; MacFarlane, D. R.; Forsyth, M. *Nature Materials* **3** (2004) 29.

[126] Rogers, R.D.; Seddon, K.R. eds. *In Ionic Liquids: Industrial Applications to Green Chemistry, American Chemical Society* (2002).

[127] Ohno, H. ed. In *Ionic Liquids: The Front and Future of Material Development, High Tech. info* (2003)

[128] (a) Hussey, C.L. *Advances in Molten Salt Chemistry* **5** (1983) 185.
(b) Cooper, E.I.; Sullivan, E.J.M. *Proceedings in 8ᵗʰ International Symposium Molten Salts: Electrochemical Society* (1992) 386.
(c) Carlin, R.T.; Wilkes, J.S. In *Chemistry of Non-aqueous Solutions: Mamantov, G.; Popov, A.I. eds. VCH Publishers* (1994).
(d) Sun, J.; Forsyth, M.; MacFarlane, D.R. *Ionics* **3** (1997) 356.
(e) Bohote, P.; Dias, A-P.; Armand, M.; Papageorgiou, N.; Kalyanasundaram, K.; Graetzel,M. *Inorganic Chemistry* **35** (1996) 1168.
(f) Bowles, C.J.; Bruce, D.W.; Seddon, K.R. *Chemical Communications* (1996) 1625.
(g) Holbrey, J.D.; Seddon, K.R. *Journal of Chemical Society: Dalton Transactions* (1999) 2133.
(h) Cooper, E.I.; Angell, C.A. *Solid State Ionics* **9 & 10** (1983) 617.
(i) Kunze, M.; Montanino, M.; Appetecchi, G.B. ; Jeong, S. ; Schonhoff, M.; Winter, M.; Passerini, S. *Journal of Physical Chemistry A* **114** (2010) 1776.

[129] Wasserscheid, P.; Welton, T. In Ionic Liquids in Synthesis 2ⁿᵈ Edition *John Wiley & Sons* (2008).

[130] Liu , H. T.; Liu, Y.; Li, J. *Physical Chemistry and Chemical Physics* **12** (2010) 1685.

[131] MacFarlane, D. R.; Meakin, P.; Sun, J.; Amini, N.; Forsyth, M. *Journal of Physical Chemistry B* **103** (1999) 4164.

[132] Davis, J. H.; Fox, P. A. *Chemical Communications* **11** (2003) 1209.

[133] Huddleston, J.G.; Visser, A.E.; Reichert, W.M.; Willauer, H.D.; Kroker, G.A.; Rogers, R.D. *Green Chemistry* **3** (2001) 156.

[134] www.**solvionic**.com

[135] Liu, H.; Zhu, G. *Journal of Power Sources* **171** (2007) 1054.

[136] Balducci, A.; Dugas, R.; Taberna, P-L. ; Simon, P.; Plee, D.; Mastragostino, M.; Passerini, S. *Journal of Power Sources* **165**(2007) 922.

[137] Lewandowski, A.; Swiderska, A. *Solid State Ionics* **161** (2003) 243.

[138] Le Bideau, J. ; Gaveau, P. ; Bellayer, S. ; Néouze, M.-A. ; Vioux, A. *Physical Chemistry Chemical Physics* **9** (2007) 5419.

[139] Galinski, M.; Lewandowski, A.; Stepniak, I. *Electrochimica Acta* **51** (2006) 5567.

[140] Balducci, A.; Bardi, U.; Caporali, S.; Mastragostino, M.; Soavi, F. *Electrochemistry Communications* **6** (2004) 566.

[141] Fletcher, S.I.; Sillars, F.B.; Carter, R.C.; Cruden, A.J.; Mirzaeian, M.; Hudson, N.E.; Parkinson, J.A.; Hall, P.J. *Journal of Power Sources* **195** (2010) 7484.

[142] Hou, Y.; Gu, Y.; Zhang, S.; Yang, F.; Ding, H.; Shan, Y. *Journal of Molecular Liquids* **143** (2008) 154.

[143] Every, H.; Bishop, A.G.; Forsyth, M.; MacFarlane, D.R. *Electrochimica Acta* **45** (2000) 1279.

[144] Kunze, M.; Jeong, S.; Paillard, E.; Winter, M.; Passerini, S. *Journal of Physical Chemistry C* **114** (2010) 12364.

[145] Henderson, W.A.; Passerini, S.; *Chemistry of Materials* **16** (2004) 2881.

[146] Zhou, Q.; Boyle, P.D.; Malpezzi, L.; Mele, A.; Shin, J-H.; Passerini, S.; Henderson, W.A. *Chemistry of Materials* **23** (2011) 4331.

[147] Kubota, K.; Nohira, T.; Goto, T.; Hagiwara, R. *Electrochemistry Communications* **10** (2008) 1886–1888.

[148] Forsyth, C. M.; MacFarlane, D. R.; Golding, J. J.; Huang, J.; Sun, J.; Forsyth, M. *Chemistry of Materials* **14** (2002) 2103.

[149] Bayley P.M.; Best, A.S.; MacFarlane D.R.; Forsyth, M.A *A European journal of Chemical Physics and Physical Chemistry* **12**. (2011) 823.

[150] Zhou, Q.; Henderson, W.A.; Appetecchi, G. B.; Passerini, S. *Journal of Physical Chemistry C* **114** (2010) 6201.

[151] Zhou, H.; Zhu, S.; Hibino, M.; Honma, I. *Journal of Power Sources* **122** (2003) 219.

[152] Fernandez, J. A. T. Morishita, M. Toyoda ,M. Inagaki , F. Stoeckli , T.A. Centeno *Journal of Power Sources* **175** (2008) 675.

[153] Fuertes, A. B.. Lota, G.. Centeno, T. A. . Frackowiak, E. . *Electrochimica Acta* **50** (2005) 2799.

[154] Chmiola, J.; Yushin, G.; Gogotsi, Y.; Portet, C.; Simon, P.; Taberna, P.-L. *Science* **313** (2006) 1760.

[155] Raymundo-Pinero, E.; Kierzek, K.; Machnikowski, J.; Beguin, F. *Carbon* **44** (2006) 2498.

[156] Chmiola, J.; Largeot, C.; Taberna, P-L.; Simon, P.; Gogotsi, Y. *Angewandte Chemie International Edition* **47** (2008) 3392.

[157] Tanaka, A. ; Iiyama, T. ; Ohba, T. ; Ozeki, S.; Urita, K.; Fujimori, T.; Kanoh, H.; Kaneko, K. *Journal of the American Chemical Society Communications* **132** (2010) 2112.

[158] Lin, R.; Taberna, P-L. ; Chmiola, J. ; Guay, D.; Gogotsi, Y.; Simon, P. Journal of the Electrochemical Society 156 (2009) A7.

[159] Levi, M.D.; Sigalov, S.; Gregory, S.; Aurbach, D.; Maier, *Journal of Chemical Physics and Physical Chemistry* **12** (2011) 854 – 862.

[160] Levi, M.D.; Levy, N.; Sigalov, S.; Gregory, S.; Aurbach, D.; Maier, J. *Journal of the American Chemical Society* **132** (2010)13220.

[161] Wang, H.;. Koster, T. K.-J.; Trease, N.M.; Ségalini, J.; Taberna, P-L.; Simon, P. ; Gogotsi, Y. ; Grey, C.P. *Journal of the America Chemical Society* **133** (2011) 19270.

[162] Lee, S.I.; Saito, K.; Kanehashi, K.; Hatakeyama, M.; Mitani, S.; Yoon, S-H.; Korai, Y.; Mochida, I. *Carbon* **44** (2006) 2578.

[163] Deschamps, M.; Gilbert, E.; Raymundo-Pinero, E.; Azais, P.; Béguin, F.; Massiot, D. Presented at the Experimental NMR Conference *Pacific Grove CA* (2011).

[164] Largeot, C.; Portet, C.; Chmiola, J.; Taberna, P-L.; Gogotsi, Y.; Simon, P. *Journal of the American Chemical Society* **130** (2008) 2730.

[165] Fedorov, M.V.; Kornyshev, A. A. *Electrochimica Acta* **53** (2008) 6835.

[166] Bazant, M. Z.; Storey, B. D.; Kornyshev, A.A. *Physical Review Letters* **106** (2011) 046102.

[167] Merlet, C.; Rotenberg, B.; Madden, P. A.; Taberna, P-L.; Simon, P.; Gogotsi, Y.; Salanne, M. *Nature Materials* **11** (2012) 306.

[168] Wu, P.; Huang, J.; Meunier, V.; Sumpter, B.G.; Qiao, R. *ACS Nano* **5** (2011) 9044–9051.

Chapter II :
Experimental

I. Introduction

This experimental section describes the as-received active materials (carbons), synthesized electrolytes (ionic liquids) and their physical characterizations as well as the characterization techniques for the three different experimental set-ups for supercapacitor cells, using (1) 4 cm^2 electrode EDLCs, (2) Cavity Micro-Electrode (CME) and (3) Swagelok cells. Techniques described are repeated in different set-ups due to the different experimental conditions used.

II. Active Materials

II-1. Titanium Carbide Derived Carbons (Ti-CDCs)

Synthesis of Ti-CDCs

The as-received titanium carbide derived carbons (Ti-CDCs) were prepared through a chlorination process of TiC under a flow of chlorine gas at different temperatures, 400, 500, 550, 600, 700, 800, 900, and 1000 °C for 3 hours in a horizontal quartz tube furnace. The reaction is represented in Eq II-1.

$$TiC + 2\ Cl_2 \rightarrow TiCl_4 + C \qquad (\text{Eq II- 1})$$

Titanium is removed as chlorides, leaving behind nanoporous carbon with a 50 to 80 % open pore volume. Maximum elimination of atmospheric gas and atoms adsorbed on the walls of reaction tube and carbide surfaces was ascertained by flushing Argon gas (99.998 %) through the reaction tube during heating and cooling of the furnace. In this way, the removal of metal chlorides and unreacted chlorine is ensured. Residual chlorine and chlorides trapped in pores were removed by annealing in hydrogen for 2 hours at 600 °C.

Properties of Ti-CDCs

Pore characteristics and measurements have been measured in the laboratory.

(a)

(b)
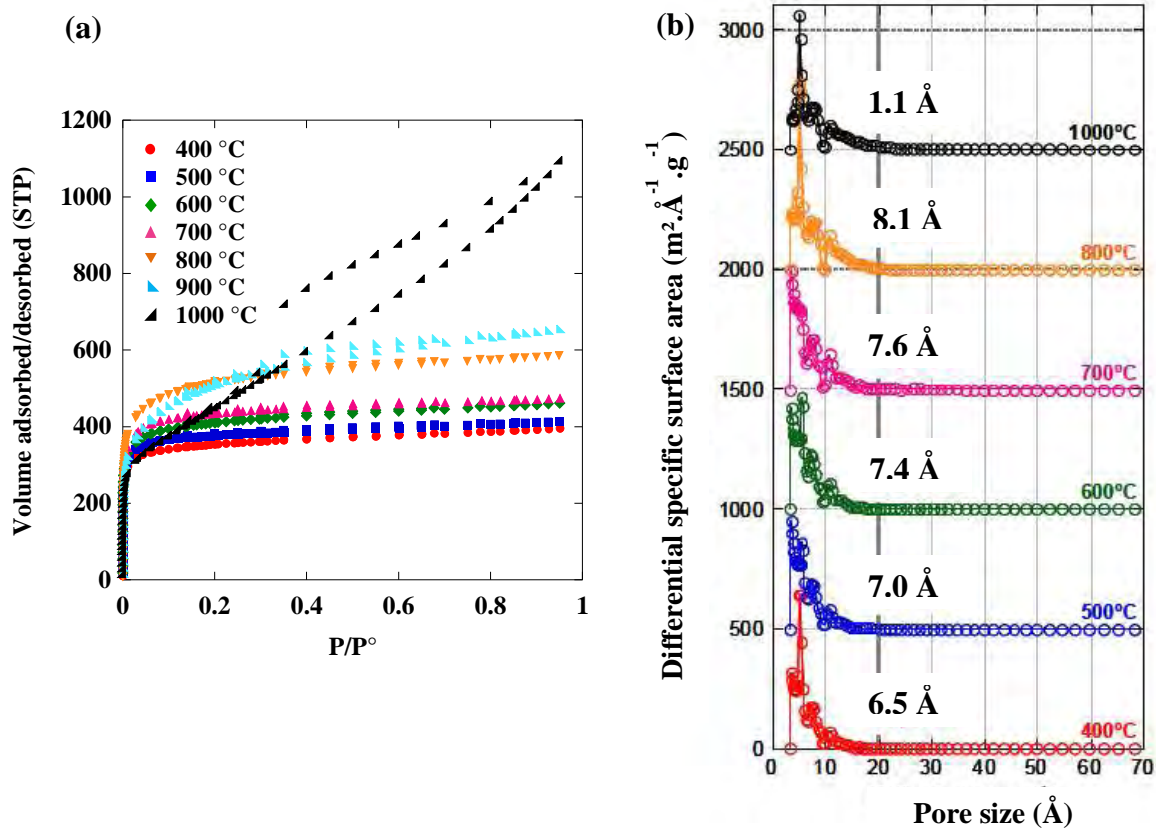
Figure II- 1: Gas sorption isotherms of TiC–CDC at different synthesis temperatures. All isotherms except for sample chlorinated at 1000 °C were reversible with no hysteresis between adsorption and desorption isotherms **(a)** and Pore size distributions of Ti-CDCs as a function of chlorination temperatures **(b)**.

The volume of argon adsorbed at a relative pressure (P/P$_0$) of ~1 increases with synthesis temperature, indicating the gain in accessibility of the adsorbing gas into the pores. The fast increase of volume at low relative pressure observed between adsorption and desorption isotherms for samples synthesized at 800 °C and below confirmed that the pores are microporous (pores less than 2 nm). On the other hand, the presence of mesopores (pores greater than 2 nm) has been deduced from the hysteresis observed in Figure II- 1a for the 1000 °C sample. These carbides are attractive in the sense as they offer narrow pore-size distribution (see Figure II- 1b) with a mean value that is tunable (by varying chlorination temperatures) in the range of ~0.5 to ~3 nm with an accuracy of more than 0.05 nm [1] for more in depth study of the EDLC.

The narrow pore size distribution measured can be explained by the International tables of Crystallography of TiC in Table II- 1. It shows that the material takes on a rock-salt structure, (space group: Fm3m No.225) with a C-C distance of 0.4328 nm, with the one and only Wyckoff position of Ti at 4a (Table II- 1). In addition, through the F mode translation of (0,0,0), (½, ½ 0), (½,0, ½) and (0, ½,½) in a cubic crystalline structure, a constant periodicity of pores is attained from the leaching of Ti by chlorination.

Table II- 1 : ICSD table for TiC.

Title	Electronic and structural properties of the layered ternary carbide Ti3 Al C2.
Authors	Zhou, Y.C.;Wang, X.H.;Sun, Z.M.;Chen, S.Q.
Reference	Journal of Materials Chemistry (2001) **11**, 2335-2339 **Link XRef SCOPUS SCIRUS Google**
Compound	C1 Ti1 - Titanium carbide **[AX] [cF8] [b a] [NaCl]**
Cell	4.344(17), 4.344(17), 4.344(17), 90, 90, 90 **FM3-M (225)** V=81.97
Remarks	TYP =NaCl : XDS THE PDC =01-070-7697 : No R value given in the paper. The coordinates are those given in the paper but the atomic distances do not agree with those calculated during testing.The coordinates are probably correct. At least one temperature factor missing in the paper. Calculated charges Ti0.94+ and C0.94- in paper.

Atom (site) Oxid.			x, y, z, B, Occupancy				
Ti1	(4a)	4	0.	0.	0.	0	1
C1	(4b)	-4	0.5	0.5	0.5	0	1

Full database (The **Full database** will be used if available after the first query is entered)
 Copyright 2003-2007 Fachinformationszentrum (FIZ) Karlsruhe
 PHP/MySQL Interface V08-05-14 copyright 2003-2007 by Peter Hewat email: hewat@ill.fr

Table II-2 shows the characteristics of the Ti-CDC samples used extracted from BET measurements. This whole range of pore sizes allows the study of the EDL by understanding the environment of the ions when entering the pores.

Table II-2: Characteristics of the TiC-CDC samples used.

Chlorination temperature (°C)	BET SSA (m².g⁻¹)	Pore volume (cc.g⁻¹)	Average pore width(nm)	Maximum pore width* (nm)
400	1113	0.51	0.65	1.12
500	1140	0.50	0.68	1.18
550	1202	0.51	0.72	1.29
600	1269	0.60	0.74	1.23
700	1401	0.66	0.76	1.41
800	1595	079	0.81	1.54
900	1600	0.81	1.0	2.50
1000	1625	0.81	1.1	2.8

*85 % of pore volume is below this size

II-2. Commercially available activated carbons

CECA AB

This activated carbon was bought from Arkema with the following characteristics as shown in Table II. 1: Characteristics of activated carbon CECA AB.

Table II. 1: Characteristics of activated carbon CECA AB.

BET surface (m².g⁻¹)	1428
Microporous volume (cm³.g⁻¹), < 2 nm	0.596
Mesoporous volume (cm³.g⁻¹), 2 – 5 nm	0.03
Macroporous Volume (cm³.g⁻¹), > 50 nm	0.141
Resistivity (Ω.cm)	0.82
Fe content (ppm)	100

YP 17

Pore size distributions (PSD) and mean pore size were calculated using the Non-Local Density Functional Theory from nitrogen gas sorption isotherms acquired by an ASAP 2020 Micromeritics equipment.
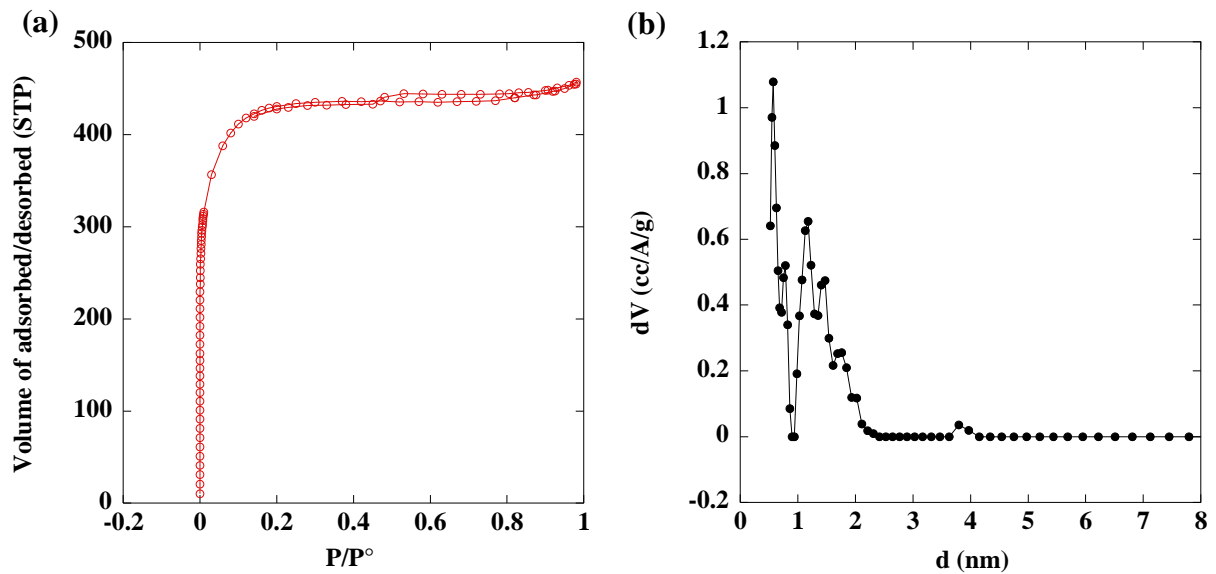
Figure II- 2 : Characteristics of YP-17 carbon powder – Gas sorption isotherm **(a)** and Pore size distribution **(b)**.

YP-17 (Kuraray Chemical Co.) is coconut based. Characteristics provided by the supplier [2] are as follows:

Table II- 3: Characteristics of coconut-based activated carbon YP 17.

Iodine adsorption (mg.g^{-1})	1700 - 1800
Benzene adsorption (wt %)	45 - 55
Total surface area (m^2.g^{-1})	1600 - 1700
pH	5 - 8
Ash content (%)	1.0 max
Diameter of particles	3 - 20

This carbon consists of 28 % of the pores being less than 1 nm, 40% which are between 1 to 1.5 nm and the remaining 32 % of the pores having pores that are larger than 1.5 nm. It is mentioned as having a large surface area (SSA = 1706 m^2.g^{-1}) and high adsorption capacity with high purity, high performance and reliability.

III. Electrolytes

Organic, ionic liquid electrolytes and their mixtures were synthesized and prepared at Solvionic SA (France). Table II- 4, Table II- 5 and Table II- 6, below show the ionic liquid-based electrolytes used, mainly consisting of two main anions (Table II- 4), several different cations (Table II- 5), and two types (Table II- 6) of solvents.

Table II- 4: Ionic liquid anions and their molecular structures.
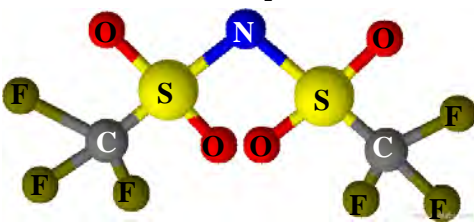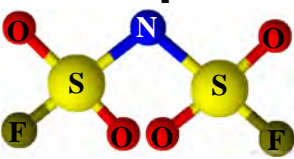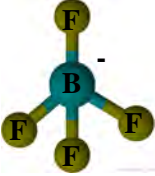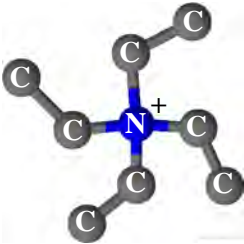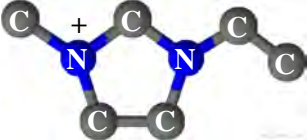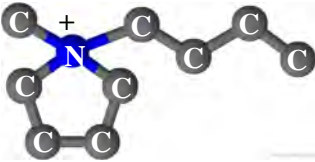
Anions	Molecular Structure
Bis(trifluoromethanesulfonyl)imide ($TFSI^-$)	
Bis(Fluorosulfonyl)imide (FSI^-)	
Tetrafluoroborate (BF_4^-)	

Table II- 5: Ionic liquid cations and their molecular structures.

Cations	Molecular structure
Tetraethylammonium (NEt_4^+)	
1-Ethyl-3-Methylimidazolium (EMI^+)	
N-Methyl-N-Butylpyrrolidinium (PYR_{14}^+)	

N-Ethyl-N-Propylpyrrolidinium (PYR$_{23}^+$)
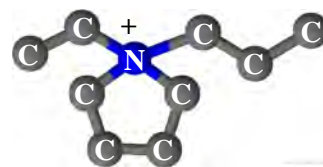
N-Methyl-N-Propylpiperidinium (PIP$_{13}^+$)
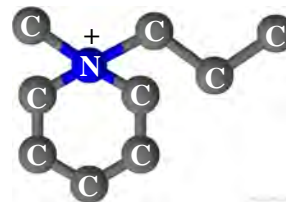
Table II- 6: Solvents and their molecular structures.

Solvents	Molecular structure
Propylene Carbonate (PC)	
Acetonitrile (AN)	

Extra-dry acetonitrile (AN) (CAS 75-05-8) and propylene carbonate (PC) (CAS #108-32-7) were purchased from Acros Organics.

III-1. Ionic Liquids

III-1.1. Synthesis

The ionic liquids are produced in a two-step process of first, a quarternization reaction and then, followed by anionic exchange reaction. In the preparation of water-immiscible ionic liquids, the most common approach is to prepare an aqueous solution of a halide salt of the desired cation through quarternization and then the cation exchange was carried out with a metal salt with the desired anion.

Quarternization reaction: Nucleophilic Substitution reaction

Quarternization usually takes place between an amine and a haloalkane. The reaction was carried out with chloroalkane and bromoalkanes depending on the rate of reaction in order to have manageable control over the temperature variation upon the addition of the

haloalkane. The reaction conditions become steadily milder in the order Cl > Br > I in nucleophilic substitution reactions [3].

Method of synthesis is in principle relatively simple by directly mixing the amine with the desired haloalkane. However temperature control was a tricky parameter throughout the quarternization process as strong exotherm can occur as the rate of reaction increases. This parameter is subjected to the haloalkane, upon which the duration of the reaction depends. The nature of the haloalkane also affects the reactivity, which generally decreases with increasing alkyl chain length. Constant temperature of synthesis ranges between 60-80 °C and duration of a complete reaction can last between 2 to 3 days with more than 70 % conversion.

Figure II- 3: Synthesis of the ionic liquid was carried out in a round-bottom flask connected to a reflux condenser under constant nitrogen atmosphere.

Prior to the addition of the reactants into the glassware, the experimental set-up (Figure II- 3) was purged with nitrogen for one hour and dried at the same time, with a heating gun externally. This step was important to remove all traces of water and oxygen in the apparatus before adding the distilled reactants. Presence of oxygen could taint the halide

salt. The general synthesis reaction of a pyrrolidinium cation is as follows in reaction (Rxn II-2):
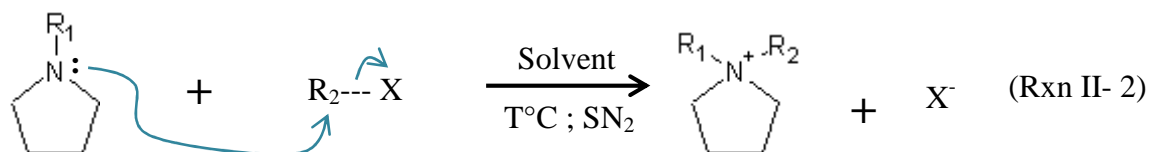
Usually the amine is placed in the round-bottom flask and heated at the synthesis temperature or at a temperature below its melting point and haloalkane is added to the amine dropwise. The rate of haloalkane addition was important to keep the exotherm under control for the synthesis. A solvent is required as most of the time the halide salts formed are solids at room temperature and the absence of solvent could result in low yields because there comes to a point where there were too much solid product to hinder the interaction of reactants in the mixture. The choice of solvents depends on the immiscibility of the halide salt in the solvent. Often, solvent that does not dissolve the halide salt was employed to facilitate the subsequent purification process as they formed a separate phase. Otherwise, an additional step of evaporation of solvent or recrystallization would be required before proceeding to the washing step. Solvents used mainly included iso-propanol and ethylacetate. After the reactions were completed, the solvents were decanted, together with unreacted matter.

Purification (removal of unreacted reactants)

The solid was then washed several times using the solvent employed to remove residual reactants until the eluent seemed clear for a few subsequent washes. After being dissolved in adequate quantity of deionized water, washed activated carbon particles were then added to the dissolved salt, and put under agitation for 48 hours at 80 °C. Upon removal of the activated carbon, a colourless mixture was usually obtained at this step. At this stage, the making of the cations is considered to be completed and thus, the mixture would be ready for anionic exchange to pair up the cations with the desired anions.

Anion Metathesis

Aqueous solution of metal salts of the desired anions (LiTFSI or KFSI) were added slowly to the aqueous mixture under vigorous agitation, at room temperature, to enhance good mixing between the halide mixture and the metal salts. Occurrence of the metathesis process could be evidently observed as the mixture became a milky emulsion of two immiscible phases comprising of the hydrophobic ionic liquid and metal-halide dissolved in water.

Although ionic liquid, being denser than water, usually form the lower layer in the separating funnel, the first decantation could be deceiving. Water with the metal-halides could sometimes be heavier than the synthesized ionic liquid, hence displacing the ionic liquid to the upper layer. Therefore it was important to introduce drops of deionized water to identify the aqueous phase for the first washings. The produce was then separated from the mixture by simple decantation.

Further purification (Halide removal)

Washing of the ionic liquid was done with successive small amount of deionized water until the washings are around pH 7, to remove the metal-halides. This was verified by a simple AgNO$_3$ test on the washings of the ionic liquid. Further verification was carried out by ion chromatography to keep impurities level down to below 20 ppm, as presence of halides could be detrimental to its electrochemical properties.

In summary, the key points for obtaining a colourless ionic liquid or minimizing its colour are:

- Starting materials for cation preparation should be distilled prior to synthesis [4].
- Experimental set-up should be purged with inert gas like nitrogen prior and during synthesis.
- Reaction temperature should be kept well below 80 °C especially for halide salt of Br$^-$.
- Glassware should be free of acetone as traces of this solvent could give rise to discoloration during the quarternization step.

The last step of synthesis before the ionic liquid would be ready for use was the removal of water. Drying was first carried out at room temperature under the BUSH vacuum for 2 hours with agitation, followed by overnight drying at elevated temperature (50-70 °C). Water content was then determined by Karl-Fischer titration and kept to well below 20 ppm, because above 50 ppm, electrochemical window of the ionic liquid was proven to be greatly affected (Figure II-4 [3]) which shows linear sweep voltammograms of different water content in trimethylpropylammonium-bis(trifluoromethyl)imide using platinum and glassy carbon as the working electrodes.
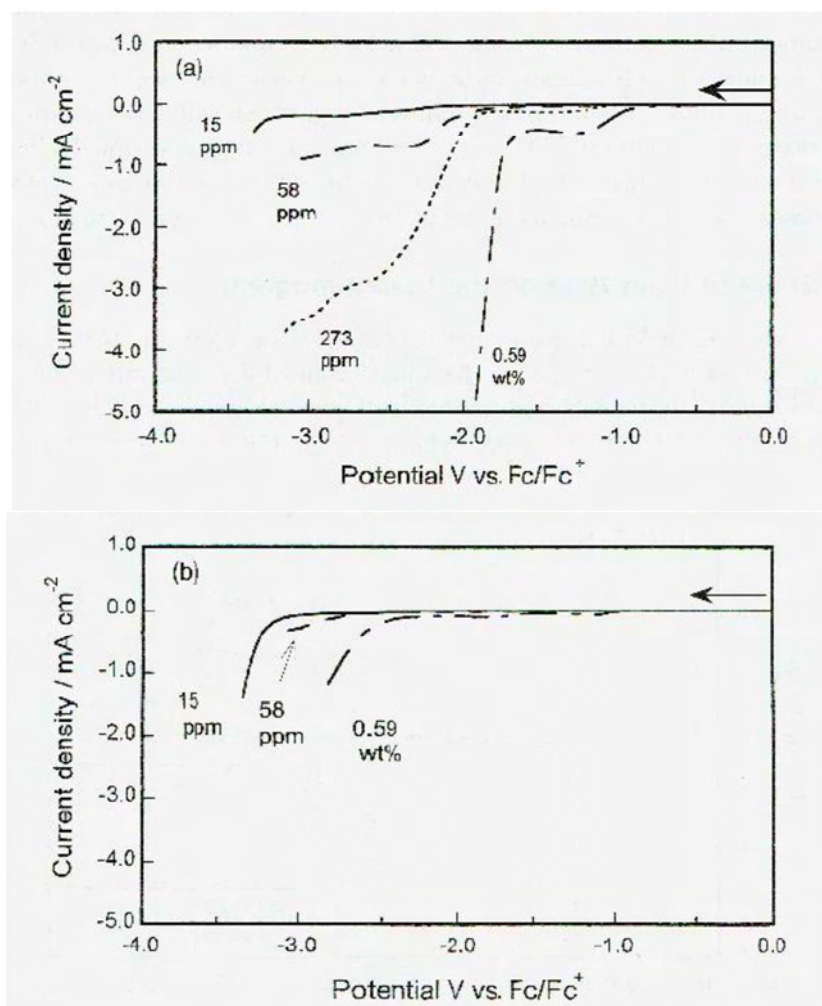
Figure II-4: Linear sweep voltammogram of trimethylpropylammonium-bis(trifluoromethylslfonyl)imide containing various amounts of water. Working electrodes: platinum **(a)** and glass carbon **(b)** used at scan rate 50 mV.s^{-1} at 25 °C (reproduced from [3]).

For both working electrodes, it is evident that the presence of water above 20 ppm can greatly reduce the electrochemical window of the electrolyte to 1V as seen in Figure II-4a.

III-2. Solvents

Acetonitrile (AN) was purchased from Acros Organics, CAS reference 75-05-8, H_2O < 10 ppm. Propylene Carbonate (PC) obtained from Acros Organics, CAS reference 108-32-7.

III-3. Physical characterization of electrolytes

III-3.1. Differential Scanning Calorimetry (DSC)

The DSC Differential scanning calorimetry (DSC) tracks associated heat effects with phase transitions and chemical reactions as a function of temperature. The difference between heat flow to the sample and a reference at the same temperature, is recorded as a function of temperature. An inert material such as alumina, or an empty aluminum pan is used as the reference. Both the sample and reference are subjected to a temperature increase at a constant rate. Since the DSC is at constant pressure, heat flow is equivalent to enthalpy changes:

$$\left(\frac{dq}{dt}\right)_p = \frac{dH}{dt} \qquad \text{(Eq II- 3)}$$

$\frac{dH}{dt}$ is the heat flow measured in mcal.sec^{-1}. The heat flow difference between the sample and the reference is:

$$\Delta\frac{dH}{dt} = \left(\frac{dH}{dt}\right)_{sample} - \left(\frac{dH}{dt}\right)_{reference} \qquad \text{(Eq II- 4)}$$

In endothermic processes, such as melting, dehydrations, reduction reactions, and some decomposition reactions, heat is absorbed. Hence, heat flow to the sample is higher than that to the reference, resulting in a positive $\Delta\frac{dH}{dt}$. Exothermic processes such as crystallization, some cross-linking processes, oxidation reactions, and some decomposition reactions, heat is released, resulting in a negative $\Delta\frac{dH}{dt}$. A DSC profile of a polymer which could have similar transitions as ionic liquids is shown below in Figure II- 5 as a typical example expressing heat flow in mW.mg.
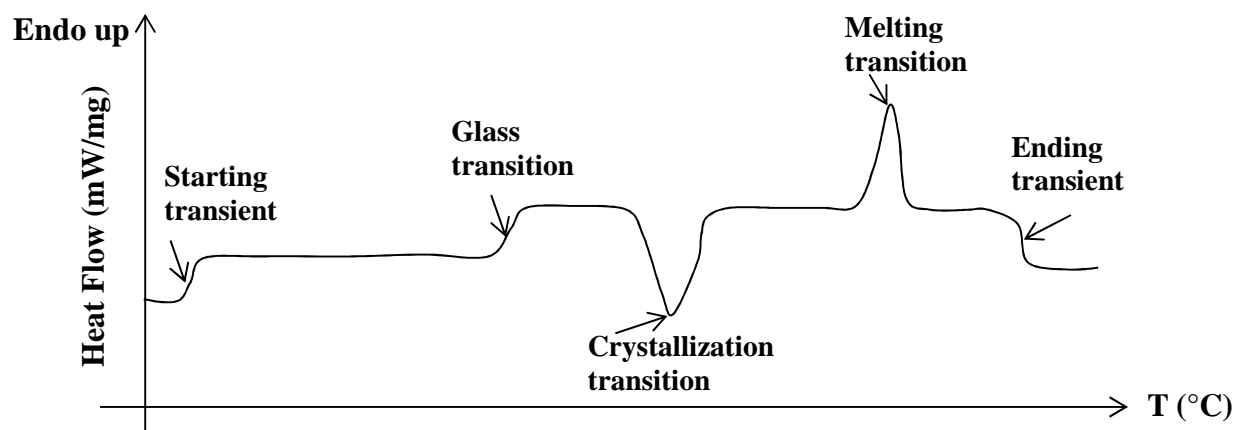
Figure II- 5: DSC scan depicting features resulting from change in heat flow due to transition.

Temperature behaviour measurements were studied using a Netzch 204 HP Phoenix differential scanning calorimeter, TASC 414/3A controller with nitrogen cooling. Recording was done under Helium gas and a temperature ramp of 5 K.min^{-1}, in the temperature profile from room temperature to -80 °C, then up to 100 °C and the cycle was repeated one more time before cooling from 100 °C to room temperature. Temperature range of this instrument was from -150 to 600 °C.

III-3.2. Conductivity

Conductivity of most electrolytes was tested under an inert atmosphere in a glovebox using a Consort C931 conductivity meter and a SK10T electrode calibrated with 0.01 M KCl standard solution.

III-3.3. Electrochemical characterizations of electrolytes

Electrochemical Impedance Spectroscopy (EIS) – Conductivity Measurements

The dependence of conductivity on temperature was studied on some ionic liquids and mixtures. They were tested in a nylon body Swagelok® cell with stainless steel pistons (see Figure II- 6) assembled in a glovebox with inert atmosphere of Argon gas, and with oxygen and water content of less than 1 ppm. Ionic resistance is determined by Electrochemical Impedance Spectroscopy (EIS) measurements by an Autolab station (PGSTAT128N).
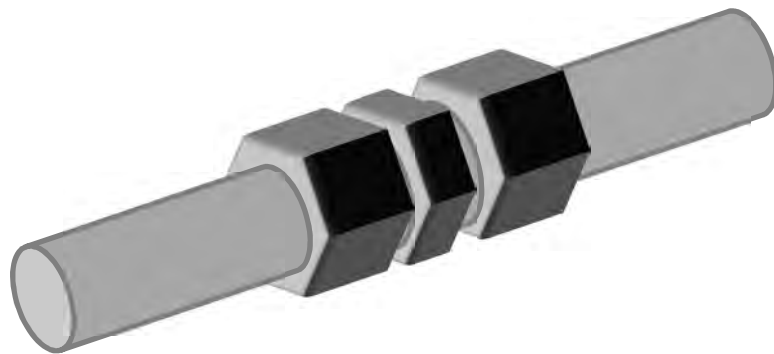
Figure II- 6 : Schematic of a nylon body Swagelok® cell.

The range of frequency applied was between 1 MHz to 1 Hz. In most cases, an amplitude voltage of 10 mV was used. However the appropriate amplitude varied with different electrolytes at different temperatures due to the changes in their physical states. Monitoring of the Lissajous curves helped determined the suitable amplitude for impedance measurements, maintaining linearity in the system.

Figure II- 7 shows an equivalent circuit and its corresponding nyquist plot for an ion conductor where a straight line (dotted) is constructed perpendicular to the real axis as the electrode surface has only a double layer capacitor.
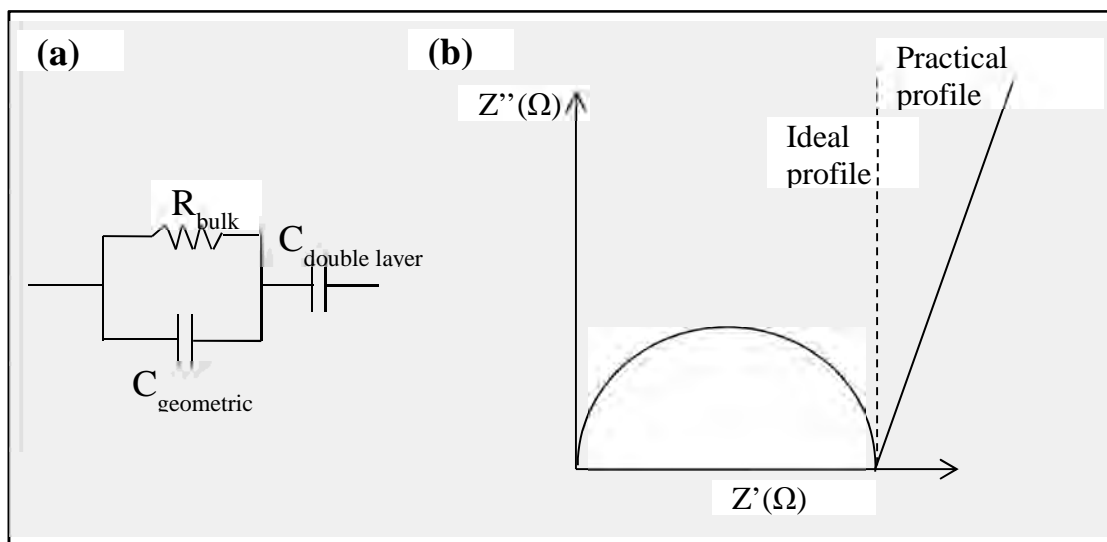
Figure II- 7: Schematic of an equivalent circuit for an ion conductor **(a)** and the corresponding Nyquist plot **(b)** [3].

However, deviation from the ideal profile vertical to the real axis is attributed to the rate limiting process as the ions diffuses to form a double layer in this frequency region.

Ionic resistance, R, values measured in the temperature range of -60 to 100 °C was then determined from the nyquist plot and used to obtain ionic conductivity values using:

$$\sigma = \frac{l}{Rs} \qquad \text{(Eq II- 5)}$$

Where, R is the ionic resistance, (l/s) is the cell constant with l, being the distance between the two electrodes and s, the mean area of the electrodes, and σ the ionic conductivity.

Linear Sweep Voltammetry (LSV)

The estimation of the electrochemical window of the ILs was carried out by using linear sweep voltammetry (LSV) with respect to a reference electrode. As the redox reactions of the ions are electrochemically irreversible in general [5,6], fresh electrolyte was prepared for each measurement of oxidation and reduction limit. A silver rod was used as the quasi reference, platinum as the working electrode and graphite as the counter electrode. Since the cathodic and anodic limiting potentials are subjected to the type of working electrode, a redox compound, bis(cyclopentadienyl)iron(II), also named ferrocene, was used as the internal reference. Redox potentials of the ILs with respect to the silver reference (V_{Ag}) were then corrected by using the redox potential of ferrocene ($E°_{(FeII/FeIII)}$) in the ionic liquid with respect to that of the ionic liquid without ferrocene. Limits of electrochemical window were determined by a cut-off current density of 0.05 mAcm^{-2} at room temperature in a linear sweep voltammogram recorded at a scan rate of 5 mV.s^{-1} as shown in Figure II- 8a [3].
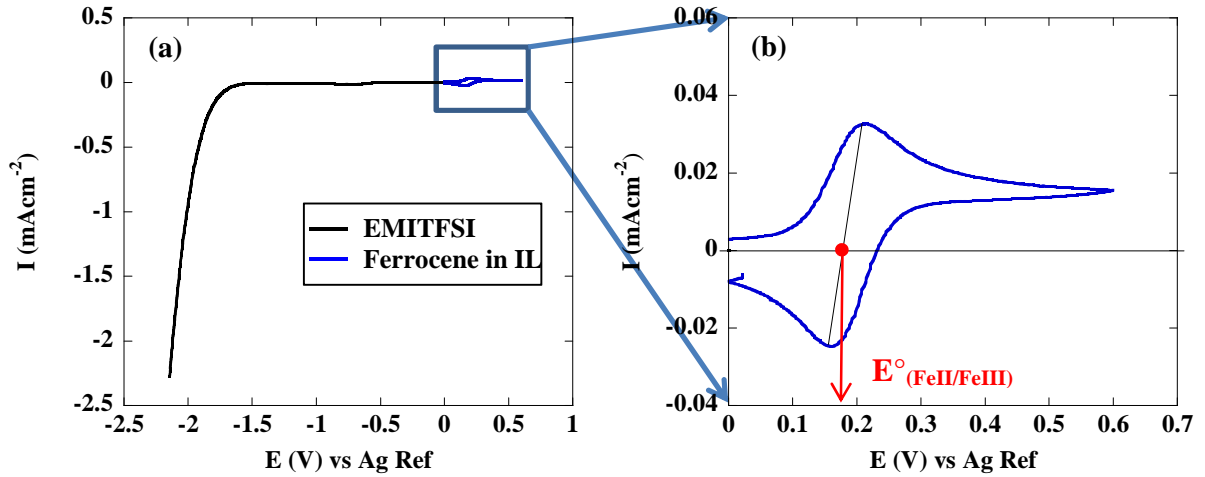
Figure II- 8: LSV of the negative potential limit for neat EMI-TFSI ionic liquid at room temperature **(a)** and the enlarged redox couple of Ferrocene (Fc) dosed in the ionic liquid **(b)**.

Since the silver wire is a quasi-reference, the distinguished redox peaks of the ferrocene enabled reproducible measurements of the electrochemical limits of the electrolyte. $E°_{(FeII/FeIII)}$ with respect to quasi Ag reference immersed in the mixture of ferrocene and the ionic liquid was determined from the CV of ferrocene at zero current, as indicated in Figure II- 8b. The potential limit of the ionic liquid under test was then referenced with respect to ferrocene, V_f by subtracting $E°_{(FeII/FeIII)}$ from the potential at cut-off current density of 0.05 mA cm^{-2} of the LSV of the ionic liquid, V_{Ag}:

$$V_f = V_{Ag} - E°_{\left(Fe^{II}/Fe^{III}\right)} \qquad \text{(Eq II- 6)}$$

The same process was applied to obtain the anodic potential limit and the entire electrochemical window of the electrolyte can be calculated from the addition of the cathodic and anodic potential limits.

IV. Study of capacitive behaviour

Electrochemical Impedance Spectroscopy (EIS), Cyclic Voltammetry (CV), and Galvanostatic Cycling (GC) are the most used electrochemical techniques for supercapacitor studies. While the EIS is a stationary technique where there is no variation in terms of voltage and current, the CV and GC techniques are transient techniques which involve the current and voltage variations to allow various form of study and characterizations of the supercapacitor.

IV-1. Electrochemical Characterization Techniques

IV-1.1. Electrochemical Impedance Spectroscopy (EIS)

   Equivalent series resistance (ESR) was measured (real resistance at high frequency) from the Nyquist plots by performing electrochemical impedance spectroscopic frequency scan in the range of megahertz to millihertz using a 2- electrode configuration. Impedance data were collected from applying a low-amplitude alternating voltage of 5 mV root mean square to the cell at its open circuit potential in a fully-discharged state.

The alternating voltage is a sinusoidal function of time given by:

$$V(t) = V_0 \sin \omega t \qquad \text{(Eq II- 7)}$$

Where:

- V_0 is the amplitude of the alternating voltage signal
- ω is the pulsation in hertz given by: $\omega = 2\pi f$, where f is the signal frequency

An accompanied sinusoidal current is also present upon the application of this alternating voltage to a resistor which follows:

$$I(t) = I_0 \sin \omega t \qquad \text{(Eq II- 8)}$$

Where *I(t)* is in phase with *V(t)* and Resistance, *R =V/I* (ohm's law)

For an ideal supercapacitor, the current response is out of phase with the voltage response by 90°C and hence using the Eulers relationship: *exp(jφ) = cosφ + jsinφ*

$$I(t) = I_0 \sin \omega t - \varphi \;\; \rightarrow \;\; I = I_0 \exp j(\omega t - \varphi) \qquad \text{(Eq II- 9)}$$

$$V(t) = V_0 \sin \omega t \;\; \rightarrow \;\; V = V_0 \exp(j\omega t) \qquad \text{(Eq II- 10)}$$

Deriving to: Impedance, $\;Z_\omega = \dfrac{V_0}{I_0} \exp(j\varphi) = Z_0 (\cos\varphi + j\sin\varphi) \qquad \text{(Eq II- 11)}$

The instantaneous charge is *Q = CV* $\rightarrow$ *Q = C V₀ sin ωt*.

Since *Q = It*,

$$I = \frac{dQ}{dt} = \omega C V_0 \cos \omega t \;\rightarrow\; \frac{V_0}{I} = \frac{\exp(j\omega t)}{\omega C} \;\rightarrow\; Z = \frac{\cos(\omega t) + j\sin(\omega t)}{\omega C} \qquad \text{(Eq II- 12)}$$

At I_{max}, $\cos(\omega t) = 1$, $\sin(\omega t) = 0$, leading to $Z = \dfrac{1}{\omega C}$

Since the impedance of a capacitor is imaginary, it takes the form of:

$$Z = \frac{1}{j\omega C} \qquad \text{(Eq II- 13)}$$

Therefore, the impedance of a purely capacitive RC circuit can be expressed as:

$$Z = R + \frac{1}{j\omega C} \qquad \text{(Eq II- 14)}$$

Several pieces of information could be obtained from the nyquist plot of an electrochemical impedance spectrogram represented by an imaginary y-axis (-Z'') and a real x-axis (Z') as shown in Figure II- 9.
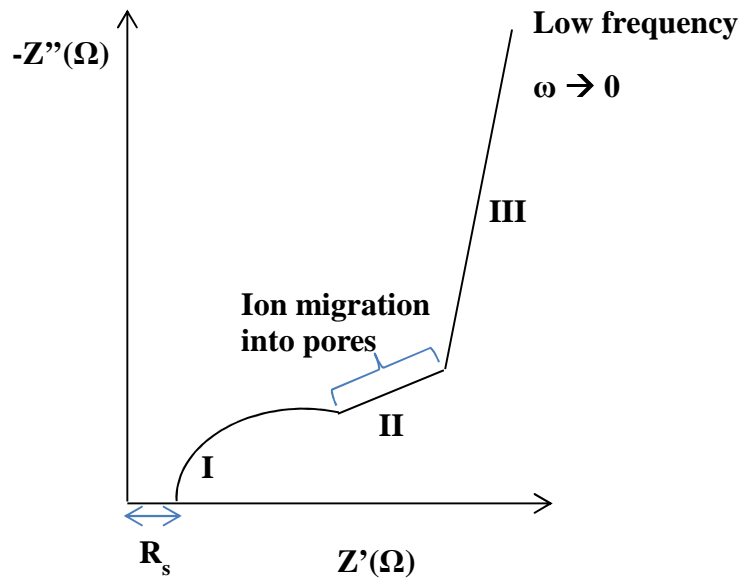
Figure II- 9: Nyquist EIS plot of a supercapacitor.

Towards high frequency (Region I), $1/j\omega C$ approaches 0 $(1/\infty)$ and hence impedance takes on a pure resistance value, R as explained in equation II-14. One of the most efficient

information obtained from the supercapacitor cell is the equivalent series resistance, ESR (See Eq II-15), which comprises of information on the current collector/activated carbon interface.

Region II, is characterized by a 45° slope which provides information on the resistance of the electrolyte inside the pores of carbon. This gives idea on the ion mobility inside the porous electrode material in the chosen electrolyte, which is especially useful in determining the compatibility and behaviour of electrolyte with material type.

As frequency diminishes in Region III, the impedance tends towards a pure capacitive value. Henceforth the vertical tail deviated in a slight angle, almost parallel to the imaginary y-axis, is an important indicator of a capacitive cell.

The common quantitative information obtained from the EIS are:

1) ESR expressed as a function of pulsation:

$$ESR(\omega) = \mathrm{Re}(Z).S \qquad \text{(Eq II- 15)}$$

Where:

- *ESR(ω)* is the equivalent series resistance ($\Omega. \mathrm{cm}^2$)

- *S* is the surface area of the electrode (cm^2)

- *Re(Z)* is the real impedance (Ω) that is, R_s in Figure II- 9

2) Capacitance from frequency:

$$C = \frac{2}{\omega \mathrm{Im}(Z)m} \qquad \text{(Eq II- 16)}$$

Where:

- *C* is the capacitance of the supercapacitor ($\mathrm{F.g}^{-1}$)

- *ω* is the pulsation (Hz)

- Im(*Z*) is the imaginary impedance (ω)

- *m* is the mass of the active material in the electrode (g)

Transmission line model

The equivalent circuit for porous electrodes has been described by de Levie [7] using the transmission line model as shown in Figure II- 10:
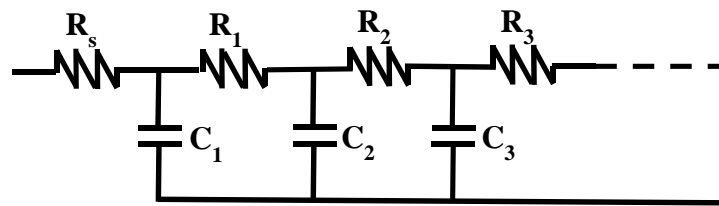
Figure II- 10 : De Levie transmission-line model for resistance/capacitance matrix in a porous electrode of high SSA.

The real impedance *Re(Z)* is approximated to R_s in both Figure II- 9 and Figure II- 10 at high frequency and towards low frequency, the impedance adds up through the series of RC circuits as shown in Figure II- 10. A schematic of EIS of a porous electrode is reported by Kaus *et al.* as shown in Figure II- 11.
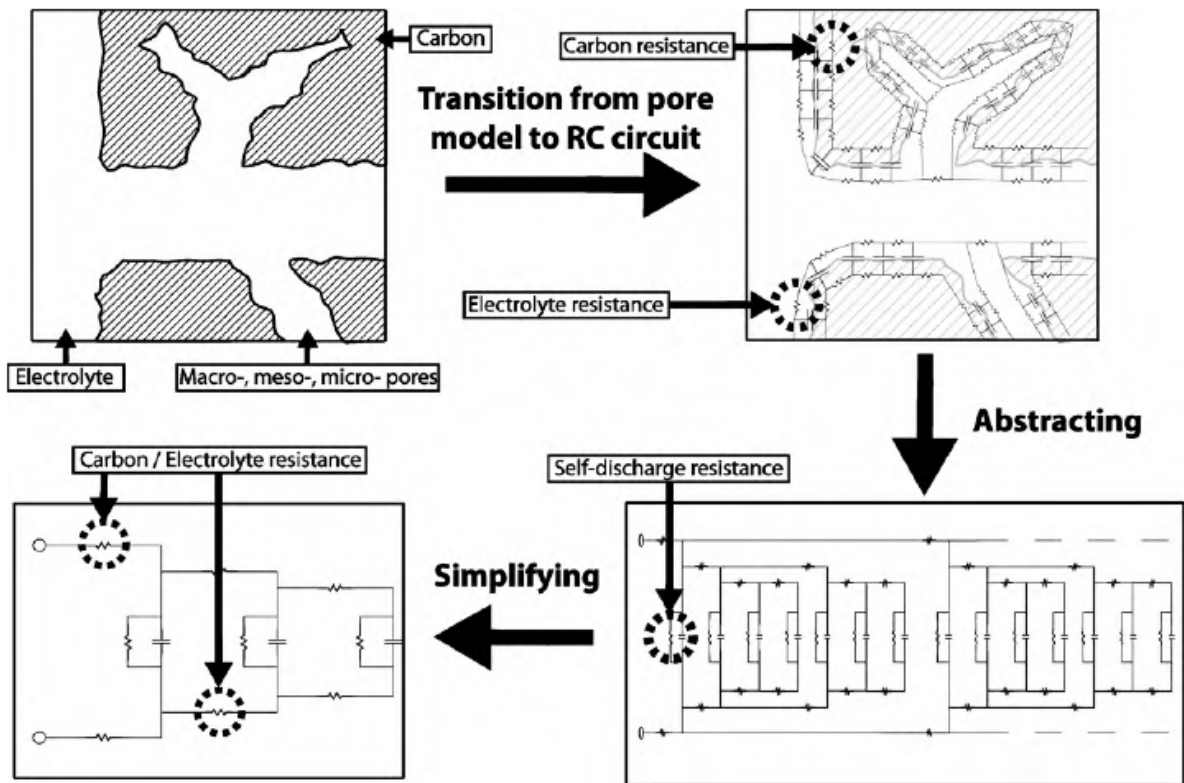
Figure II- 11: Transition from the illustrative pore model to the descriptive RC circuit [8].

IV-1.2. Cyclic voltammetry (CV)

Cyclic voltammetry is a qualitative and yet pseudo-quantitative method which gives information on the interactions between the electrolyte ions and the carbon interface. The ability to use a large range of scan rates, kinetic analysis can be carried out qualitatively. Furthermore, other electrochemical information, such as the electrochemical window, could be obtained.
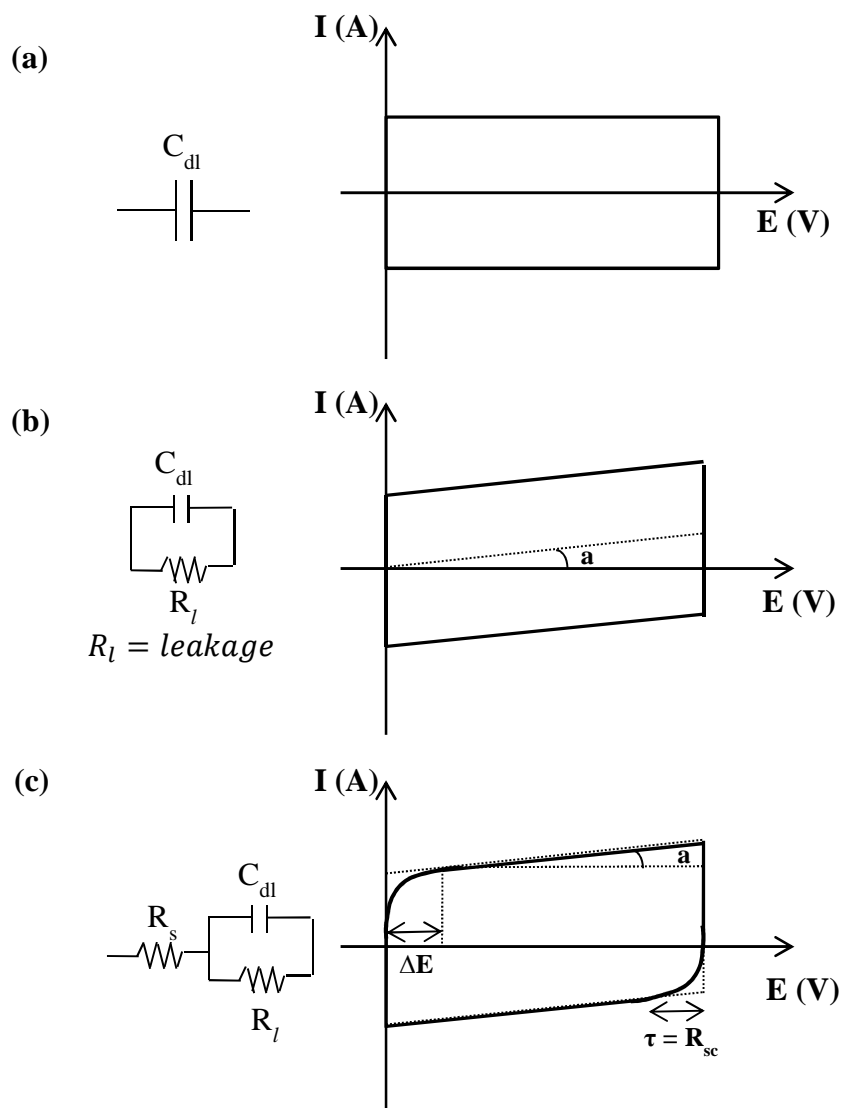
Figure II- 12: Cyclic voltammograms and the respective equivalent circuits of an ideal supercapacitor (a), a supercapacitor with resistance in parallel (b) and of a real supercapacitor (c)

The ideal capacitive behaviour produces a perfect rectangular CV profile as shown in Figure II- 12. Several situations due to (1) compatibility among electrolyte ions, electrode materials, current collectors separator material and thickness and (2) the effect of electrolyte

resistance, could result in the deviation from the perfect rectangular CV in Figure II- 12a to CVs shown in Figure II- 12c respectively.

The capacitance, C in Farads per gram (F.g^{-1}), can be calculated from the cyclic voltammogram using Eq II- 17, where I is the current in Amperes (A), $\dfrac{dV}{dt}$ is the scan rate used in V.s^{-1} and m is the mass of the electrodes in grams (g).

$$C = \frac{2I}{\left(\dfrac{dV}{dt}\right) \times m} \qquad \text{(Eq II- 18)}$$

IV-1.3. Galvanostatic cycling (GC)

From galvanostatic cycling, it is possible to obtain the ESR, capacitance and the cyclability of the supercapacitor. This technique was used to record the cycling profile of the assembled cells for 10000 cycles at a charging and discharging current density of ±5 mA.cm^{-2} in a two-electrode and three-electrode configurations. All electrochemical measurements were made using a VMP3 Potentiostat/Galvanostat/EIS (from BioLogic Science Instruments).
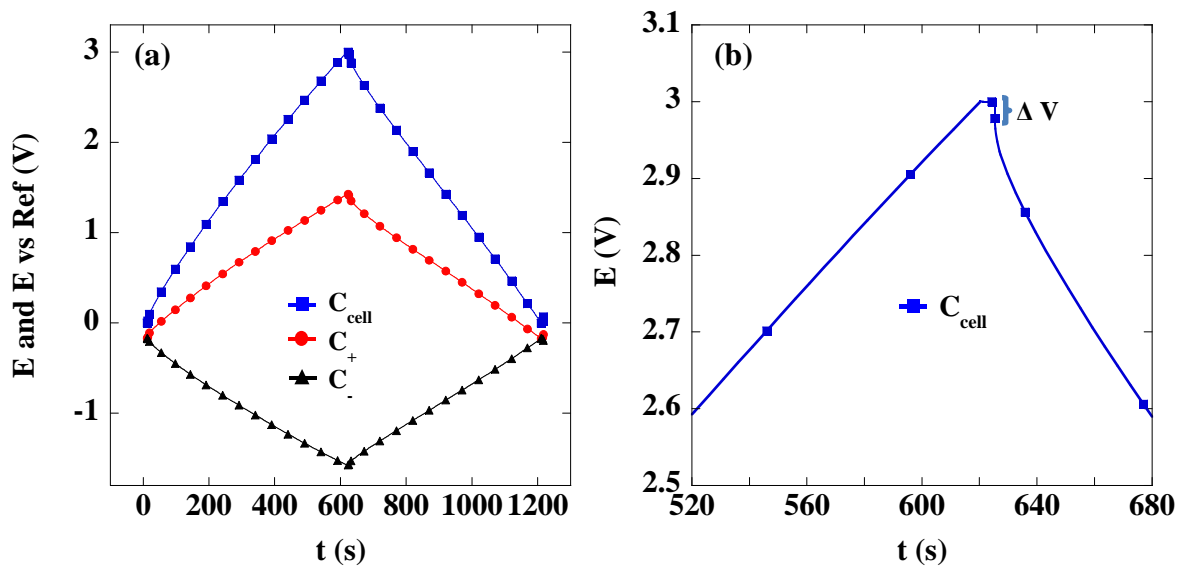
Figure II- 13: Galvanostatic cycling profile of an EDLC in a 3-electrode cell configuration **(a)** and the magnified ohmic drop of the cell capacitance profile **(b)**.

During the charge/discharge process in experiment shown in Figure II- 13a, the cell voltage was controlled to the voltage window of the electrolyte and the negative electrode capacitance was measured. Hence the positive electrode capacitance is calculated, resulting in a galvanostatic cycling profile as depicted in Figure II- 13a.

A sudden drop of cell voltage magnified in Figure II- 13b is attributed to the ohmic drop due to the electrolyte or contact resistance. This ohmic drop therefore, determines the time constant of the supercapacitor.
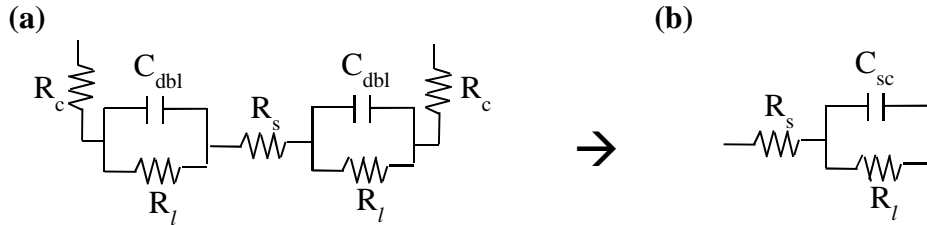
Figure II- 14: Equivalent circuit of a supercapacitor consisting of resistance components from contacts between electrodes and current collectors, R_c, electrolyte resistance, R_s, leakage current, R_l and the double layer capacitance, C_{dbl} **(a)** and the simplified equivalent circuit **(b)**. (Reproduced from Chapter I)

The time constant is equal to R_sC_{sc} depicted in Figure II- 14b, while the time constant for self-discharge is equal to R_lC_{sc}. Hence R_l should be at its possible maximum value. Generally, a lower energy density (W-h.kg^{-1}) is required in order to lower the RC_{sc} time constant, and in turn, increase the power capability (W.kg^{-1}) of the supercapacitor. In material terms, electrode thickness and electrolyte conductivity could have direct impact on the time constant. The resistance of the load, R_l must be high so that the resistance of the capacitor is relatively low. In terms of charging and discharging rates, as the discharging becomes faster, capacitance resistance increases, resulting in higher losses. On the other hand, as the time constant decreases, capacitor resistance follow suit and thereby decreasing losses as well.

At time zero of the discharging process, the sudden drop of cell voltage due to the current in the series resistance, R_S, is often associated with the electronic conductivity within the cell. The discharging process across a load resistance, R, then leads to a time constant:

$$\tau = (R + R_s)C \qquad \text{(Eq II- 19)}$$

Capacitance was calculated from the galvanostatic discharge cycle of a symmetrical cell by:

$$C = \frac{nI}{\dfrac{\Delta V}{\Delta t} \times m} \qquad \text{(Eq II- 20)}$$

where:

- $n = 2$: electrode discharge; $n = 1$: cell discharge
- I is the discharge current applied (A)

78

- $\dfrac{\Delta V}{\Delta t}$ is the slope of the discharge profile of the cell or individual electrodes (V. s^{-1})

- C is the capacitance of two capacitors in series (F. g^{-1})

- m is the mass of active material in the electrode (g)

As shown in Figure II- 14, where the total capacitance of the supercapacitor cell, C_{sc} consist of the addition of two electrochemical double layer, C_+ and C_- in series:

$$\frac{1}{C_{SC}} = \frac{1}{C_+} + \frac{1}{C_-} \qquad \text{(Eq II- 21)}$$

Therefore in a symmetrical supercapacitor cell,

$$C_{SC} = \frac{C^{+,-}}{2m} \qquad \text{(Eq II- 22)}$$

IV-2. Set-ups

Three different set-ups were used for studying the electrochemical double layer and will be discussed in the later sub-sections. Two of which are assembled into full cells with two- and three-electrode configuration, namely the Swagelok® cells and the 4 cm² electrode EDLCs respectively. The last one consisted of a three-electrode half-cell configuration.

IV-2.1. 4cm² Electrode EDLCs
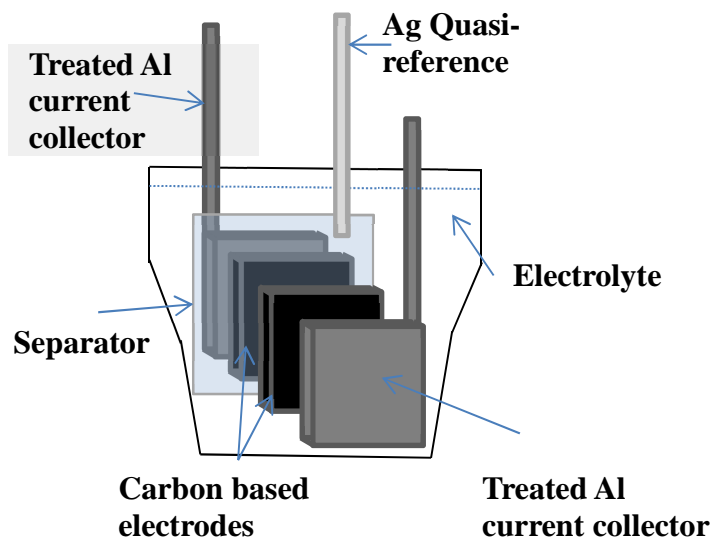
Figure II- 15: Assembly of the large area electrode EDLC cells.

4 cm² supercapacitor cells were assembled in a glove box with an Argon atmosphere of less than 1 ppm of O_2 and H_2O content. The 4 cm^2 active materials were laminated onto

treated aluminium current collectors [9] and the stack was completed with a polytetrafluoroethylene (PTFE) separator (2x25 μm thick) inserted between the two electrodes. A constant pressure of about 5.10^5 Pa was applied to the stack with the help of PTFE slabs and stainless steel clamps, (Illustrated in Figure II- 15). All cells tested were assembled symmetrically. Silver wire (2 mm in diameter) was used as a quasi-reference electrode.

Current Collectors

Current collectors were prepared as follows: aluminium foil was first laminated to a thickness of about 250 μm and then subjected to two chemical etching steps beginning with an immersion of current collectors in 1M NaOH solution for 20 minutes at room temperature. This step served as a preliminary step in degreasing the surfaces of the Al foil as well as to generate nucleation sites for aluminium dissolution. Next, the current collectors were rinsed with distilled water and promptly placed in a 1 M HCl solution maintained at 80 °C for 2 minutes. They were then rinsed thoroughly again with distilled water upon removal from the HCl solution and then blown dry.

Conductivity was enhanced by dip coating at a withdrawal rate of 50cm/min from slurry consisting of a few percent of cabonaceous material powder suspended in a polymeric sol. Lastly, the collectors were subjected to thermal treatment for 4 hours at 470 °C in air to remove the polymeric sol, leaving the surface covered with the conducting carbonaceous particles. Contact was then made by welding Al wires onto the Al treated current collectors.

Carbon Electrodes

Electrode films of 4 cm^2 were prepared with a composition of 95 wt % CDC and 5 wt % PTFE [10] using ethanol as the medium for mixing the slurry. The thickness of the active material ranged from 250 to 270 μm depending on the type of activated carbon (Ti-CDCs from Drexel University, YP 17 from Kurakay and CECA AB from Arkema), as well as the synthesis temperature of Ti-CDCs, while keeping the weight density constant at 15 mg.cm^{-2}.

Separator

Separator, as its name suggests, separates the electronic conductivity between the electrodes and yet allows the passage of electrolyte ions for achieving the effective charge separation at the oppositely charged electrodes, preventing a short circuit. Many types of separators exist and the choice of separator lies in its low resistivity and reactivity in the

electrolyte used. In this set-up, two layer of 25 µm porous PTFE film with 65% porosity and 0.1 µm in pore diameter was used as the separator, supplied by W.L. Gore & Associates.

Electrolytes and conditions used

Table II- 7: Electrochemical parameters used with the respective electrolytes.

Electrolytes	Electrochemical Window (V)	Temperature (°C)	Concentration (M)
EMITFSI	3.0	60	Neat
EMITFSI / AN	2.8	20	2
EMIFSI / AN	2.8	20	2

Electrochemical characterizations of EDLCs

Characterization of the assembled cell was determined by the three principle electrochemical techniques, namely the Electrochemical Impedance Spectroscopy (EIS), Cyclic Voltammetry (CV) and lastly, the Galvanostatic Cycling (GC). All tests except for impedance measurements were performed under a 3-electrode cell configuration.

Electrical series resistance (ESR) was measured (real resistance at high frequency) from the Nyquist plots by performing electrochemical impedance spectroscopic frequency scan from 50000 kHz to 10 mHz for the solvent–based electrolytes and 75000 kHz to 10 mHz for neat electrolytes (without solvent) using a 2- electrode configuration. Impedance data were collected from applying a low-amplitude alternating voltage of 5 mV root mean square to the cell at its open circuit potential in a fully-discharged state.

Cyclic voltammetry tests were conducted at a scan rate of 20 mV.s^{-1} with the different activated carbon and electrolytes at room temperature for solvent-based electrolytes and at 60 °C for electrolytes consisting of neat ionic liquids as laid out in Table II- 7. Galvanostatic cycling was used to record the cycling profile of the assembled cells for 10000 cycles at a charging and discharging current density of ±5 mA.cm^{-2} in a two-electrode and three-electrode configurations. All electrochemical measurements were made using a VMP3 Potentiostat/Galvanostat/EIS (from BioLogic Science Instruments).

IV-2.2. Cavity Micro-Electrode (CME)

Electrochemical characterization of the electrode/electrolyte couple was realized using the cavity micro-electrode technique. The microelectrode was prepared according to C.

Cachet-Vivier *et al.* [11] with a cavity for packing the carbon powder for testing. It consisted of a platinum wire sealed in a glass rod and the micro-cavity of approximately 10^{-6} cm^3 and characteristic depth of about 100 µm for sample packing was created by a controlled dissolution of the Pt wire in hot *aqua regia* solution at 80 °C.
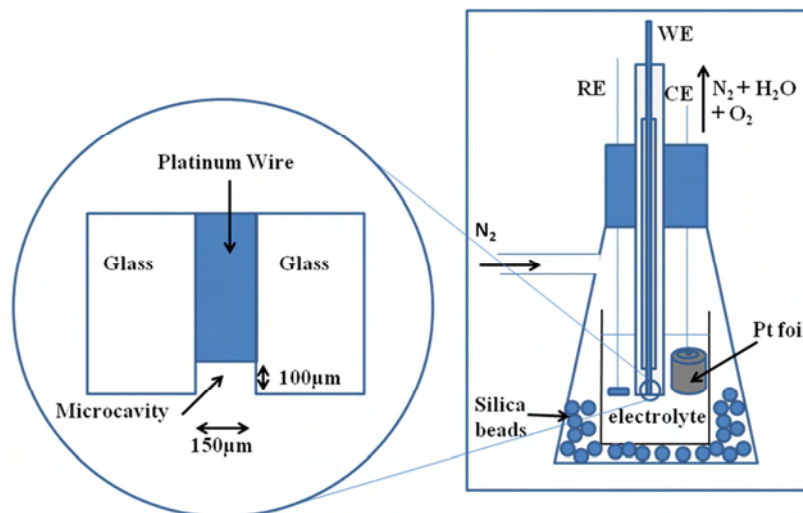
Figure II- 16: Schematic of the Cavity Micro-Electrode (CME) set-up.

Three-electrode cell configuration was used as shown in Figure II- 16. The counter electrode is a rolled platinum foil of 1 cm^2, a silver rod is used as a quasi-reference electrode. Constant nitrogen gas was supplied to the set-up to purge moisture and oxygen out of the atmosphere. The open circuit potential was also tracked to ensure that a coherent starting point between different batches of the same sample is maintained. Maximum and minimum current values were also measured in view to correlate with cyclic voltamograms collected from 4cm² electrode EDLCs. New batch of carbon powder (sample) was used for each voltammogram recorded.

IV-2.3. Swagelok Cells

The 2-electrode cell set-up
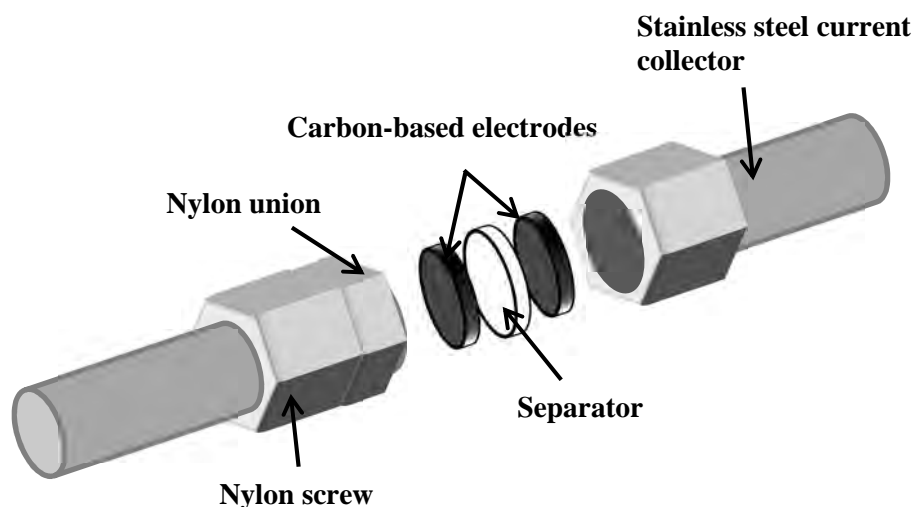
Figure II- 17: Schematic of a 2-electrode nylon Swagelok cell assembly.

V. References

[1]   Yushin, G.; Nikitin, A.; Gogotsi, Y. Nanomaterials Handbook, Gogotsi, Y. Ed. *CRC Press: Boca Raton* (2006) 237.
[2]   http://www.kuraraychemical.com/Products/SC/capacitor.htm.
[3]   Ohno, H. *Electrochemical Aspects of Ionic Liquids* (2005).
[4]   Wasserscheid, P.; Welton, T. *Ionic Liquids in Synthesis* (2003).
[5]   Lipsztajn, M.; Osteryoung, R. A. *Electrochimica Acta,* **29** (1984) 1349.
[6]   Xiao, L.; Johnson K.E., *J Electrochemical Society,* **150** (2003) E307.
[7]   De Levie, R. *Electrochimica Acta* **8** (1963) 751.
[8]   Kaus, M. ; Kowal, J.; Sauer, D.U. *Electrochimica Acta* **55** (2010) 7516.
[9]   Portet, C.; Taberna, P. L.; Simon, P.; Laberty-Robert, C. *Electrochimica Acta,* **49** (2004) 905.
[10] Bonnefoi, L.; Simon, P.; Fauvarque, J. F.; Sarrazin, C.; Sarrau, J. F.; Dugast, A. *Journal of Power Sources Proceedings of the 1999 21st Internatoinal Power Sources Symposium 'Research and Development in Non-Mechanical Electrical Power Sources', May 10-May 12 1999,* **80** (1999) 149.
[11] Cachet-Vivier, C.; Vivier, V.; Cha, C. S.; Nedelec, J. Y.; Yu, L. T. *Electrochimica Acta* **47** (2001) 181.

Chapter III :

Microelectrode study of pore size, ion size and solvent effects on carbon capacitance

I. Introduction

There was a long held axiom that the larger the pore size (in the range of 2-5 nm), the higher the capacitance. However this relationship was overturned when pore sizes smaller than 1 nm were explored for EDLC understanding. This breakthrough discovery was seen with an anomalous increase in capacitance when activated carbon material, such as carbide-derived carbons (CDCs), of well-defined pore sizes of less than 2 nm was used [1]. It was shown that pore sizes of less than 1 nm were greatly contributing to the capacitance, suggesting that the solvated ions were capable of removing partially their solvation shell to enter such pores. The understanding and idea of the electrochemical double layer conceptualizes that the maximum capacitance might be due to the matching pore sizes to the effective sizes of the electrolyte ions.

This work of anomalous increase of capacitance using a solvated electrolyte of 1.5 M tetraethylammonium tetrafluoroborate (NEt_4BF_4) dissolved in acetonitrile (AN), then set off a series of questions over (1) the size relationship between pore size and ion size, to which extent of proportion can the maximum capacitance be optimized, and (2) the effect of solvation on the capacitance.

The objective of this chapter is hence to study the effect of ion size and solvent on the charge/discharge behaviour of microporous carbons for EDLC applications under dynamic conditions using a Cavity Micro-Electrode (CME). Four different pore sized samples (with pore sizes of 0.68, 0.74, 0.76 and 1 nm) which correspond to three regimes of pore sizes that are (1) smaller than the ion size, (2) similar to those of the ions, and (3) larger than the ions, were studied and their corresponding characteristics have been presented in Table III-1. The average pore size ranges from 0.68 nm to 1 nm depending on the temperature of synthesis: the higher the temperature, the larger the pore size.

II. Cavity Micro-Electrode

A cavity Micro-Electrode (CME) [18] was employed to perform a qualitative assessment of the adsorption of NEt_4^+, BF_4^- ions in Ti-CDCs. This technique allows the collection of information on the carbon surface / electrolyte interactions with no influence of binders, separators, current collectors and other components of conventional electrochemical cells that can obscure the fine features of carbon-electrolyte interaction. Moreover, the small

size of the electrochemical interface can record voltammograms over a large scan rate range of > 50 mV.s^{-1} [2], allowing the characterization of a small amount of powder (hundreds of micrograms, subjecting to cavity size). On the grounds of fast acquisition of the voltammograms, first-hand information can quickly be obtained by screening the samples for primary analyses of the electrolyte/carbon interface interactions. With the current existence of a vast number of electrolytes and materials, this is a powerful technique and complementary tool to quickly evaluate the performance of materials and highlight possible trends to explore further through the use of conventional techniques.

The conventional method of the EDLC testing involves the need to prepare active material paste, long duration of tests especially when ILs are used in the testing due to their high ionic resistances. Consolidation of reproducible results would probably take weeks. Moreover, in such conventional cells, the electrochemical interface between the electrode and the electrolyte is large, resulting in large current and thus large ohmic drop and cyclic voltammograms (CVs) that are distorted when usual scan rates (from fractions of millivolts per second up to tens of millivolts per second) are used. The ohmic drop thus hinders the study of fast electrochemical processes. In comparison with conventional electrodes, the real electrochemical interface area is around a fraction of square millimetres and the ohmic drop arising from the bulk of the electrolyte can be neglected, allowing the use of scan rates of a few volts per second [12,18] to characterize the powder electrode.

With the implementation of the cavity micro-electrodes (CME) in EDLC testing, collection of results is much faster, within 10 minutes as compared to days for 4 cm² electrodes EDLC, enabling combinatorial electrochemistry studies [12,18]. This does not include the time required to carefully assemble the 4 cm² EDLC cell in the glove box. Changing of sample in the microcavity does not need more than 3 minutes and only minimal amount of sample is required.

III. Titanium Carbide Derived Carbons (Ti-CDCs)

As previously mentioned in Chapter II, CDCs are produced by high-temperature chlorination of carbides whereby metals and metalloids are removed as chlorides, leaving behind nanoporous carbon with a 50 to 80 % open pore volume:

$$TiC + 2\ Cl_2 \rightarrow TiCl_4 + C$$
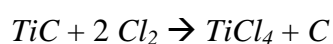
Thus, TiC acts as a template in producing a carbon material with narrow pore size distributions.

Table III-1: Characteristics of the TiC-CDC samples used (recall from Chapter II).

Chlorination temperature (°C)	BET SSA (m².g⁻¹)	Pore volume (cc.g⁻¹)	Average pore width(nm)	Maximum pore width* (nm)
400	1113	0.51	0.65	1.12
500	1140	0.50	0.68	1.18
550	1202	0.51	0.72	1.29
600	1269	0.60	0.74	1.23
700	1401	0.66	0.76	1.41
800	1595	079	0.81	1.54
900	1600	0.81	1.0	2.50
1000	1625	0.81	1.1	2.8

*85 % of pore volume is below this size

The pore size of the CDCs is recalled in Table III-1 (for more details, see Chapter II). These carbides are attractive in this sense as they offer narrow pore-size distribution with a mean value that is tunable (by varying chlorination temperatures) in the range of ~0.5 to ~3 nm with an accuracy of more than 0.05 nm [3] for more in depth study of the EDLC. This whole range of pore sizes allowed the study of the environment of the ions when entering the pores.

Such uniformity of pore sizes also means that the whole active material is being fully utilized with no dead pore volume, thereby contributing to the escalated capacitance. Ti-CDCs have not only served as a breakthrough for the material limitation (due to poor pore size distribution) faced previously by Anis *et al.* [4] in the study of the EDLC using activated carbons and ionic liquids, but have provided excellent explanations on the ion sieving effect of the active material in an EDLC too [5,6]. Many different CDCs like SiC, ZrC, Ti_2AlC, B_4C, TaC and Mo_2C have been studied extensively before [7,8], however, TiC supplies a range of pore sizes corresponding to the ionic sizes of electrolytes of interest, ranging from 0.6 nm to 1.1 nm without monumental graphitization of the CDCs at high synthesis temperatures [9]. Amorphous carbon is preferred for the study of pure capacitive behaviour as graphitized carbon could lead to non-capacitive capacitance contributions from intercalation of electrolyte ions between the graphite layers.

IV. Electrolytes

Table III- 2 lists the characteristics of the electrolytes used. The conductivity of the acetonitrile AN-based electrolyte is the higher than at of the PC-based one due to the higher ion mobility in AN. From this table, the solvated sizes of the ions are bigger in PC than in AN.

Table III- 2: Characteristics of the electrolytes studied.

Electrolyte	Electrochemical Potential Window (V)	Size of Ions (nm)				Conductivity (mS.cm^{-1})
		Bare [5,10]		Solvated[10]		
		Cations	Anions	Cations	Anions	
1.5 M NEt$_4$BF$_4$ in AN	-1.3 to 1.0			1.30	1.16	60
1 M NEt$_4$BF$_4$ in PC	-1.5 to 1.1	0.67	0.48	1.35	1.40	13

V. Results

V-1. Selection of scan rate

Since the Ti-CDC$_{900°C}$ has the largest pore size of 1 nm among the chosen samples to be tested, it was used to determine the best scan rate for the study of these electrolytes. Limitations in these large pores would likely be ion transport due to conductivity rather than steric effects of electrolyte ions during the adsorption and desorption processes especially at fast rates. Figure III- 1a shows the Cyclic Voltammograms (CVs) of the 900 °C CDC sample at different scan rates from 20 to 1000 mV.s^{-1} in 1.5 M NEt$_4$BF$_4$ in AN electrolyte. As I = C(dv/dt), the current response increases as the scan rate increases. Hence there is a need to normalize the current (I) response with the scan rate (dv/dt) to obtain capacitive current for comparison purposes.
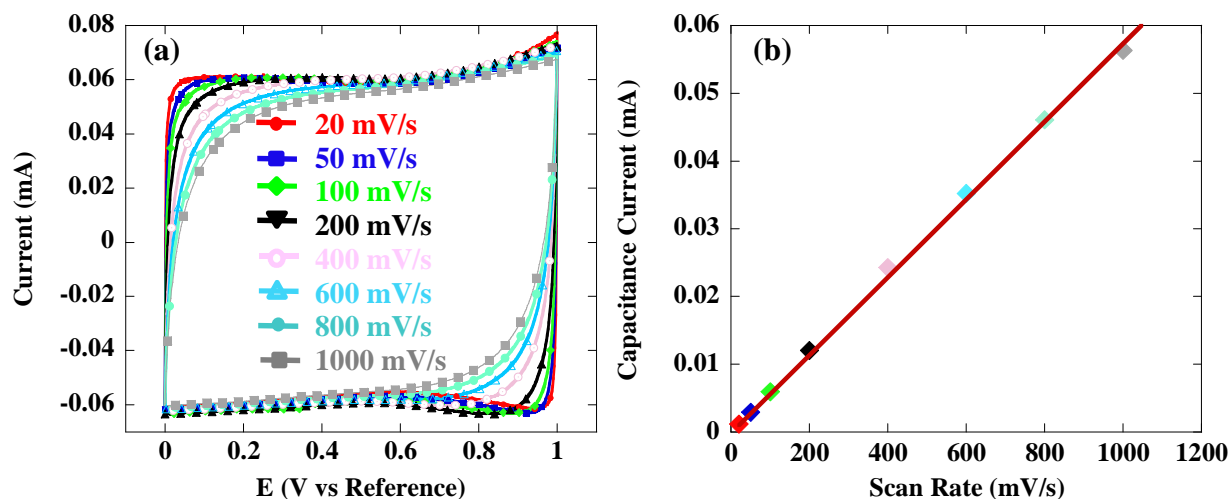
Figure III- 1: CVs collected at different scan rate for CDC 900 °C in 1.5 M NEt$_4$BF$_4$ in AN **(a)** and The linear relationship that shows the capacitive behaviour of the sample at different scan rates **(b)**.

The potential range was fixed between 0 V/Ref and 1 V/Ref. All the CVs exhibit a rectangular box shape, associated with a pure capacitive behaviour [11]. The trend follows that there is an increasing degree of distortion as the scan rate is increased especially at high values (600 mV.s^{-1} to 1 V.s^{-1}) in the positive as well as in the reverse potential scan. However, the symmetry and the capacitive behaviour are still preserved. These symmetrical distortions strongly suggest that the significance of ohmic drop in the bulk electrolyte increases with the scan rate [11]. Figure III- 1b shows the correlation between the capacitive current (i.e. the current value at the plateau observed in the CVs) and the scan rate. The linear relationship confirms that a potential scan rate of 100 mV.s^{-1} provides a good compromise between fast data acquisition and negligible ohmic drop in the electrolyte bulk, displaying the pure capacitive behaviour of the CDCs tested.

V-2. 1.5 M NEt$_4$BF$_4$ in AN electrolyte

Positive polarization: E > OCV

The raw CVs of the various CDC samples collected at 100 mV.s^{-1} in 1.5 M NEt$_4$BF$_4$ in AN at 25 °C, between the rest potential of the CME up to positive values are presented in Figure III- 2a. The rest potential is the zero current potential, also denoted as the Open Circuit Voltage (OCV) is approximated to be similar to the point of zero charge (PZC), OCV ≈ PZC. All the CVs exhibit the rectangular shape characteristic of a pure capacitive behaviour as previously mentioned. Charging of the electrochemical double layer (EDL) occurs during the positive scan from 0 V/Ref up to 1 V/Ref, while EDL capacitive discharging happens during

the reverse scan, from +1 V/Ref down to 0 V/Ref. The capacitive current differs from one sample to another because i) the weight of powder in the CME cannot be kept the same in every experiment and ii) the specific capacitance is different for every sample. This huge difference in the capacitive currents introduced some difficulties in the analysis through the comparison of the CVs based on shape. Despite these parameters which could not be specifically controlled, data averaged over a number of tests describes the behaviour of the materials well [12]. Henceforth, all intensity values (current) have been normalized to the current value measured at 0.45 V/Ref. during the charge, i.e. in the pure capacitive region. Shapes of the CVs were preserved through normalization of the linear region of all CVs to the same arbitrary capacitance, as shown in Figure III- 2b, allowing easier comparisons compared to CVs in Figure III- 2a. According to Table III-1, the pore sizes of the Ti-CDC samples (0.68 to 1 nm) increased with the synthesis temperatures from 500 to 900 °C respectively. Both figures share the same legend.
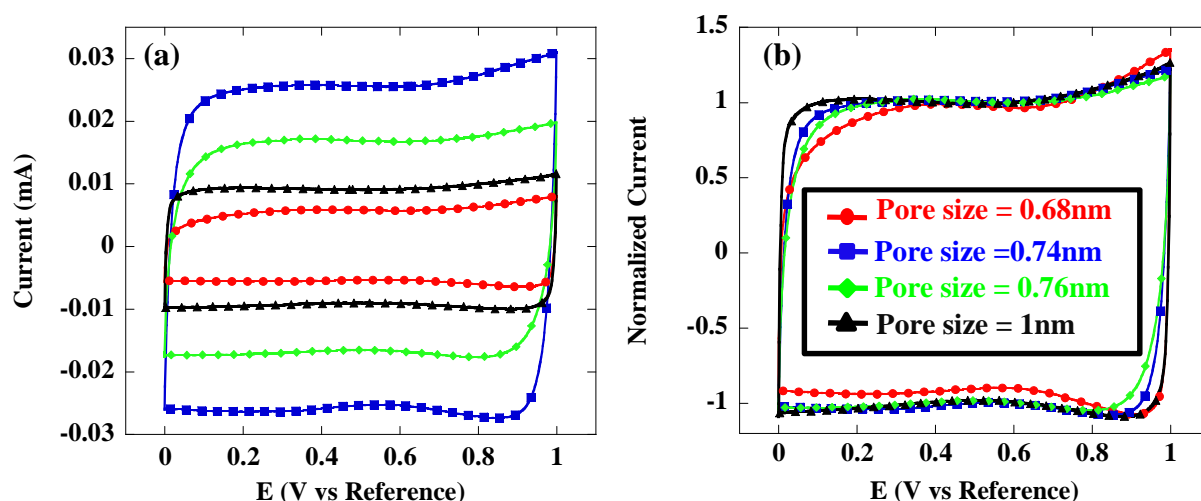
Figure III- 2: Raw CVs of the positive scanning of the samples in 1.5 M NEt$_4$BF$_4$ in AN (non-normalized) at 100 mV.s^{-1} **(a)** and normalized CVs on discharge at 100 mV.s^{-1} **(b)**.

The potential explored is always higher than the OCV such that all electrodes are kept positively charged during the whole scan. Here, charging and discharging of the EDL is mainly achieved with the adsorption/desorption of the anions, BF$_4^-$ [13], of the electrolyte. Despite the prominence of some small differences at the corners of the CVs, there is no significant distortion for pore sizes ranging between 0.68 to 1 nm. Therefore, BF$_4^-$ ion adsorption/desorption onto the carbon surface does not seem to be limited here, that is, the carbon pore sizes are all large enough to accommodate the BF$_4^-$ ions (bare ion size is 0.48 nm [5], solvated ion size, BF$_4^-$/9AN is 1.16 nm) [10].

Negative polarization: E < OCV

Figure III- 3a shows the CVs of the CDC samples being scanned from OCV down to the negative potentials (-1.3 V/Ref.) at 100 mV.s^{-1}. All samples are negatively charged with the whole potential scan. Charging of the EDL occurs from 0 down to -1.3 V/Ref and discharging is carried out from -1.3 V/Ref up to 0 V/Ref and the ions participating in this scan window are mainly the Et_4N^+ cations [13]. Normalized version of Figure III- 3a is presented in Figure III- 3b by normalizing current values to the constant value on discharge at the maximum current acquired.
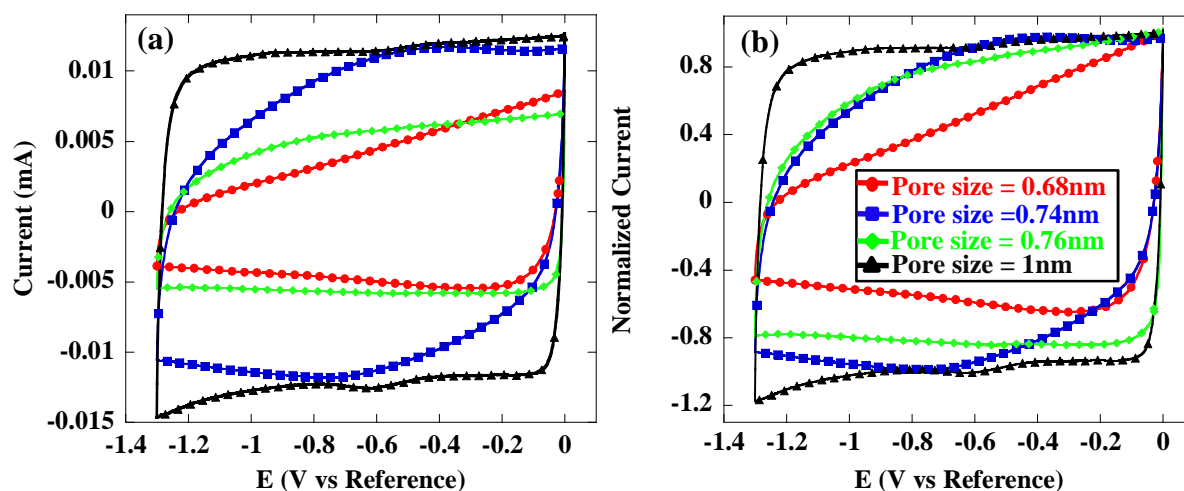
Figure III- 3: Raw CVs of the negative scanning of the samples in 1.5 M NEt_4BF_4 in AN (non-normalized) at 100 mV.s^{-1} (a) and normalized CVs on discharge to a maximum of 1 V/Ref at 100 mV.s^{-1} (b)

The electrochemical behaviours of the samples have stark differences in Figure III- 3 as compared to Figure III- 2. Only the Ti-CDC$_{900°C}$ sample (1 nm) exhibits a pure capacitive behaviour with a rectangular CV profile. Distortion becomes more prominent as the synthesis temperature (thus pore size) is decreased. This shift from the capacitive behaviour is clearly visible during discharge scan (between -1.3 V/Ref. up to -0.6 V/Ref.) where the current response for a given potential is largely decreased (0.74 and 0.68 nm samples). The general profile of the 500 °C (0.68 nm) sample is largely distorted with the least rectangular discharge profile relative to that of the other samples. On charging, the current decreases constantly during the negative scan while the increase in current is much more pronounced on the reverse scan, leading to an asymmetrical CV. This behaviour is far from the one expected for the capacitive charge/discharge of the EDL such that in this specific case, the capacitance changes with the applied potential.

Entire potential range: Positive and negative polarization
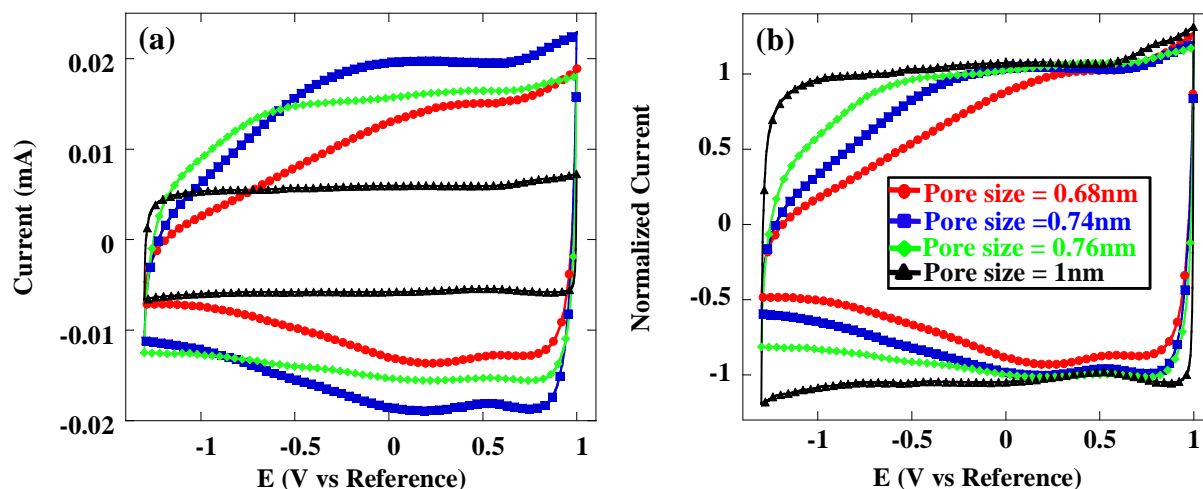
Figure III- 4: Raw CVs of the whole range scanning of the samples in 1.5 M NEt$_4$BF$_4$ in AN (unnormalized) at 100 mV.s^{-1} **(a)** and normalized CVs at 100 mV.s^{-1} **(b)**.

Figure III- 4a above shows the CVs of all the four Ti-CDC samples within the whole potential range between -1.3 V/Ref. and +1 V/Ref in 1.5 M NEt$_4$BF$_4$ in AN electrolyte. All the plots have been normalized at the maximum current at 1 V/Ref and presented in Figure III- 4b. In these experiments, each sample was being characterized in the whole potential range, i.e. potential scan crosses the OCV. Below the OCV (which was measured close to 0 V/Ref for all samples), the capacitive behaviour originates from the cationic adsorption of Et$_4$N$^+$ ions and above the OCV, from the anions BF$_4^-$ ions. Two potential ranges can hence be attributed in Figure III- 4, to namely above and below the OCV. In the potential range higher than OCV, the CVs are rectangular in shape (capacitive behaviour), but on the other hand, when the potential scan is reversed at 1 V/Ref towards descending positive potential value, only slight changes in the CVs can be observed above the OCV. This potential range corresponds to the discharge of the positive electrode, where anions are removed from the porous carbon. This homogeneous behaviour is in good agreement with Figure III- 2. However, when the potential scan goes below the OCV (0 V/Ref.), the rectangular shape of the CV is lost for all the samples except for the 900 °C that has the largest pore size (1 nm). Evidently, the lower the pore sizes, the more distorted are the CVs, as observed previously in Figure III- 3. This shift is also present when the potential scan rate is reversed from -1.3 V/Ref to positive values. Such asymmetrical CV distortions were also reported by Salitra *et al*. [14] using an activated carbon cloth as the active material in a three-electrode cell. These plots collected in the whole potential range provide clearer comparison of cationic adsorption

(below OCV) in the different Ti-CDC samples by using the more capacitive (less distorted) behaviours of the anionic adsorption (above OCV) profiles for aligning the CVs in entirety.

Cyclic voltammetry has also been performed at low scan rates to check if these particular electrochemical behaviours observed for the small pore size samples were dependent on the scan rate and if there exists any kinetic effects. Figure III- 5 shows the CV plots that were recorded at 10 mV.s^{-1}, a slow scan rate that is usually applied for electrode characterization in 4 cm² electrode cells.
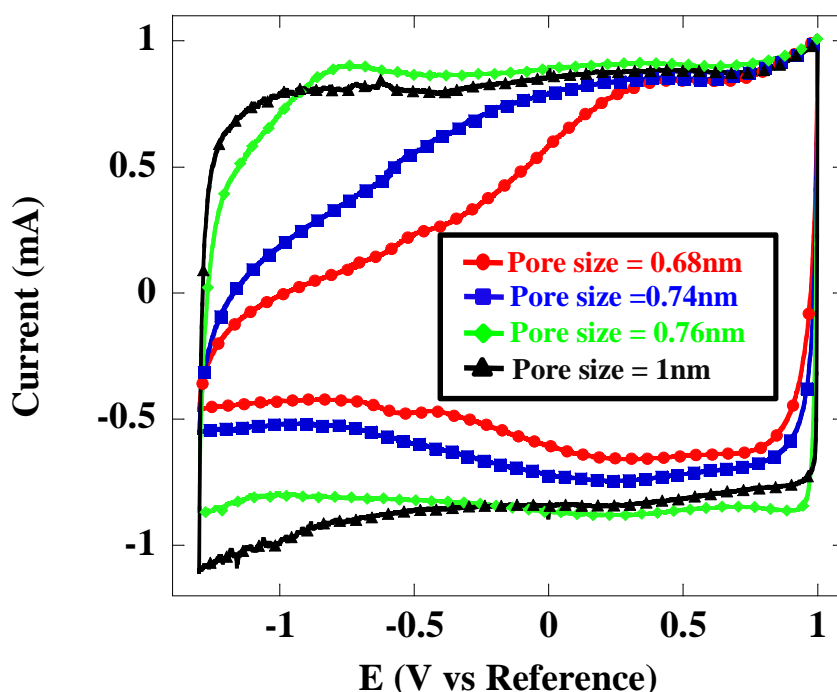
Figure III- 5: Normalized CVs of the entire range scanning of the samples in 1.5 M NEt$_4$BF$_4$ in AN at 10 mV.s^{-1}.

At 10 mV.s^{-1}, the shapes of the plots (Figure III- 5) are preserved and consistent with that for testings performed at 100 mV.s^{-1} (Figure III- 4) previously. The extent of distortion increases with decreasing pore size. All the CVs appear to be distorted asymmetrically, except for the larger pore size sample (900 °C). Among the other samples, less distortion was observed for the 700 °C Ti-CDC (0.76 nm) sample, with the shape of the CV becoming closer to the rectangular one. This suggests that kinetics does play a role in the process, leading to CV distortion for samples with pore size close to that of the adsorbed one. A poor capacitive behaviour of the small pore size samples (500 and 600 °C) is observed while the large pore size sample (900 °C) shows a pure capacitive behaviour.

BF₄⁻ adsorption - Maximization of the capacitance is achieved by minimizing the unoccupied volume in the porous structure of the carbon. In our experiments, pores of 1 nm are for instance too large since the anion adsorption occurs without any severe limitation even for pore size of 0.68 nm, although on discharging, there is a very slight deviation from the rectangular ideal capacitive profile. Therefore, it can be inferred from these information that the pore size that is matching to that of the real size of the ion in the electrolyte (different from the bare ion size), which is termed as the "effective ion size" here, can be estimated to be ~0.68 nm. This is in good agreement with previous work that showed that the maximum specific capacitance for the 500 °C sample (pore size equals to 0.68 nm) using 4 cm² 3-electrode cells in Figure I-20 [5]. Hypothesis of ion desolvation upon adsorption in sub-nanometer pores is supported by the findings here. Due to the fact that the pore size is smaller than the solvated ion size, (Table III- 2) fully solvated ions would not be able to enter the Ti-CDC pores. In spite of this, it also shows that there is little resistance to ion adsorptions in the pores in the pore range of 0.7 to 1.0 nm, fostering a potential for high power EDLC development adapted for fast delivery/uptake of charges [1,15].

Et₄N⁺ adsorption - Although graphitization of the samples decreases [16] with their pore sizes, distortions observed in the CVs presented in Figure III- 3 for small pore size samples could not be solely caused by an increase of the cell series resistance due to reduced graphitization. Three main contributions to the cell series resistances include the bulk electrical resistance of the Ti-CDCs, the bulk electrolyte resistance and the electrolyte resistance in the pores of the carbon.

The distortions observed in Figure III- 3 and Figure III- 4 for small pore size samples can be explained by an increase of the time constant of the electrode [17]. Fundamentally, the time needed to reach the constant capacitive current value is defined by:

$$\tau = ESR \times C \qquad \text{(Eq III- 1)}$$

where τ is the time constant (s), C is the capacitance (F) and ESR is the equivalent series resistance (Ω). The time can be deduced from the potential axis via the scan rate. Here, with normalized current and the same scan rate, the trend of increasing time constant when the sample pore size decrease as observed in Figure III- 3 and Figure III- 4 during the cationic adsorption can be explained by an increase of the resistance.

The CDC electrical conductivity is in the order of tens of S.cm^{-1}, that is, a thousand times more than that of the electrolyte [1] (see Table III- 2). Hence resistance owing to CDC bulk is negligible and the increase in the time constant observed in Figure III- 4 is associated with an increase of the electrolyte resistance. However the same trend in Figure III- 5 is also observed for CV plots collected at 10 mV.s^{-1}, where the ohmic drop in the bulk of the electrolyte is about an order less. As a result, the limitation observed at small pore size samples is neither linked with bulk electrolyte resistance, nor due to CME polarization which is generally observed for high scan rates when ohmic drop gets too large [18], but with the ion transportation in the carbon porous network (squeezing the larger Et$_4$N$^+$ ions into the small pores). This has also been affirmed by the asymmetric profile of the plots recorded for small pore size samples.

The ion-sieving effect can be clearly seen from Figure III- 4b. As the screening proceed to decreasing values of pore sizes below 1 nm (900 °C sample), pores start to become too narrow to efficiently accommodate the cations (1.30 and 0.67 nm with Et$_4$N$^+$.7AN and without the solvation shell respectively [5,10]). For pore sizes equal or smaller than 0.76 nm (700 °C sample), the capacitive behaviour of the carbons is very poor, with a huge resistive contribution linked to the cationic transportation limitation in the pores due to a size effect; adsorption of cations is, however, only possible at the cost of the decrease of the energetic efficiency. For pore size of more than 1 nm, these sizes offer good accessibility to the carbon porous network, given the much varied tortuousity. The optimum pore size for Et$_4$N$^+$ ion adsorption on carbon in AN electrolyte is therefore between 0.76 and 1 nm. Ti-CDC with 0.76 nm pores shows little distortion at low rate (Figure III- 5) [1]. Henceforth, the effective size of the ion in AN during EDL charging/discharging can be estimated to be between 0.76 and 1 nm.

Considering that the size of the solvated Et$_4$N$^+$ and BF$_4^-$ ions in AN (1.3 and 1.16 nm respectively), these results confirm that ions must be at least be partially de-solvated to enter these small pores. Previous results obtained by us showed that the optimum pore size to maximize the carbon capacitance were about 0.7 and 0.8 nm for the BF$_4^-$ and Et$_4$N$^+$ in AN respectively [5]. Data presented in Figure III- 3 and Figure III- 4 are in unison with these recent findings that were obtained in a series of experiments carried out at a scan rate of 20 mV.s^{-1} using 4 cm^2 cells assembled with 60 mg of CDC [5].

However, it is observed that a resistance to cation transport exists in pores smaller than ~0.8 nm. Taking into account that this size is fairly close to that of the desolvated ion (Table III- 2), there exist error possibilities in the average pore size measurement which may lead to overestimation of the pore size such that the real pore size is somewhat smaller, too close to the ion dimensions. It is also expected that bottlenecks exists between pores. Thus, even if the average pore size of 0.7 nm would be sufficient to accommodate an $Et_4 N^+$cation, a material with a larger pore size is needed to ensure that bottlenecks connecting the pores do not restrict the passage of the ions. Moreover, the distance between the ion and the pore wall that would provide the minimum energy is not known. This can also lead to the pore size being larger than the ion size. However, if the assumption of complete desolvation of ions upon double-layer charging is correct, the electrode behaviour should be solvent independent, because no solvent enters the pores. To prove this hypothesis, the Ti-CDC samples have been characterized using the same technique but in a different electrolyte of 1 M NEt_4BF_4 in PC.

V-3. 1 M NEt_4BF_4 in PC electrolyte

The purpose of the change in solvent type in this section is first to validate the hypothesis of removal of solvation shells during EDL charging and second, to study the influence of the solvent on the effective solvated ion size. Figure III- 6a shows the CVs of the various carbon samples between -1.5 V/Ref up to 1 V/Ref at 100 $mV.s^{-1}$. OCV were measured between +0.3 and +0.5 V/Ref, depending on the sample studied. This figure is then similar to Figure III- 4a, with the potential scan crossing the OCV. All the plots have been normalized in Figure III- 6b at the maximum current at 1 V/ref.
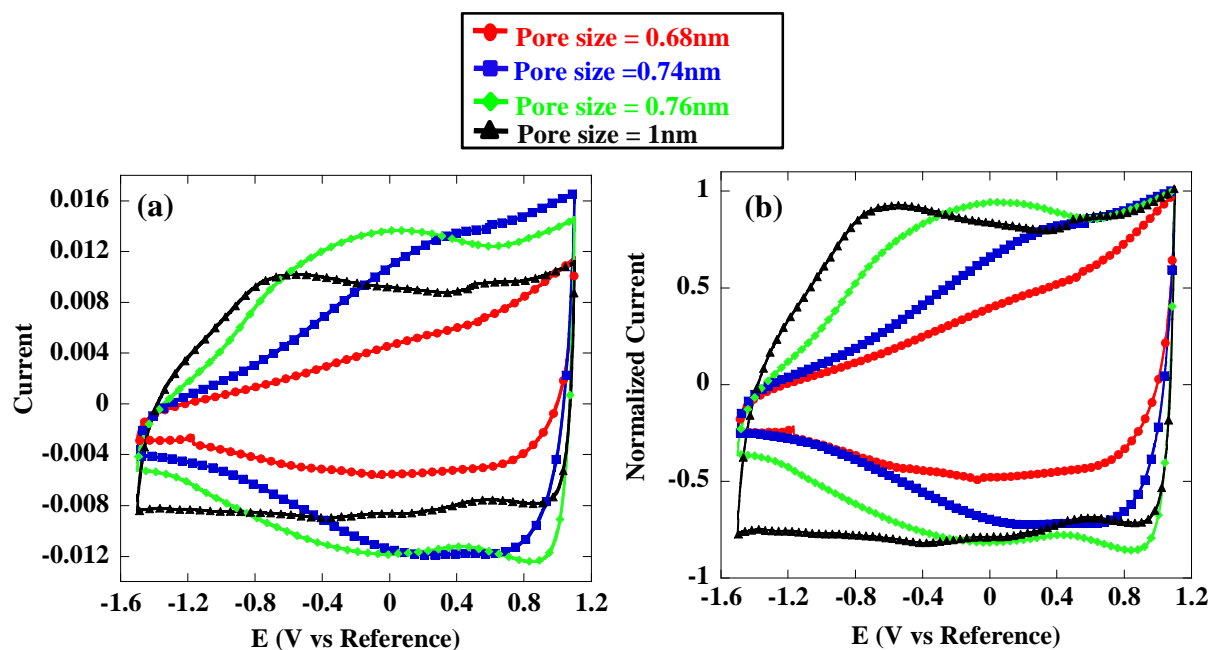
Figure III- 6: Raw CVs of the entire range scanning of the samples in 1.0 M NEt_4BF_4 in PC (unnormalized) at 100 mV.s^{-1} (a) and normalized CVs at 100 mV.s^{-1} **(b)**.

Within the potential range of anion adsorption, that is from +0.3 V/Ref to +1 V/Ref (above the OCV), larger pore size samples (1 and 0.76 nm, for Ti-CDC samples 900 and 700 °C respectively) exhibit a capacitive behaviour. The small pore size carbons (0.74 and 0.68 nm, for Ti-CDC samples 600 and 500 °C respectively) show a different electrochemical response, with an asymmetric distortion of the rectangular-shape CV, indicating a disparity from a pure capacitive behavior. CVs with analogous distortions were also noticed in the same electrolyte using activated carbon cloth as electrodes [14], affirming that such electrochemical prints were not originating from the CME. If these results are to be compared with Figure III- 4, the optimum pore size for the anion here is shifted to somewhat larger values, i.e. from ≤ 0.68 nm in AN- up to about ~0.75 nm in PC-based electrolyte. This means that the effective size of the BF_4^- anion in a PC-based solution is larger than in AN-based electrolytes, suggesting that desolvation of ions in pores may be partial. Otherwise, we would not have seen any effect from the change in the electrolyte. This deduction is in accordance with previous results [19] and suggests the existence of a stronger ion-solvent interaction in the case of PC.

Ranging from the potential of 0 V/Ref to -1.5 V/Ref, the electrochemical signature varies from one sample to another. Current responses in this potential range is mainly due to cationic adsorption (negative scan) and desorption (positive scan). All the plots are distorted

and none of them presents a typical capacitive behavior such as presented in Figure III- 2. The lower the pore size, the lower the current for a given potential. Interestingly, even the large pore size sample CV (900 °C; 1 nm) fails to show a pure electrochemical capacitive signature. From Figure III- 4b, it was proposed that the optimum pore size for the adsorption of the Et_4N^+ cation in AN-based electrolyte was between 0.76 nm and 1 nm. When PC is used instead of AN, the optimum pore size is increased to a value > 1 nm. These results are in good agreement with the calculated solvated size of $BF_4^-.8PC$ and $Et_4^+N.4PC$ [10] that are 1.40 nm and 1.35 nm, respectively (Table III- 2).

For consistency, CV experiments were recorded at low scan rate 10 mV.s^{-1} in the PC-based electrolyte to check if the electrochemical behaviour was kept constant and presented in Figure III- 7. As previously observed in the case of AN-based electrolyte, the asymmetric shape of the plots for PC-based electrolytes at both 100 and 10 mV.s^{-1} were preserved, thus demonstrating that the poor capacitive behaviour of the small pore size samples was not due to bulk resistance [18] and also, the ion-sieving effect is again observable.
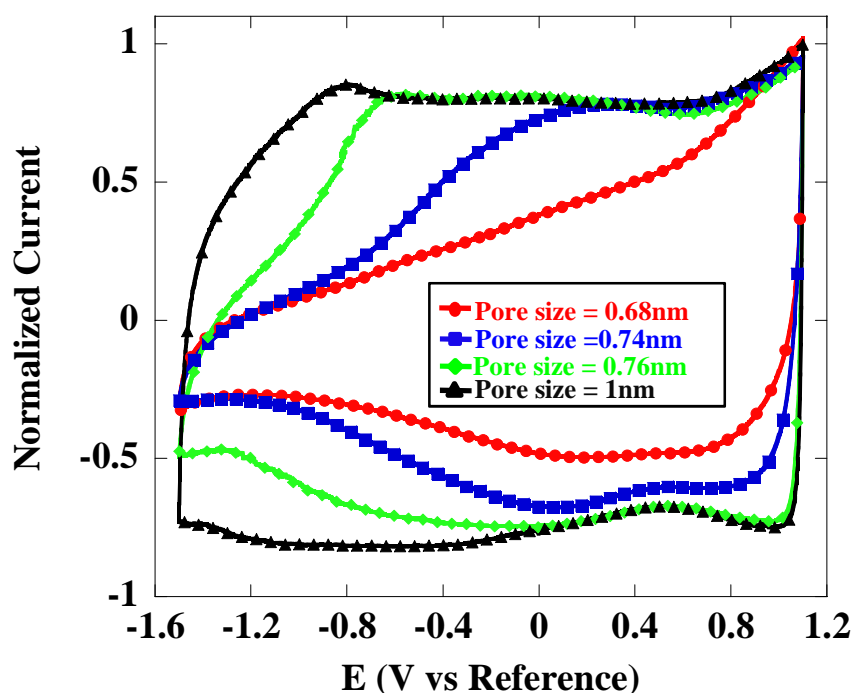
Figure III- 7: Normalized CVs of the entire range scanning of the samples in 1.5 M NEt$_4$BF$_4$ in PC at 10 mV.s^{-1}.

Estimation of effective ion sizes could be possible by studying the CVs from Figure III- 6 and Figure III- 7. Distortion of CV profiles in the positive potential range starts to be

apparent for samples of pore sizes, 0.65 and 0.74 nm while asymmetric distortions were prominent to the largest pore size of 1 nm in the negative potential range.

With regards to the perceived solvent effect, the accuracy of pore size measurement [20] is not to be accounted for the observed discrepancies between the desolvated ion size and the minimal pore size producing rectangular CVs. Accordingly, we can assume that ions were partially desolvated and thus squeezed to enter into small pores. Such steric hindrance could lead to an increase in resistance. Partial desolvation (a decreased number of solvent molecules in the solvation shell of an ion) has been suggested to occur in aqueous electrolytes in narrow-slit pores or nanotubes by regulating the dimension of the nano-window for assessing interior surface area [10], and for Li^+ in organic electrolytes in porous carbons [14]. If the energy of removing the last few solvent molecules is higher than that required to remove the first molecules, partial desolvation is probable. The observed dependence of adsorbed ion size on the solvent supported this hypothesis. Different solvation energies are thus expected for NEt_4BF_4 in PC and AN.

All these viable factors highlight the difficulty to predict the optimal pore size of the carbon electrode based on just the size of a bare or solvated ion and the need to transcend conventional thinking for proper carbon–electrolyte pairing. Distortion of the CVs with decreasing pore sizes of the Ti-CDC samples demonstrated the ion sieving effects reported in aqueous electrolytes [21, 22], and cogently enabled the establishment of a scale of ionic effective sizes in aqueous media. Correspondingly the use of a cavity microelectrode, estimation of the average effective size of the adsorbed ions could be carried out through visual deduction from the distinctive ion sieving effects due to the steric hindrance of the electrolyte ions when adsorbing into the nanopores of defined dimensions. Results confirm that these electrolyte ions enter the pores at a partially desolvated state. Reverse Monte-Carlo simulations from Tanaka et al. [23] based on the alteration of solvent bulk structure when confined in micropores tend to confirm our experimental findings. The solvent molecules are subjected to space availability between the adsorbing ion and the carbon pore wall across the pore diameter.

VI. Conclusions

Cavity Micro-Electrode (CME) was used to study the electrochemical behaviour of porous CDC presenting a tailored and uni-modal pore size distribution ranging from 0.68 nm up to 1 nm. The first-hand information of the effective real ion sizes of the Et_4N^+ and BF_4^-

were found to be different depending on the solvent (AN or PC). The effective ion size during transportation and charge/discharge of the double layer, estimated from the CVs recorded at 100 mV.s^{-1}, was found to decrease according to the following: Et_4N^+ in PC > Et_4N^+ in AN > BF_4^- in PC > BF_4^- in AN. Upon comparison between the deduced effective ion sizes and the fully solvated ion size, it appears that ions have to be partially de-solvated to enter small sub-nanopores. These results concede well with recent findings obtained in a series of experiments using 4 cm^2 CDC electrodes in AN-based electrolytes [1,5]. While using the CME technique, we were able to reproduce these previous results that were obtained within few weeks of continuous work in a few days. Microelectrode studies provide a convenient mean for quick measurement of the correlations between the pore size and electrode performance for a variety of carbons, electrolytes, and solvents. More importantly, we obtained *in situ* direct information about the effective size of the same ions in electrolytes of different solvents during the adsorption/desorption process in the carbon double layer. Despite using the same ions, carbon electrodes with different pore sizes will be required depending on whether the maximum energy storage (capacitance) or charge/discharge rate or low energy losses in cycling are required. Ultimately, different pore sizes are needed for the negative and positive electrodes. Due to the fact that the ideal pore size may neither be that of the bare nor that of the solvated ion, it is currently impossible to predict it a priori. Such technique, combining high-rate CVs and tailored uni-modal porous carbons is thus well adapted to the study of the capacitive behaviour of EDLC electrodes but more generally for any situation where ion size / pore size interactions play a crucial role, for example, in water desalinization and/or biological systems where ions have to exchange between porous membranes. In the next chapter, the study of solvent effects will be presented using ionic liquids.

VII. References

[1]   Chmiola, J.; Yushin, G.; Gogotsi, Y.; Portet, C.; Simon, P.; Taberna, P.-L. *Science* **313** (2006) 1760-1763.

[2]   Zuleta, M.; Bjornbom, P.; Lundblad, A.; Nurk, G.; Kasuk, H.; Lust, E. *Journal of Electroanalytical Chemistry* **586** (2006) 247.

[3]   Yushin, G.; Nikitin, A.; Gogotsi, Y. <u>Nanomaterials Handbook, Gogotsi, Y. Ed</u>. *CRC Press: Boca Raton* (2006) 237-280.

[4]   Ania, C. O.; Pernak, J.; Stefaniak, F.; Raymundo-Piñero, E.; Béguin, F. *Carbon* **44** *(*2006) 3126-3130.

[5]   Chmiola, J.; Largeot, C.; Taberna, P-L.; Simon, P.; Gogotsi, Y. *Angewandte Chemie International Edition* **47** (2008) 3392.

[6]   Largeot, C.; Portet, C.; Chmiola, J.; Taberna, P.-L.; Gogotsi, Y.; Simon, P. *Journal of the American Chemical Society* **130** (2008) 2730-2731.

[7]   Yanul', N. A.; Kukushkina, Y. A.; Sokolov, V. V.; Gordeev, S. K.; Kravchik, A. E.; Kirsh, E. *Russ. Journal of Applied Chemistry* **72** (1999) 2159-2163.

[8]   Chmiola, J.; Yushin, G.; Dash, R. K.; Hoffman, E. N.; Fischer, J. E.; Barsoum, M.; Gogotsi, Y. *Electrochemical and Solid-State Letters* **8** (2005) A357-A360.

[9]   Gogotsi, Y.; Nikitin, A.; Ye, H.; Zhou, W.; Fischer, J. E.; Yi, B.; Foley, H. C.; Barsoum, M. W. *Nature Materials* **2** (2003) 591-594.

[10]   Yang, C. M. ; Kim, Y. J.; Endo, M.; Kanoh, H.; Yudasaka, M.; Iijima, S.; Kaneko, K. *Journal of the American Chemical Society* **129** (2007) 20.

[11]   Conway, B. E.; Pell, W. G.; *J. Power Sources* **105** (2002) 169.

[12]   Portet, C.; Chmiola, J.; Gogotsi, Y.; Park, S.; Lyan, K. *Electrochimica Acta* **53** (2008) 7675.

[13]   Shiraishi, S.; Kurihara, H.; Shi, L.; Nakayama, T.; Oya, A. *Journal of the Electrochemical Society* **149** (2002) A855.

[14]   Salitra, G.; Soffer, A.; Eliad, L.; Cohen, Y.; Aurbach, D. *Journal of the Electrochemical Society* **147** (2000) 2486.

[15]   Segalini, J.; Daffos, B.; Taberna, P-L.; Gogotsi, Y. ; Simon, P. *Electrochimica Acta* **55** (2010) 7489.

[16]   Conway, B. E.; Pell, W. G. *Journal of Power Sources* **96** (2001) 57.

[17]   Conway, B. E.; Pell. W. G. <u>Proceedings of the "11th International Seminar on Double Layer Capacitors", Florida Educational Seminars Inc, December 3-5 2001</u>*, Deerfield Beach (USA).* (2001) 1.

[18]   Cachet-Vivier, C.; Vivier, V.; Cha, C. S.; Nedelec, J. Y.; Yu, L. T. *Electrochimica Acta* **47** (2001) 181-189.

[19]   Janes, A.; Permann, L.; Nigu, P.; Lust, E. *Surface Science* **560** (2004) 145.

[20]   Laudisio, G.; Dash, R. K.; Singer, J. P.; Yushin, G.; Gogotsi, Y.; Fischer, J. E. *Langmuir* **22** (2006)8945.

[21]   Eliad, L.; Salitra, G.; Soffer, A.; Aurbach, D. *Journal of Phyical Chemistry B* **105** (2001) 6880-6887.

[22]   Levi, M.D.; Sigalov, S.; Gregory, S.; Aurbach, D.; Maier, J. *ChemPhysChem* **12** (2011) 854 – 862.

[23]   Tanaka, A. ; Iiyama, T. ; Ohba, T. ; Ozeki, S.; Urita, K.; Fujimori, T.; Kanoh, H.; Kaneko, K. *Journal of the American Chemical Society Communications* **132** (2010) 2112-2113.

Chapter IV:

Study of solvent influence on capacitance using Room-Temperature Ionic Liquids (RTILs)

I. Introduction

In the precedent aspect of optimizing pore size for the chosen electrolytes, the tacky part lies in the variety of "adsorbate" sizes due to different degree of solvation. This is especially true when the electrolyte ions are subjected to potential differences be it being applied externally or from the surrounding ions or solvent molecules, that can somehow affect the extent to which there is a matching pore size for the respective ions within an electrolyte. For example, two adjacent cations might have different degrees of solvation owing to the potential gradient established due to movement of the ions or some pores might be filled with only solvent molecules. Hence, it was believed that the use of solvent-free ionic liquids could eliminate the tangible consideration of solvation issues to study the size effect on capacitive behaviour.

Earlier findings by our team [1] support the notion of increased capacitance upon close approximations of the sizes of the pores of the electrodes and the solvent-free ions of the electrolyte in a two-electrode cell configuration as presented in Figure I-26 in Chapter I (recalled as Figure IV- 1).
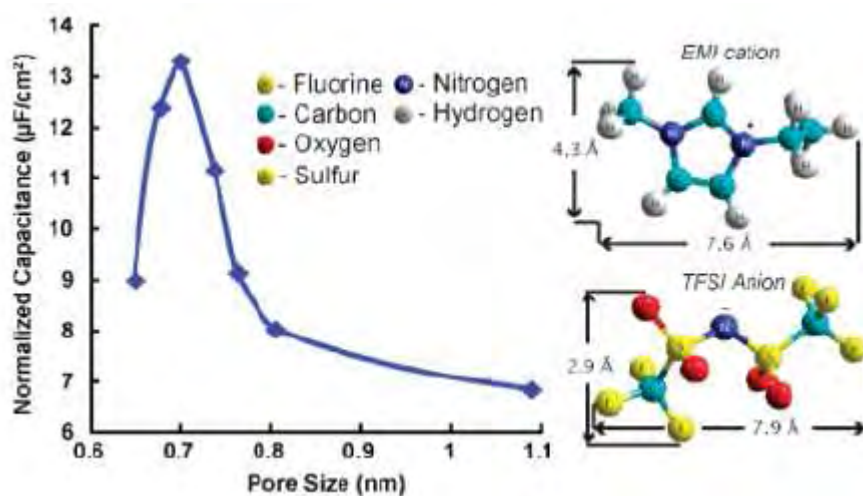
Figure IV- 2: Normalized capacitance change versus the pore size of the CDC samples prepared at different temperatures; normalized capacitance is obtained by dividing the specific capacitance by the SSA. HyperChem models of the structure of EMI and TFSI ions show a size correlation. [1]

In this literature, the cell capacitance was shown to scale to a peak at a pore size of ~0.7 nm, which corresponds to the size of the electrolyte ions, using Titanium-Carbide Derived Carbons (Ti-CDCs) with narrow pore size distributions that serve as models for well-defined pore sizes in the electrodes. From these previous results [2,3], it is impossible to

conduct a solvent-less environment for NEt_4BF_4 as they exist in solid form. Hence, a fair basis of completely solvent-less ionic liquid (neat EMI-TFSI) can eliminate the effect of solvation.

Therefore, in this chapter, a step by step approach was followed in view to first deal with a solventless system using a 3-electrode cell in neat ionic liquid electrolyte, EMI-TFSI. Second, an organic solvent, acetonitrile, was introduced to the neat ionic liquid system, EMI-TFSI/AN, in order to observe effects, if any, on the capacitance as well as on the capacitive behaviour upon adsorption/desorption processes, in the presence of solvent molecules. With a three-electrode cell configuration, we explore the possibility of in-depth investigation by distinguishing the capacitances contribution from cations and anions pertinent to their different steric effects in a solvated environment. Lastly, the CME technique was used to further affirm the findings.

To systematically carry out this study, electrochemical tests were performed using the same batches of Ti-CDCs used in the two-electrode cell configuration.

II-Electrochemical behaviour of ionic liquid based electrolyte in 3-electrode cells

II-1. Choice of ionic liquids as electrolytes

In order to verify the hypothesis of whether capacitance is optimized when the pore size is in proximity to the ion size, neat EMI-TFSI was being employed. However the conductivity of neat EMI-TFSI (~8.5 mS.cm^{-1}), with in intrinsic concentration of 3.9 M, is relatively poor compared to other acetonitrile (AN) or propylene-carbonate (PC) based organic electrolytes, the experiments were thus conducted at an elevated temperature of 60 °C.

II-2. Synthesis of EMI-TFSI

1-Ethyl-3-Methylimidazolium bis(trifluorosulfonyl)imide (EMI-TFSI)

As mentioned in Chapter II, the cation, 1-Ethyl-3-methylimidazolium, (EMI$^+$) is first produced by preparing its halide salt through quaternization. The chemical reaction for quarternization of 1-methylimidazole by 1-bromoethane to yield its halide salt, EMI-Br as shown in (Rxn IV- 1):

1-Methylimidazole   1-Bromoethane   EMI-Br
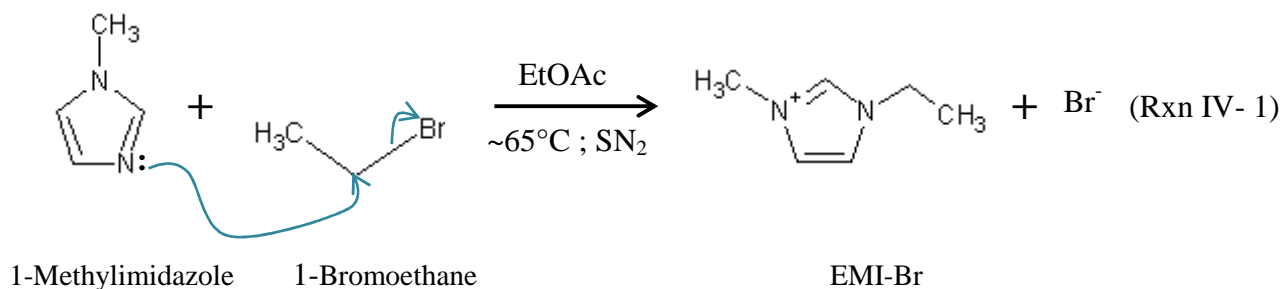
Physical properties of the reactants for the synthesis of EMI-TFSI are tabulated in Table IV- 1. The boiling temperatures of the reactants are important in starting the reaction to avoid non-stoichiometry in the reaction and as well as their decomposition.

Table IV- 1: Physical properties of reactants for making EMI-TFSI.

Reactants	T_B (°C)	T_M (°C)	T_f (°C)	M_w (g.mol^{-1})	CAS No.
1-Methylimidazole	198	-60	92	82.1	616-47-7
1-Bromoethane	38.4	-119	-20°C	108.97	74-96-4
Ethylacetate	77.1	−83.6	-4	88.11	141-78-6
Li-TFSI	-	234-238	-	287.1	90076-65-6

The experimental set-up comprised of a heating plate, a 3-neck round bottom flask fitted with a thermometer, condenser and a dropping funnel with pressure balance to the 3 necks is shown in Figure IV- 3, and the condenser is then connected to a bubble counter. The set-up is purged with nitrogen continuously for one hour while heating before introducing the reactants into the apparatus. This step is important to eliminate any water or contaminants that could lead to side reactions, thereby affecting the quality and the yield of the resulting halide salt.

Figure IV- 3: Experimental set-up of the synthesis of EMI-Br.

1-Methylimidazole is first introduced into the round bottom flask together with ethylacetate and heated to ~65 °C under constant stirring and purging with nitrogen. Besides, haloalkane are often sensitive to heat and light, and hence it is usually added to the heated amine when the temperature is stable at ~65 °C. An excess of 1-bromoethane is then added dropwise to the heated amine from the dropping funnel, while monitoring the temperature and under constant stirring. The rate of addition is then adjusted according to the temperature change. As this reaction is exothermic, temperature regulation is very important to keep the reaction under control, without decomposing the reactants. After all the 1-bromoethane has been completely added, the temperature is maintained at ~65 °C for 2 hours. At the end of this step, agitation is stopped. A big volume of ethylacetate and a few grains of EMI-Br are then added to initiate recrystallization of EMI-Br. The precipitated product (white powder) is then washed for three times with ethylacetate under vigorous agitation to remove the unreacted reactants until the decanted solvent is not tainted with colours of the reactants. Following this, the solid halide is then dried under vacuum to remove the solvent. Deionized water is then added to dissolve EMI-Br at room temperature for metathesis. The metathesis reaction for obtaining the EMI-TFSI is shown in Rxn IV-2:

EMI-Br   Li-TFSI   EMI-TFSI   Li-Br
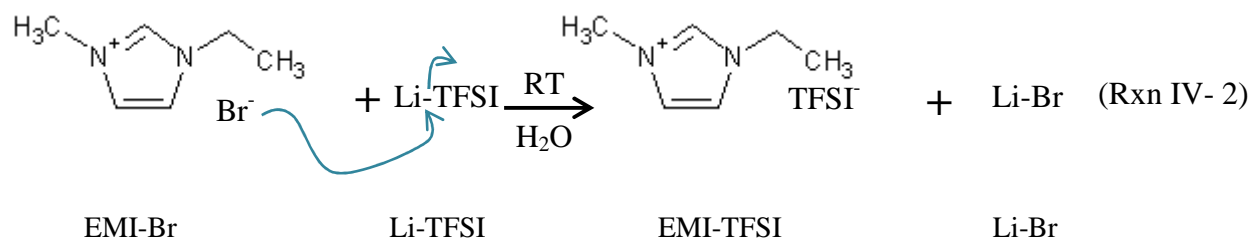
A solution of excess Li-TFSI in deionized water is then poured into the dissolved EMI-Br under vigorous mechanical agitation for anionic exchange. A two-phase liquid can then be observed, with the aqueous phase consisting of K-Br (hydrophilic) and water, while the non-aqueous phase is the desired EMI-TFSI ionic liquid. The aqueous phase is then decanted from the ionic liquid using a separating funnel. EMI-TFSI is then thoroughly washed with deionized water until the decanted aqueous phase show negative result for halide test with $AgNO_3$. The product is then dried under vacuum at 50 °C for the first 2 hours and followed by at ~70 °C overnight. Quality test for water content is then carried out using karl-fischer to know if further drying is required and drying continues until water content of less than 20 ppm is obtained. The product is then sent for ion chromatography test for halide contents. Washings are repeated when halide contents exceeded 50 ppm and the consequent drying procedures mentioned are followed. The IL is now ready for electrochemical applications.

Figure IV- 4: Planar illustration of EMI^+ ion **(a)** and $TFSI^-$ ion **(b)** in the pure IL.

In this EMI-TFSI electrolyte, the sizes of the non-solvated ions are 0.76 and 0.79 nm for EMI^+ and $TFSI^-$ respectively as shown in Figure IV- 4. The EMI^+ ions enter the negatively polarized electrode while the $TFSI^-$ ions enter the positively charged pores during charging of the EDLC. On discharge, these ions are being flushed out of the pores, in a way which is almost the same as them entering the pores. This could be deduced from the symmetrical charge/discharge galvanostatic cycling graphs, indicating that the adsorption and desorption of the ions are purely non-faradaic.

II-3. 4 cm^2 Ti-CDC Electrode EDLCs: Ti-CDCs with neat ionic liquid: *EMI-TFSI*

4 cm^2 electrode EDLCs were assembled in a 3-electrode cell configuration, using silver as the quasi-reference wire. Cells were conditioned at 60 °C prior to electrochemical measurements. This set-up allows us to study the anion and cation adsorption separately, to have better insight on the charge storage mechanism.

II-3.1. Electrochemical Impedance Spectroscopy (EIS)

a) Nyquist plots

EIS tests describe the supercapacitor by using resistance and capacitance that are functions of the pulsation ω and noted as *R(ω)* and *C(ω)* as illustrated earlier in Chapter II as follows in Eq IV- 1 [4]:

$$Z(\omega) = R(\omega) + \left[\frac{1}{jC(\omega) \times \omega} \right]$$

(Eq IV- 2)

Nyquists plots of supercapacitor cells assembled from Ti-CDCs of pore sizes, from 0.65 to 1.1 nm, as active material in a pure ionic liquid electrolyte, 1-Ethyl-3-MethylImidazolium bis{(trifluoromethyl)sulfonyl}imide(EMI-TFSI) are presented in Figure IV- 5. All electrodes prepared for the supercapacitor cells are of the same weight. For the sake of clarity, only Ti-CDCs of 0.68, 0.8 and 1.1 nm (low, medium and large pore size samples) are presented as shown in Figure IV- 5. The YP-17 carbon is given as a standard, since it is used in most of the commercial cells. The YP 17 carbon is a microporous activated carbon with an average pore size of 1.5 nm and has a slightly broader pore size distribution than the Ti-CDCs. Characteristics of the YP 17 carbon has been shown in Chapter II.
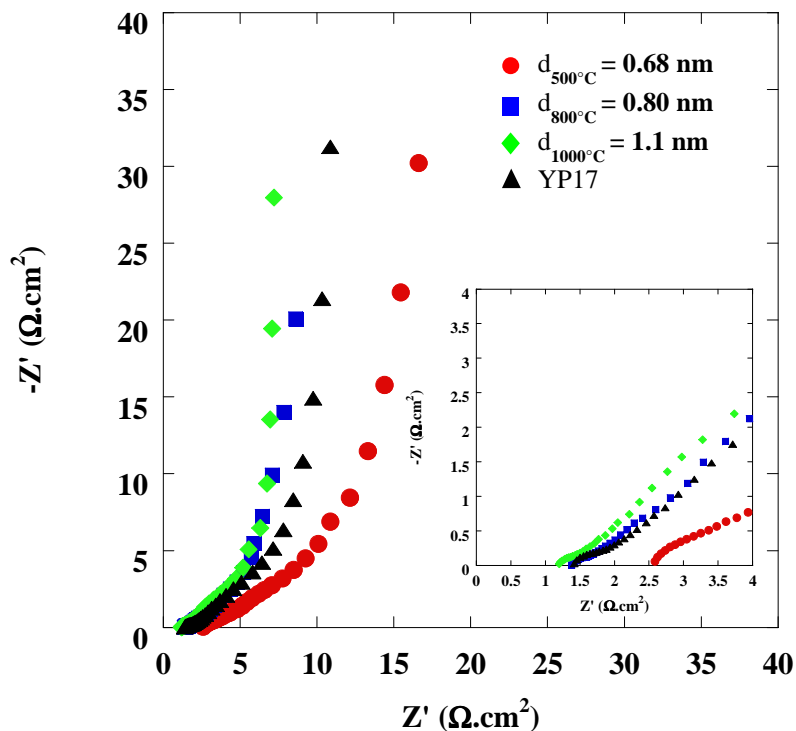
Figure IV- 5: Electrochemical impedance spectrograms scanned from 75 kHz to 10 mHz of Ti-CDCs of pore sizes from 0.68 to 1.1 nm and commercial carbon YP 17 and a zoom-in of high frequency region (inset).

An ideal capacitance has no real part as there is only a reactive contribution to the power. Supercapacitors show behaviours between two extreme states of being a pure resistor and a pure capacitor (Eq II-14), which behave like resistance-capacitance (RC) transmission line circuits [5].

The inset of Figure IV- 5 shows the electrochemical impedance from 75 kHz to 10 mHz for cells using Ti-CDCs and the YP-17 commercial carbon from Kuraray Co., Japan, of the same electrode weight as those of the Ti-CDCs, at open circuit potential of ~ < 0.2 V versus Ag reference.

In the high frequency region of the inset of Figure IV- 5, towards the left side of the x-axis, supercapacitors behave like a resistor with ESR, ranging from 1-3 $\Omega.cm^2$. These values are close to that obtained from commercial active carbon of YP 17 in the same electrolyte as shown in Figure IV- 5. Evolution of the ESR lies in the intrinsic conductivities of the Ti-CDCs, where the higher temperature carbons tend to be more graphitic, yielding a higher conductivity (Ti-CDC$_{1.1nm}$ = 150 S.cm^{-1}) than those synthesized at lower temperatures (Ti-CDC$_{0.68}$ = 25 S.cm^{-1}) [2]. One of the influences on the ESR values is the ionic conductivity of the electrolyte. However, given in the same electrolyte, since Ti-CDC$_{500°C}$ has the lowest conductivity, it logically results in the highest ESR value as obtained in the inset of Figure IV-

5. In Figure IV- 5, towards the right side of the x-axis, at low frequency, the imaginary part of the impedance increases sharply to almost a vertical line characteristic of an ideal capacitor [4]. Ti-CDC$_{1.1nm}$ displayed an almost perfect vertical line at the low frequency region, while the least vertical tails in the same region correspond to smaller pore size and YP17 carbon which has a wider pore size distribution as compared to CDCs. Ti-CDC of the smallest pore size (0.68 nm) led to the highest deviation from the 90 ° theoretical vertical line, characteristic of an ideal capacitive behavior as compared to Ti-CDCs of larger pore sizes (0.8 and 1.1 nm). Qualitatively, such observed deviation could be attributed to the increase in the capacitor resistance in a RC circuit due to the increased difficulty of electrolyte ions accessing to the interior of the small pore sizes as described by de Levie, where the impedance of a pore, Z_{pore}, increases with decreasing of pore size, r. Investigations on the impedance of adsorption/desorption of electrolyte ions during charging/discharging processes respectively have been performed [6], showing amplified deviation upon decreasing of the pore size of Ti-CDCs. With the conventional YP17 carbon, the nyquist plot shows that the pores have similar wettability of pores in the carbon, with fast ion transport in micropores like reported in [2].

Expressing equation IV-1 in its complex form:

$$Z(\omega) = Z'(\omega) + jZ''(\omega) \qquad \text{(Eq IV- 3)}$$

Where Z'(ω) and Z''(ω) are the real and the imaginary parts of the impedance respectively

Combining equations IV-1 and IV-2:

$$C(\omega) = \frac{1}{\omega \times (jZ'(\omega) - Z''(\omega))} = \frac{-(Z''(\omega) + jZ'(\omega))}{\omega |Z(\omega)|^2} \qquad \text{(Eq IV- 4)}$$

Capacitance can thus be quantitatively calculated using this complex model [4]:

$$C'(\omega) = C'(\omega) - jC''(\omega) \qquad \text{(Eq IV- 5)}$$

Hence, the real and imaginary parts of capacitance can be expressed as:

$$C'(\omega) = \frac{-Z''(\omega)}{\omega |Z(\omega)|^2} \qquad \text{(Eq IV- 6)}$$

$$C''(\omega) = \frac{Z'(\omega)}{\omega |Z(\omega)|^2} \qquad \text{(Eq IV- 7)}$$

Where:

- C'(ω) is the capacitance of the supercapacitor, varying with frequency, C(ω).
- C''(ω) is the imaginary capacitance of the supercapacitor, C(ω) [7, 8, 9].

The capacitance of the cell during constant current discharge corresponds to the low frequency value of C'(ω)]. C''(ω) corresponds to the dissipation of energy by irreversible processes that can lead to a hysteresis such as dielectric losses in water occurring during the rotation or the movement of the molecules [4].

b) C' and C'' vs f plots

Plots of C'(ω) and C''(ω) provide a handful of information such as the modulus impedance, capacitance and the time constant of the cell.

C' vs f plots - Figure IV- 6 shows real part of the capacitance (from Eq IV-5) against the log scale of the frequency range.
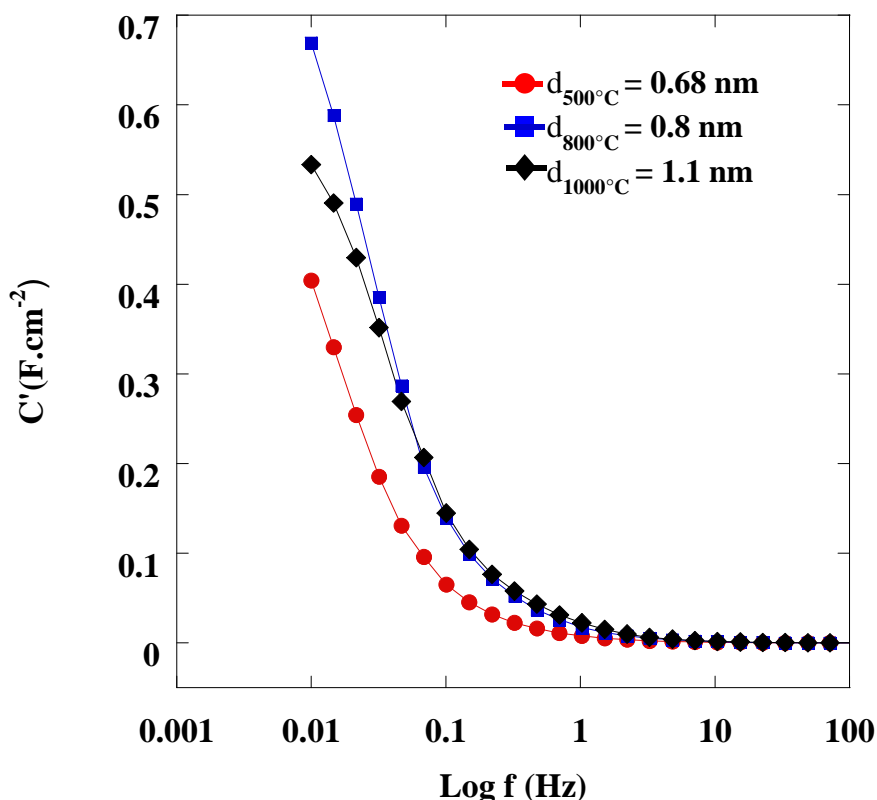
Figure IV- 6: Real capacitance, C' vs log of frequency, f, scanned from 75 Hz to 10 mHz for Ti-CDCs of pore sizes from 0.68 to 1.1 nm expressed at the Y-axis as capacitance. (For clarity means, only 500, 800 and 1000 °C samples are shown)

The low frequency region corresponds to the capacitance of the cell. In this region, the capacitance values differ more significantly from one another compared to regions of higher

frequencies. Below the logarithm of frequency at 0.05 Hz, the capacitance values diverge to slightly higher values for Ti-CDCs of 0.68 and 0.8 nm while to a lower value for the 1.1 nm Ti-CDC sample. Values of real capacitance are closer to the plateau of the graphs for samples with larger pore sizes as seen in the 1.1 nm sample approaching a near maximum at 0.01 hz.

Ti-CDC$_{500°C}$ has a small pore size of 0.68 nm, and could pose accessibility difficulties for electrolyte cations to enter into the pores upon charging (see chapter III). Even if electrolyte ions were able to be adsorbed into the pores, exiting the pores could also be a problem due to possible bottle necks within the pores. This could explain the lower capacitance values for the smaller pore sized sample.

On the other hand, Ti-CDC$_{1.1nm}$ which has larger pore size, exhibited lower capacitance values compared to Ti-CDC$_{0.68nm}$ and Ti-CDC$_{0.8nm}$. Evidently in Table II-2 (recall from Chapter II), these samples have the highest pore volume of 0.81 cc.g^{-1} of active material. Although they have the highest surface area, ($\sim$1600 cm^2.g^{-1}), lower pore density in a given volume of Ti-CDC synthesized at higher temperatures could lead to a lower capacitance. Moreover, it is noteworthy to take into account the structural changes of Ti-CDCs synthesized at 1000 °C to be more graphitic than the smaller pore size samples [10], which could change the electrolyte/carbon interaction and hence be a contributing factor in the low capacitance value.

C'' vs f plots - The time constant, where C'' is maximum, is a direct measure of power capability of the supercapacitor cell as discussed earlier in chapter II that this is the minimum time taken to discharge the energy with an efficiency $\geq$ 50 %. This parameter can be obtained by plotting the C'' derived from Eq IV-6 against frequency and reading off the peak frequency as shown in Figure IV- 7.
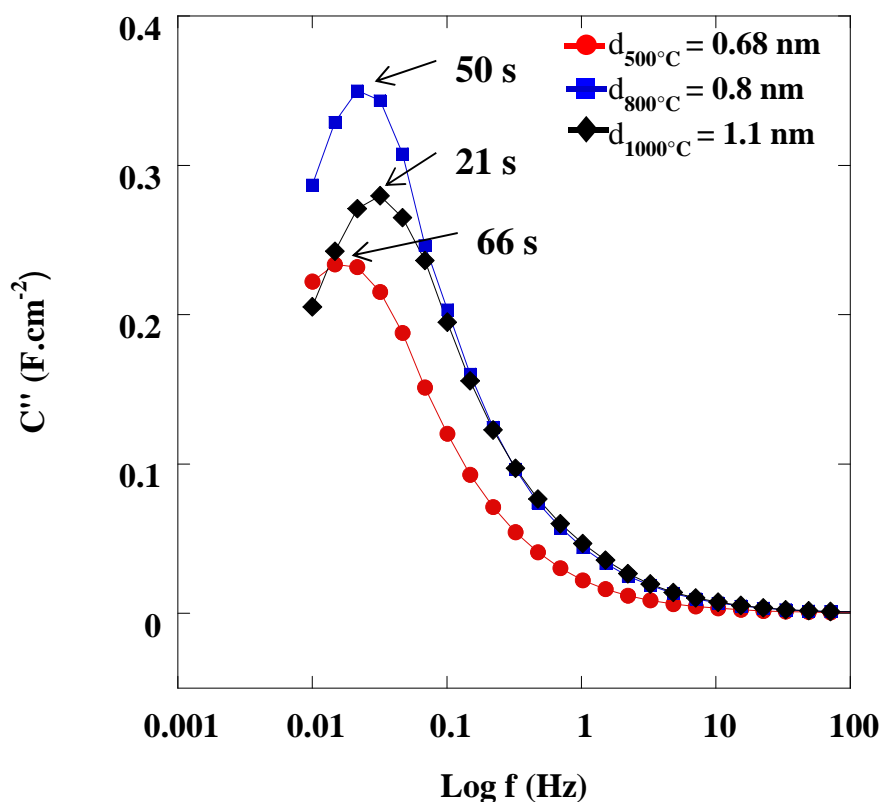
Figure IV- 7: Profile of imaginary capacitance, C" against frequency for same mass loading of 15 g.cm^{-2} cells assembled with Ti-CDCs in EMI-TFSI neat electrolyte.

A faster time constant of 21 seconds was observed for Ti-CDCs of pore sizes 1.1 nm and 66 seconds for the small pore size of 0.68 nm. Such observation can be associated to the ease of electrolyte ions to get out of the pores and diffuse away from the charged surfaces of the electrodes. Logically, the larger the pore size, the easier it is for the electrolyte ions to desorb from the charged pores. Likewise, when the pores are too small to be accessible to the electrolyte ions, ions tend to reside on the charged surfaces, and could increase their ease of diffusing away from the charged surfaces. This could give an idea on the desorption mechanism related to ion size and pore size and their effect on power delivery on discharging.

II-3.2. Cyclic Voltammetry

As discussed before, the cyclic voltammograms (CVs) are efficient in giving the first qualitative analysis of an electrochemical system. The corners of the voltammograms where the scan rate is reversed, give a straightforward qualitative evaluation of the capacitive behaviour and resistivity of the electrolyte, given the prior confirmation of a well assembled cell by EIS and good connection established to carry out the tests.

Connections were arranged to control the cell voltage and to measure the voltage response from the positive electrode. Voltage from the negative electrode was then calculated.
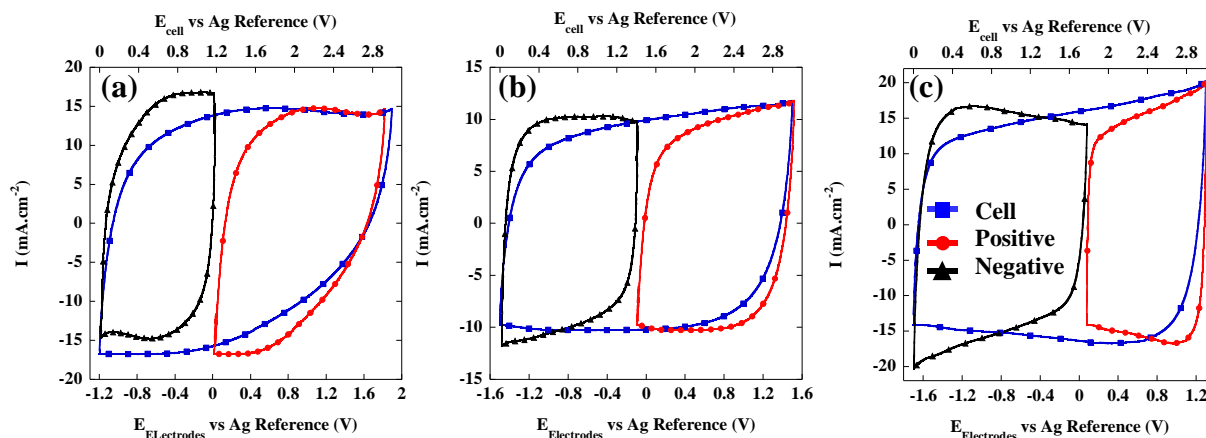
Figure IV- 8: Cyclic voltammograms of TiC-CDC synthesized at 500 °C (0.68 nm) **(a)**, 800 °C (0.8 nm) **(b)** and 1000 °C (1.1 nm) **(c)** respectively in EMI-TFSI measured in a 3-electrode cell configuration at 20 mV.s^{-1} and 60 °C.

Cyclic voltammetry was performed on all the supercapacitor cells at a scan rate of 20 mV.s^{-1}. CVs of cells assembled with small ($d_{500°C}$ = 0.68 nm), medium ($d_{800°C}$ = 0.8 nm) and large ($d_{1000°C}$ = 1.1 nm) pore sized Ti-CDCs are presented in Figure IV- 8.

All Figure IV- 8a, b and c show the CVs that were typically obtained from the characterization and testing of the Ti-CDCs cells assembled using Ti-CDCs of different microporous sizes in EMI-TFSI at 60 °C. They show capacitive behaviour of different extents owing to the interactions between the electrolyte ions and the Ti-CDCs depending on the synthesis temperatures and hence the pore sizes.

As shown in Figure IV- 8, the potential window for the positive and negative electrodes were 0 to 1.8 V and -1.2 to 0 V for Ti-CDC$_{500°C}$, 0 to 1.5 V and -1.5 to 0 V for Ti-CDC$_{800°C}$ and 0 to 1.3 V and -1.7 to 0 for Ti-CDC$_{1000°C}$ versus Ag reference respectively. Given the same potential window applied as the cell voltage, the individual potential ranges of the positive and negative electrodes vary with the synthesis temperature of the Ti-CDCs that evidences a difference in the capacitance value from one sample to another. The distortion on the positive electrode in Figure IV- 8a is the most prominent in the small pore sized sample, 0.68 nm, among all the other samples, displaying the existence of the ion-sieving effect due to the bigger ion size of the adsorbing anions as described in Chapter III.

II-3.3. Galvanostatic Cycling

Galvanostatic cycling of the samples gave reproducible capacitance values and typical linearity of a supercapacitor discharge curve as shown in Figure IV- 9. This technique allows both quantitative and qualitative evaluation of the capacitance as well as the cyclability of the cell to be determined. The cells were cycled from open circuit potential (OCV ~ 0 V vs Ag reference) to 3 V versus Ag reference at a current density of 5 mA.cm^{-2}, controlling the cell voltage while measuring the electrical response from the positive and negative electrodes. Despite the similar discharge behaviour for both Ti-CDC samples, the voltage responses seen in Figure IV- 8 were not the same for the individual electrodes as encountered already with the CVs presented in previous section.
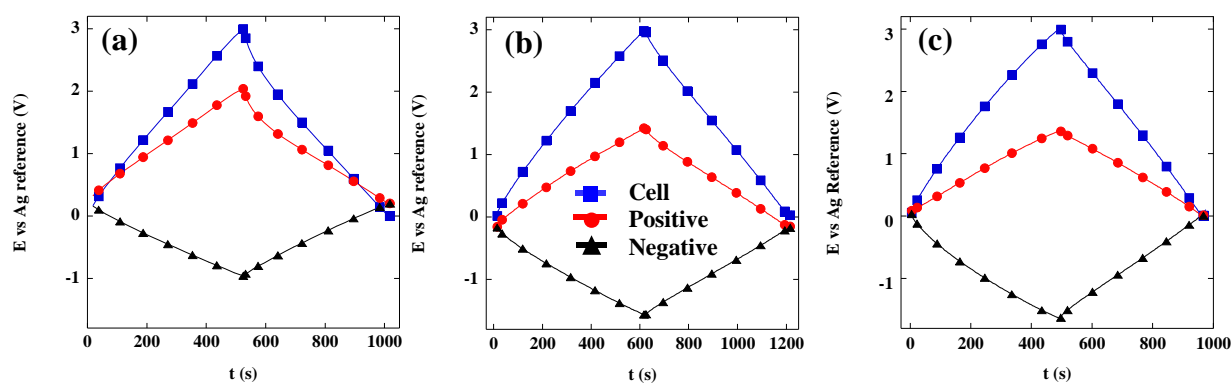
Figure IV- 9: Galvanostatic cycling (Voltage against time) profiles of TiC-CDC synthesized at 500 °C (0.68 nm) **(a)** and 800 °C (0.8 nm) **(b)** and 1000 °C (1.1 nm) **(c)** respectively in EMI-TFSI measured in a 3-electrode cell configuration at 5 mA.cm^{-2} and 60 °C.

Linearity from Figure IV- 9 ensures that the values collected were purely on adsorption of electrolyte ions on to the carbon surface, that is, absence of faradaic reactions. The capacitance values presented in this report have been calculated from the discharge plot of galvanostatic cycles using Eq II-7. Values from cyclic voltammograms of the samples tested were coherent with those of the galvanostatic ones. Differences between capacitance values measured from voltammograms and galvanostatic cycles are not more than 5 F.g^{-1} which accounts to less than ±5 % in error. ESR value can be obtained from the ohmic drop at the peak of the charge/discharge curve at 1 kHz. Similar to Figure IV- 8a, distortion is again observed in the discharge profile of the cell and positive electrodes in Figure IV- 9a, where there is a larger ohmic drop compared to that of (b) and (c), indicating that distortion at small pore size certainly comes from the ion size (ion-sieving effect). Such anomalies have been observed in the galvanostatic plots such as an asymmetrical charge-discharge pattern for a

symmetric cell as reported by T. Sato et al [11]. Distortions could be attributed by either the decomposition of the ILs or to the decomposition of the functional groups on the surface of the activated carbon. Since there is no evidence of any faradaic reactions, the ohmic drop could certainly be attributed to the larger ion size with respect to the size of the pores.

a) **Capacitance as a function of Ti-CDC pore sizes**
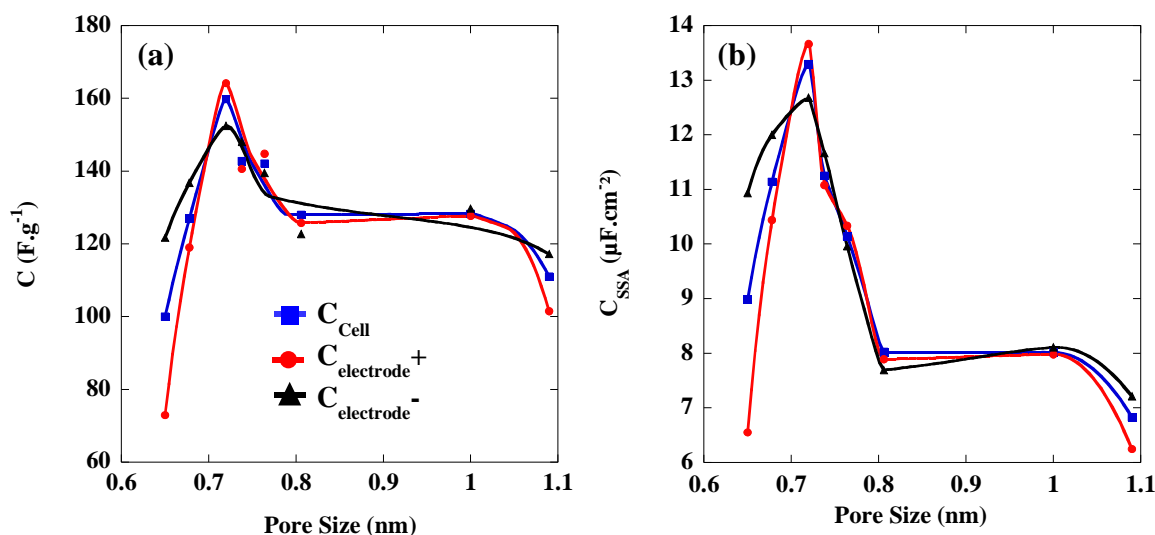
Figure IV- 10: Capacitance (F.g^{-1}) versus pore size **(a)** and normalized capacitance (µF.cm^{-2}) versus pore size **(b)** plots for the cell, positive and negative electrodes of Ti-CDCs in neat EMI-TFSI at 60 °C.

The cell capacitance and capacitance of the individual electrodes in neat EMI-TFSI electrolyte at 60 °C obtained for the different Ti-CDCs are plotted in Figure IV- 10a above (F.g^{-1} versus pore size), and Figure IV- 10b (normalized capacitance in F.cm^{-2} versus pore size).

The cell capacitance values of all the cells tested in EMI-TFSI were found to be reproducible with the previous published data from 2-electrode cells [1]. A new data point for an additional pore size value has been added in this plot at 1 nm and did not the change the previous trend. In this work, capacitances of both positive and negative electrodes were measured while controlling the cell voltage, in order to gain an understanding of capacitance contributions from the individual electrodes and results were in accordance with equation (II-19) for two capacitors connected in series in our cell set-up.

Upon charging, the EMI$^+$ ions are attracted to the negatively polarized electrode, adsorbed into the pores, contributing to the capacitance of the negative electrode, C$_{electrode}$-, while the opposite is true for TFSI$^-$ ions, which contribute to the capacitance of the positive

114

electrode, $C_{electrode}+$. On discharging, these adsorbed ions desorbed from the porous electrodes.

All of the 3 capacitance values calculated from galvanostatic cycling at the 10th cycle of each electrode have maxima that converged to the pore size value of 0.72 nm (Ti-$CDC_{550°C}$), which corresponds to a dimension that is in the same range as the molecular diameters (Figure IV- 4a and b). Results obtained show a maximum cell capacitance value of 160 F.g^{-1} at 0.72 nm. Individually, at the positive electrode, the anionic (TFSI$^-$ = 0.79 nm) adsorption registered a maximum value of capacitance, $C_{electrode}+$, 165 F.g^{-1} at 0.72 nm, while at the negative electrode, the cationic (EMI$^+$ = 0.76 nm) adsorption was at the same pore size with a peak capacitance value, $C_{electrode}-$, of 153 F.g^{-1}. It is assumed that the movement of ions towards electrode surfaces, linked with thermal agitation, within the electrolyte under an applied potential, adopts a tumbling motion such that they can be effectively described as spheres. Therefore, the effective diameter of the ions takes into account the longest dimension of the molecule. Whilst in pores smaller than the diameter of the ions, ions could be adsorbed longitudinally or laterally, depending on where the charges which are participating in the formation of a double layer, are residing on the ion. These results bring the conclusion of maximum capacitance reached when pore size is in close proximity to that of the ion size.

Results presented in Figure IV- 10a did not take into account of the change of total surface area within the porous volume. In order to support the conclusion further, the normalized capacitance values of cell, positive and negative electrodes were plotted against the pore sizes of the Ti-CDCs used as shown in Figure IV- 10b. Normalized capacitances of the cell, the positive and negative electrodes were obtained by dividing the gravimetric capacitance by the BET specific surface area (SSA). By taking normalized values, it is clearer and more accurate in presenting the results for better comparison of capacitance maxima irrespective of the carbon surface area, which varies with the synthesis temperature [10]. Figure IV- 10b shows direct convergence of the three maxima and offers a better representation of capacitance measured against pore size values where the peaks are clearly defined at one value of pore size, 0.72 nm. Both graphs in Figure IV- 10 are in agreement with the postulation of matching pore size to ion size in yielding the maximum capacitance. Effectively, this confirms that in the absence of any solvation shell for neat EMI-TFSI, matching pore size to the ion size yields the highest capacitance.

Owing to the ease of direct comparison to be made with specific areas reported for other supercapacitor carbons, Brunauer-Emmett-Teller Specific Surface Area (BET SSA) was

used. Although this method has an extent of inaccuracy with very small pore sizes, Non-Local Density Functional Theory (NLDFT) SSA was also used with the assumption of slit-shaped pores. Normalizing the gravimetric specific capacitance by the NLDFT SSA resulted in the same trend with a maximum of the specific capacitance at 0.72 nm. A decrease in the normalized capacitance was observed for the 1.1 nm pore size (TiCDC$_{1000°C}$). This could be attributed to the change of the carbon structure from disordered and amorphous to a more organized and graphitized one as described in [2]. Evidently, the large difference could also be observed from the area under the cyclic voltammetry plots as shown below.
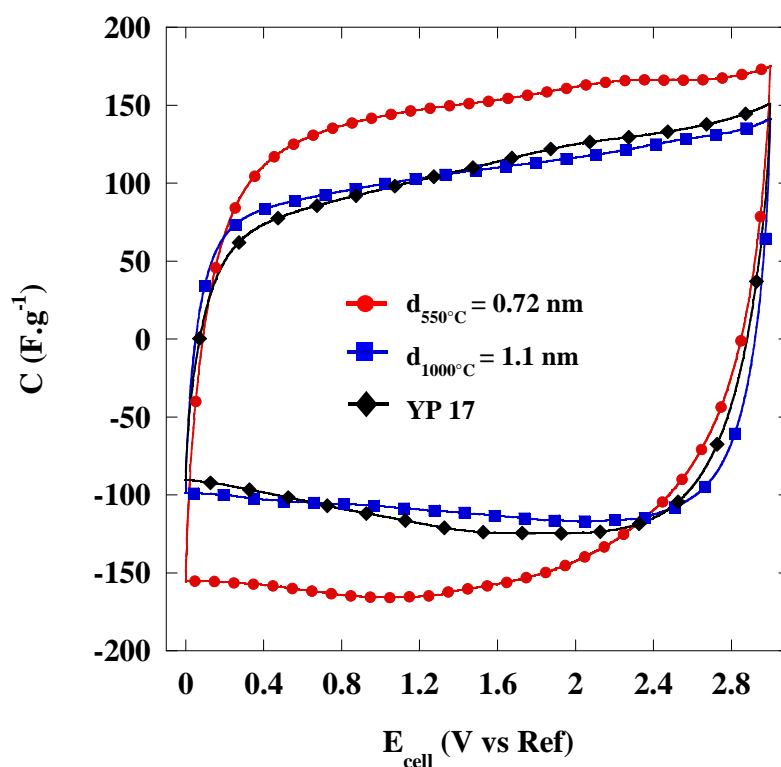
Figure IV- 11: Comparison CV plots of samples of the same weight of active material between high capacitance and low capacitance values, at a scan rate of 20 mV.s^{-1}.

Figure IV- 11 shows the CV of the highest capacitance sample synthesized at 550 °C overlaying that of the relatively lower capacitance sample synthesized at 1000 °C. Both CVs were acquired from samples of the same mass of active material. The area under a CVs, as well as the current responses shows that $C_{0.72nm} \approx 2C_{1.1nm} \approx 2C_{YP\ 17}$. Although EIS of YP 17 showed good wettability of the pores like those of the microporous Ti-CDCs of pore sizes larger than 0.7 nm (See Figure IV- 5), due to the wider pore size distribution, charge storage remained equivalent to that of the largest pore sized Ti-CDC sample (1.1 nm).

Conceptualization of the results obtained with neat EMI-TFSI electrolyte

Investigations have shown the importance of drawing the relationship between ion size and pore size of electrolyte/carbon systems in supercapacitors. Fundamentally, the capacitance gives a measure of the amount of charge stored by the equation:

$$C = \frac{\varepsilon_r \varepsilon_0 A}{d} \quad \text{(Eq IV- 8)}$$

where:

- ε_r is the relative dielectric constant of the electrolyte.

- ε_0 is the permittivity in vacuum, ($F.m^{-1}$).

- *A* is the specific surface area of the electrode, ($m^2.g^{-1}$).

- *d* is the thickness of the electrochemical double layer, (m).

From this equation, the parameters do not only depend on the nature of the electrolyte and the area of the electrodes, but more importantly on the thickness of the electrochemical double layer. Given that the electrochemical double layer is made up of charges residing on the electrode and the electrolyte ions, the 4 cm^2 electrode EDLC systems described in the results presented in this chapter offer a nanometric dimension of the double layer on the basis of *d* taking values of the diameters of participating electrolyte ions.

Most simulations have been reported on mainly the behaviour of ions in the pore. Palmer *et al* [12] has successfully developed morphologically realistic models for amorphous Ti-CDCs from simulated HRTEM images (high-resolution transmission electron microscope) using quenched molecular dynamics as mapped out in Figure IV- 12.
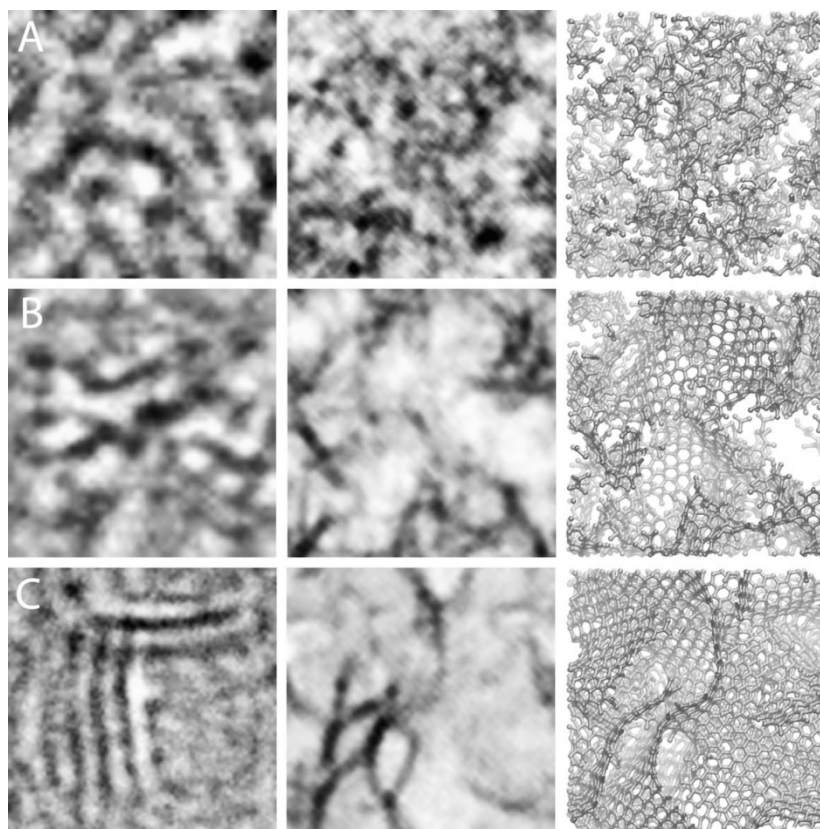
Figure IV- 12: Comparison of experimental HRTEM images (left column), simulated HRTEM images (center column) and snapshots of the model structures (right column). Each images has been scaled such that the edge length corresponds to 4 nm; HRTEM images of Ti-CDC synthesized at 600 °C and QMD structure quenched at 64x, respectively**(A)**. Same as **(A)** except for 800 °C and 8x **(B)**. Same as **(A)** except for 1200 °C and 1x **(C)** [12].

Structural changes in the models fit well with experimental values in main pore characterization techniques which can bring variety to modelling parameters for studying electrolyte/electrode systems.
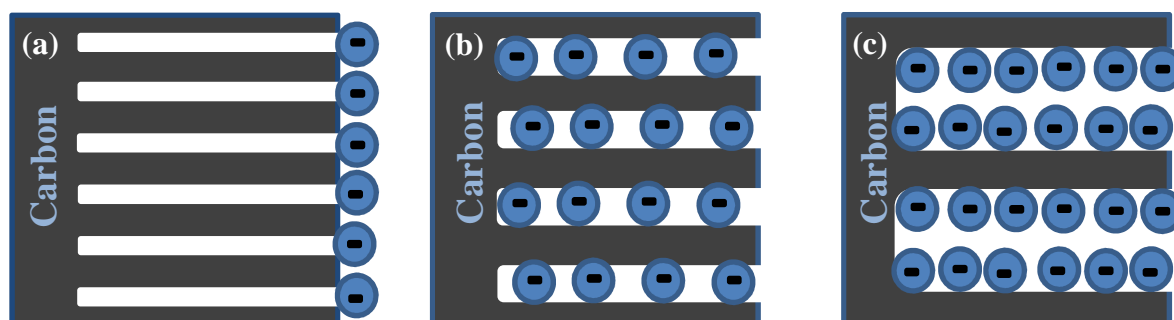
Figure IV- 13: Schematic of adsorption of ions in carbon of ultra-micropores **(a)**, micropores **(b)**, macropores **(c)** in a liquid salt.

Schematics in Figure IV- 13 are simplified cylindrical and parallel pores which depict the different possible hypotheses of electrolyte interactions in the different pore ranges.

Schematic (a) shows a simplified microporous carbon structure where the pores are too small to be accessible to the electrolyte ions, EMI-TFSI, leading to charge storage capacitance obtained merely at the outer surface of the porous structure which could be the case in the Ti-CDC$_{400°C}$ sample registering a relative low value of ~70 F.g^{-1} for the anion; (b) depicts the microporous carbon with pores that are large enough ($\geq$ 0.72 nm of Ti-CDC$_{550°C}$ sample) to accommodate a single diameter of ion, where capacitance is maximum in this configuration; Beyond pore sizes of larger than 0.80 nm, electrolyte ions experience less 'sieving' effect and can enter with associative counter ions or with more than two ions per pore size diameter as shown in (c).

With these results, we have shown and ascertained that the traditional belief in the achievement of maximum capacitance when the pore sizes were substantially larger than two times the size of the solvated ions is incorrect. In other words, maximum capacitance contribution which was previously thought to be only possible for "compact" layers in which ions reside on both adjacent pore walls as shown in Figure IV- 13c is not true. Moreover, the breakdown of the capacitance contributions from the individual electrodes in the 3-electrode configuration set-up have further affirmed and defined the "compact" layers necessary for maximal obtainable capacitance by proving the "matching pore size to ions" electric double layer concept as shown in Figure IV- 13b.

Ions have different lateral dimension to start with in this case, making the location of solvated molecules difficult although knowing it could be of paramount importance in further optimizing capacitance. As discussed earlier, all 3 maxima of the cell, and its constituent electrode capacitances had similar values of 0.72 nm for neat EMI-TFSI. Hence, hypothetically, these solvated ions could possibly conform to the pore architecture, meaning that these ions could have either accessed the pores longitudinally and/or that these ions are partially "distorted" from their originally adopted conformation when they exist as freely moving ions. Hartree-Fock and DFT quantum mechanics simulations reported a C-C bond elongation, resulting in the distortion of the carbon hexagonal rings with increasing surface density (potential applied). This could also be one of the explanations for the maximum capacitance obtained at pore size slightly smaller than the ion size because at higher potential, the C-C bond elongations allow more intense packing of ions into the porous structure [13]. Thus it could be suggested that, besides matching pore size to ion size being the fundamental criterion for optimum capacitance, conformational dynamics of the process and phenomena taking place when ions are entering the pores could be important too. Hitherto, intensive

research on modelling and simulations has been inspired by our work to provide better insight on this consideration [14].

Jiang et al. has recently reported in December 2011, oscillatory trend of capacitance about a mean value at higher pore sizes (> 3 nm) by employing classical density functional theory (DFT) [14a]. Diameters close to those of ions in EMI-TFSI were used as the size of electrolyte ions in this study using electrode with slit pores.
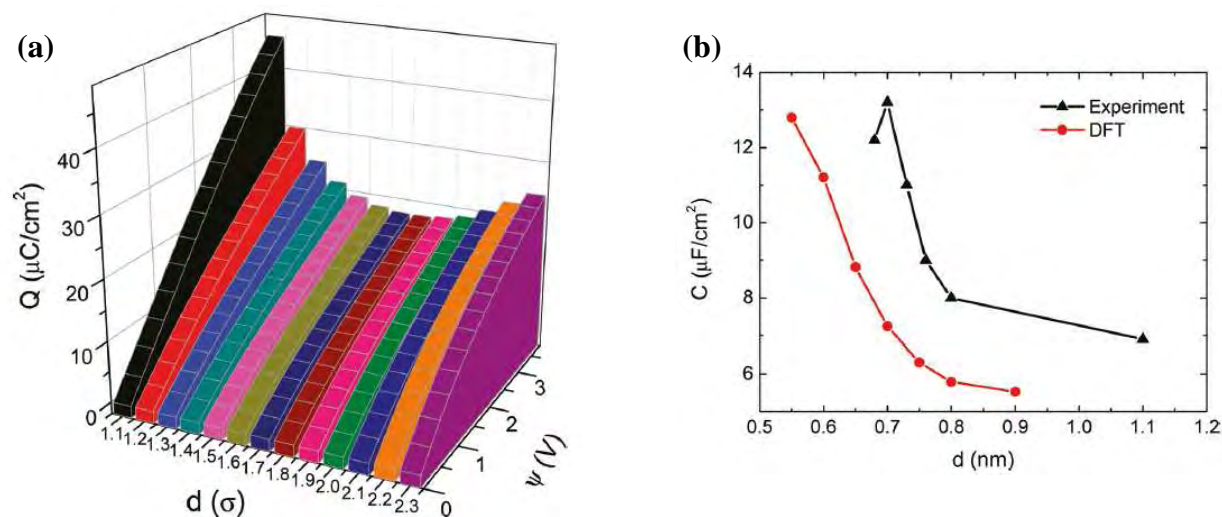
Figure IV- 14: Surface charge density, Q vs. surface potential, ψ and pore size, d. Here $\sigma = 0.5$ nm in **(a)** and capacitance of a nanoporous electrode as a function of the pore size, in comparison with experiment **(b)** [14a].

Results of this work confirm our experimental results since they show that the surface charge increases distinctly when the pore and ion sizes are in proximity as shown in Figure IV- 14a, where the highest charge density was recorded in pore size around 0.7 nm. Using the DFT method, the trend of higher cell capacitance as the size of pore approaches that of the ion, this finding is also in agreement with the reported results as shown in Figure IV- 14b, given the explanation by the team that the DFT plot is slightly shifted towards smaller pore size due to the use of approximate models.

II-4. 4 cm^2 Ti-CDC Electrode EDLCs - Ti-CDCs with solvated ionic liquid: EMI-TFSI in Acetonitrile (AN)

The idea of the 'optimized' pore size has been established in section I-3-3 of this chapter, that is, close to that of the diameters of the electrolyte ions [15]. This section deals with the intriguing question on what happens upon the addition of solvent molecules. Studies on EMI-TFSI done in two-electrode configuration have rendered increasing capacitance with adjacency of pore size and ion size [1]. Therefore the same neat ionic liquid (EMI-TFSI) and

completely solvated (2 M EMI-TFSI in excess AN) environment is established to investigate the introduction of the solvent, if it would lead to any changes in the adsorption behaviour.

Nonetheless, this study involves the comparison through impedance, qualitative analysis of cyclic voltammograms, time constant difference and the influence on the power delivery and energy storage in presence of a solvent.

Concentration of the solvated electrolyte was prepared at 2 M EMI-TFSI in AN in order to ensure excess of electrolyte ions over the electrode surface. Previously experiments have been conducted at 1 M but starvation effect [16] was observed at 2.4 V/Ref where the capacitive current in the CVs took on a dip to lower values with increasing potential applied to the electrodes. At 2 M, no starvation effect was observed at the limit of the electrochemical window, assuring that there is an excess of electrolyte ions for the electrochemical tests.

II-4.1. Electrochemical Impedance Spectroscopy (EIS)

a) Nyquist plots: ESR comparisons between solvated/non-solvated electrolyte
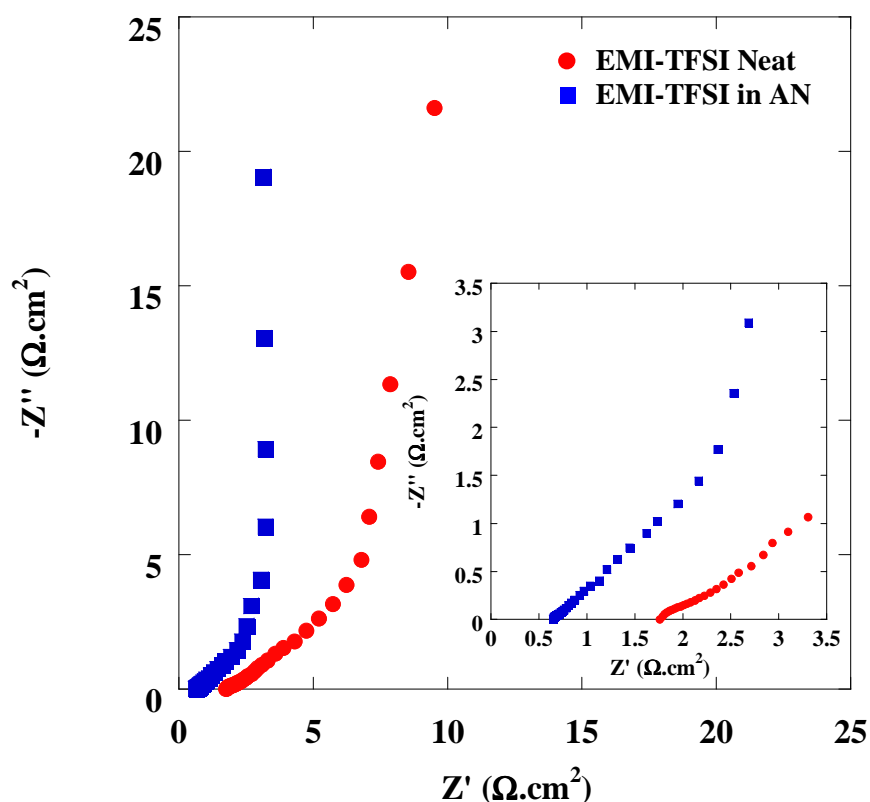
Figure IV- 15: Comparison of EIS spectra of Ti-CDC$_{800°C}$ (0.8 nm) in neat and AN-solvated EMI-TFSI and the zoom-in of the EIS (inset).

Figure IV- 15 above shows a comparison of the EIS spectra of the same sample in neat and solvated EMI-TFSI. Results presented are consistent with the measured conductivity of

the electrolytes using a conductivity meter prior to carrying out the tests. The ESR is determined from the real value of the plot and here, the resistance of neat EMI-TFSI is higher than that of solvated EMI-TFSI as can be seen from the shift of the plot corresponding to neat EMI-TFSI to higher x-values of the graph. Both show capacitive behaviour at the low frequency region of the Nyquist plot. In the middle part of the plot, the influence of electrode porosity and thickness on the migration rate of the ions from electrolyte inside the porous electrode can be observed. The thicker the electrode, the larger is the shift of the low frequency capacitive behaviour towards a more resistive value along the real axis. Here, the shift is due to the electrolyte resistance of neat EMI-TFSI, as it is more difficult for the ions to access the pores due to the higher viscosity and lower conductivity of EMI-TFSI with respect to EMI-TFSI dissolved in AN (conductivity of EMI-TFSI at 60 °C is 25 mScm^{-1} [17] and while that of 2 M EMI-TFSI dissolved in AN was measured to be 47.7 mScm^{-1} at 25 °C).

C' and C'' vs f plots of solvated/non-solvated electrolyte
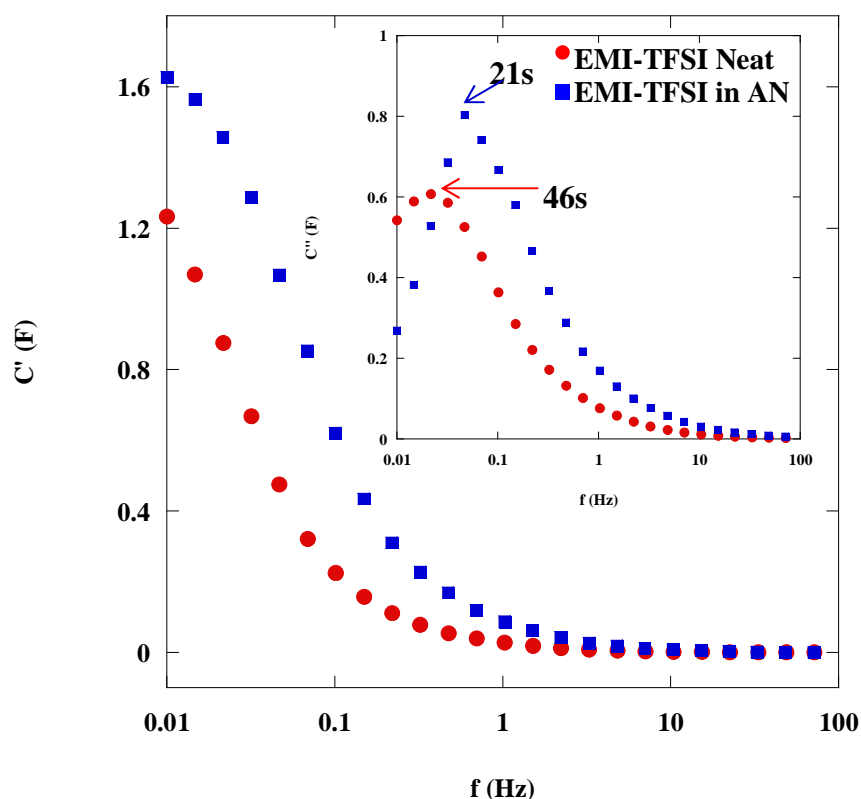
Figure IV- 16: Comparison of bode spectra of Ti-CDC$_{800°C}$ (0.8 nm) in neat and AN-solvated EMI-TFSI and their respective time constants (inset).

Real capacitance of both samples are similar considering the fact that the maximum of the profile for neat EMI-TFSI is lower than 0.01 Hz as shown in Figure IV- 16; the inset shows a faster time constant for the solvated electrolyte. Time constants calculated show that

the conductivity of an electrolyte has a great influence and in this case, the addition of AN resulted in 50 % reduction of the time constant. It can be interesting to compare the power delivery as a result of different time constants, and these calculations are presented in the later section of this chapter.

II-4.2. Cyclic Voltammetry
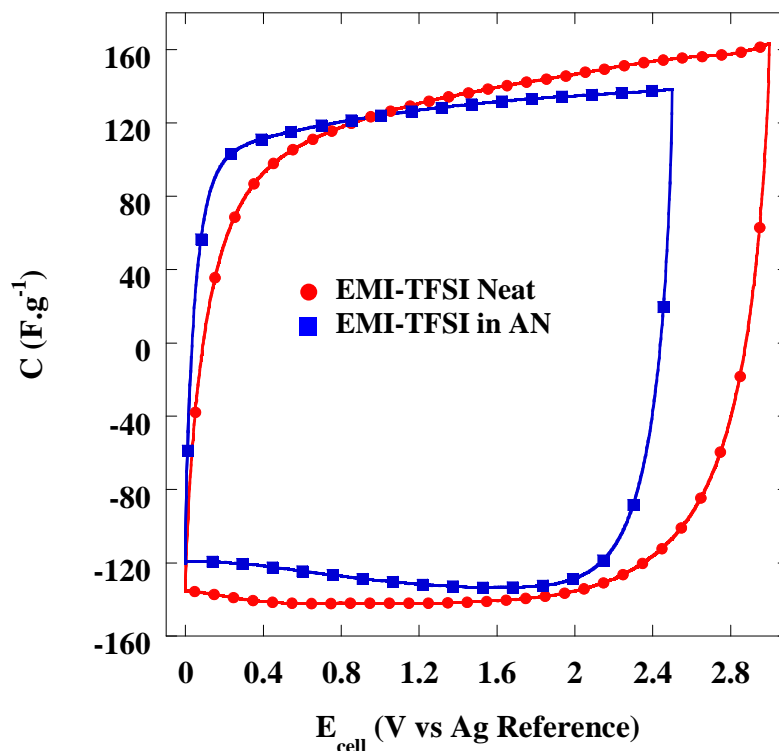
Figure IV- 17: Cyclic voltammograms of Ti-CDC$_{800°C}$ (0.8 nm) in neat EMI-TFSI and AN-solvated EMI-TFSI (same weight loading of 15 mg.cm^{-2}).

The cyclic voltammograms above in Figure IV- 17 are collected from the same batch of powder (Ti-CDC$_{800°C}$) which were processed into electrodes and tested in different electrolytes: Neat EMI-TFSI and EMI-TFSI in AN. Globally, these CVs exhibit capacitive behavior. Due to the instability of organic solvents at higher voltage windows, the electrochemical window for EMI-TFSI in AN was limited to 2.5 V/ref instead of the wider electrochemical window of neat EMI-TFSI at 3 V/ref.

As can be observed, the cyclic voltammograms do not overlap totally due to the narrower potential window offered by the organic electrolyte, AN. The higher ionic conducting AN indeed gives a more rectangular shaped voltammogram, with corners approaching right angles compared to that of the neat EMI-TFSI. The symmetric distortions of both the opposite corners of the two cyclic voltammograms are due to the electrolyte

resistance, as discussed earlier. Here, calculated capacitance gives C_{neat} = 140 F.g^{-1} and $C_{solvated}$ = 130 F.g^{-1}. Despite compromise of capacitance due to the higher ionic resistance in neat EMI-TFSI, capacitance is still higher due to the larger potential window.

II-4.3. Galvanostatic Cycling (CG)
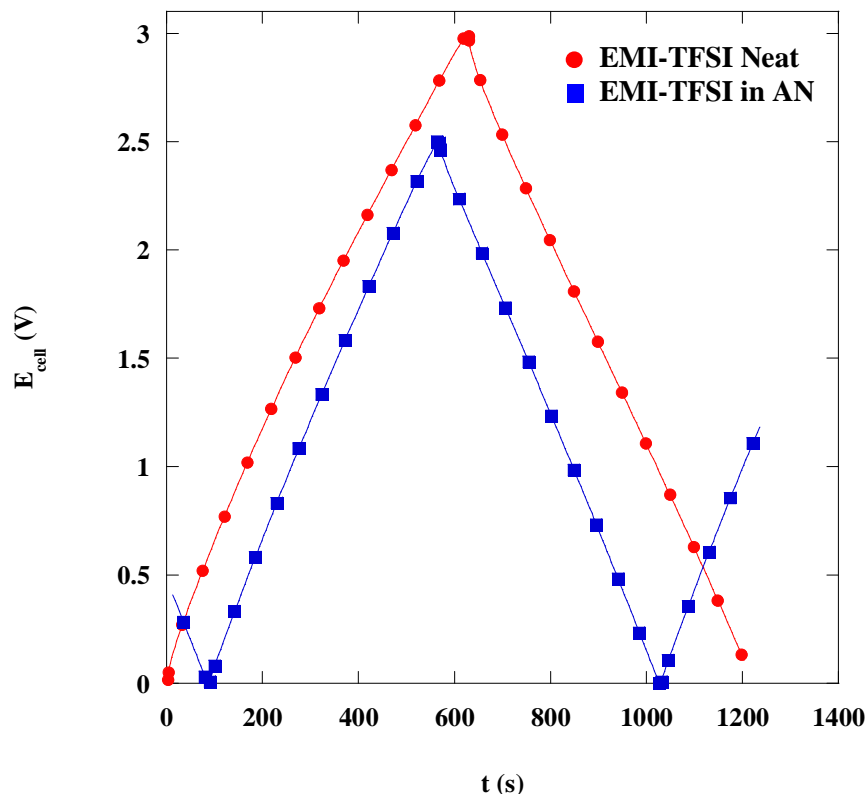
Figure IV- 18: Comparison of galvanostatic cycling between neat and AN-solvated EMI-TFSI in Ti-CDC$_{800°C}$.

Galvanostatic cycles are generated by first applying a constant positive current of 5 mA.cm^{-2} to charge up the capacitive cell to 2.5 V/ref and 3.0 V/ref for solvated and neat ionic liquid electrolyte respectively, then conversely, a negative constant current of the same magnitude, -5 mA.cm^{-2} was applied to discharge the capacitive cell to 0 V/ref.

Relative charge and discharge durations between solvated and neat EMI-TFSI electrolytes are distinctively displayed in the overlay of their respective galvanostatic cycles of Ti-CDC$_{800°C}$ sample in Figure IV- 18. From these galvanostatic cycling, the capacitances of the samples were calculated and the profiles also show that there is no faradaic reaction.

Solvated capacitance as a function of Ti-CDC pore sizes
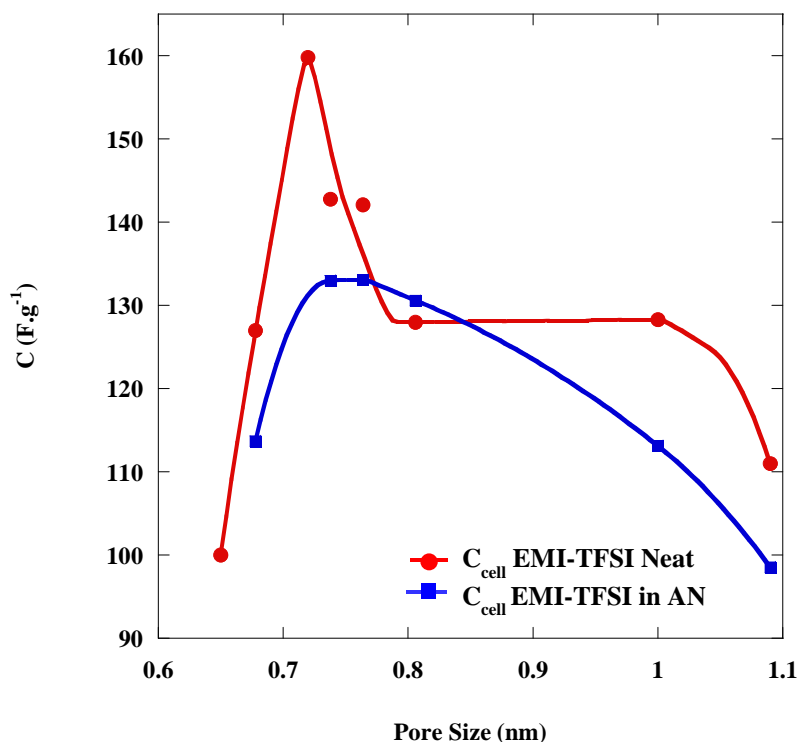
Figure IV- 19: Cell capacitance versus pore size of the TiC-CDC samples prepared at different temperatures in AN-solvated and non-solvated EMI-TFSI.

Gravimetric capacitance of the various TiC-CDC samples in both neat EMI-TFSI and solvated EMI-TFSI in AN were recorded and plotted against the pore sizes for comparison in Figure IV- 19. The general trend of lower capacitance values was observed across all Ti-CDC samples tested in 2M EMI-TFSI in AN and the peak of the plot is not as well defined as that observed for samples tested in neat EMI-TFSI. This observation draws the inference that indeed, solvent molecules do play a part in the lowering of capacitance values to a certain extent.

An acetonitrile molecule was reported in literature [18] to be 0.44 nm in length and 0.40 nm in width. Accordingly, a solvated EMI$^+$ molecule with one complete solvation shell would have an average diameter from 1.16 to 1.2 nm while that of a TFSI$^-$ molecule would have an average of diameter from 1.19 to 1.23 nm. Attributions to this result could perhaps be explained in terms of solvated ion size, which is larger than the ions and thereby reducing the charge density stored within the same amount of material. By analogy, in a given area on a pore wall adsorbed by two solvated ions can easily be accessed by three or more non-solvated ions for instance (number of ions cited here are arbitrary and used only for this analogy as the

effective sizes of solvated ions are not known). Consequently, more charges are being stored in a given pore volume and hence the elevated capacitance is achieved when all accessible pore volume is being fully made use of.

Power delivery and energy storage evaluation

Both values of cell capacitance almost similar in magnitude from Figure IV- 19 and it could be interesting to use these results to evaluate the extent of contribution of gravimetric capacitance/power from increased conductivity and reduced times constant as well as the compromise in energy storage due to a more restricted electrochemical window with AN.

Specific capacitance was calculated using equation (II.18) which yields values of 128 $F.g^{-1}$ and 130 $F.g^{-1}$ for neat and solvated EMI-TFSI respectively. Maximum specific power and energy could be thus estimated at their fully charged state of 2.5 V and 3.0 V according to equations IV-8 and IV-9:

$$P_{max} = \frac{V^2}{4(ESR) \times m_{AM}} \qquad \text{(Eq IV- 9)}$$

$$E_{max} = \frac{CV}{2 \times 3600 \times m_{AM}} \qquad \text{(Eq IV- 10)}$$

where m_{AM} is the total active material of both electrodes (30 $mg.cm^{-2}$), C is the capacitance in Farads and ESR is obtained from EIS values of Figure IV- 15 (0.78 and 1.67 $\Omega.cm^2$ for solvated and neat respectively). In the case of neat EMI-TFSI as electrolyte, the calculated values of $P_{max, neat}$ = 46 $kW.kg^{-1}$ and $E_{max,neat}$ = 27 $Wh.kg^{-1}$ while those in solvated EMI-TFSI electrolyte gave $P_{max, solv}$ = 69 $kW.kg^{-1}$ and $E_{max, solv}$ = 23 $Wh.kg^{-1}$. E_{max} values were calculated with unit kilogram of active material for the whole cell. Although the specific energy between the two systems do not differ a great deal, but there is a 1.5 times increase of power in the solvated system compared to the system with neat EMI-TFSI as electrolyte.

Besides, literature values of P_{max} = 55 $kW.kg^{-1}$ and E_{max} = 17 $Wh.kg^{-1}$ were reported under the same experimental conditions using 1.5 M NEt_4BF_4 dissolved in AN as an electrolyte within a 2.3 V electrochemical window [19]. The calculations approximated above for solvated and neat EMI-TFSI showed that as compared to a conventional salt in AN electrolyte, offers mediocre increase in specific energies but a 20 % increase in specific power. Moreover, the EMI-TFSI exists as a liquid at room temperature and is stable in AN mixture. This draws the advantage over the solid NEt_4BF_4 in AN as the salt can easily

precipitate out under slight elevation in temperatures that could be generated by energy devices during operation.

Solvated capacitances of individual electrodes as a function of Ti-CDC pore sizes
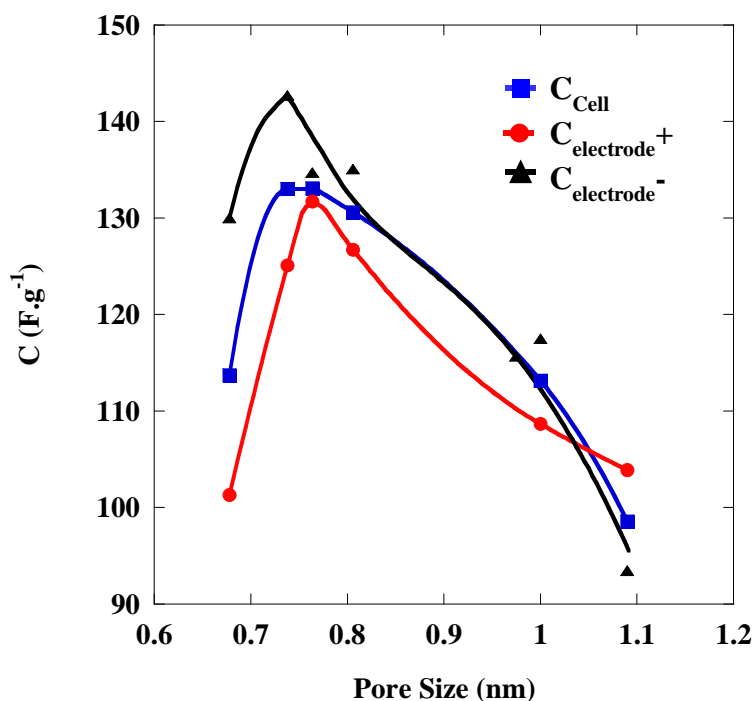
Figure IV- 20: The dependence of capacitance on pore size for individual electrodes in AN + 2 M EMI-TFSI at room temperature.

Differences between the pore sizes are very small and hence there exist a significant error margin. From the breakdown of capacitance contributions from the individual negative and positive electrodes in Figure IV- 21, it seems that corresponding pore sizes at the 3 peak maxima are consistent with the size of the solvated ions. From earlier deductions of diameters of fully solvated EMI^+ (1.16 to 1.2 nm) and $TFSI^-$ (1.19 to 1.23 nm) ions, these numericals suggest that the extent of solvation of the respective ions when entering the pores is different and partial, that is, these ions have different affinities for the solvent molecules.

Owing to the fast and conformational dynamics of the solvation shells upon entering the pore, the results presented in Figure IV- 20 could only suggest approximations to the effective ion sizes on the basis of quantitative analysis of the assembled cells. To further confirm our findings, a cavity microelectrode was used as a qualitative tool to observe the capacitive behaviours of the solvated electrolyte in the Ti-CDCs of different pore sizes.

III. Electrochemical study using a cavity microelectrode

III-1. 2 M EMI-TFSI in AN electrolyte

Electrochemical behavior of solvated EMI-TFSI was studied using a cavity microelectrode to further investigate the relationship between pore size and ion size of the electrolyte. CME as the working electrode, was packed with the Ti-CDC samples of different pore sizes, 0.68, 0.74, 0.80 and 1.0 nm synthesized at 500 °C, 600 °C, 800 °C and 900 °C respectively, and used to study the effective ion sizes of the EMI^+ and $TFSI^-$ ions in AN. The experimental set-up was completed with a rolled platinum foil as the counter electrode and a silver wire as a quasi- reference electrode. All procedures, that is, packing of the Ti-CDC powder, preparation of the electrolyte and sealing the set-up, proceeded in a glove-box of inert argon environment, of less than 1 ppm in both water and oxygen content. The set-up was then purged under nitrogen gas throughout the measurements. Cyclic voltammograms were recorded at a scan rate of 100 $mV.s^{-1}$, under ambient temperature and pressure, within the electrochemical voltage window of the electrolyte of 2.5 V: -1.2 to 1.3b V/Ref. Within this EDL range of potentials, the CVs are electrochemical signatures of in fact, the electroadsorption and electrodesorption of ions, which can be affected directly by the relations between the ion and the average pore size [20].

The open circuit voltage (OCV) of the Ti-CDC samples was measured to be ~ 0.2 V/Ref and although the carbon charge is neutral, there can be minimal ions adsorbed. Hence it can be considered that the PZC ≈ OCV.

In the 4 cm^2 electrode capacitors, the electrodes are polarized specifically in the adsorption of only one type of ions, either the cations or the anions, throughout the whole testing process of the cell by controlling the cell voltage. On the other hand in this case of the CME technique, the carbon particles that were packed in the cavity of the CME were subjected to the adsorption and desorption of both the cations and anions upon each charge/discharge cycle depending on the polarity of the working electrode.
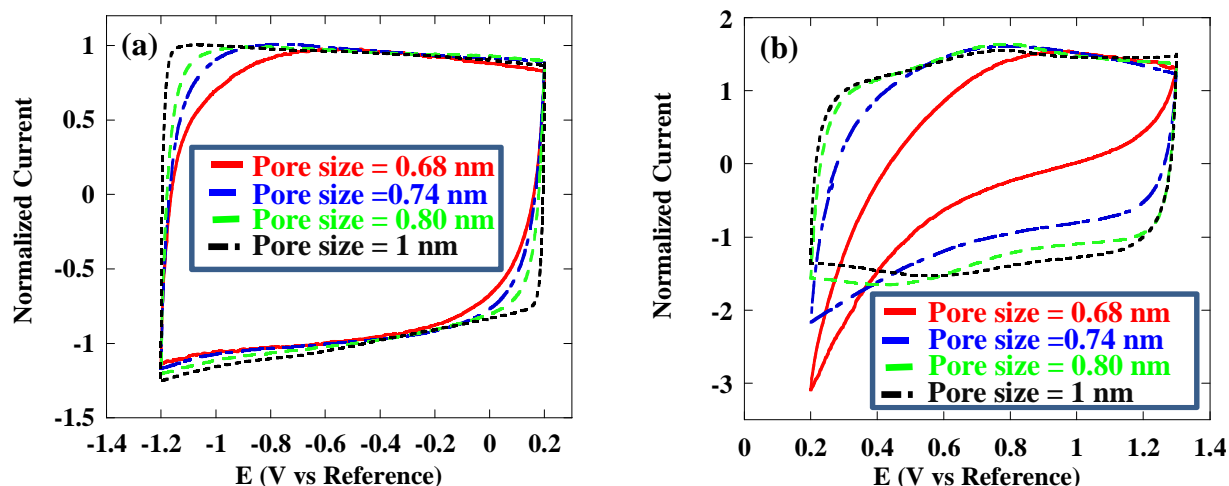
Figure IV- 21: Normalized CVs of the samples in AN + 2 M EMI-TFSI at 100 mV.s^{-1} in the negative range **(a)** and in the positive range **(b)**.

All CVs have been normalized in current with respect to the pure capacitive behaviour region (at -0.4 V/Ref in Figure IV- 21a and 1.0 V/Ref in Figure IV- 21b). Normalization was necessary because the raw CVs measured were of different current response owing to the (i) varying weight of the Ti-CDC powder packed in the CME for each run of experiment and (ii) the difference in the gravimetric capacitance of the respective samples. Consequently, the CVs were normalized to close to unity capacitance in the capacitive region, while preserving the shape of the CV scans, allowing easier comparisons. Normalization will be further discussed in the next chapter.

Symmetry of the CVs provides insights on the ion size/pore size relation as well as the carbon/electrolyte interactions. By using the CME, the symmetrical distortions of the CVs arise from the resistance in the bulk of the electrolyte in terms of conductivity, that is, the intrinsic property of the electrolyte as a whole. On the other hand, ion accessibility to the carbon porous network, i.e., the ion migration into the pores, could be deduced from asymmetrical current response in the CVs.

EMI$^+$ adsorption

Figure IV- 21a shows the normalized CVs of the samples from OCV (~0.2 V/Ref) to -1.2 V/Ref. During the charging process from the OCV to -1.2 V/Ref, the EMI$^+$ ions are adsorbed into the CDC pores and subsequently desorbed from the pores upon discharging from -1.2 V/Ref to the OCV.

Information on the capacitive behavior of the carbon/electrolyte couple owing to the interaction between electrolyte ions and the surface of the carbon pores could be inferred from the CVs profiles of the samples. Here, the CVs of the samples displayed similar 'rectangular' profiles, evidencing a pure capacitive behavior. An exception was however recorded for the carbon powder with the lowest pore size at 0.68 nm, where a slight asymmetry of the CV profile upon discharging (from −1.2 up to 0.2 V/Ref) can be seen as compared to charge (from 0.2 down to −1.2 V/Ref). The CVs of other samples with larger pore sizes (0.74 – 1 nm) exhibit little deviation from the pure capacitive behaviour and little asymmetry of the CVs was also observed. Accordingly, for these larger pore size CDCs, the carbon pore accessibility is not limited for the EMI$^+$ ions; they are able to be adsorbed into the pores of these samples without constraints. Thus, the effective size of the EMI$^+$ ions when adsorbed in carbon pores can be estimated to be close to 0.7 nm.

TFSI$^-$ adsorption

Figure IV- 21 shows the CVs of the different CDCs samples recorded in the potential range of the OCV to 1.3 V/Ref. Above the OCV in this potential range, only anions, that is, the TFSI$^-$ ions, contribute to the current response during the charging/discharging processes. Anions are adsorbed into the pores of the carbon powders during the positive scans from 0.2 up to +1.3 V/Ref and upon discharging from +1.3 V/Ref down to the OCV value, TFSI$^-$ ions vacate from the pores.

CDC samples of pore sizes 0.68 and 0.74 nm produced CVs which are severely distorted asymmetrically while the greater pore size samples (0.8 and 1.0 nm) show near pure capacitive behaviour. These results clearly show that the effective TFSI$^-$ size described by the carbon during the adsorption process is larger than 0.75 nm. The CV profiles of the positive potential range (TFSI$^-$ adsorption) are very different from those of the negative potential range (EMI$^+$ adsorption), especially for the low pore sized samples, 0.68 and 0.74 nm. This observation is confirmed when the samples are scanned within the whole potential range such as depicted in the figure below.
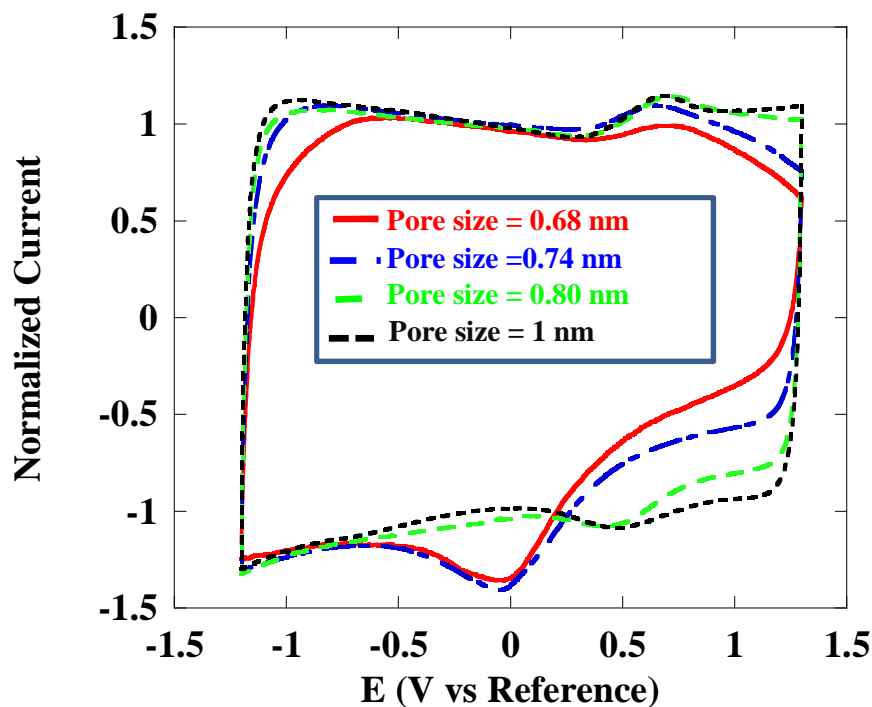
Figure IV- 22: Normalized CV for all four samples in AN + 2 M EMI-TFSI at 100 mV.s^{-1}.

Figure IV- 22 shows the CVs collected at a scan rate of 100 mVs[-1] over the entire potential range from -1.2 to 1.3 V/Ref. Two different potential ranges can be easily distinguished on Figure IV- 22: above and below the OCV that was measured at 0.2 V/Ref. For the large pore size samples (0.80 and 1 nm pore size), the CVs exhibit the traditional rectangular shape characteristics of pure capacitive behaviour for both the anion (E > OCV) and the cation (E < OCV), this draws the inference that the effective ion size was smaller than 0.8 nm for both the cations and the anions. This finding confirms the previous results obtained in Figure IV- 21a and b.

Conversely, in the case of the smaller pore size samples, (0.68 and 0.74 nm) the charge/discharge profiles display some extent of inconformity which infers the increase of ion size limitation by the pores for the TFSI⁻ adsorption side, in the positive scan. The severe distortions in the CV are prominent at high potential and confirm that the effective size of the TFSI⁻ ion is larger than ∼0.75 nm, as previously observed. In the low potential range (− 0.5 to − 1 V/Ref), where the cation adsorption occurs, the slight distortion of the CV for the smallest pore size sample (0.68 nm) suggests that the effective EMI⁺ is close to 0.7 nm, which is again in good agreement with the result deduced from Figure IV- 21.

Deductions drawn from these analyses of distortions suggest that (i) the average effective ion size of the solvated EMI⁺ ions in pores is somewhat lower than that of the TFSI⁻

ions, in spite the size of the bare ions being almost the same and (ii) the ideal capacitive behaviour is observed at pore sizes larger than 0.74 nm. This analysis when combined with the 4 cm^2 electrode EDLCs measurement, agree perfectly with each other, where the individual electrodes have maxima in the same range of 0.74 and 0.80 nm as shown in Figure IV- 20.

Larger effective size of the solvated TFSI$^-$ as compared to that of the solvated EMI$^+$ ion, could be explained by the different affinities of the electrolyte ions for the solvent molecules taking into consideration the different solvation energies involved. One explanation could involve the desolvation energy that is required for the ions to enter the pores. As observed in Figure IV- 21, the positive electrode seems to be more limited than the negative one. This also suggests that the extent of solvation of TFSI$^-$ ions are higher than that of the EMI$^+$ ions. Hence, a possible attribution to this observation of higher resistance for the charging and discharging at the positive potentials, could be the solvation affinity and thus the energy involved in the partial desolvation required for the entering the pores.

Complementary studies such as computational studies thus come in as a useful tool to study and as well as to model the extent of desolvation of ions upon entering the pores. Computer simulations show the peaks for EMI$^+$ at 1.77, 2.16 and 2.53 nm and for TFSI$^-$ at 2.24 and 2.74 nm in the radial distribution function. These values provide for the most probable solvation radii for the respective ions solvated in AN in the absence of carbon. Thus, while TFSI$^-$ ions have a larger solvation shell compared to EMI$^+$ ions, which holds in agreement with the effective ions sizes estimated from CME experiments, both solvated ions are too big to be accommodated in CDC pores. This supports our previous findings that there is at least partial desolvation of electrolyte ions when they enter pores under an applied potential [1].

III-1.1. Kinetics study of the TFSI$^-$ adsorption on CDCs

However, one of the most remarkable feature of the CVs shown in Figure IV- 22 are the additional current peaks observed at ~0.7 V/Ref on the positive scan and ~-0.1 V/ref on the negative scan. These peaks are more pronounced for samples of the two lower pore sizes at 0.68 and 0.74 m at 0 V/Ref, which corresponds to the potential range including the OCV value where the charge storage mechanism changes from the cationic adsorption to anionic adsorption.

In the light to gain understanding on the significance of these peaks, a complete series of cyclic voltammetry study has been carried out with the smallest and largest pore size samples (0.68 and 1 nm), at scan rates ranging from 10 to 1000 mV.s^{-1}. Figure IV-22 shows recorded CVs in the 2 M EMI-TFSI in AN electrolyte between 10 and 100 mV.s^{-1} for the largest pore size sample, 1.0 nm, in the entire potential range from -1.2 to +1.3 V/Ref.
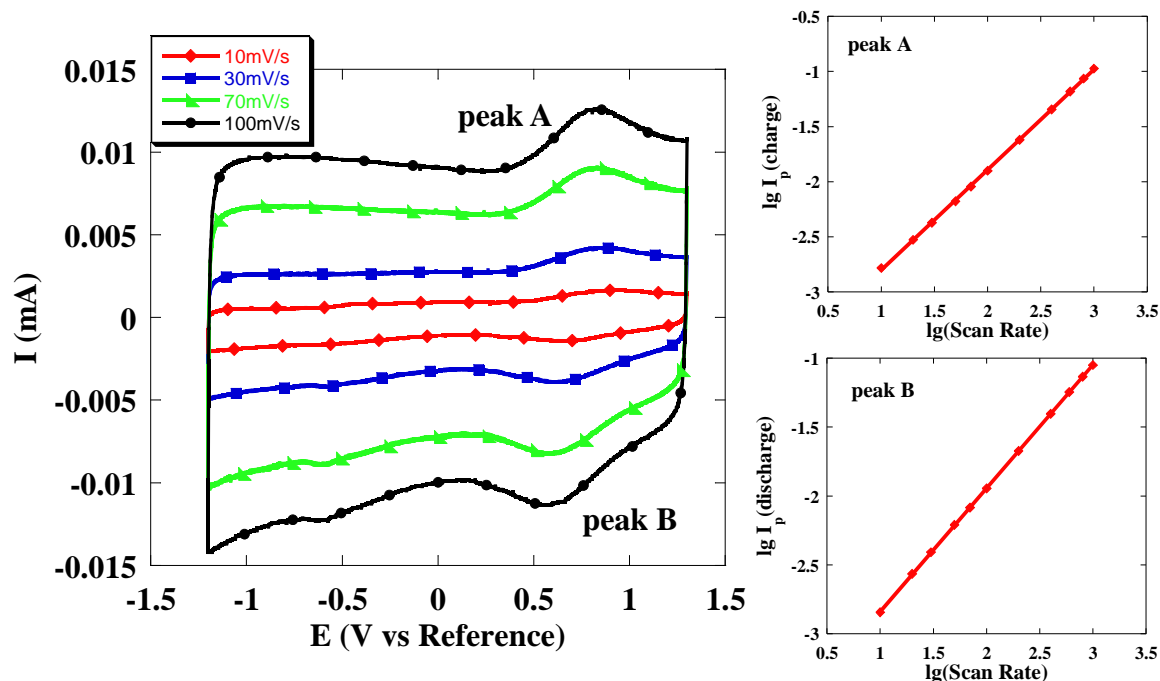
Figure IV- 23: CVs recorded at 10, 30, 70 and 100 mVs^{-1} for the 1 nm pore size sample, in AN + 2 M EMI-TFSI electrolyte. Inset: change of the logarithm of the peak current versus the logarithm of the potential scan rate, for peaks A and B.

Two peaks can be observed, marked as peaks A and B on the anodic positive scan and the cathodic negative scan respectively; the intensity of these peaks changes with the scan rate. Figure IV- 23 insets present the change of the logarithm of the peak A and B versus the logarithm of the scan rate on the full potential scan range. Gradients of both the insets were 0.91 and 0.9 respectively for peaks A and B. These values, being close to unity, attribute these peaks to a capacitive charge storage mechanism, and not due to a diffusion limited process, according to Eq IV-10:

$$I = C_d A v \qquad \text{(Eq IV- 11)}$$

Where *I* is the current (A), C_d the capacitance (F.m^{-2}), *A* the surface area (m^2) and *v* the scan rate (V.s^{-1}) [21].

Eq IV-10 is applicable on charge/discharge of the double layer capacitance or on fast redox surface reactions leading to pseudo-capacitive storage [22], without any diffusion

limitation due to accessible electrode surface. From the peak potentials observed, this surface process is highly reversible and occurs in addition to the capacitance from the charge/discharge double layer.

The CV for the 0.68 nm pore size sample recorded at 10 mV.s^{-1} in AN + 2 M EMI-TFSI electrolyte is shown in Figure IV- 24. It indicates a double layer capacitive behaviour when the potential scan range is limited between -1.2 and 0.5 V/Ref. Upon scanning up to the potential of 1.3 V/Ref, the electrochemical signature deviates from that for the large pore size (1 nm) sample presented in Figure IV- 23. Along the positive scan, a sharp current decrease is visible after a bump, A' at potentials higher than 0.8 V/Ref. On the reverse scan, a pronounced cathodic peak B' can be seen at about 0.2 V/Ref, before the current returns back to a constant value associated with the traditional double layer capacitive behaviour.
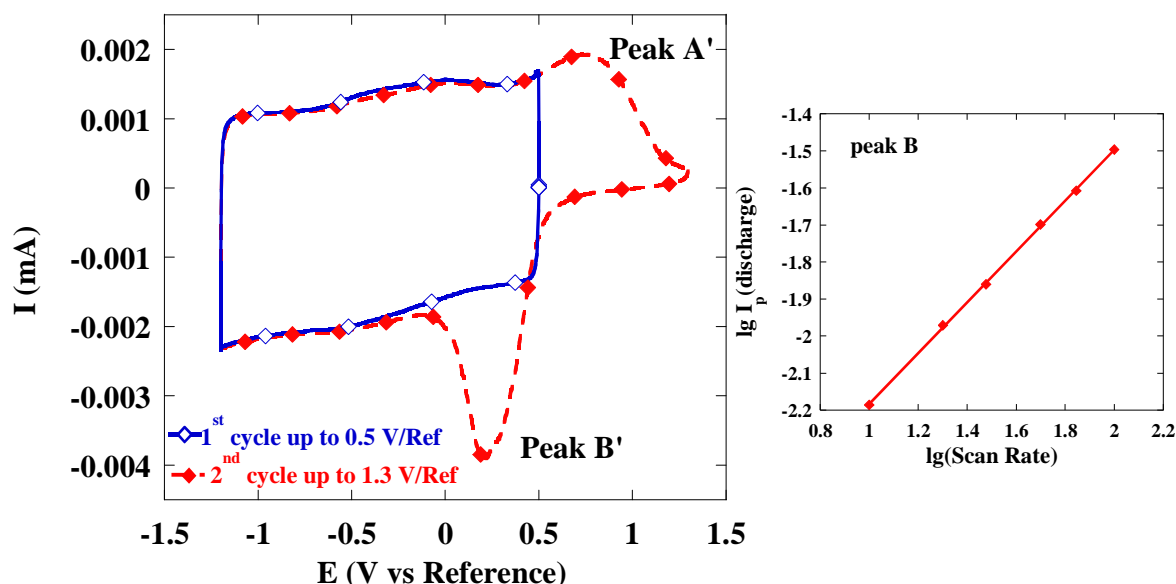
Figure IV- 24: CV for the 0.68 nm pore size sample recorded at 10 mV.s^{-1} in AN + 2 M EMI-TFSI electrolyte, in the −1.2 up to 0.5 V/Ref potential range (1st cycle) and the −1.2 up to1.3 V/Ref potential range (2nd cycle).

The current decrease in region A'and the cathodic peak B' thus appears to be linked to each other since peak B' is not present when the potential scan is limited to +0.5 V/Ref. The variation of the logarithm of the peak current has been plotted against the logarithm of the scan rate, in the 10-100 mV.s^{-1} potential scan rate range, for peak B'. At scan rates above 100 mV.s^{-1}, the peak current can no longer be distinguished from the current contributed by the capacitive double layer.

This variation of maximum peak current with the potential scan rate or a reversible diffusion-controlled reaction is expressed through the Randles-Sevcik equation [23]:

$$I_{peak} = 0.4463(nF)^{3/2} AC(\frac{D}{RT})^{1/2} \times V^{1/2} \qquad \text{(Eq IV- 12)}$$

where I_{peak} is the maximum current (A), n the number of electrons involved, F the Faraday constant (As), C the concentration of the diffusing species (mol.cm^{-3}), D the diffusion coefficient of the diffusing species (cm^2.s^{-1}) and v the potential scan rate (V.s^{-1}). This equation is applicable to any charge transfer reaction where the approach of reactants towards the electrode surface and/or the removal of products away from the electrode surface are under the diffusion control. Hence, it could be used to describe a redox reaction and also to correlate an ion transfer at an interface [23].

The gradient of the plot of log(I_{peak}) against log(v) is 0.65 for peak B' (see inset of Figure IV- 24). This value of the gradient is close to 0.5, inferring that the reaction observed with the 0.68 nm pore size sample appears to be under diffusion control. The small deviation from the theoretical value of 0.5 can be explained by the nature of the electrode used in these experiments. Owing to the use of porous carbon as electrodes, this is not the ideal case of a smooth, planar electrode defined in Eq IV-11. Moreover, the geometric dispersion due to the porous network may explain the observed difference.

Figure IV- 25 shows the influence of a potentiostatic holding at 1.3 V/Ref for the smaller pore sized sample, 0.68 nm. A first cycle of CV was initially scanned at 10 mV.s^{-1} within the full potential range, and then the scan was stopped at 1.3 V/Ref on positive scan and the potential was held at this value for 30 minutes; a second CV of full cycle was further recorded within the full potential range. In Figure IV- 25, it can be observed that the intensity of peak B' increases after being imposed a potential holding at 1.3 V/Ref for 30 minutes in the reverse scan. This draws a clear relationship between the decreased current observed in region A' and the cathodic peak B'.
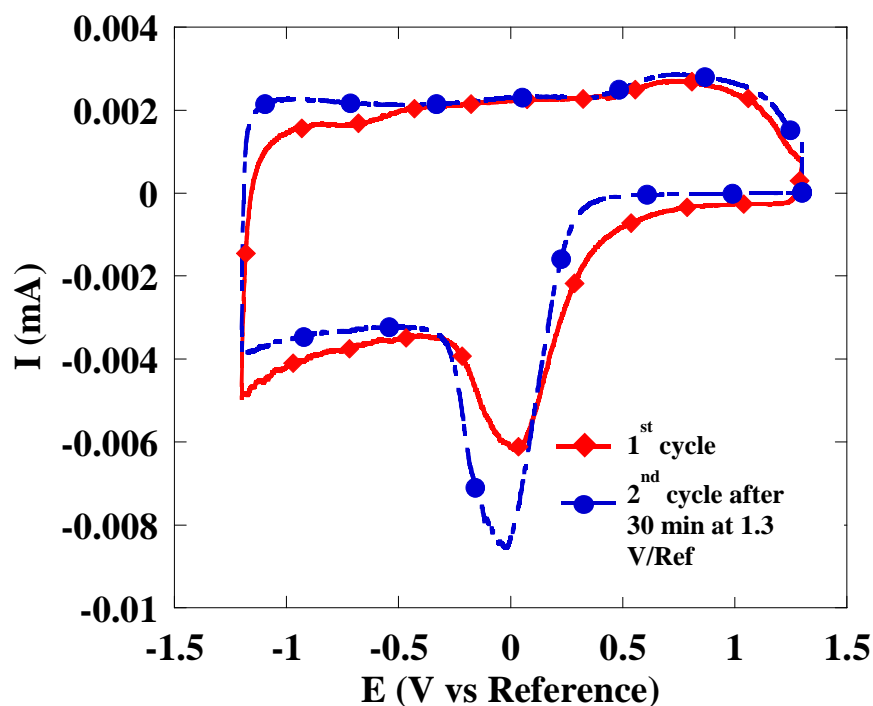
Figure IV- 25: CVs for the 0.68 nm pore size sample recorded at 10 mV.s^{-1} within the −1.2 up to 1.3 V/Ref potential range in AN + 2 M EMI-TFSI, before (◆ diamonds) and after (● circles) a 30 min potentiostatic holding at 1.3 V/Ref.

Correlation of results with ion adsorption mechanism

By looking at Figure IV- 23 and Figure IV- 24, it is obvious that the large pore sized (1 nm) and the small pore sized (0.68 nm) samples exhibit different electrochemical signatures in the 0 to 1.3 V/Ref potential range which corresponds to the TFSI$^-$ anion adsorption.

Large pore size sample (1 nm) - For a carbon with pore size which is slightly larger than that of the anion size, that is, for the 1 nm pore size sample, two reversible peaks which appear at 0.7 V/Ref, are inferred to be linked to a fast surface storage process as no limitation due to diffusion is observed within the 10-1000 mV.s^{-1} potential scan range. Furthermore, these peaks appear in addition to the double layer capacitance determined on the CV by its characteristic rectangular shape [22]. Both the double layer- and pseudo-capacitive storage can be correlated by Eq IV-10. The latter should involve the presence of a reversible redox shuttle in the electrolyte or some redox surface functional groups on the carbon surface. All the carbon samples studied here were annealed for one hour at 600 °C under hydrogen atmosphere to reduce any potential surface functional group. Moreover, the CV of the same 1 nm pore size carbon sample in acetonitrile + 1.5 M NEt$_4$BF$_4$ electrolyte did not show any reversible peak in the 0-1 V/Ref potential range (see chapter 3, Figures III-4 and III-6) [24],

and even up to 1.3 V/Ref (not shown). Hence, the solvent/carbon interface is not likely to be involved in a pseudo-capacitive storage mechanism linked with any reversible surface redox reaction that could be due to the presence of surface functional group or redox shuttle.

Small pore size sample (0.68 nm) - Upon the decrease of the carbon pore size to below the effective size of the anion (0.68 nm carbon sample), the current decreases sharply at potential higher than 0.7 V/Ref on the positive scan. Similar electrochemical behaviour has been previously reported [24,25] and has been assigned to a decrease in the pore accessibility for the adsorbing ions. In the present case, the CV shows the limited accessibility of the TFSI$^-$ anions into the small 0.68 nm pores. On the reverse scan, the huge cathodic peak occurring at 0.3 V/Ref is mainly associated with a diffusion-controlled process. During this reverse scan, the TFSI$^-$ ions are forced by the electrostatic repulsion to leave the carbon surface. Henceforth, we assume that this peak is linked with the removal of the TFSI$^-$ anions that were forced to enter the small pores during the positive scan. TFSI$^-$ ions have a high form factor so that ion removal from these narrow pores is hindered, therefore, rotation and alignment of ions in specific direction will be required to move them through the porous network. It is the diffusion of these anions to exit the carbon pores which controls the cathodic discharge process. Necks between the pores smaller than the average pore size might be present in the carbon structure and enhances this diffusion control. These CVs in Figure IV- 25 confirm this hypothesis, where the increase of the peak current B' could be due to the increased number of TFSI$^-$ adsorbed forcefully during the potentiostatic holding at 1.3 V/Ref.

These results are consistent with data reported by Aurbach's group with microporous carbons in Propylene Carbonate + 1 M NEt$_4$BF$_4$ electrolyte [26]. They proposed a mechanism whereby desolvated Et$_4$N$^+$ cations could be partially trapped into small pores of comparable diameter after overcoming an activation barrier associated with the partial ion desolvation and the re-organization of the solvent molecules inside the pores. Once the barrier is overcome, the gain in free energy to accommodate the ions in these sites is positive due to the ion–carbon pore wall interaction [26], and this situation is compared with an ion in a potential well. Cation de-trapping was observed by applying a high anodic overvoltage leading to the electrostatic repulsion between the pore walls and the cations. In the present work, the same mechanism is suspected to have occurred during the anion adsorption/desorption for the 0.68 nm pore size sample, except that the ion desorption can be achieved for a cathodic overvoltage of –0.55 V, which is the peak potential difference $\Delta E_p' = E_{\text{peak}}B' - E_{\text{peak}}A'$ between peaks B' and A' (Figure IV- 24).

As the pore size increased to 1 nm, that is, when the pore size is in the same range or slightly larger than the effective ion size, TFSI$^-$ ions have access to the carbon pores, and hence the charge storage mechanism is no longer controlled by the diffusion of the anions (see Figure IV- 23. The activation barrier to overcome is thus decreased as compared to the small pore size sample since TFSI$^-$ ions have easier access to the pores. Ions stand in an energetically favourable configuration with specific interactions owing to a closer distance from the carbon pore walls; this is associated with the appearance of peaks A and B on the CV (see Figure IV- 23). These couple of peaks A and B are related to a highly reversible process since the peak potential difference $\Delta Ep = E_{peakB} - E_{peakA}$ is decreased down to -0.22 V as compared to $\Delta Ep'$, and ΔEp is roughly constant within the 10–100 mV.s^{-1} range (see Figure IV- 23) [29]. Peaks A and B define a potential for this reversible process, which correspond to an activation energy.

Under a specific case where the effective size of the ion falls within the same range as that of the carbon pore, such as the 1 nm pore size sample, the peak A observed on charging (positive scan) could be associated with the activation energy barrier to overcome partial desolvation of the ions and to aid in the reorganization of solvent molecules inside the pores, as suggested by Aurbach's group [26]. This process is reversible on the reverse scan, and about 25–30 % of the total capacitance is contributed by an extra-capacitance at scan rate of 10 mV.s^{-1}. It is one rare occasion that such a reversible phenomenon is observed with double layer capacitance and it is difficult to propose some definitive answers at this stage to explain this reversible extra-capacitance. The re-organization of the solvent molecules in the pores or an increase of the electrostatic interactions between the ions and the carbon pore walls in this confined environment leading to an electrosorption- or a chemisorption-like sorption process could explain this extra-capacitance observed when the ion size is in the same range as the pore size. In this case, the associated reversible peaks A and B would be linked with the additional activation energy created by this process, differently from the case of a standard ion adsorption process in larger pores.

Dzubiella and Hansen used molecular dynamics simulations to show that there is ample ion motion and diminished dielectric permittivity in pores less than the size of their solvation shells under an applied potential [27]. High extent of solvation shell distortion when the ions are squeezed into pores which are less than the size of their solvation shell, could probably contribute to the extra capacitance from the larger solvation shell of TFSI$^-$ ions than that of EMI$^+$ ions. In the case of severe distortion, the ion center is brought closer to the

electrode surface. According to equation IV-7, this leads to the improved capacitance. Wang *et al.* have recently studied the correlation between ion transport time and ion-pore diameter ratio, explained this elevated value as attributed by the ion-pore diameter ratio being close to 1, thereby minimizing the spaces for ion-wall collisions [28]. The ion transport time, expressed as [29]:

$$\tau = \frac{L^2}{D} \qquad \text{(Eq IV- 13)}$$

where τ is the ion transport time, L is the ion transport length and D is the ion transport coefficient. In our experiments, an ion-pore diameter of close to 1 could be easily achieved. The resulting ion transport length is thus too small to allow ion-wall collisions, resulting in a near zero value of the ion transport time.

Further work will be needed to get a better understanding of this reversible process, and a set of experiment has been launched in different electrolytes. Beyond that, from a fundamental point of view, there is a clear lack of understanding of the double layer charging in the confined space of micropores, in which there is no room for the formation of the Helmholtz layer and diffuse layer expected at a solid–electrolyte interface. Computational modelling using Molecular Dynamics or ab-initio methods would be for instance of great help in addressing the ion size in these sub-nanometer pores as well as understanding the solvent reorganization, that are one of the keys to design the next generation of high energy density EDLCs.

III-2. 2 M EMI-FSI in AN electrolyte

The FSI⁻ anion, ensues after the TFSI⁻ as an anion owing to its smaller size, attaining better ionic conductivities in ILs with the same cations as compared to the latter. Having a near C_2 symmetry, the sulfonyl moieties take on a distorted tetrahedral symmetry with bond angles ranging from 102 to 115° for TFSI⁻ ion [30]. The FSI⁻ anion is assumed to have a similar geometry with a more compact structure due to the smaller substituent group.

(a)   **(b)**
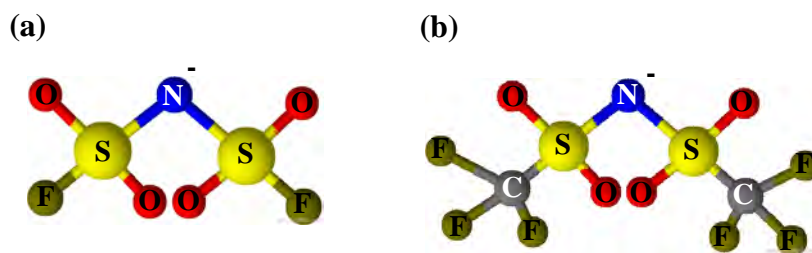
Figure IV- 26: Molecular structures of anions, FSI^- **(a)** and $TFSI^-$ **(b)**

III-2.1. Synthesis of EMI-FSI

The synthesis of EMI-FSI is similar to that of EMI-TFSI in the first quaternization step of producing EMI-Br (Rxn IV- 3). The only difference is the anionic exchange in which K-FSI is used in place of Li-TFSI as shown in (Rxn IV- 4:

1-Methylimidazole   1-Bromoethane   EMI-Br

EMI-Br   K-FSI   EMI-FSI   K-Br
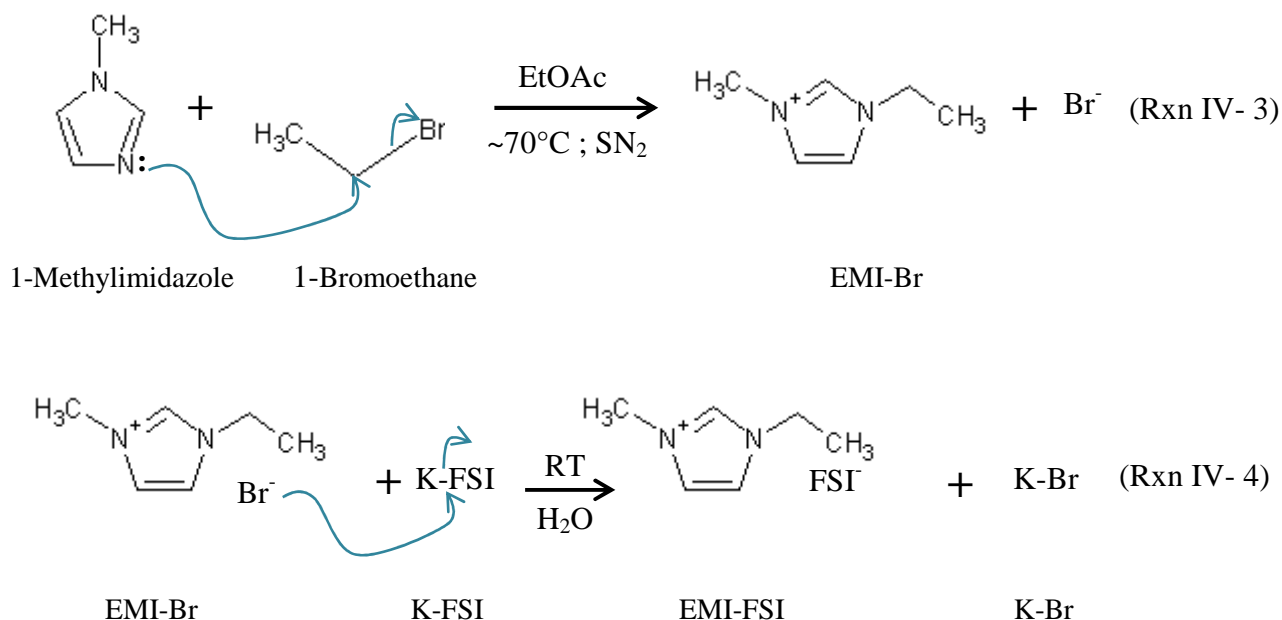
Table IV- 2: Physical properties of reactants for making EMI-FSI.

Reactants	T_B (°C)	T_M (°C)	T_f (°C)	M_w (g.mol^{-1})	CAS No.
1-Methylimidazole	198	-60	92	82.1	616-47-7
1-Bromoethane	38.4	-119	-20°C	108.97	74-96-4
Ethylacetate	77.1	−83.6	-4	88.11	141-78-6
K-FSI	-	145	-	219.23	14984-76-0

A solution of K-FSI in deionized water is then poured into the dissolved EMI-Br under vigorous mechanical agitation for anionic exchange at room temperature. A two-phase liquid

is can then be observed, with the aqueous phase consisting of K-Br (hydrophilic) and water, while the non-aqueous phase is the desired EMI-FSI ionic liquid. The aqueous phase is then decanted from the ionic liquid using a separating funnel. EMI-FSI is then thoroughly washed with deionized water until the decanted aqueous phase show negative result for halide test with $AgNO_3$. The product is then dried under vacuum overnight at $50 - 70$ °C. Quality test for water content is then carried out using karl-fischer to know if further drying is required and drying continues until water content of less than 20 ppm is obtained. The product is then sent for ion chromatography test for halide contents. Washings are repeated when halide contents exceeded 50 ppm and the consequent drying procedures mentioned are followed. The IL is now ready for electrochemical applications.

Conductivities usually increase by a factor of two upon the substitution of TFSI⁻ with FSI⁻ anions (Measured conductivities of: EMI-TFSI$_{Neat}$ = 8.6 mS.cm^{-1}; EMI-FSI$_{Neat}$ = 15.4 mS.cm^{-1}). In 2 M solutions of acetonitrile, they have conductivities of 46.7 mS.cm^{-1} and 54.7 mS.cm^{-1} respectively; hence it is of great interest to explore cations-FSI combinations. CME has been proven precedentially, to be a fast technique to check the compatibility of an electrolyte/carbon pair without any binder. On this account, the aim of this experiment was on one hand, to explore the FSI⁻ ion, and on the other hand, to study the ion-sieving effect of this electrolyte with different pore sizes.
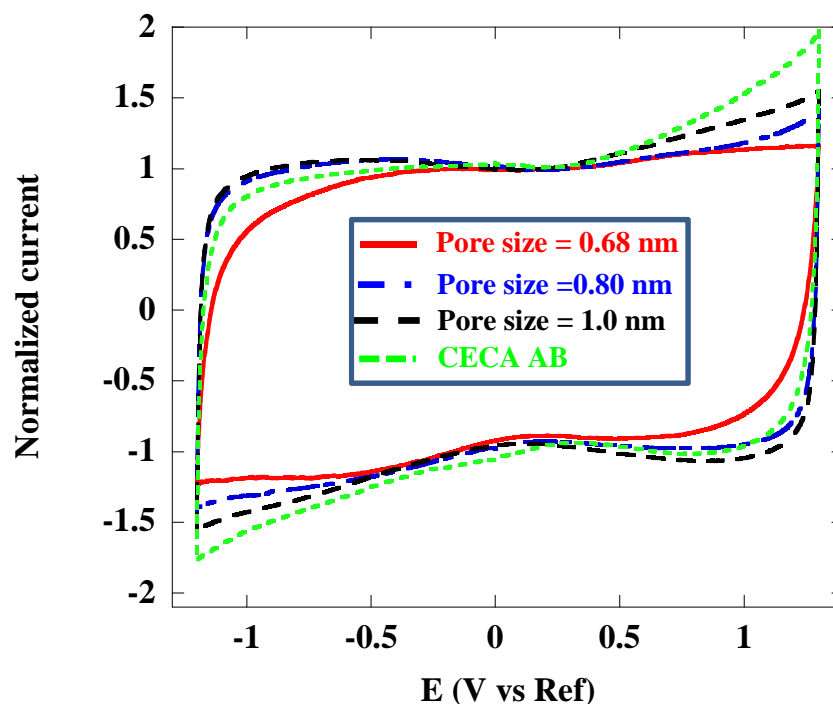
Figure IV- 27: Normalized CV for all four samples in 2 M EMI-FSI in AN at 100 mV.s^{-1}.

CVs tested using the CME technique were recorded at 100 mV.s^{-1} within the same electrochemical window (2.5 V) as that of EMI-TFSI, and overlaid in Figure IV- 27. Ti-CDCs synthesized at 500 (0.68 nm), 800 (0.8 nm) and 900 °C (1 nm) were used. A commercial carbon, CECA AB, was also used as a standard with a more varied pore distribution compared to Ti-CDCs. As explained, above OCV of ~0.2 V/Ref, adsorption of FSI$^-$ ions takes place and below which, the EMI$^+$ ions are adsorbed. Whilst there is the same slight deviation from the rectangular standard at negative potential range of CV profile of the smallest pore size (0.68 nm), the effective ion size of EMI$^+$ is still consistent with values reported using 2 M EMI-TFSI/AN, there is no significant distortions observed in EMI-FSI/AN for the 0.68 nm pore size Ti-CDC, in contrast to EMI-TFSI/AN reported in Figure IV- 22. Distortions in EMI-TFSI/AN were observed in the smaller pore sizes of 0.68 and 0.74 nm, the normalized current decreased from ~0.7 V/Ref to 1.3 V/Ref.

These CVs collected in EMI-FSI/AN display the concurrence of improved capacitance behaviour on optimization of pore size for the electrolyte ions. The absence of severe distortions means that the FSI$^-$ ions, being smaller, are able to be adsorbed without the dominance of steric effect, contributing to an improved capacitive behaviour at smaller pore size at positive potential. Hereby, the effective ion size of the FSI$^-$ ion in this electrolyte is smaller or equal to 0.68 nm.

Conceptualization of the results obtained with solvated electrolytes, EMI-TFSI and EMI-FSI in Acetonitrile

The schematics of ions adsorption in the three main ranges of pore sizes namely, micropores, mesopores and macropores are shown in Figure IV- 28, under solvated conditions (a, b and c).
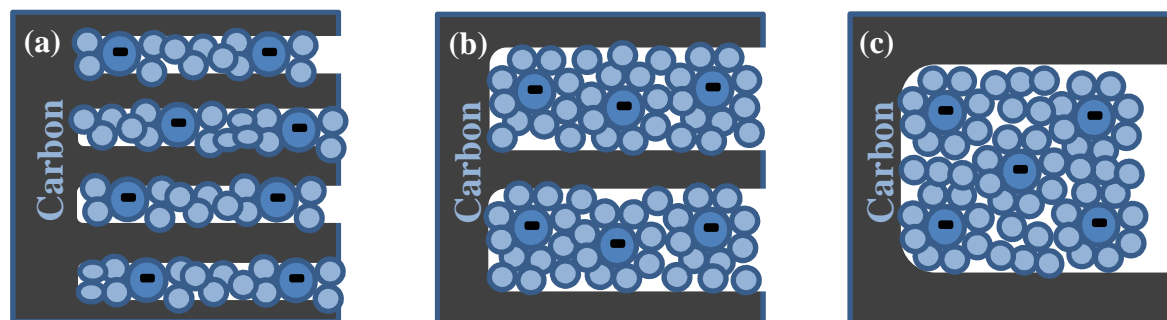
Figure IV- 28: Schematic of adsorption of ions in carbon of micropores (**a**), mesopores (**b**) and macropores (**c**) in solvated liquid salt.

Owing to the advantage of the ability to tune the pore sizes of the active material, capacitance values were increased by 30 % (~130 F.g^{-1}) as compared to using commercial activated carbon (100 F.g^{-1} [19]) in solvated situation. Such fine-tuned pores allows just enough space for one effective electrolyte ion size across the pore diameter, thereby reducing 'd' value in Eq IV-7, and consequently bring out about the increase in capacitance.

In the presence of solvent molecules, the situations become more complicated as it involves taking into account the solvation shells, which often depends on the ions' affinities to the solvent molecules. That is, every combination of salt and solvent could give very different results, leading to various energies demanded in order to remove the solvent molecules so that the ions can enter the small pores.

Cavity microelectrode study made on 2 M EMI-TFSI/AN not only affirmed results on the effective pore sizes of the partially desolvated electrolyte ions in support of results obtained from 4 cm^2 electrode cells, but the CVs obtained also gave other valuable information and insights by simple and fast experiment preparation. As such, by replacing the TFSI$^-$ anion with a smaller FSI$^-$ anion in the AN-based electrolyte, the effects of ion-sieving are still prominently observed for the EMI$^+$ ions but not for the FSI$^-$ anions. This observation is in line with our previous findings [1, 2, 3, 24], confirming good capacitive behaviour can be achieved when pore sizes are tuned to the effective size of the adsorbing ions. The smaller ion

could bring about a higher energy density as more ions could be adsorbed in a carbon with higher pore density due to smaller pore sizes required.

IV. Conclusions

This work demonstrates that optimizing the EDL capacitor systems for high capacity depends on both the carbon electrodes' pore design and the molecular dimensions of the electrolyte without solvent. The capacitance increase in pores less than 1 nm has been ascertained in this chapter by using solvent-less electrolyte, EMI-TFSI. This finding indeed has strongly overturned the old traditional belief that the mesoporous materials gave the best capacitance values, where pores have to be large enough to accommodate the ion and its solvation shell intact [31]. Here, we have addressed the issue of solvation shells that was speculated to be important in the contribution of the capacitance by using an electrolyte without any solvation shells. The capacitance maxima for the EMI^+ ions at 0.74 nm and $TFSI^-$ ions at 0.72 nm is in good agreement with the average cell capacitance (0.72 nm) registered in previous work [1]. Hence, this has further confirmed the double layer concept of matching pore size to ion size definitively. These results have established a new ground-breaking concept of the double layer in which huge increase in capacitance values are observed in microporous material with well-controlled pore size distribution. Results also displayed the capacitance distinguished from the individual electrodes for the first time, (in a 3-electrode cell configuration) which have further affirmed this correlation of matching pore size to ion size for the anomalous increase in capacitance for micropores carbons. In this chapter, the use of ionic liquids have also enabled better energy density due to the smaller ion size (without its solvation shells) and fitting pore size despite their main drawback of having high ionic resistance.

CME does save a lot of time for preliminary understanding of a system by providing a convenient mean for quick measurement of the correlation between the pore size for a variety of carbons, electrolytes and solvents. Whilst the CME technique can be easy to use, but due to the complicated solvation issues that have been ongoing in research, it can reach its limit in providing profound understanding. Lastly, modelling is an important technique complementary to the affirmation of these fruitful findings, aiding in the visualization of the charge storage mechanism, bringing us to a better level in understanding the electrochemical double layer in view to progress further in increasing capacitance through this ion-pore size optimization approach.

V. References

[1]   Largeot, C.; Portet, C.; Chmiola, J.; Taberna, P.-L.; Gogotsi, Y.; Simon, P. *Journal of the American Chemical Society,* **130** (2008) 2730-2731.

[2]   Chmiola, J.; Yushin, G.; Gogotsi, Y.; Portet, C.; Simon, P.; Taberna, P.-L. *Science* **313** (2006) 1760-1763.

[3]   Chmiola, J.; Largeot, C.; Taberna, P.-L.; Simon, P.; Gogotsi, Y. *Angewandte Chemie International Edition* **47** (2008),3392-3395.

[4]   Taberna, P.L.; Simon, P.; Fauvarque, J. F. *Journal of the Electrochemical Society* **150** (2003) A292-A300.

[5]   Qu, D.; Shi, H. *Journal of Power Sources* **74** (1998) 99-107.

[6]   Segalini, J; Daffos, B.; Taberna, P.L.; Gogotsi, Y.; Simon, P. *Electrochimica Acta* **55**, (2010) 7489–7494.

[7]   Keddam, M. ; Takenouti, H., Electrochemical Capacitors II, Delvick, F.M.; Ingersoll, D.; Andriev, X.; Naoi, K. Ed *The Electrochemical Society proceedings series: Pennington,* **NJ PV 96-25** (1996) 220.

[8]   Frichet, A. ; Gimenez, P. ; Keddam, M. *Electrochimica Acta* **38** (1993) 1957.

[9]   Guo, M.; Diao, P.; Tong, R.; *Journal of Chinese Chemical Society (Taipei)* **47** (2000) 1197.

[10]   Dash, R.; Chmiola, J.; Yushin, G.; Gogotsi, Y.; Laudisio, G.; Singer, J.; Fischer, J.; Kucheyev, S. *Carbon* 44 (2006) 2489.

[11]   Sato, T.; Masuda, G.; Takagi, K. *Electrochimica Acta* **49** *(*2004) 3603-3611.

[12]   Palmer, J.C.; Llobet A.; Yeon, S.-H.; Fischer, J.E.; Shi, Y.; Gogotsi, Y.; Gubbins, K.E. *Carbon* **48** (2010) 1116.

[13]   Guo, W. ; Guo, Y. *Physical Review Letters* **91** (2003) 115501.

[14]   (a) Jiang, D.; Jin, Z.; Wu, J. *Nano Letters,* **11** (2011) 5373–5377.
         (b) Feng, G.; Qiao, R.; Huang, J.; Sumpter, B.G.; Meunier, V. *Journal of Physical Chemistry C* **114** (2010) 18012–18016.

[15]   Lin, R. ; Huang, P. ; Ségalini, J. ; Largeot, C. ; Taberna, P.L. ; Chmiola, J. ; Gogotsi, Y. ; Simon, P. *Electrochimical Acta* **54** (2009) 7025-7032.

[16]   Pell, W.G; Conway, B.E.; Marincic, N. *Journal of Electroanalytical Chemistry* **491** (2000) 9–21.

[17]   Lazzari, M.; Soavi, F.; Mastragostino, M. *Journal of Power Sources* **178** (2008) 490–496.

[18]   Thamm, H. *Journal of. Physical Chemistry* **92** (1988) 193-196.

[19]   Portet, C; Taberna, P.L.; Simon, P.; Laberty-Robert, C. *Electrochimica Acta* **49** (2004) 905-912.

[20]   Eliad, L.; Salitra, G.; Soffer, A.; Aurbach, D. *Journal of Phyical Chemistry B* **105** (2001) 6880-6887.

[21]   Bard, A.J.; Faulkner, L.R. Electrochemical methods, fundamentals and applications, *Wiley editor, 2nd edition* (2001).

[22]   B.E. Conway, Electrochemical Supercapacitors: Scientific Fundamentals and Technological Applications, Kluwer, 1999.

[23]   Girault, H. Analytical and Physical Chemistry *EPFL editors* ISBN: 2-940222-03-7.

[24]   Lin, R.; Taberna, P.L.; Chmiola, J.; Guay, D.; Gogotsi, Y.; Simon, P. *Journal of the Electrochemical Society* **156** (2009) A7.

[25]   Mysyk, R.; Raymundo-Pinero, E.; Beguin, F. *Electrochemistry Communications* **11** (2009) 554.

[26]   Aurbach, D,; Levi, M.D.: Salitra, G.; Levy, N.; Pollak, E.; Muthu, J. *Journal of The Electrochemical Society* **155** (2008) A745.

[27] Dzubiella, J. ; Hansen, J. P. Journal of Chemical Physics **122** (2005) 234706.

[28] Wang, D.W.; Li, F.; Liu, M.; Lu, G.Q.; Cheng, H.M. *Journal of Physical Chemistry C* **112** (2008) 9950-9955.

[29] Bard, A.J.; Faulkner, L.R. Electrochemical Methods : Fundamental and applications *John Wiley & Sons* : *New York* (2001).

[30] Golding, J.J.; MacFarlane, D.R.; Spiccia, L.; Forsyth, M.; Skelton, B.W.; White, A.H. *Chemistry Communications* (1998) 1593-1594.

[31] Endo, M.; Maeda, T.; Takeda, T.; Kim, Y. J.; Koshiba, K.; Hara, H.; Dresselhaus, M. S. *Journal of the Electrochemical Society* **148** (2001) A910.

Chapter V:

Capacitive energy storage in extended temperature range using an ionic liquid mixture electrolyte

I. Introduction

Operation temperatures of supercapacitors below -60 °C have been reported by using carbon electrodes in NEt_4BF_4/AN mixed with various proportions of co-solvents with low boiling points such as methyl formate, methyl acetate, or 1,3-dioxolane [1]. An AN-based electrolyte limits its operation in the temperature range of -40 °C to 70 °C due to the boiling point of AN at 80 °C. Due to the low flash point of AN at 5 °C, PC has been used as its replacement. However a PC-based electrolyte restricts the operating temperature further from -25 °C to 70 °C, with limited power arising from its lower ionic conductivity compared to AN-based systems.

Room Temperature Ionic liquids (RTILs) with their commendable electrochemical properties (as discussed in chapter I), have thus been studied as potential and promising alternative electrolytes over their organic-based counterparts in electrochemical energy storage devices. Despite intensive research using RTILs, they are still not widely implemented in ECs or batteries. This is largely blamed on drawbacks owing to their high viscosities and melting points near room temperatures, limiting their applications to high temperatures (T > 50 °C). Although some ILs consists of sub-zero temperatures [2], the low ionic mobility in these ILs effectively impede their roles as electrolytes at sub-zero temperatures due to high ESR values arising from difficulty in accessing and wetting porous structured ACs. Current reports in the literature have mostly been on the performances of RTILs at elevated temperatures at 60 °C or higher [3,4,5] and there has been no report found in the literature that demonstrates the use of RTILs that could operate in temperature ranges wider than those offered by organic-based electrolytes.

In the precedent chapters, the adaption of the porous electrode to the effective sizes of the electrolyte ions has been shown to have a great impact on the capacitive behaviour in EDLCs. Hence it is important to optimize the electrode/electrolyte interface such that they conform well to each other. Tailoring the carbon structure, specific surface area, pore size, and pore size distribution is important for improving EC performance, and examples include composites of carbon nanotubes (CNTs) and activated carbon [6], self-assembled CNT on graphene [7], or activated cup-stacked CNT electrodes [8]. However, device performance is not solely determined by the electrode material but by the behaviour and properties of the electrical double layer, and, thus, it is the electrode/electrolyte combination [9,10] that finally defines cycle lifetime, capacitance, usable voltage window, and charge/discharge rate.

In this chapter, a demonstration of a dramatic expansion of the operation temperature range for supercapacitor electrodes will be elaborated. This was in conjunction with the concoction and utilization of an IL mixture with a substantially low melting point (lower than its constituents) combined with the use of exohedral carbon nanomaterials.

# II-Concocting of an electrolyte applicable under a wide temperature range

Since the electrolyte characteristics are largely affected by anion/cation pair, selection of functional groups of the electrolyte constituents is crucial in obtaining the desired improved concoction.

II-1. Choice of anion

Amongst popular anions such as hexafluorophosphate (PF_6^-), tetrafluoroborate (BF_4^-), bis(trifluorosulfonyl)imide ($TFSI^-$) and bis(fluorosulfonyl)imide (FSI^-) anions, the imides ($TFSI^-$ and FSI^-) have been increasingly being used as alternatives to the PF_6^- and BF_4^- anions due to the susceptibility to hydrolysis for PF_6^- and BF_4^- anions, leading to the production of hydrogen fluoride [11,12,13,14,15]. HF evolution is toxic and could tremendously affect electrode stability, and eventually cycling life and efficiency of a supercapacitor. Therefore the more hydrophobic $TFSI^-$ and FSI^- anions are thus seemingly being more studied as electrolytes for energy storage [16,17,18]. The FSI^- ion has been selected to be the anion for the electrolyte formula due to its generally higher conductivity (lower viscosity) as compared to the $TFSI^-$ ion when paired with the same cation [19] because of the smaller size and hence higher mobility of the FSI^- ion.

II-2. Choice of cations

The choice of the cations was by means of comparing their stability. The electrochemical stability of commonly used cations of ionic liquids are usually in the order of Ammonium ≈ Piperidinium ≥ Pyrrolidinium > Imidazolium [20]. Although the imidazolium-based ILs offers higher conductivity values over other cationic functional groups when paired with the same anion, the instability of imidazole ring renders it susceptible to low cathodic limit through the proposed scheme (Rxn V-1) [21]:
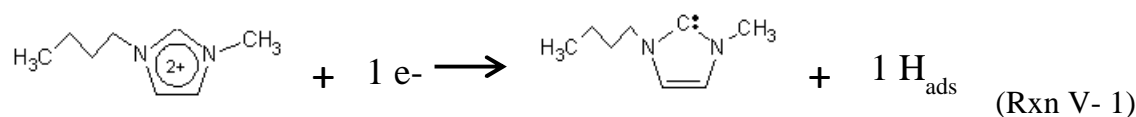
(Rxn V- 1)

Rxn V-1 shows the proposed scheme of the electrochemical reduction mechanism of 1-n-butyl-3-methyl-imidazolium trifluoroacetate. Hence, cations with functional groups of pyrrolidium (PYR) and piperidinium (PIP) with relatively higher electrochemical stability were explored.

II-3. Synthesis of ionic liquids, (PYR$_{14}$-FSI and PIP$_{13}$-FSI)

N-methyl-N-butylpyrrolidinium bis(fluorosulfonyl)imide (PYR$_{14}$-FSI)

As mentioned in Chapter II, the cation, N-methyl-N-butylpyrrolidinium, (PYR$_{14}^+$) is first produced by preparing its halide salt through quaternization. The chemical reaction for quarternization of methyl-pyrrolidine by 1-bromobutane to yield its halide salt, PYR$_{14}$-Br as shown in Rxn V-2:

N-Methylpyrrolidine   1-Bromobutane   PYR$_{14}$-Br
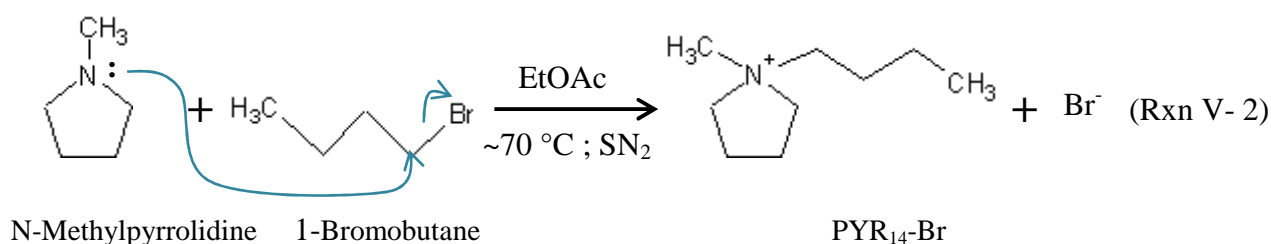
Physical properties of the reactants for the synthesis of PYR$_{14}$-FSI are tabulated in Table V- 1. The boiling temperatures of the reactants are important in starting the reaction to avoid non-stoichiometry in the reaction and as well as their decomposition.

Table V- 1: Physical properties of reactants for making PYR$_{14}$-FSI.

Reactants	T$_B$ (°C)	T$_M$ (°C)	T$_f$ (°C)	M$_w$ (g.mol^{-1})	CAS No.
N-Methylpyrrolidine	76-81	-90	-21	85.15	120-94-5
1-Bromobutane	101.4	-112	10°C	137.02	109-65-9
Ethylacetate	77.1	−83.6	-4	88.11	141-78-6
KFSI	-	145	-	219.23	14984-76-0

The experimental set-up comprising of a heating plate, a 3-neck round bottom flask fitted with a thermometer, condenser and a dropping funnel with pressure balance to the 3

necks as shown in Figure V- 1, the condenser is then connected to a bubble counter. The set-up is purged with nitrogen continuously for one hour while heating before introducing the reactants into the apparatus. This step is important to eliminate any water or contaminants that could lead to side reactions, thereby affecting the quality and the yield of the resulting halide salt.
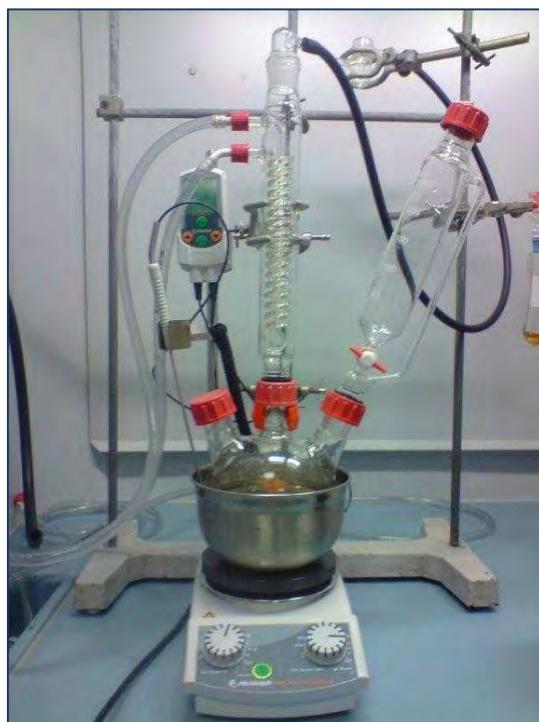
Figure V- 1: Experimental set-up of the synthesis of PYR_{14}-Br.

N-methylpyrrolidine is first introduced into the round bottom flask as it has a lower temperature than 1-bromobutane. The amine is then heated to under its boiling point (~65 – 70 °C) under constant stirring. Besides, haloalkane are often sensitive to heat and light, and hence it is usually added to the heated amine when the temperature is stable at ~65 °C. An excess of 1-bromobutane is then added dropwise to the heated amine from the dropping funnel, under constant stirring while the temperature is constantly being monitored. The rate of addition is then adjusted according to the temperature change. As this reaction is exothermic, temperature regulation is very important to keep the reaction under control, without decomposing the reactants. Reaction is initiated when the mixture turns turbid, and reaction temperature is always kept below the melting point of the N-methylpyrrolidine even after all the 1-bromobutane has been completely added. The temperature is then increased to ~70 °C when the mixture is mostly cloudy, indicating the constant formation of PYR_{14}-Br. Ethylacetate is then added to facilitate stirring and dispersing the products and allowing

unreacted reactants to come together since PYR_{14}-Br is a solid and is not soluble in the solvent. The reaction is then left for a few hours for reaction to be completed with close monitoring of the temperature.

The PYR_{14}-Br obtained is then constantly being rinsed with ethylacetate to remove the unreacted reactants until the decanted solvent is not tainted with colour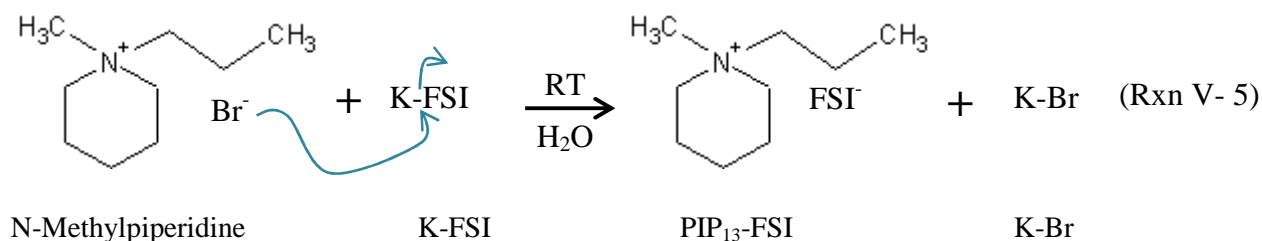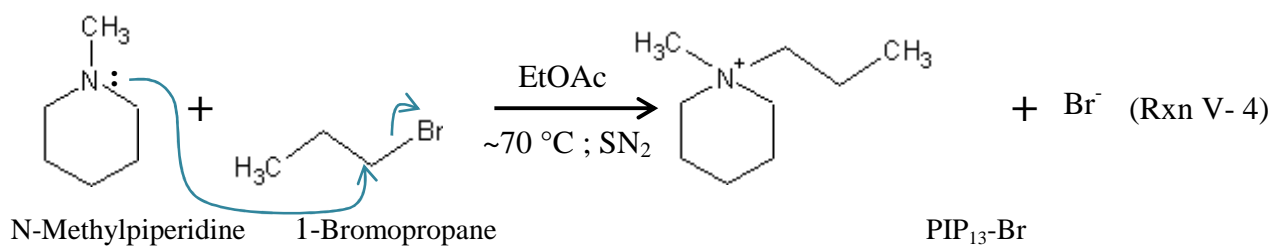s of the reactants. Following this, the solid halide is then dried under vacuum to remove the solvent. Deionized water is added to dissolve PYR_{14}-Br at room temperature and activated charcoal is introduced to remove further impurities at elevated temperatures (~70 to 80 °C) for at least 24 hours. After filtrating off the activated carbon, PYR_{14}-Br in solution is ready for metathesis as shown in Rxn V-3:

| N-Methylpyrrolidine | K-FSI | PYR_{14}-FSI | K-Br |
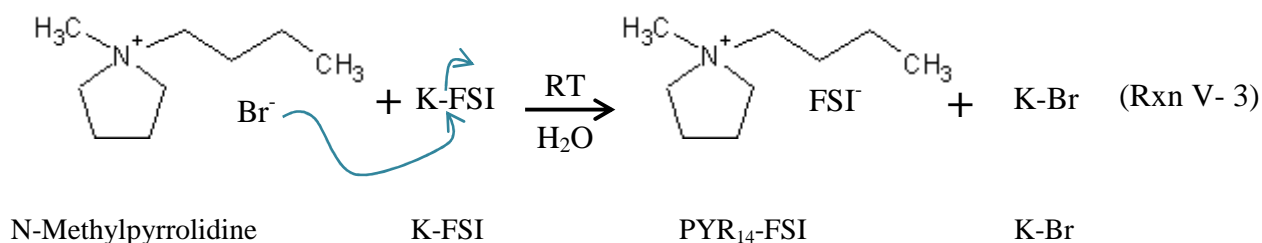
A solution of K-FSI in deionized water is then poured into the dissolved PYR_{14}-Br under vigorous mechanical agitation for anionic exchange. A two-phase liquid is can then be observed, with the aqueous phase consisting of K-Br (hydrophilic) and water, while the non-aqueous phase is the desired PYR_{14}-FSI ionic liquid. The aqueous phase is then decanted from the ionic liquid using a separating funnel. PYR_{14}-FSI is then thoroughly washed with deionized water until the decanted aqueous phase show negative result for halide test with $AgNO_3$. The product is then dried under vacuum at 50 °C for the first 2 hours and followed by at 70 °C overnight. Quality test for water content is then carried out using karl-fischer to know if further drying is required and drying continues until water content of less than 20 ppm is obtained. The product is then sent for ion chromatography test for halide contents. Washings are repeated when halide contents exceeded 50 ppm and the consequent drying procedures mentioned are followed. The IL is now ready for electrochemical applications.

N-methyl-N-propylpiperinidium bis(fluorosulfonyl)imide (PIP_{13}-FSI)

The chemical reaction for quarternization of N-methylpiperidine by 1-bromopropane to yield its halide salt, PIP_{13}-Br and metathesis for the product PIP_{13}-FSI are shown in Rxn V-4 and Rxn V-5 respectively:

$$\text{N-Methylpiperidine} \quad \text{1-Bromopropane} \xrightarrow[\sim 70\,°C\;;\; SN_2]{EtOAc} \text{PIP}_{13}\text{-Br} + Br^- \quad (\text{Rxn V- 4})$$

$$\text{N-Methylpiperidine} + \text{K-FSI} \xrightarrow[H_2O]{RT} \text{PIP}_{13}\text{-FSI} + \text{K-Br} \quad (\text{Rxn V- 5})$$

Reactants	T_B (°C)	T_M (°C)	T_f (°C)	M_w	CAS No.
N-Methylpiperidine	105-108	-50	3	99.17	626-67-5
1-Bromopropane	71	-108	22	122.99	106-94-5
Ethylacetate	77.1	−83.6	-4	88.11	141-78-6
KFSI	-	145	-	219.23	14984-76-0

The experimental set-up and preparation for the synthesis of PIP_{13}-FSI is similar to that shown in Figure V- 1, except for the reactants. N-Methylpiperidine is being contained in the round-bottom flask while 1-Bromopropane in the dropping funnel. Like the previous synthesis, N-methylpiperidine is being heated to ~65 °C prior to the addition of 1-Bromopropane. Despite the higher boiling point of the amine in this synthesis, the starting temperature is kept low as amine can be easily tainted with yellow at high temperature. The procedure follows with the addition of ethylacetate after all the 1-Bromopropane has been added into the round-bottom flask and when the reaction is seen to be stable (observation of precipitate in the mixture). The temperature is then increased to 70 °C and left for a few hours under agitation for the reaction to be completed. The subsequent procedures of washing the PIP13-Br salt, purifying it by activated charcoal, metathesis as shown in Rnx V-5 (anion exchange), washing and drying follow that of the synthesis of PYR_{14}-FSI previously described and the eventual product of PIP_{13}-FSI has been obtained.

II-4. Characterization of the synthesized ionic liquids and their mixtures

In order to obtain an extended liquidus range and yet preserve the electrochemical properties of both PYR and PIP functional groups, both constituent ILs were designed to have exactly the same anion (FSI), same molecular weight, and same number of atoms of the same nature, and the only difference is their cation molecular structure, based on a six-member or five-member heterocycle, respectively, for piperidinium cation and pyrrolidinium cation. Hence, this is the reason for the selection of methy + propyl substituent groups (total of 4 carbons on side chains) for synthesizing the PIP-based cation (I) and methyl + butyl substituent groups (total of 5 carbons on side chains) for synthesizing the PYR-based cation (II), (molecular structures shown in Figure V-2). This approach is based on the idea of maintaining similar intermolecular interactions for sake of miscibility due to the similar constituent atoms of the two cations, while increasing disorder between them, in the aim of increasing difficulty in lattice forming and hence lowering the melting point.

An eutectic mixture composed of (1:1 by weight or molar ratio) N-methyl-N-propylpiperidinium bis(fluorosulfonyl)imide (PIP$_{13}$-FSI) and N-butyl-N-methylpyrrolidinium bis(fluorosulfonyl)imide (PYR$_{14}$-FSI) was formulated and used as electrolyte. Each constituent IL of this mixture shows near room-temperature melting point of 6 °C (PIP$_{13}$-FSI) and -18 °C (PYR$_{14}$-FSI) (Figure V-2). The latter is consistent with reported data [22]. The liquid state of the designed IL eutectic mixture (III) can be maintained several tens of degrees lower compared to the constituent ILs when measured individually as shown in Figure V-2.
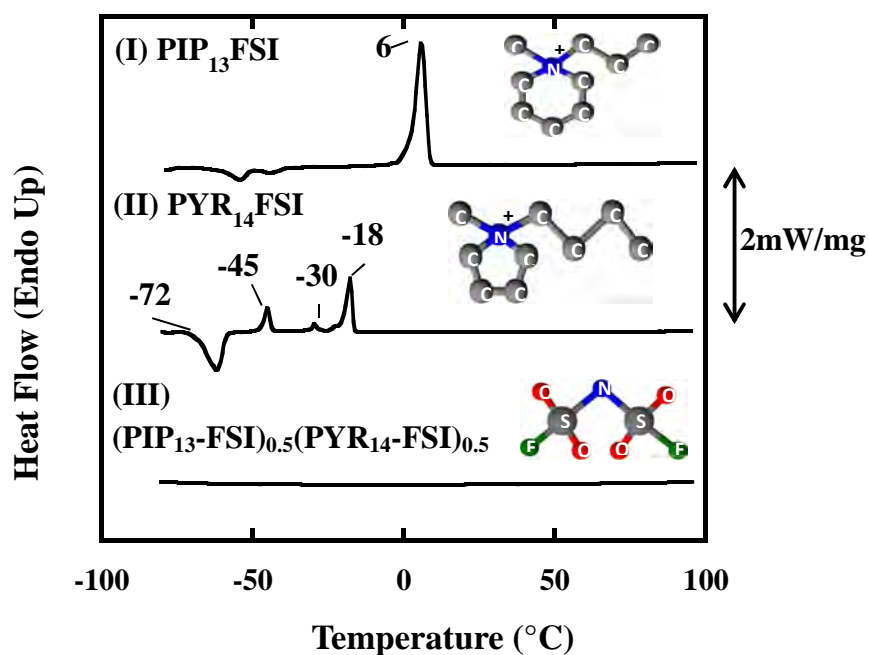
Figure V-2: DSC profiles of **(I)** PIP$_{13}$-FSI, **(II)** PYR$_{14}$-FSI and **(III)** (PIP$_{13}$-FSI)$_{0.5}$(PYR$_{14}$-FSI)$_{0.5}$ mixture, and their chemical structures (I) PIP$_{13}^+$, (II) PYR$_{14}^+$ and (III) FSI$^-$.

Mixing PIP$_{13}$-FSI (I) with PYR$_{14}$-FSI (II) resulted in an IL with two different cationic species and only one anion (namely, (PIP$_{13}$-FSI)$_{0.5}$(PYR$_{14}$-FSI)$_{0.5}$), which possess a liquid range lowered to -80 °C, which was the lowest measurable value with our apparatus. The DSC curve of the mixture (III) displays no peaks between -80 and 100 °C, without any presence of first- or second-order phase transitions in this temperature range. This confirms previously published studies on mixtures with common cations and anions that show that the crystallization process is mainly influenced by the anions [19, 22]. Our results demonstrate that selection of a proper combination of cations with the same anion prevents an ordered arrangement in the liquid, thereby inhibiting the formation of a lattice and hence hinders crystallization. A similar behaviour is observed for another cationic mixture of ILs using the same approach of maintaining the same number of atoms of the same nature using PYR$_{14}$-FSI and PYR$_{23}$-FSI as shown in Figure V- 3.
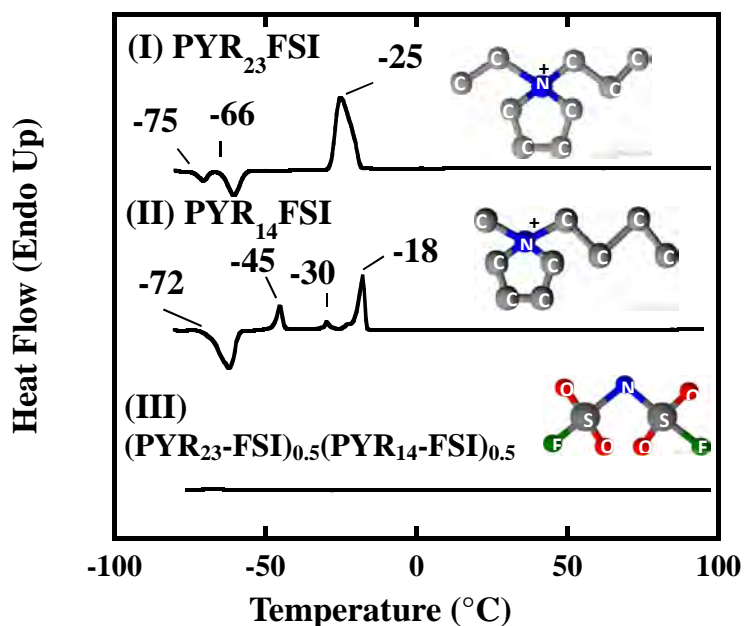
Figure V- 3: DSC profiles of **(I)** PYR$_{23}$-FSI, **(II)** PYR$_{14}$-FSI and **(III)** (PYR$_{23}$-FSI)$_{0.5}$(PYR$_{14}$-FSI)$_{0.5}$ mixture, and their chemical structures (I) PYR$_{23}^{+}$, (II) PYR$_{14}^{+}$ and (III) FSI^{-}.

As discussed above that the functional group of piperidinum has a higher electrochemical window than pyrrolidinium, the first mixture, (PIP$_{13}$-FSI)$_{0.5}$(PYR$_{14}$-FSI)$_{0.5}$ was used more extensively as the testing electrolyte for application in supercapacitors, although some electrochemical characterization using the second IL mixture, (PYR$_{23}$-FSI)$_{0.5}$(PYR$_{14}$-FSI)$_{0.5}$, will be shown in the later section.

Figure V- 4 depicts the Arrhenius plots of the PIP$_{13}$-FSI, the PYR$_{14}$-FSI, and the 1:1 IL mixture, (PIP$_{13}$-FSI)$_{0.5}$(PYR$_{14}$-FSI)$_{0.5}$. Conductivity values of 28.9 mS.cm^{-1} and 4.9 mS.cm^{-1} were measured at 100 and 20 °C, respectively, for the mixture.
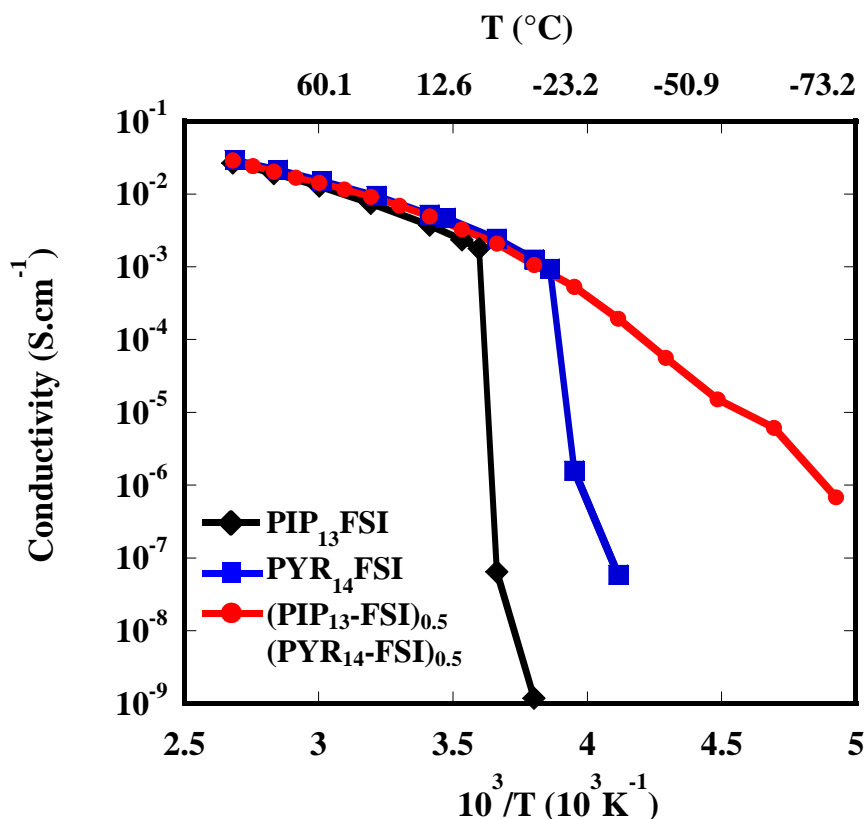
Figure V- 4: Change of the conductivity versus the inverse temperature for PIP_{13}-FSI, PYR_{14}-FSI and $(PIP_{13}$-FSI$)_{0.5}(PYR_{14}$-FSI$)_{0.5}$ ionic liquid mixture.

This clearly shows the extended temperature range of ionic conductivity of the $(PIP_{13}$-FSI$)_{0.5}(PYR_{14}$-FSI$)_{0.5}$ mixture compared to the single constituents, thus enabling its operation at temperatures as low as -50 °C; however, devices operating at such low temperatures are expected to suffer from a reduced rate capability whereas device operation under normal conditions will remain unaffected.

Table V- 2: Electrochemical and physical properties of the electrolyte and its constituents.

Ionic Liquids	Electrochemical Window (V)			Conductivity @ 20 °C $(mS.cm^{-1})$
	0.05 mA.cm^{-2}	0.1 mA.cm^{-2}	1 mA.cm^{-2}	
PYR_{14}-FSI	4.86	5.25	5.70	6.9
PIP_{13}-FSI	5.39	5.48	5.83	4.3
$(PIP_{13}$-FSI$)_{0.5}(PYR_{14}$-FSI$)_{0.5}$	5.23	5.39	5.79	5.7

III. Implementation of electrolyte in carbon electrodes for supercapacitor application in extended temperature range

III-1. Porous carbon electrodes

Using this eutectic IL mixture as the electrolyte in a supercapacitor cell assembled using a conventional high surface area porous activated carbon (1700 $m^2.g^{-1}$) as active material as shown in Figure V- 5, resulted in very poor electrochemical performance below 0 °C. The carbon electrode weight is 5.5 $g.cm^{-2}$. Cyclic voltammograms (CVs) collected by charging the cell to 3 V showed highly resistive behaviour resulting from poor accessibility of carbon pores to the ions.
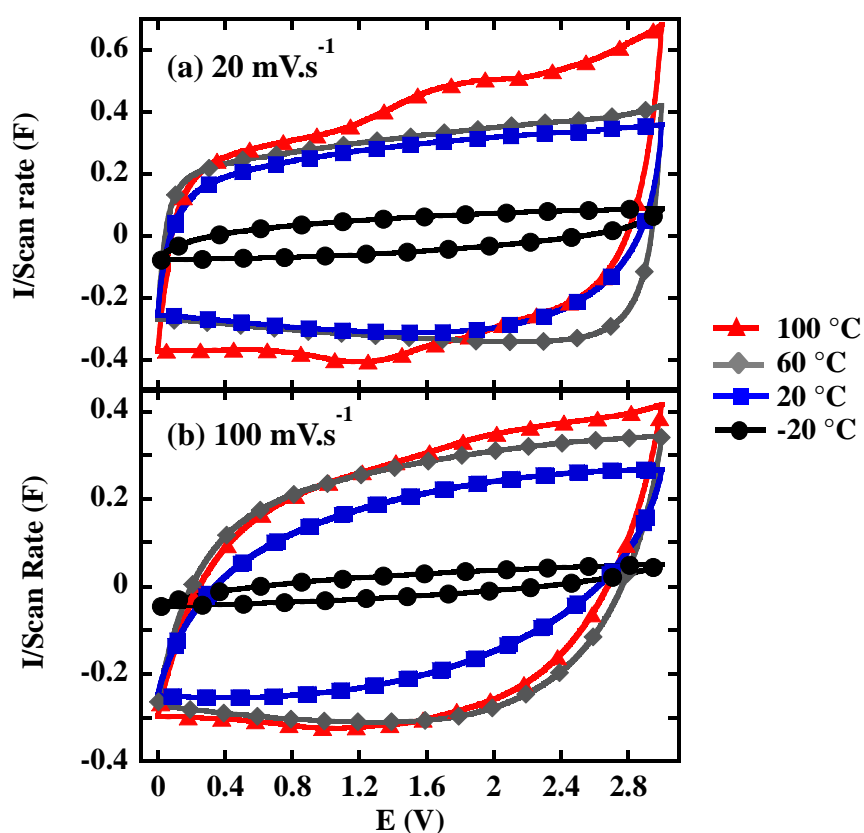
Figure V- 5: Cyclic voltammograms of a 2-electrode cell assembled with activated carbon electrodes (YP17 from Kuraray Company) at 20 $mV.s^{-1}$ **(a)** and 100 $mV.s^{-1}$ **(b)**; Electrolyte: $(PIP_{13}\text{-}FSI)_{0.5}(PYR_{14}\text{-}FSI)_{0.5}$; Electrode weight = 5.5 $mg.cm^{-2}$.

The CV profiles depict the poor performance of the IL mixture electrolyte when used in combination with a conventional porous carbon at sub-zero temperatures. This infers that the carbon/electrolyte interface must be specifically designed to match the properties of the electrolyte and to cater to the need of increasing accessibility of the electrolyte ions to the

electrode surface. Figure V- 5 provides evidence that the electrode structure must be tailored to match the electrolyte if capacitive performance at low temperatures is desired.

III-2. Exohedral carbon electrodes

In order to address ion transport limitations in nanometric pores of activated carbons, exohedral carbons, namely Onion-Like Carbons (OLCs) [23] and Vertically Aligned – multiwall carbon nanotubes (VA-CNTs) [24] with open structured electrodes were explored. Electron microscopic images of OLCs and VA-CNTs are presented in Figure V- 6.

Figure V- 6: High-surface area exohedral electrode materials that only adsorb ions on their outer surface. HRTEM image of onion-like structured carbon [23] **(a)** SEM image of the CNT electrode **(b)**, SEM image of CNT brush [36]**(c)**, and TEM image of individual CNTs [36] **(d)**.

As their external surface can be fully accessed by the ions, exohedral carbon nanomaterials can therefore overcome ion transfer limitations, depending on their size and curvature, to provide a way to increase the capacitance per unit of surface area [25]. Thus, the formation of the electrical double layer occurs exclusively on the outer surface of carbon

nanoparticles and the process of ion adsorption/desorption on the surface replaces the process of ion transport into internal pore of carbon particles as the rate controlling mechanism as shown in the schematics of OLCs and CNTs respectively (Figure V- 7a and b).

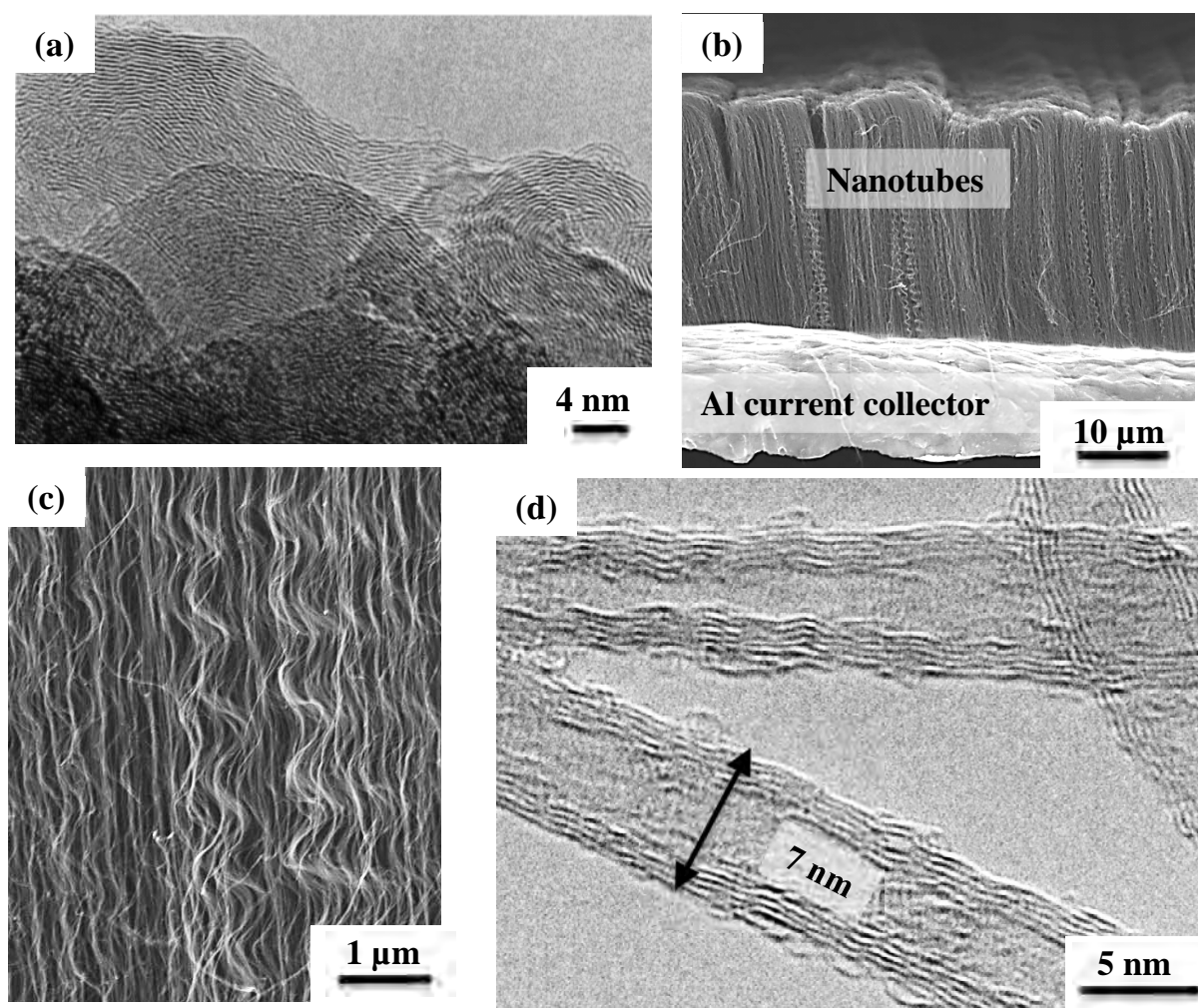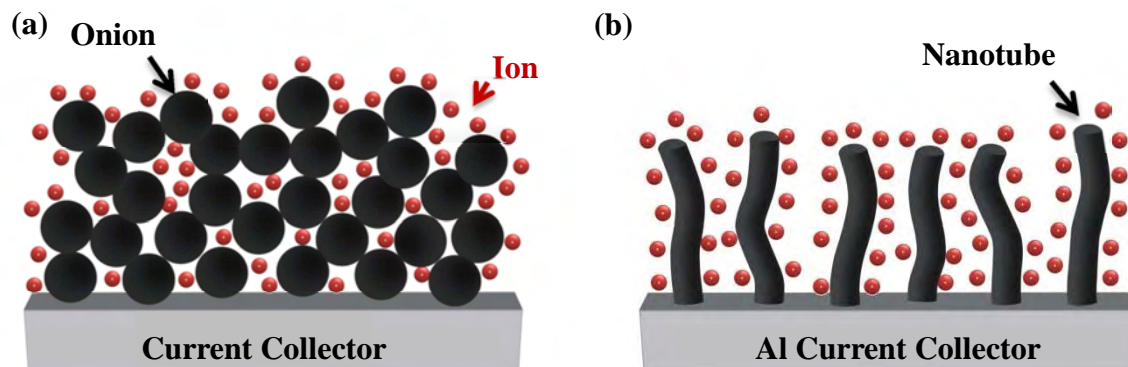**Figure V- 7**: High-surface area exohedral electrode materials that only adsorb ions on their outer surface. Schematic of a carbon onion electrode **(a).** Schematic of a CNT electrode **(b)**.

By using onion-like carbon (OLC) and the CNTs (Figure V- 7a and b), the concepts and approaches towards designing next-generation supercapacitors with improved temperature range and a widened voltage window will be illustrated and discussed in the following sections.

Onion- like carbons (OLCs) - were derived from detonation of nanodiamond UD -50 (diamond soot) supplied by NanoBlox, Inc. (USA). Approximately 5 nm in average particle size, 25-30 % of the powders consisted of sp^3 carbons. OLCs were formed by the annealing of nanodiamond at 1200 to 2000 °C for a duration of 3 hours in a furnace equipped with graphite heating elements (Solar Atmospheres, Lansdale, USA) under a vacuum ($\sim 10^{-5}$ to 10^{-6} torr) [26]. OLCs can be visualized as multishell fullerenes with concentric graphitic shells and the OLC electrodes consist of agglomerated nonporous particles ($\sim$5 nm) with a specific surface area of approximately 500 $m^2.g^{-1}$. Their synthesis [27] and application as electrodes in supercapacitors at up to 100 $V.s^{-1}$ charge/ discharge rates [28] have been reported elsewhere. In order to obtain mechanically stable electrodes with $\sim$200 μm thickness, OLC was mixed with 5 wt % polytetrafluoroethylene (PTFE) [24] and OLC loading was maintained at 5.5 $mg.cm^{-2}$ (unless another weight is specified).

CNTs - The Vertically Aligned Carbon NanoTubes (VA-CNTs) were grown directly and supported by 10 µm thick aluminium foil as substrate. The preparation of these substrates began by coating 3 nm of iron using physical vapor deposition (PVD). The iron acts as a catalyst for CNT growth. Synthesis of the VA-CNTs was carried out in an AIXTRON Black Magic PECVD CNT growth system (cold wall reactor) using 50:700 sccm of acetylene (C_2H_2): hydrogen (H_2) for 5 minutes at 500 °C. The swatches of CNT were produced with a carbon loading of 0.25 mg.cm^{-2} were 2x2 cm^2. This technique allows the preparation of the supercapacitor electrodes in one step, as the supporting thin Al foil serves directly as a current collector in a supercapacitor cell. Low-temperature CVD synthesis allows direct CNT growth on Al, which is a major advantage given the consideration that other technologies require high temperatures. Such high temperatures limit the substrate choice to much heavier metals such as Ti, Ni, or steel, which also have lower electrical conductivity and narrower voltage stability windows [29,30,31].

The resulting CNT density allows easy electrolyte access (Figure V- 6b). These obtained homogeneous CNT films in terms of thickness and tube density, with the average inter-tube distance varying between tens and hundreds of nanometres (Figure V- 6c), is typical for such grown nanotubes [32]. The CNT diameters ranged between 5 and 10 nm with 4-7 carbon walls (Figure V- 6d). While there was a small residual amount of the iron catalyst (< 0.5 wt % and < 0.05 wt % versus carbon and Al substrate weight respectively), no binder or additive was required in manufacturing these electrodes. Such binder-free electrodes, with improved contact between the active material and the Al current collector, have a lower equivalent series resistance (ESR) and can be used at higher rates compared to binder-containing pressed powder electrodes [33,34]. CNT electrodes of 1.1 cm^2 were cut from AIXTRON electrodes. Both types of materials were tested in Swagelok® cells [35] using two layers of a 25 µm thick porous alumina separator as described in further details in Chapter II.

III-3. Electrochemical behaviour of IL mixture in exohedral carbons

Electrochemical characterization of OLCs and VA-CNTs has been performed in a two-electrode setup under the same temperature conditions.

Current Collectors

Stainless steel bars of the Swagelok® cell set up in Figure II-7 (Chapter II) were the current collectors.

Active Material

Onion-like Carbons (OLCs), Vertically-aligned Carbon nanotubes (VA-CNTs), activated graphene and YP 17 commercial activated carbon were used in this study. Both OLCs and YP 17 powders were made into electrode films with 5 wt % of PTFE as binder, with a thickness of about 200 µm. VA-CNTs and graphene [36] were used as received. All electrodes were cut in a disc shape with a diameter of 12 mm (Area = 1.13 cm²).

Separator

Two layers of 25 µm thick porous Al_2O_3 separator (Separion®, average pore size of 240 nm, > 40% porosity, Evonik Industires, Germany)

Electrolytes and conditions used

Pure ionic liquids of PYR_{23} – FSI and PYR_{14} – FSI, eutectic mixtures of, $(PYR_{14}\text{-}FSI)_{0.5}(PIP_{13}\text{-}FSI)_{0.5}$ and $(PYR_{14}\text{-}FSI)_{0.5}(PYR_{23}\text{-}FSI)_{0.5}$ and 1.0 M $NEt_4\text{-}BF_4$ / PC were studied as electrolytes.

For electrochemical tests, a frequency range of 100 kHz to 10 mHz was applied in EIS to record the impedance plots, cyclic voltammetry scans were carried out at 100, 20 and 5 $mV.s^{-1}$ at different temperatures.

III-3.1. Onion-like Carbons (OLCs) electrodes

III-3-1-1 Comparison between $(PIP_{13}\text{-}FSI)_{0.5}(PYR_{14}\text{-}FSI)_{0.5}$ IL mixture and PC-based conventional electrolyte

The CVs of OLC electrodes (weight = 5.5 $mg.cm^{-2}$) in the IL mixture and a conventional electrolyte of 1 M NEt_4BF_4/PC are shown in (Figure V- 8 respectively) where the Y-axes are expressed as F. Attention is drawn towards the large usable temperature range between -50 and 100 °C in which capacitive behaviour is observed, with a maximum voltage up to 3 V in the IL mixture as they exhibit pure capacitive behaviour as can be seen from the close-to-rectangular shape of the CV.
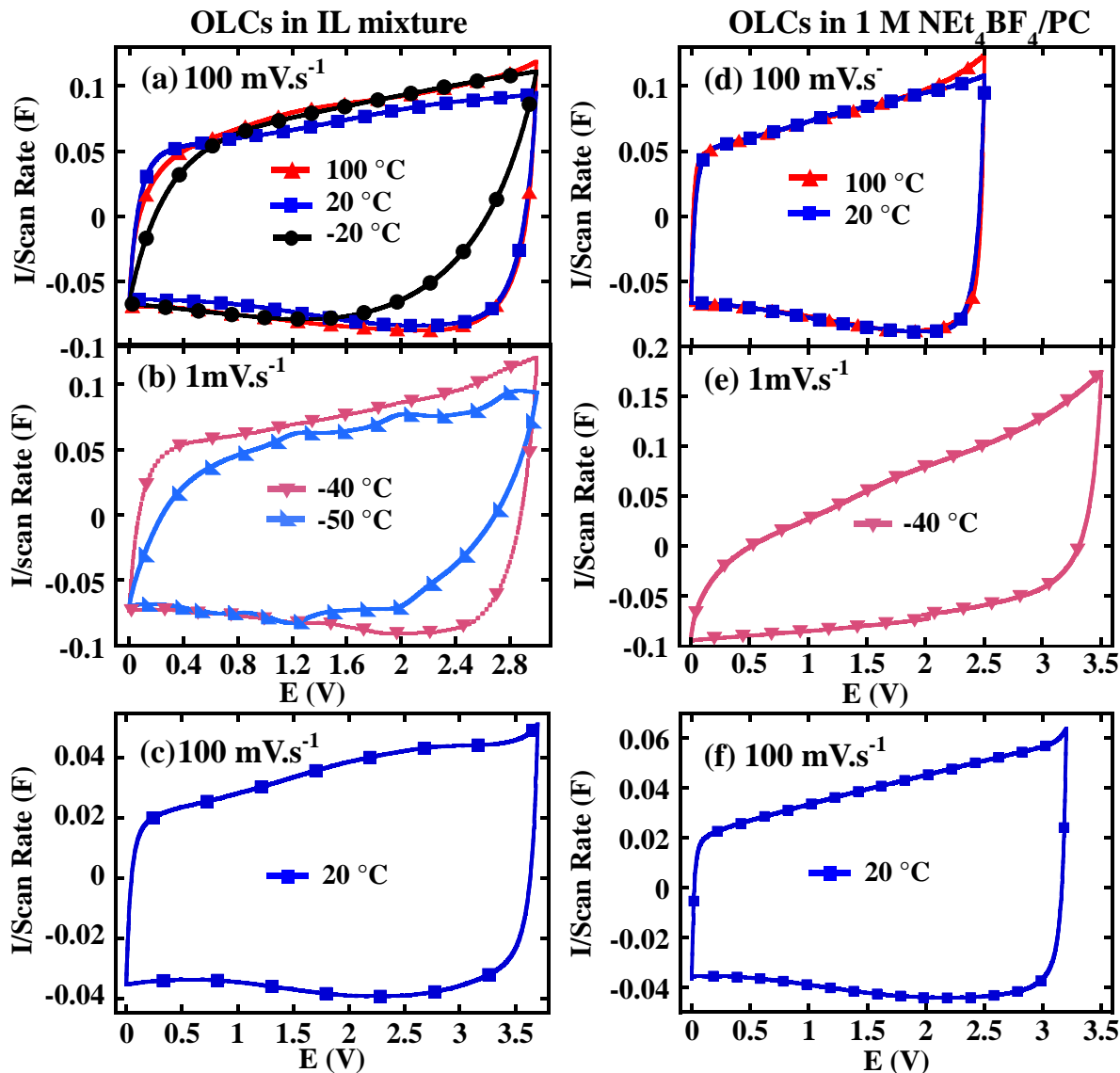
Figure V- 8: Cyclic voltammetry data for OLC electrodes. CVs at temperatures from -50 to 100 °C for OLCs in IL mixture recorded at 100 mV.s^{-1} **(a)** and 1 mV.s^{-1} **(b)**, CV at 20 °C and 100 mV.s^{-1} for OLCs; OLCs in the IL mixture show a large cell voltage of 3.7 V at room temperature **(c)** CVs at temperatures from -40 to 100 °C recorded in PC+TEAMS electrolyte at 100 mV.s^{-1}**(d)** and 1 mV.s^{-1} **(e)**; maximum voltage window is limited to 2.5 V at 100 °C and CVs shows a sharp limitation in the capacitive behavior with low capacitance at -40 °C. CV recorded at 20 °C for OLCs at a scan rate of 100 mV.s^{-1}**(f)**; maximum voltage window is limited to 3.2 V. OLC weight is 2.2 mg.cm^{-2} in panels (c) and (f). Weight of OLCs = 5.5 g.cm^{-2} for panels **(a), (b), (d)** and **(e)**; and 2.2 mg.cm^{-2} for panels **(c)** and **(f)**.

While the scan rate and, therefore, the power handling ability at very low temperatures is reduced (Figure V- 8b), it clearly defies the conventional wisdom stating that IL electrolytes cannot operate at all under such conditions. A 150 °C temperature window for

this IL mixture is far beyond the 100 °C temperature window for PC-based supercapacitors (-30 to 70 °C) as demonstrated in Figure V- 8d and e.

Besides varying scan rate to applicable values as a function of the temperature, the usable voltage window is also sensitive to temperature. While low scan rates are used at sub-zero temperatures below -20 °C, wider voltage range is possible. At higher temperatures such as 100 °C (Figure V- 8a), the usable voltage range is limited to 3 V, whereas room temperature operation enables a broader potential window of 3.7 V; that is, ~1 V higher than in current supercapacitors based on organic electrolytes. Since the energy density, E is proportional to V^2, (E = ½ CV^2, where C is capacitance), it is twice that of the organic electrolyte. For the OLC electrodes, when employing PC instead of the IL mixture, a maximum voltage window is 2.5 V at 100 °C and 3.2 V at room temperature, with a limited capacitive behaviour and a modest capacitance at -40 °C (Figure V- 8e).

III-3-1-2 Demonstration with $(PYR_{23}-FSI)_{0.5}(PYR_{14}-FSI)_{0.5}$ IL mixture

The CVs recorded using OLCs in the $(PYR_{23}-FSI)_{0.5}(PYR_{14}-FSI)_{0.5}$ IL mixture are shown in Figure V- 9.
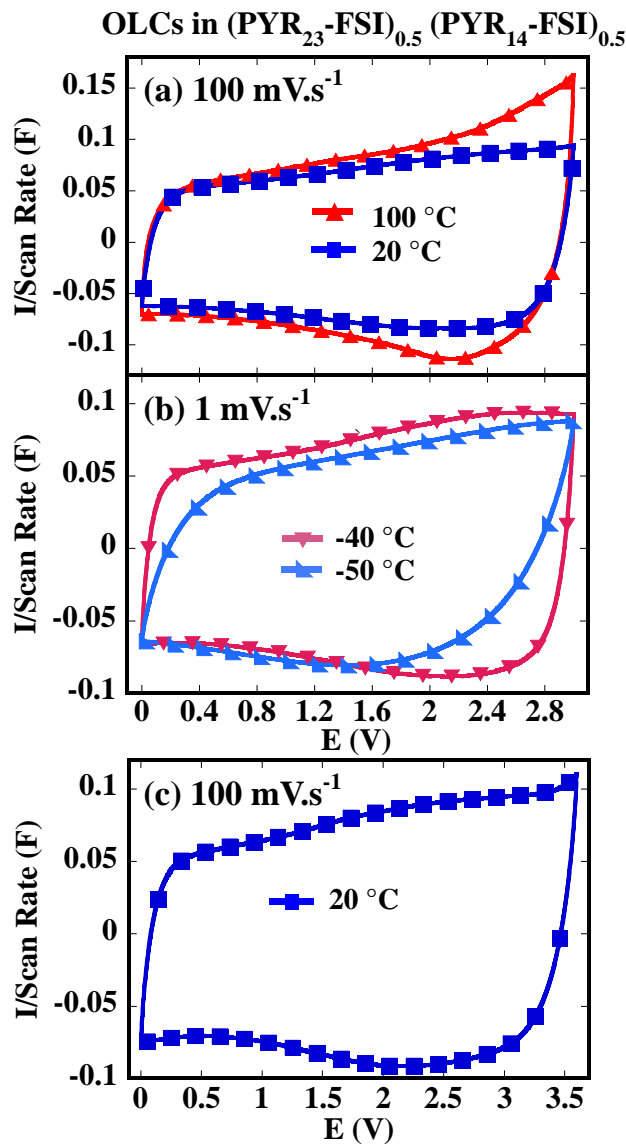
Figure V- 9: CVs at temperatures from -50 to 100 °C for OLCs in $(PYR_{23}-FSI)_{0.5}(PYR_{14}-FSI)_{0.5}$ mixture recorded at 100 mV.s^{-1} **(a)** and 1 mV.s^{-1} **(b)**, CV at 20 °C and 100 mV.s^{-1} for OLCs; OLCs in the $(PYR_{23}-FSI)_{0.5}(PYR_{14}-FSI)_{0.5}$ mixture show a slightly smaller cell voltage of 3.6 V at room temperature than the previous $(PIP_{13}-FSI)_{0.5}(PYR_{14}-FSI)_{0.5}$ mixture 3.7 V). OLCs weight = 5.5 mg.cm^{-2}.

CVs recorded again confirm the wide temperature range application of such eutectic IL mixture concocted using the same approach whereby the individual IL have the same molecular mass but different cationic structures. In this mixture, CVs showed better capacitive behaviour at -50 °C (Figure V- 9b) as compared to the piperidinium-based mixture

(Figure V- 8b) due to the generally higher conductivity offered by the pyrrolidinium functional group when considering similar alkyl side chain lengths [37,38].

However, as mentioned earlier that the piperidinium functional group is more electrochemical stable than the pyrrolidinium functional group [20], the replacement of (PIP$_{13}$-FSI) by (PYR$_{23}$-FSI) in the ionic liquid mixture has been observed to be stable within a smaller potential window at higher temperatures (100 °C) as seen from the fast increase of current above 2.4 V (Figure V- 9a).

III-3.2. Vertically aligned Carbon Nanotubes (VA-CNTs)

Cyclic Voltammetry - The CVs of the VA-CNT electrodes in the IL mixture are shown in Figure V- 10. Like in the OLCs electrodes, the IL mixture exhibit pure capacitive behaviour when tested in VA-CNTs seen from the close-to-rectangular shape of the CV like those in panels (a), (b) and (c) of Figure V- 8.
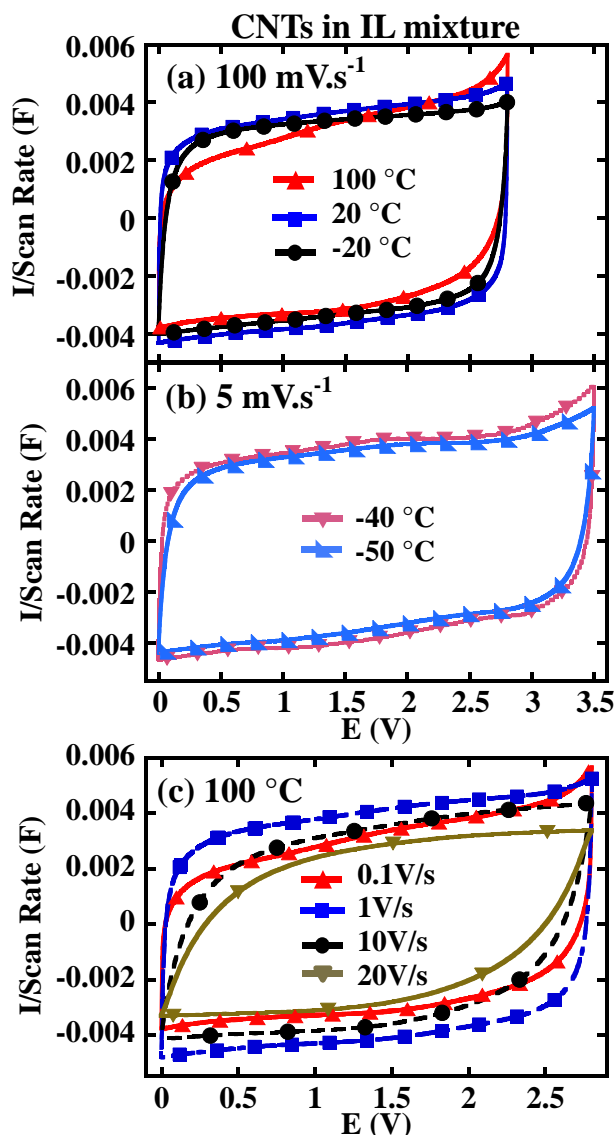
Figure V- 10: CVs at temperatures from -50 to 100 °C for CNTs at 100 mV.s^{-1} to 2.8 V **(a)**, at 5 mV.s^{-1} to 3.5 V **(b)** and CVs of CNTs at 100 °C and scan rates from 100 mV.s^{-1} to 20 V.s^{-1} to 2.8 V **(c)**.Weight of VA-CNTs= 0.3 mg.cm^{-2}.

Again here, the attention is drawn towards the large usable temperature range between -50 and 100 °C in which capacitive behaviour is observed, with a maximum voltage up to ~3 V for both OLCs and CNTs. Moreover at low temperatures as shown in Figure V- 10b, credits go to the large inter-tube distance that enhances the electrochemical accessibility of the CNT surface to the ions; a low temperature of -50 °C could be reached while maintaining the

capacitive behaviour at faster potential scan rates (5 mV.s^{-1}) than OLC electrodes (1 mV.s^{-1}). VA-CNT electrodes showed less capacitance dependence on the operation temperature, but the usable voltage window (2.8 V at 100 °C) was narrower, probably as a result of impurities (catalyst residue). At 100 °C, the capacitive behaviour of VA-CNT electrodes was almost independent of the charge/discharge rate up to 20 V.s^{-1}, thus demonstrating high power capabilities of this system (Figure V- 10c).

Electrochemical Impedance Spectroscopy - All the Nyquist plots of the VA-CNT cell recorded in the IL mixture display typical capacitive behaviour as depicted from the sharp increase of the imaginary part at low frequency [39] as shown in Figure V- 11a.
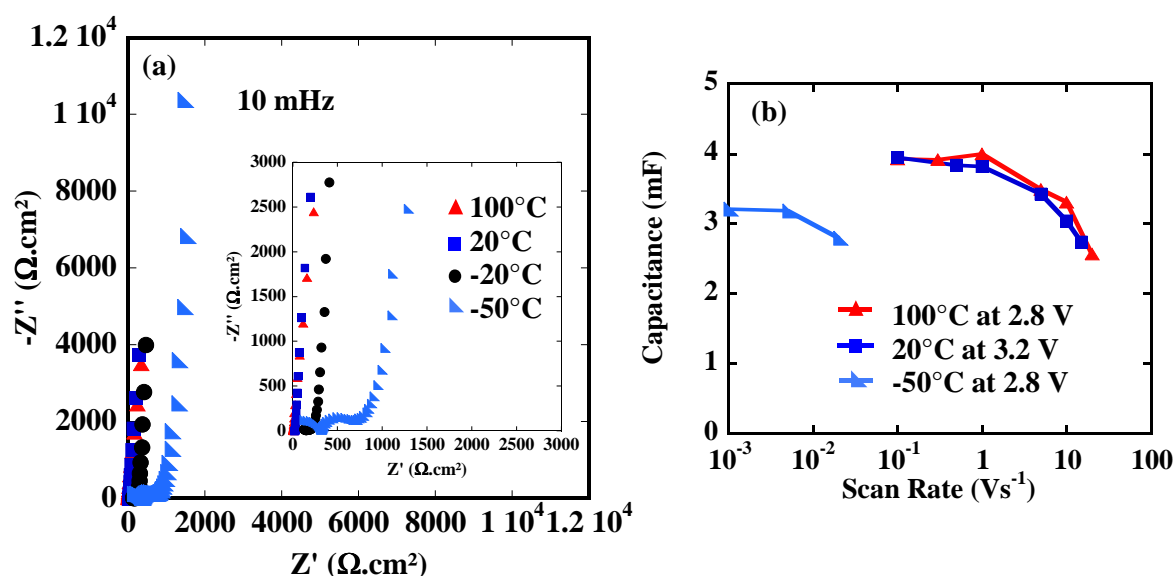
Figure V- 11: Effect of temperature and scan rate. EIS plots from -50 to 100 °C for CNT samples in the IL mixture **(a)**; CVs at temperatures from -50 to 100 °C for CNTs, at various scan rates in the IL mixture **(b)**. Electrode area for both OLCs and VA-CNTs = 1.1 cm^2.

Although resistance has been shifted to higher values, with decreasing temperatures, the CV recorded at the lowest measured temperature of -50 °C show that remarkable capacitive behaviour is still preserved despite being shifted towards higher resistance. This demonstrates that the device assembled with VA-CNT electrodes is still capable of delivering energy needed, *e.g.*, for small handheld outdoor devices at -50 °C. The change of the capacitance versus the potential scan rate at room temperature and above shows an excellent power performance since 60 % of the cell capacitance is still delivered at 20 V.s^{-1} (Figure V-11b). At – 50 °C, as expected, the capacitance drop noticeably but 75 % of the capacitance is still retained at the usual testing rate of 20 mV.s^{-1} for supercapacitors.

IV. Relative comparison between different carbon and electrolyte systems

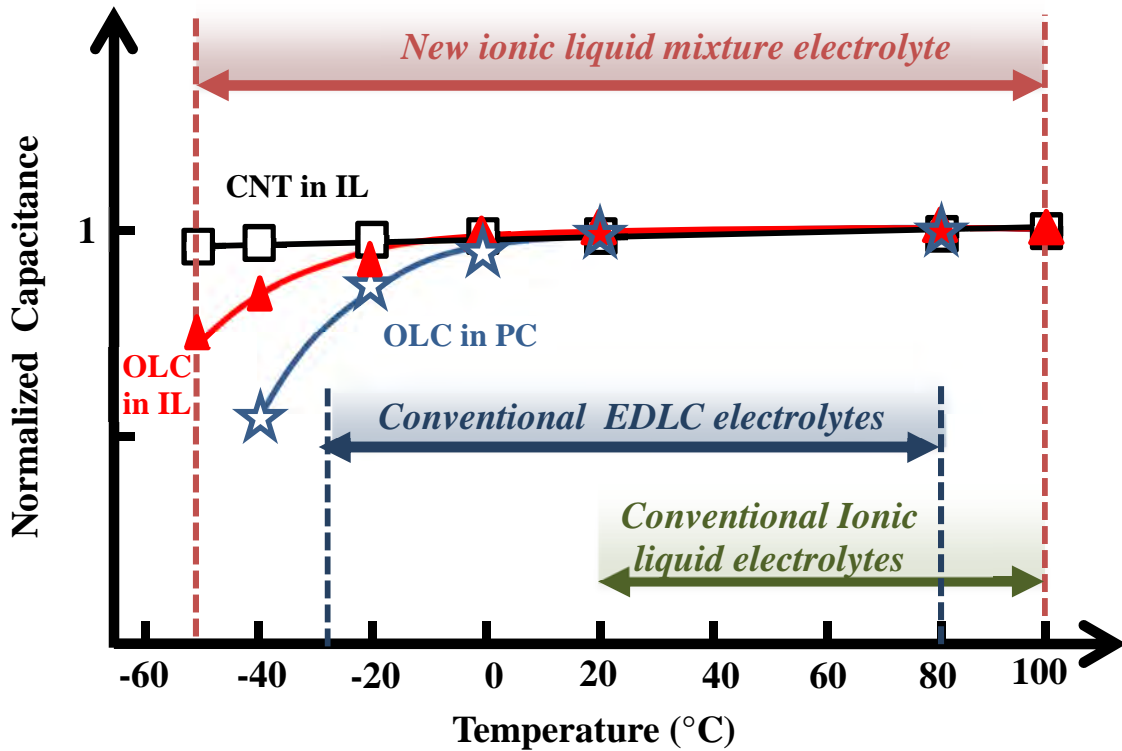**Figure V- 12:** Normalized capacitance ($C/C_{20\ °C}$) for the OLC and VA-CNT electrodes in PIP_{13}-$FSI)_{0.5}(PYR_{14}\text{-}FSI)_{0.5}$ IL mixture and PC + 1 M NEt_4BF_4 electrolytes. Capacitances were calculated at 100 mV.s^{-1}, except for the -50 °C (1 mV.s^{-1}) and -40 °C (5 mV.s^{-1}) experiments. This plot shows that the use of the IL mixture extends the temperature range for supercapacitors into the -50 to 100 °C range while conventional electrolytes using PC as solvent are limited to the -30 to 80 °C range. $C_{20°C}$ was 80 mF.cm^{-2} and 4 mF.cm^{-2}, respectively, for OLC and VA-CNT cells. All cells were cycled from 0 up to 2.8 V.

Figure V- 12 shows the change of capacitance versus the temperature for OLC (calculated from cycling up to 3 V) and VA-CNT electrodes (calculated from cycling up to 2.8 V). The capacitance values have been normalized to unity for ease of comparison, by dividing capacitance values by capacitance obtained at 20 °C in their respective electrolyte/carbon systems. When using 1 M NEt_4BF_4 in PC as electrolyte with OLC electrodes, the temperature range was limited to 110 °C (-30 to 80 °C) because of the capacitance drop at low temperatures and electrolyte oxidation at high temperature for cell voltage beyond 2.5 V, in agreement with commercial supercapacitors. This figure clearly shows the widening of the temperature range on both the low and high temperature limits with the use of the $(PIP_{13}\text{-}FSI)_{0.5}(PYR_{14}\text{-}FSI)_{0.5}$ mixture in conjunction with different architected OLC and VA-CNT electrodes. Such a wide temperature window of 150 °C around room temperature has, to the best of our knowledge, never been reported before - especially not for

IL-based electrochemical capacitors. Moreover, VA-CNT electrodes in a eutectic IL mixture show improved power performance in the same temperature range of -50 to 100 °C, thanks to the large accessible surface area, the binder-free electrode setup, and the improved carbon-metal interface as a result of the CVD process. This demonstration has shown the approach to well architected electrode design for enhancing good capacitive behaviour in a given electrolyte/electrode system. Moreover, this is an interesting approach to optimize electrolyte/electrode interface in the aspect of increasing charge storage density in the extended range of temperature. The weak point is the low capacitance due to the carbon structure.

V. Improving capacitance and energy density by optimizing electrolyte/electrode interface using graphene as electrode

Having shown that capacitive behaviour is greatly enhanced even at low temperatures when the architecture of the electrode is well accustomed for the IL mixture electrolyte ions, microstructure of the electrode plays a very important role in increasing charge storage as well. Graphene, as discussed in chapter I, offers interesting specific surface area (recall: ~2630 $m^2.g^{-1}$) in addition to its opened structure. A recent paper from Ruoff *et al.* reported the synthesis of activated graphene with high capacitance (150 $F.g^{-1}$) in AN-based electrolyte. Therefore activated graphene has been used as electrodes and tested in the eutectic IL mixture of $(PIP_{13}-FSI)_{0.5}(PYR_{14}-FSI)_{0.5}$ electrolyte at different temperatures.

V-1. Activated Graphene (a-MEGO)

Activated graphene electrodes have been prepared from microwave exfoliated graphitic oxide (MEGO) followed by and a KOH activation process and annealing as shown in Figure V- 13a. Details on the conditions of the preparation of activated graphene have been reported by Zhu *et al.* [36]. Electron microscopic images have been reproduced in panels B to F of Figure V- 13.
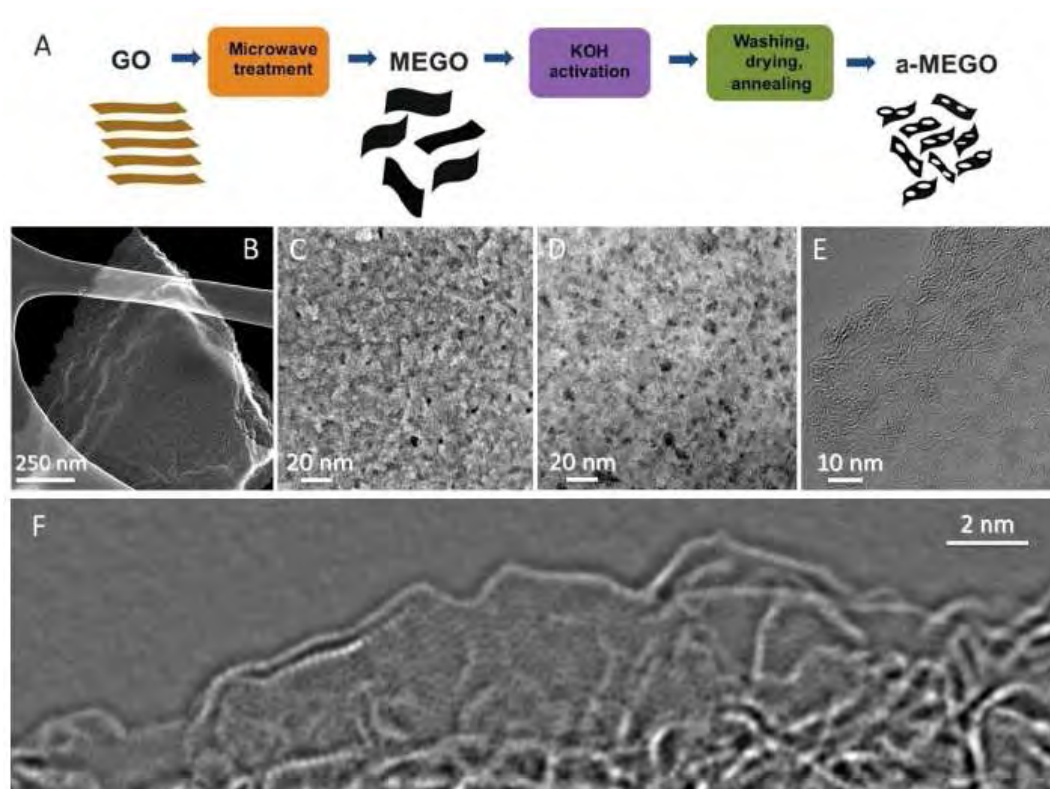
Figure V- 13: Schematic showing the microwave exfoliation/reduction of GO and the following chemical activation of MEGO with KOH that creates pores while retaining high electrical conductivity (A). Low magnification SEM image of a 3D a-MEGO piece (B). High-resolution SEM image of a different sample region that demonstrates the porous morphology (C). ADF-STEM image of the same area as (C), acquired simultaneously (D); As seen, a-MEGO contains micro- and mesopores with a distribution of sizes between ~1 and ~10 nm. High-resolution phase contrast electron micrograph of the thin edge of an a-MEGO chunk, taken at 80 kV (E); There is a variation in focus across the image because of the sloped nature of the sample and changes in sample thickness. The image shows the presence of a dense network of nanometre-scale pores surrounded by highly curved, predominantly single-layer carbon. Exit wave reconstructed HR-TEM image from the edge of a-MEGO (F); The in-plane carbon atoms are clearly resolved, and a variety of n-membered carbon rings can be seen. Substantial curvature of the single-carbon sheets is visible, with the in-plane crystallinity being preserved [36].

Cumulative pore volume and pore size distribution of the a-MEGO has been reported and reproduced in Figure V- 14 [36]. Surface and pore-size characterization was performed by coupling high-resolution nitrogen (77.4 K) and argon (87.3 K) adsorption/desorption experiments with advanced methods based on density functional theory (DFT). A hybrid nonlocal DFT (NLDFT) kernel, which is based on the assumptions of slit pore geometry for the micropores and cylindrical pore geometry for the mesopores, in conjunction with the microscopy results, was used to map out the pore size distribution of the a-MEGO as shown in the inset of Figure V- 14. According to the reported data, a-MEGO well-defined micro ~1 nm range) and mesopores (in the ~4 nm range) were determined through the analysis of the

nitrogen adsorption data while some ultramicropores seen from the CO_2 data. This graphene is thus a micro-/meso- porous carbon.
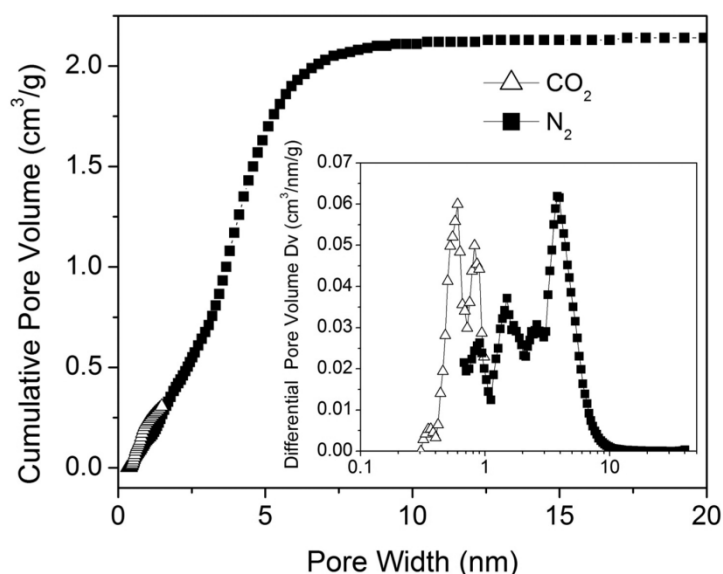
Figure V- 14: Cumulative pore volume and (inset) pore-size distribution for N_2 (calculated by using a slit/cylindrical NLDFT model) and CO_2 (calculated by using a slit pore NLDFT model) [36].

V-2. Electrochemical behaviour of activated graphene electrodes in IL eutectic mixture

Cell preparation

The assembly of the supercapacitor cell using the activated graphene electrodes has been carried out in the glovebox with < 0.1 ppm of water and oxygen content according to the set-up shown in Figure V- 15 (recall from Chapter II).
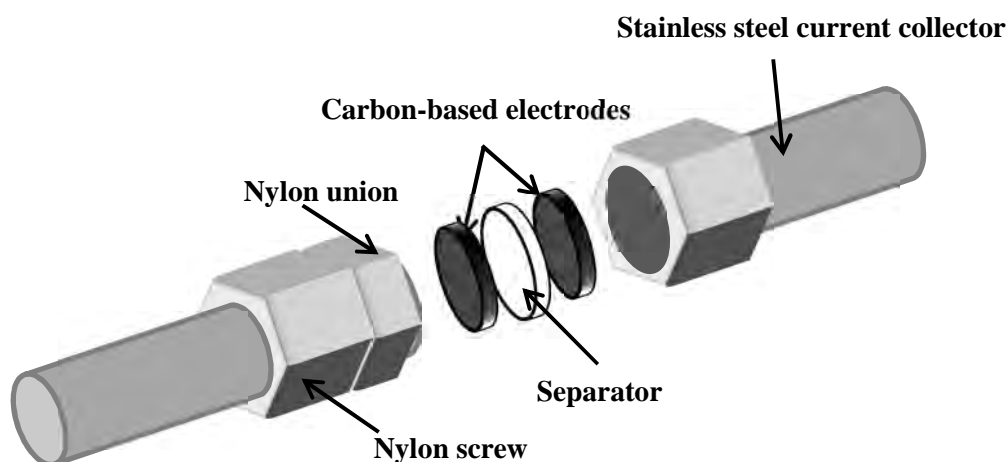
Figure V- 15: Schematic of a 2-electrode nylon Swagelok® cell assembly.

Room Temperature - Figure V- 16 below shows the CV scanned at 100 mV.s^{-1} at room temperature. The CVs recorded are plotted in terms of capacitance versus voltage of the cell and confirmed once and again the feasibility of using the eutectic IL mixture in a different carbon. A maximum operation voltage of 3.7 V (same as in OLCs) was obtained at room temperature with an impressive capacitance of ~160 F.g^{-1}, a 5-fold increase in capacitance compared to OLCs and CNTs.
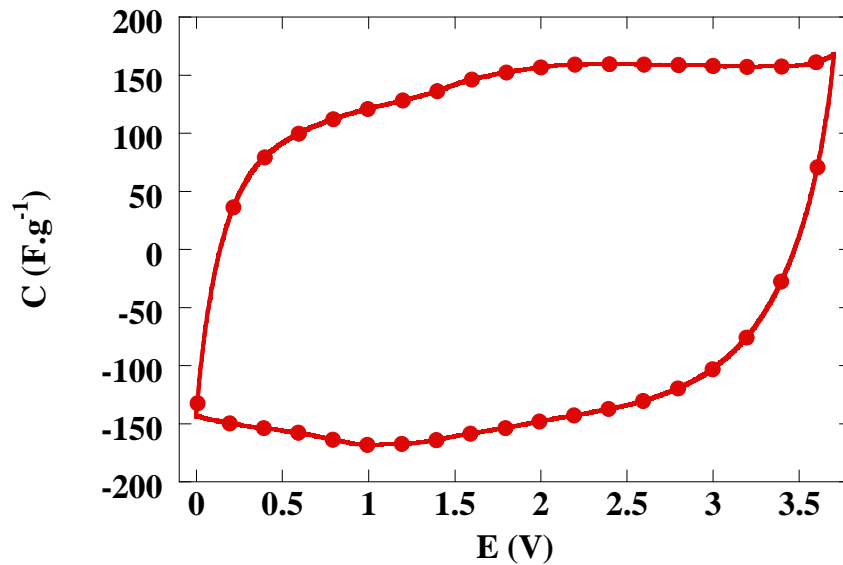
Figure V- 16: CV at 20 °C and 100 mV.s^{-1} using activated graphene electrodes; a-MEGO electrodes in IL mixture show a large cell voltage of 3.7 V at room temperature (same as in OLC electrodes). Weight = 1.65 mg.cm^{-2}.

An ESR of 3.4 Ω.cm^{2} was measured at room temperature (see Figure V- 17b). As discussed in Chapter I, since both sides of the graphene layer can be used in charge storage, once the electrolytes gain access to these interlayer surfaces, tremendous amount of charges could be stored as observed in the 5-fold increase in capacitance by using graphene instead of OLCs. This capacitance value is in agreement with value reported by Zhu *et al.* [36] using neat EMI-TFSI using a-MEGO electrodes.

High Temperature (20 ≤ T ≤ 80 °C) – Figure V- 17a shows CVs recorded at 100 mV.s^{-1} up to 3 V, with a gradual increase of capacitance (area under CV curve). The increase can explained by the higher ionic conductivity of the electrolyte ions at elevated temperatures, as can be evidently seen in the more rectangular shape of the CVs with increasing temperatures. Electrochemical impedance measurements further confirm the decrease in ionic resistance as shown in Figure V- 17b, ESR value decreases from 3.4 to 1.3 Ω.cm^{2} upon increasing the temperature from 20 to 80 °C. High capacitance is maintained, with an increase from 170 to 180 F.g^{-1} from RT to 80 °C.
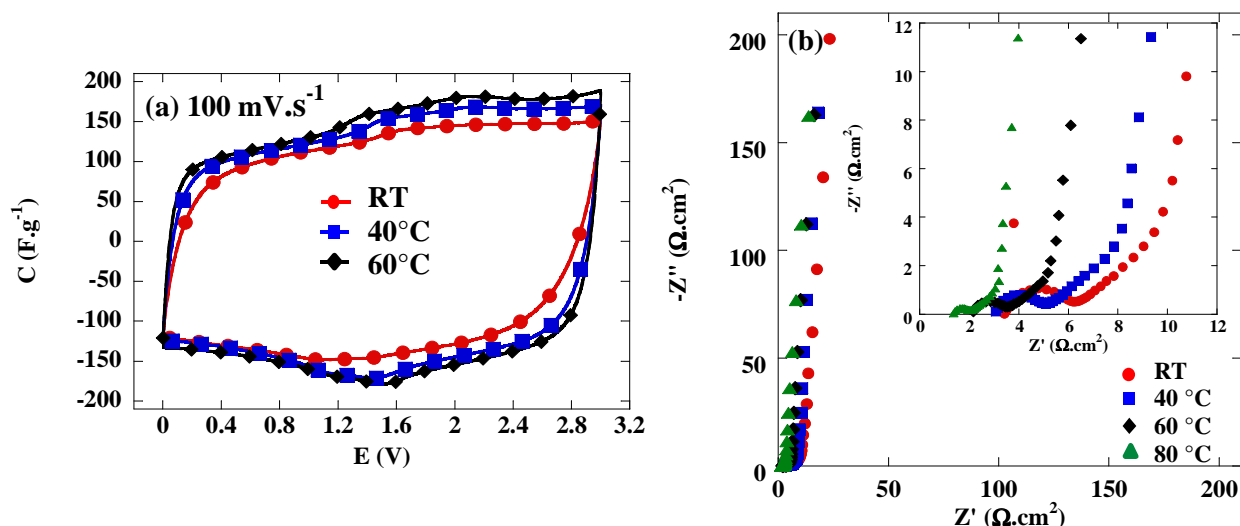
Figure V- 17: High temperature electrochemical characterizations of graphene electrodes in (PIP$_{13}$-FSI)$_{0.5}$(PYR$_{14}$-FSI)$_{0.5}$ electrolyte - at 100 mV.s^{-1} to 3 V at 20, 40 and 60 °C **(a)**, EIS measurements at 20 ≤ T ≤ 80 °C **(b)**; Weight = 1.65 mg.cm^{-2}.

The maximum voltages at each temperature (20 ≤ T ≤ 80 °C) was measured at 100 mV.s^{-1} and presented in Figure V- 18.
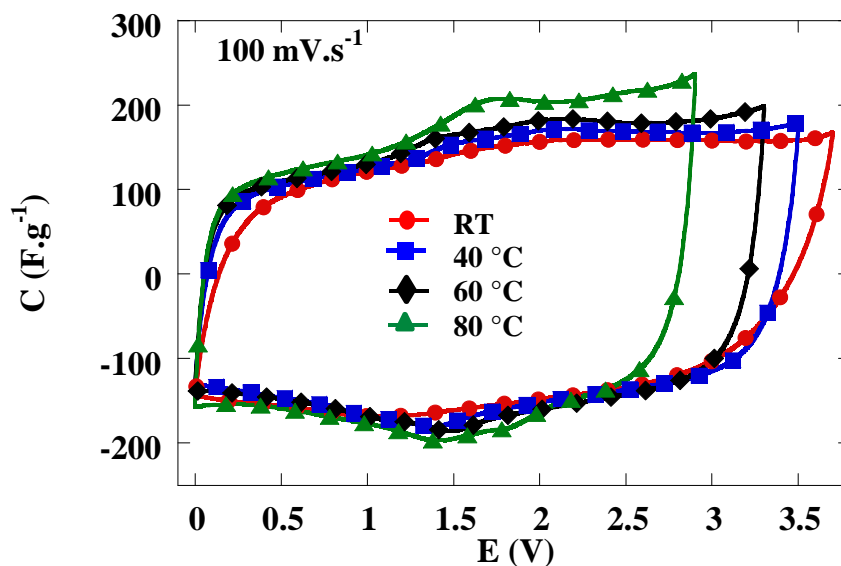
Figure V- 18: Maximum voltage windows for 20 ≤ T ≤ 80 °C at 100 mV.s^{-1}; Weight of graphene electrodes = 1.65 mg.cm^{-2}.

At 100 mV.s^{-1}, the potential is limited to 2.9 V. This narrowing of the electrochemical stability with increasing temperature could be attributed to the decomposition of the surface functional groups of the KOH activated graphene and their reactions with the electrolyte at elevated temperatures.

Sub-zero temperatures (-40 and -50 •C) - At sub-zero temperatures of -40 and -50 °C, ~70 % of the capacitance is still retained at 1 mV.s^{-1} (which is a reasonable scan rate taking into account the reduced ion mobility for such low temperatures) and CVs show good capacitive behaviour at -40 °C (See Figure V- 19a). High capacitance values of 100 to 120 F.g^{-1} have been achieved when charged to 3 V.
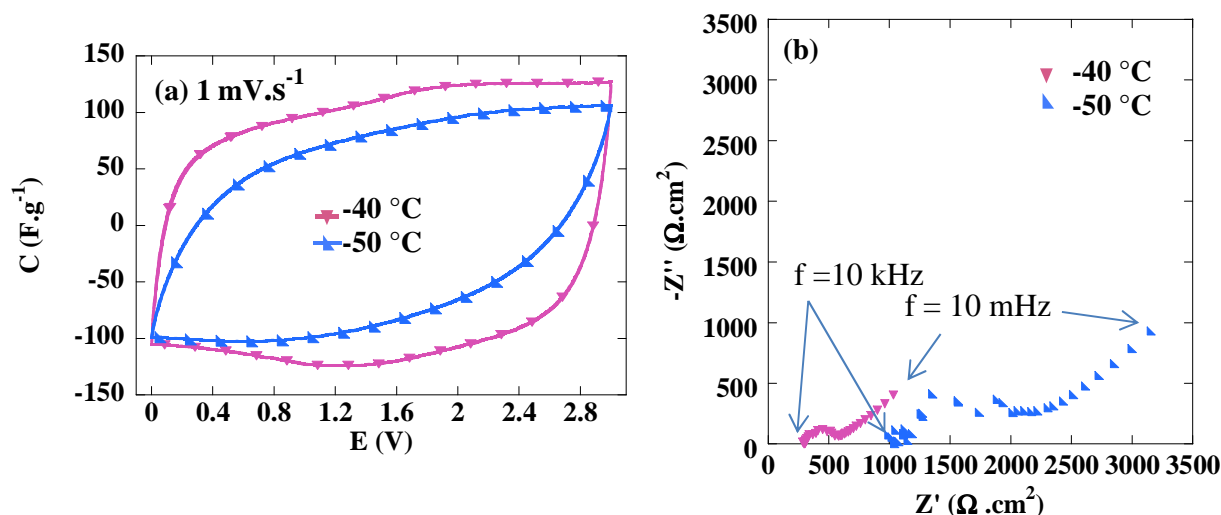
Figure V- 19: Sub-zero temperature (at - 40 and -50 °C) electrochemical characterizations of graphene electrodes in (PIP$_{13}$-FSI)$_{0.5}$(PYR$_{14}$-FSI)$_{0.5}$ electrolyte - at 1 mV.s^{-1} to 3 V **(a)**, EIS measurements from 10 kHz to 10 mHz **(b).**

EIS measurements still show a capacitive behaviour, despite the extra semi-circle at high frequency range. This extra RC semicircle could be due to the onset of the gelation or increased immobility of the electrolyte ions in the graphene layers at such low temperatures. The capacitive behaviour seen at -50 °C in graphene is less rectangular than that seen in the CNTs.

VI. Conclusions

In this work, we have demonstrated for the first time in literature, the dramatic extension of the temperature range of electrical energy storage with the right combination of the exohedral nanostructured carbon (nanotubes and onions) electrodes and a eutectic mixture of ionic liquids. Electrical double layer capacitors have been proven to be able to operate at sub-zero temperatures, from as low as -50 to 100 °C in a wide voltage window of 3.7 V. These findings greatly liberate the restriction of RTILs being commonly regarded as electrolytes for applications above room temperatures. Not only did we observe the good capacitance retention at the cold extreme of the temperature range (~70 % at -50 °C), very

high charge/discharge rates of up to 20 V.s^{-1} have also been achieved when cycled at 100 °C. This shows the extended threshold for extreme climatic conditions, which clearly proved the robustness of ILs as electrolytes for electrical storage.

Furthermore, tremendous improvements in charge storage has been achieved through the use of activated graphene by a 5-fold increase in capacitance, 160 F.g^{-1} with a maximum voltage at 3.7 V attained over a 150 °C (from -50 to 100 °C) temperature window as compared to conventional organic electrolytes of 110 °C (from -30 to 80 °C). These achievements have never been reported before and these findings would greatly contribute to the advances in electrical storage based on ILs, pushing the limits of energy storage to greater heights.

Herein, the long-held restriction of the ILs to energy storage applications above the room temperature has been lifted, the door is open for research that by optimizing the carbon accessible surface area (e.g., by using activated graphene [36], de-bundled single-walled nanotubes [40], or mesoporous templated carbons [41], together with designing the IL- based electrolyte. As most ILs are made up of hydrocarbons, the design of the molecules can be easily engineered with desired properties which could be pulled limits wider, thereby increasing the capacitance and energy density, and extending the applications of supercapacitors and accelerating the transition to "electrical economy" and hence wider use of renewable energy.

VII. References

[1]   Brandon, E.; Smart, M.; West, W. *NASA Tech Briefs* **32** (2008) 32.
[2]   Zhou, Q.; Henderson, W. A.; Appetecchi, G. B.; Montanino, M.; Passerini, S. *Journal of Physical Chemistry B* **112** (2008) 13577.
[3]   Armand, M.; Endres, F.; MacFarlane, D. R.; Ohno, H.; Scrosati, B. *Nature Materials* **8** (2009) 621.
[4]   Balducci, A.; Dugas, R.; Taberna, P. L.; Simon, P.; Pl_ee, D.; Mastragostino, M.; Passerini, S. Journal of Power Sources 167 (2007) 922.
[5]   Lockett, V.; Sedev, R.; Ralston, J.; Horne, M.; Rodopoulos, T. *Journal of Physical Chemistry C* **112** (2008) 7486.
[6]   Lu,W.; Hartman, R.; Qu, L.; Dai, L. *Journal of Physical Chemistry Letters* **2** (2011) 655.
[7]   Yu, D.; Dai, L. *Journal of Physical Chemistry Letters* **1** (2009) 467.
[8]   Jang, I. Y.; Ogata, H.; Park, K. C.; Lee, S. H.; Park, J. S.; Jung, Y. C.; Kim, Y. J.; Kim, Y. A.; Endo, M. *Journal of Physical Chemistry Letters* **1** (2010) 2099.
[9]   Dash, R.; Chmiola, J.; Yushin, G.; Gogotsi, Y.; Laudisio, G.; Singer, J.; Fischer, J.; Kucheyev, S. *Carbon* **44** (2006) 2489.
[10]   Dzubiella, J.; Hansen, J. P. *Journal of Chemical Physics* **122** (2005) 234706.

[11] Swatloski, R. P.; Holbrey, J. D.; Rogers, R. D. *Green Chemistry* **5** (2003) 361.

[12] Lall, S. I.; Mancheno, D; Castro, S.; Behaj, V.; Cohen, J. I.; Engel, R.; *Chemistry Communications* (2000) 2413.

[13] Gubicza, L.; Nemestothy, N.; Frater, T.; Belafi-Bako, K. *Green Chemistry* **5** (2003) 236.

[14] Villagran, C.; Deetlefs, M.; Pitner, W. R.; Hardacre, C. *Analytical Chemistry* **76** (2004) 2118.

[15] Bernot, R. J.; Brueseke, M. A.; Evans-White, M. A.; Lamberti, G. A. *Environmental Toxicology and Chemistry* **24** (2005) 87.

[16] Arbizzani, C.; Biso, M.; Cericola, D.; Lazzari, M.; Soavi, F.; Mastragostino, M. *Journal of Power Sources* **185** (2008) 1575.

[17] Largeot, C.; Portet, C.; Chmiola, J.; Taberna, P-L.; Gogotsi, Y.; Simon, P. *Journal of the American Chemical Society* **130** (2008) 2730.

[18] Handa, N.; Sugimoto, T.; Yamagata, M.; Kikuta, M.; Kono, M.; Ishikawa, M. *Journal of Power Sources* **185** (2008) 1585.

[19] Kunze, M.; Montanino, M.; Appetecchi, G. B.; Jeong, S.; Schonhoff, M.; Winter, M.; Passerini, S. *Journal of Physical Chemistry A* **114** (2010) 1776.

[20] Wasserscheid, P.; Welton, T. Ionic Liquids in Synthesis 2nd Edition *John Wiley & Sons* (2008).

[21] Suarez, P.A.Z. ; Consorti, C. S. ; De Souza, R. F. ; Dupont, J. ; Gonçalves, R.S. *Journal of the Brazilian Chemical Society* **13** (2002) 106

[22] Kunze, M.; Jeong, S.; Paillard, E.; Winter, M.; Passerini, S. *Journal of Physical Chemistry C* **114** (2010) 12364.

[23] Zheng, J.; Ekstrom, T. C.; Gordeev, S. K.; Jacob; M. *Journal of Materials Chemistry* **10** (2000) 1039.

[24] Portet, C.; Yushin, G.; Gogotsi, Y. *Carbon* **45** (2007) 2511.

[25] Huang, J.; Sumpter, B. G.; Meunier, V.; Gogotsi, Y. G.; Yushin, G.; Portet, C. *Journal of Materials Research* **25** (2010) 1525.

[26] Portet, C.; Yushin, G. ; Gogotsi, Y. *Carbon,* **45** (2007) 2511-2518

[27] Mykhaylyk, O. O.; Solonin, Y. M.; Batchelder, D. N.; Brydson, R. *Journal of Applied Physics* **97** (2005) 074302.

[28] Pech, D.; Brunet, M.; Durou, H.; Huang, P.; Mochalin, V.; Gogotsi, Y.; Taberna, P.-L.; Simon, P. *Nature Nanotechnology* **5** (2010) 651.

[29] Gao, L.; Peng, A.; Wang, Z. Y.; Zhang, H.; Shi, Z.; Gu, Z.; Cao, G.; Ding, B. *Solid State Communications* **146** (2008) 380.

[30] Fang, W.-C.; Chyan, O.; Sun, C.-L.; Wu, C.-T.; Chen, C.-P.; Chen, K.-H.; Chen, L.-C.; Huang, J.-H. *Electrochemistry Communications* **9** (2007) 239.

[31] Zhang, H.; Cao, G.; Yang, Y.; Gu, Z. *Carbon* **46** (2008) 30.

[32] Wei, S.; Kang, W. P.; Davidson, J. L.; Huang, J. H. *Diamond Related Materials* **17** (2008) 906.

[33] Talapatra, S.; Kar, S.; Pal, S. K.; Vajtai, R.; Ci, L.; Victor, P.; Shaijumon, M. M.; Kaur, S.; Nalamasu, O.; Ajayan, P. M. *Nature Nanotechnology* **1** (2006) 112.

[34] Presser, V.; Heon, M.; Gogotsi, Y. *Advanced Functional Materials* **21** (2011) 810.

[35] Heon, M.; Lofland, S.; Applegate, J.; Nolte, R.; Cortes, E.; Hettinger, J. D.; Taberna, P.-L.; Simon, P.; Huang, P.; Brunet, M.; Gogotsi, Y. *Energy Environmental Science* **4** (2011) 135.

[36] Zhu, Y.; Murali, S.; Stoller, M. D.; Ganesh, K. J.; Cai, W. ; Ferreira, P. J. Pirkle, A. ; Wallace, R. M.; Cychosz, K.A. ; Thommes, M. ; Su, D. ; Stach, E.A.; Ruoff, R. S. *Science* **332** (2011) 1537.

[37] Yim, T.; Lee, H.Y.; Kim, H-J.; Mun, J.; Kim, S.; Oh, S.M.; Kim, Y.G. *Bulletin Korean Chemical Society* **28** (2007) 1567.

[38] Salminen, J.; Papaiconomou, N.; Kumar, R.A.; Lee, J-M.; Kerr, J.; Newman, J.; Prausnitz, J.M. *Fluid Phase Equilibria* **261** (2007) 421.

[39] Taberna, P. L.; Simon, P.; Fauvarque, J. F. Journal of the Electrochemical Society **150** (2003) A292.

[40] Izadi-Najafabadi, A.; Yasuda, S.; Kobashi, K.; Yamada, T.; Futaba, D. N.; Hatori, H.; Yumura, M.; Iijima, S.; Hata, K. *Advanced Materials* **22** (2010) E235.

[41] Kyotani, T.; Chmiola, J.; Gogotsi, Y. Carbon Materials for Electrochemical Energy Storage Systems; Beguin, F., Frackowiak, E., Eds.; CRC Press/Taylor and Francis: Boca Raton, FL, (2009) 77.

General Conclusion

General Conclusion

The main objective of this work has been set out to formulate electrolytes based on ionic liquids for supercapacitor applications. In order to realize this, the project was kick started first by the molecular-scale study and conceptualization of the electrochemical double layer through (1) effects of solvent on the capacitive behaviour conventional electrolytes, (2) corroboration of the pore-size relationship in using a neat IL (non-solvated) and a solvated IL and followed by (3) the optimization of electrode/electrolyte interface at the EDL through the study on effects of architected electrodes in electrolytes consisting of pure ILs on capacitive behaviour and capacitance.

In the first chapter, bibliography in the three main subjects of this research of supercapacitor has been presented; Active material for electrodes, liquid electrolytes and the current EDL investigations closely related to the research path taken by this work. This chapter also supports that electrolytes of different nature and properties have been extensively studied to extend the current supercapacitor limits for different applications. Finally several complementary techniques for understanding of the EDL through different electrodes, different categories of electrolytes as well as complementary modelling and experimental techniques, that have earned their important role in towards the advancement of the energy storage technology have been presented.

Conventional electrolytes (NEt_4BF_4/PC and NEt_4BF_4/AN) were first studied with the objective to investigate the effective size of the electrolyte ions to address the question on degree of solvation of electrolyte ions in different solvents when entering the pores of the electrode have been presented in Chapter III. This is a continuation from our team results reported by Chmiola *et al*. (Science 2006 and Angewandte Chemie 2008) and has been realized through the systematic study of capacitive behaviour using Ti-CDCs with narrowly varied pore sizes. Results obtained from using a microcavity electrode have confirmed that the electrolyte ions are partially desorbed when being adsorbed into the pores, with ideal capacitive behaviour observed at pore size between the size of bare and fully solvated electrolyte ions. Also, it has been shown that the effective ion sizes of the electrolyte ions vary with the type of solvent.

The confirmations of partial desolvation then led to the question if maximum capacitance is due to the matching of ion-pore size of the electrode/electrolyte couple. To address this issue of how the EDL is being optimized in terms of ion-pore size, investigations were carried out first by using a neat IL without solvent (EMI-TFSI) using Ti-CDCs in a 3-

electrode cell configuration to study the adsorption/desorption of cations and anions separately. Introduction of solvent into the electrolyte, (EMI-TFSI/AN) allow the corroboration of the effect of solvation on the ion-pore size relationship to achieve maximum capacitance. Results presented in Chapter IV indeed confirm that (1) maximum capacitance has been obtained when pore size is in proximity to ion size in neat IL electrolyte and to the effective ion size in solvated IL electrolyte, (2) the maximum capacitance is depressed to a lower value due to the presence of solvent molecules which increase the distance between electrolyte ions and pore walls, thereby decreasing the capacitance. Such an observation shed retrospective light on the unrealistic grounds of pore sizes larger than that of solvated electrolyte ions are required for optimized EDL and maximum capacitance. Nanopores, that were previously deemed as empty voids that do not participate in EDL formation, have been reinstated of their important role in capacitive charge storage. Through results presented in Chapter IV, the use of ILs has also shown that in a solventless electrolyte, energy density can be increased through the high potential stability of the electrolyte and hence the enhanced capacitance.

Preparation of ILs is direct, with the matching of a main functional group and its substituent chain. Such versatility greatly simplifies the ease of obtaining the desired IL and paves countless combinations of functional-substituent ILs. To fully exploit the physical and electrochemical properties of the ionic liquids, and to address the safety concerns due to the presence of volatile substances in conventional electrolytes, electrolyte formulations consisting of purely ILs with the desired electrochemical properties have been prepared and were being studied with different electrode materials. The results of this part of the study have been presented in Chapter V, and brought about the achievement of two eutectic IL mixtures which do not solidify above -80 °C. These eutectic IL mixtures have been obtained for the first time by using the approach of mixing ILs of the same molecular mass but different molecular structures. Due to the relative lower conductivity (high viscosity) of ILs as compared to conventional electrolytes, ionic conductivity is further impeded when porous electrodes are used. It has been shown in this work that this problem can be overcome by proper designing of electrode architecture such that excellent capacitive behaviour has been achieved even at -50 °C. In this chapter, it has been shown for the first time, the implementation of electrolytes which are based on purely ILs in supercapacitors operating at sub-zero temperatures. The importance of electrode design and material in optimizing the electrolyte/electrode interface has also been demonstrated, to fully take advantage of the wide

liquidus temperature range of the eutectic IL mixtures, thereby widening the operating temperature range of supercapacitors, while achieving good capacitance.

These results contribute to the advancement in understanding the electrochemical double layer in the different electrolyte/electrode systems in order to attribute to different applications and give a direct insight in designing new electrode materials to stretch out the limit of energy density by using neat ILs. These conclusions also convey the key message on the importance of optimization of the electrolyte/electrode interface to fully benefit from properties of both the electrode and electrolyte. Without such optimization at the interface, advances such as widening of the operating temperature range would not have been achieved.

Future Work

Future Work

Ionic Liquids (ILs) have shown to be interesting electrolytes in terms of their commendable properties and as well as the fact that they consist of only ions. Engineering of the ILs can help in better conformation, in view of lowering resistance and increasing the possibility of ILs having better ionic conductivities be it in its pure state or in mixtures. The ease of designing ILs based on the wide variety of functional groups in both cations and anions, provide tremendous perspectives as electrolyte probes in the quest for the understanding the adsorption/desorption mechanism in EDL and as excellent working electrolytes for supercapacitors. The results obtained in this research work have brought about the reconceptualization of the adsorption/desorption mechanism in porous electrodes, and the extension of the operating temperature range of ILs in supercapacitors.

As seen in the application of ILs as electrolytes for supercapacitors, electrode structures ought to possess an open structure to overcome the low fluidity of ILs, offering easy access of the electrode surface area to the electrolyte ions. Therefore the understanding of the optimization of the electrolyte/electrode interface ought to be urgently sought. With regards to the eutectic IL mixtures, despite the wide liquidus temperature range of -80 °C measured, the lowest practical operating temperature was limited to -50 °C, with some structures (CNTs) showing better capacitive behaviour than the others (OLCs and graphene). How do the structures affect the lowest operational temperature? Do the stacking of the OLCs particles and the graphene sheets give rise to 'quasi-pores' which sort of confine adsorbed electrolyte ion, thereby increasing order among the ions, and resulted in partial freezing/gelation that limited the temperature to -50 °C? Do the different cations have preferential/random orientation or molecular environment within the charged electrode?

Today, many powerful and improvised techniques have been developed to aid in answering these questions. Three different tracks can be explored to obtain information that could possibly contribute to the visualizing of the actual charging/discharging mechanisms in such open structured systems: NMR, EQCM and Computational simulations and modelling.

Real-time in-situ NMR study allows the analysis on the migration of ions during the process of charge/discharge. Particularly when employed as an electrolyte in ECs, ILs can be subjected to different behaviour owing to the interactions between surfacial groups of the electrode and the ions. This technique is powerful in the sense that both cationic and anionic analyses are possible with the nuclei from isotopes of many elements. This is especially

interesting in studying the migration of the different cations in ionic liquid mixture at different temperatures.

Electrochemical Quartz Crystal Microbalance (EQCM) technique probes the mass change arising from compositional changes in micropores of the electrodes which holds information on the solvation environment through different regimes of applied potential, that is, near the OCV, or at the extremes of the electrochemical stability window of the electrolyte. This technique has the prospects of offering more in-depth inquiry into the aspect of solvation and can be a complementary technique to the CME technique in this perspective.

Lastly, computational simulations and modelling provides information that can be visualized for better understanding the exchange of ions between the bulk and electrode as well as the confinement effect of ILs within the systems through the compilation of experimental data.

Résumé de Thèse

Résumé de Thèse

Introduction

L'énergie est le fondement de notre société sans laquelle, la vie sur terre ne serait pérenne. Comme le disent les rapports du Portail de l'Energie Européen de 2010, l'énergie fossile, compte pour près de 80% du total des émissions de gaz à effet de serre en Europe et presque 45% de la génération d'électricité Européenne est basée sur des sources faible émission de carbone, principalement nucléaire et stockage hydraulique[1]. L'actuel objectif de l'UE est d'augmenter la part de production des énergies renouvelables à hauteur de 20%. Il devient d'autant plus urgent de diversifier la génération de l'énergie vers des solutions renouvelables.

Depuis plusieurs directives rédigées par le Département de l'Energie (Department of Energy – DOE) des USA [2] et du Portail de l'Energie Européen [3] et pays émergeants, des efforts approfondis ont été réalisés durant ces dernières décennies. Leur objectif est le développement et la distribution des énergies renouvelables en vue de limiter l'accroissement des dommages sur l'environnement et le climat. L'intensification de l'industrialisation, la mondialisation faisant suite à la croissance démographique et le rapide développement des nations sont en effet la cause du réchauffement climatique. Les énergies alternatives à faibles émission de carbone, comme le solaire, l'éolien, l'énergie de la houle sont destinées à relever le défi de l'énergie d'aujourd'hui pour lutter contre les émissions de gaz à effet de serre responsables du réchauffement de la planète. Cependant, ces types d'énergies alternatives appelées « propres » sont des sources intermittentes ne pouvant pas satisfaire les besoins en continu : ceci pose le problème du stockage de l'énergie. Afin d'accompagner le développement des énergies renouvelables, des systèmes complémentaires de stockage doivent être mis en place de manière efficace afin de permettre la distribution et l'accès à cette énergie [4]. Ceci répond au principal objectif de la politique énergetique qui inclut aujourd'hui la sécurité des réserves, la compétitivité et la viabilité des énergies listées dans le traité de Lisbonne [5].

Suivant les directives issues du DOE et de l'EEP, les systèmes de stockage jouent un rôle important dans l'organisation d'une telle production d'énergie sporadique. Grâce à l'instauration de systèmes de stockages d'énergies efficaces, un vaste panel d'énergies renouvelables pourra être exploité en vue d'accroitre le rendement énergétique.

Le stockage de l'énergie est indispensable pour répondre aux besoins énergétiques quotidiens. Sans le recours à ces systèmes, l'énergie surproduite sera gaspillée et le manque d'énergie sous produite entraînera des interruptions des activités quotidiennes.

Les systèmes de Stockage Electrochimiques de l'Energie (SEE) sont basés sur une technologie qui retient particulièrement l'attention dans le monde de la recherche en vue réponses qu'ils peuvent apporter au défi énergétique sociétaux. Le SEE jouent un rôle important dans l'électro-mobilité, en raison de leur facile intégration dans des systèmes autonomes de transport et d'électronique.
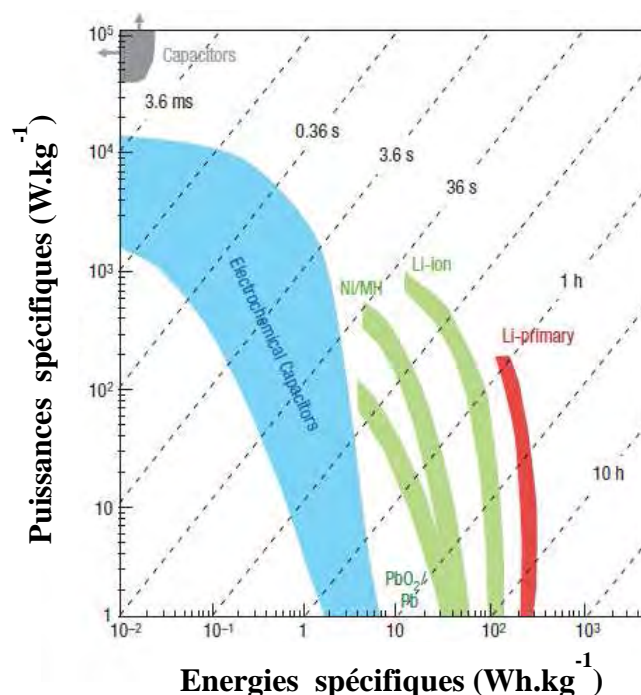
Figure 1: Diagramme de Ragone – Comparaison des principaux systèmes de stockage de l'énergie [6].

Les systèmes SEE sont traditionnellement divisés entre les systèmes de forte densité d'énergies (batteries) et les systèmes de forte puissance (Condensateurs). Les batteries sont caractérisées par un cycle charge/décharge de l'ordre de la minute ou de l'heure, alors que les condensateurs peuvent délivrer une grande puissance (~10 kW/kg) avec une densité d'énergie moyenne (~5 Wh/kg) qui peut être chargée/déchargée en l'espace de quelque seconde [7, 8] comme représenté sur la Figure 1. La recherche dans les batteries connaît un essor grandissant, particulièrement dans le développement des batteries Li-ion [9]. Malgré ces avancées, le développement des batteries de Li-ion dans le stockage de l'énergie et l'électro-mobilité a été entravée par des problèmes de sécurité liés à la réactivité du Lithium dans des électrolytes inflammables.

Par conséquent, les systèmes de stockage d'énergie, parmi lesquels on trouve les supercondensateurs jouent un rôle primordial. Ceux-ci présentent un grand intérêt dans les applications de puissance puisqu'ils peuvent stocker et fournir de l'électricité rapidement (quelques secondes) grâce à un fonctionnement basé sur le stockage électrostatique des charges électriques : les ions d'un électrolyte sont adsorbés/désorbés à la surface de la matière active des électrodes.

Les objectifs de cette thèse sont (1) d'étudier la charge de la double-couche électrochimique, constituée par l'adsorption des ions d'un électrolyte et consécutif à l'application d'un potentiel externe au niveau des électrodes, en vue d'augmenter la capacité et (2) de formuler des électrolytes à base de liquides ioniques dans le but d'augmenter la tension de fonctionnement et donc l'énergie. Ces travaux de recherches ont été réalisés en partenariat avec la société industrielle Solvionic [10], spécialisée dans le développement et la production de liquides ioniques, et le laboratoire du CIRIMAT de l'université Paul Sabatier.

Chapitre I

Le premier chapitre de cette thèse présente une étude bibliographique en trois parties. Après une présentation des supercondensateurs à double couche électrochimique - ou supercondensateurs carbone/carbone - qui ont fait l'objet de cette thèse, la deuxième partie est consacrée à la présentation des matières actives d'électrode en carbone et des électrolytes. Leur fonctionnement et leur impact sur les performances des supercondensateurs sont détaillés. Des matériaux carbones avec différentes nano-structures ont été obtenu grâce à différentes méthodes de synthèse afin d'augmenter les performances des supercapacités et ont été présentés. Les électrodes à base de carbone présentent un grand intérêt grâce à la polyvalence du carbone qui permet une grande variété d'électrode nanostructurées, offrant une vaste plage de propriétés physiques [11].

Différents carbones nanostructurés sont présentés : les oignons de carbone (OLCs) [12], Nanotubes de Carbone (NTCs) [13], Graphène [14] et le carbones dérivé de carbure [15] qui sont des structures à zéro, une, deux et trois dimensions. Ils sont présentés en tant que matériaux d'électrode pour les supercondensateurs dans ce chapitre. Les différents électrolytes liquides utilisées dans les supercondensateurs et leurs propriétés sont ensuite présentées. Les électrolytes conventionnels commercialisés aujourd'hui sont souvent composés de solvant volatiles. Malgré que ce type de solvant offre une stabilité électrochimique de plus de 1,23 V comparée aux électrolytes aqueux, ils sont souvent inflammables. Les liquides ioniques (LIs) ont retenu l'attention pour une utilisation en

qu'électrolyte sécurisants pour la réalisation de systèmes de stockage de l'énergie. Ils offrent en effet stabilité életrochimique (> 3 V) et thermique (stable jusqu'à > 200 °C), permettant ainsi d'augmenter la densité d'énergie (E = ½ CV²) ainsi que la sécurité. La figure 2 montre la stabilité électrochimique des différentes types d'électrolytes rencontré dans les supercondensateurs : aqueux, organiques et liquides ioniques.
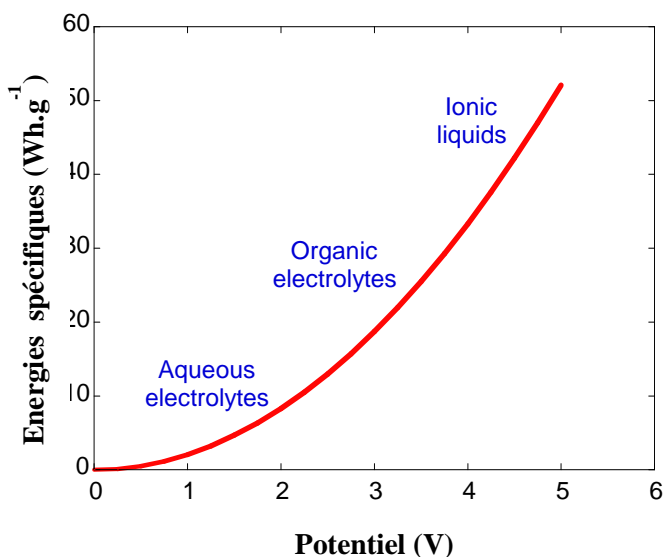

Figure 2: Augmentation de la densite d'énergie en utilisant les LIs comparé aux autres électrolytes.

La dernière partie de ce chapitre traite de l'interface matière active / électrolyte (au carbone/électrolyte). Il a été montré que cette interface a un rôle très important sur la capacité des carbones et donc sur sa densité d'énergie.
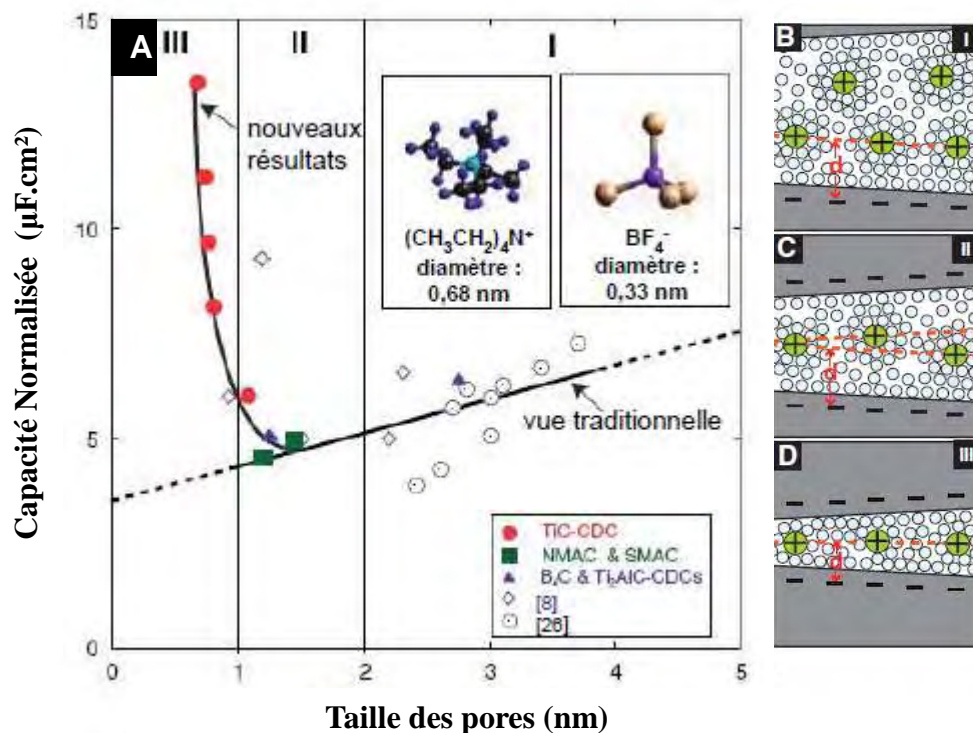
Figure 3: Variation de la capacité spécifique en fonction de la taille des pores pour des charbons actifs mésoporeux **(A)**, Illustration de l'absorption des ions dans des pores de > 2 nm **(B)**, 1-2 nm **(C)** et < 1 nm **(D)**. [16]

La figure 3a montre que lorsque les micropores de carbones ont une taille inférieure à 1 nm sont utilisés comme matériaux d'électrode dans les supercondensateurs, les capacités normalisées augmentent d'environ 50% bien que les pores serait inférieure à la taille des ion solvatés. Les figures 3B à 3D montrent des représentations schématiques des ions de l'électrolyte avec leurs couches de solvants confinés dans différents tailles de pores. Ceci pose à la question de l'effet du solvant sur la change de la capacité (l'adsorption des ions) dans les carbones poreux. Des nombreux travaux ont été effectués en utilisant différentes électrodes, électrolytes, et techniques expérimentales dans le but de comprendre le rôle de la porosité duc carbones sur la formation de la double couche électrochimique. Ils sont présentés dans ce chapitre.

Chapitre II

Le deuxième chapitre présente les conditions expérimentales, les matériaux et leurs synthèses (carbone et électrolytes), l'élaboration des supercondensateurs, des montages et les techniques de caractérisations physiques et électrochimiques utilisés dans ce travail. La plupart des matériaux de carbone ont été reçus sous forme de poudre mis en forme sous forme d'électrodes en utilisant des liants. Trois montages expérimentaux différents ont été réalisés et utilisé : une cellule de supercondensateur de 4cm², une électrode à microcavité et une cellule

de type swagelok®. Les techniques utilisées pour caractériser les électrolytes sont : la spectroscopie d'impédance électrochimique (SEI) pour la mesure des conductivités, la voltammétrie cyclage pour determiner la fenêtre de stabilité électrochimique et la calorimétrie différentielle à balayage pour la mesure de transition de phase des électrolytes. Les caractérisations électrochimiques des cellules de supercondensateurs onts été faits pour spectroscopie d'impédance électrochimique, voltamétrie cyclique et cyclage galvanostatique.

Chapitre III

Le troisième chapitre étudie les effets du solvant sur le comportement dans les électrolytes conventionnelles utilisant le même sel, NEt_4BF_4 dans deux solvants différents : le carbonate de propylène (PC) et l'acétonitrile (AN). L'objectif est de comprendre les effets de solvatation sur le comportement capacitif durant l'adsorption/désorption des ions, suivant les recherches précédemment effectuées au sein de notre équipe (voir figure 3). Cette étude a été menée en utilisant une électrode à microcavité et des carbones dérivés de carbure de titane.

Carbone

La synthèse des carbones derives de carbure de titane (Ti-CDCs) utilisés dans cette etude a été effectuée à l'université de Drexel à Philadelphie (USA) dans l'équipe du Professeur Gogotsi. La poudre de Ti-CDCs est obtenue par extraction des atomes de titane dans les carbures précurseurs (TiC) par chloration à haute température de 400 à 1200 °C selon la réaction :

$$TiC + 2\ Cl_2 \rightarrow TiCl_4 + C$$
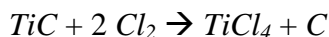
Les propriétés physiques et structurales (porosité et surface spécifique etc.) des Ti-CDCs dépendent des conditions expérimentales, de la température et la durée de la chloration en particulier (Tableau 1). Le carbure de titane précurseur utilisé dans cette étude a une structure de type NaCl et son groupe d'espace est le Fm3m. Dans cette structure, la distance entre les carbones plus proches voisins est petite et uniforme dans le cristal et permet d'obtenir un carbone avec une haute porosité de 56 % et volume de 0,56 $cm^3.g^{-1}$. La porosité créé par le départ des atomes titanes du carbure, donne une distribution de pore étroite est obtenu.

Tableau 1 : Taille des pores et les surfaces spécifiques pour le Ti-CDC en fonction de la température de synthèse.

Chlorination temperature (°C)	BET SSA (m²/g)	Pore volume (cc/g)	Average pore width(nm)	Maximum pore width* (nm)
400	1113	0,51	0,65	1,12
500	1140	0,50	0,68	1,18
550	1202	0,51	0,72	1,29
600	1269	0,60	0,74	1,23
700	1401	0,66	0,76	1,41
800	1595	0,79	0,81	1,54
900	1600	0,81	1,0	2,50
1000	1625	0,81	1,1	2,8

Les Ti-CDCs, qui possèdent des tailles de pore : 0,68 nm, 0,74 nm, 0,76 nm et 1 nm sont représentatifs de petites, moyennes et grands taille de pores.

Electrolyte

Tableau 2 : Taille des ions de l'électrolyte solvatés par une couche de solvant et totalement désolvatés

Electrolyte	Potentiel Electrochimique (V)	Taille des ions(nm)				Conductivité (mS.cm^{-1})
		Nue [17,18]		Solvaté [18]		
		Cations	Anions	Cations	Anions	
1,5 M NEt$_4$BF$_4$ dans AN	-1,3 to 1,0			1,30	1,16	60
1 M NEt$_4$BF$_4$ dans PC	-1,5 to 1,1	0,67	0,48	1,35	1,40	13

L'électrolyte utilisé est dans un premier temps une solution de 1,5 M de tétraéthylammonium tétrafluoroborate (Et$_4$NBF$_4$), dans le solvant acétonitrile. Le tableau IV.1 donne la taille des ions de l'électrolyte. La taille des ions et du solvant a été calculée en utilisant le logiciel Gaussian 98 dans le logiciel HyperChem8.0 et en supposant que les ions et les molécules de solvant sont des sphères dures et que les ions sont totalement liés aux molécules de solvant.

Le diamètre des ions solvatés a été calculé en considérant que chaque ion est entouré d'une seule couche de solvant. Il est donc égal à la somme du diamètre de l'ion et de deux fois le diamètre d'une molécule de solvant.

Résultats

Un montage à trois électrodes a été utilisé pour étudier le comportement capacitif des électrodes de CDC dans cet électrolyte. Les anions s'adsorbent à l'électrode lorsqu'elle est chargée positivement, et les cations à l'électrode lorsqu'elle est négative. Une électrode de quasi-référence constituée d'un fil d'argent dont le potentiel est constant a été utilisée afin d'enregistrer les réponses en courant ou en tension d'électrode de travail.
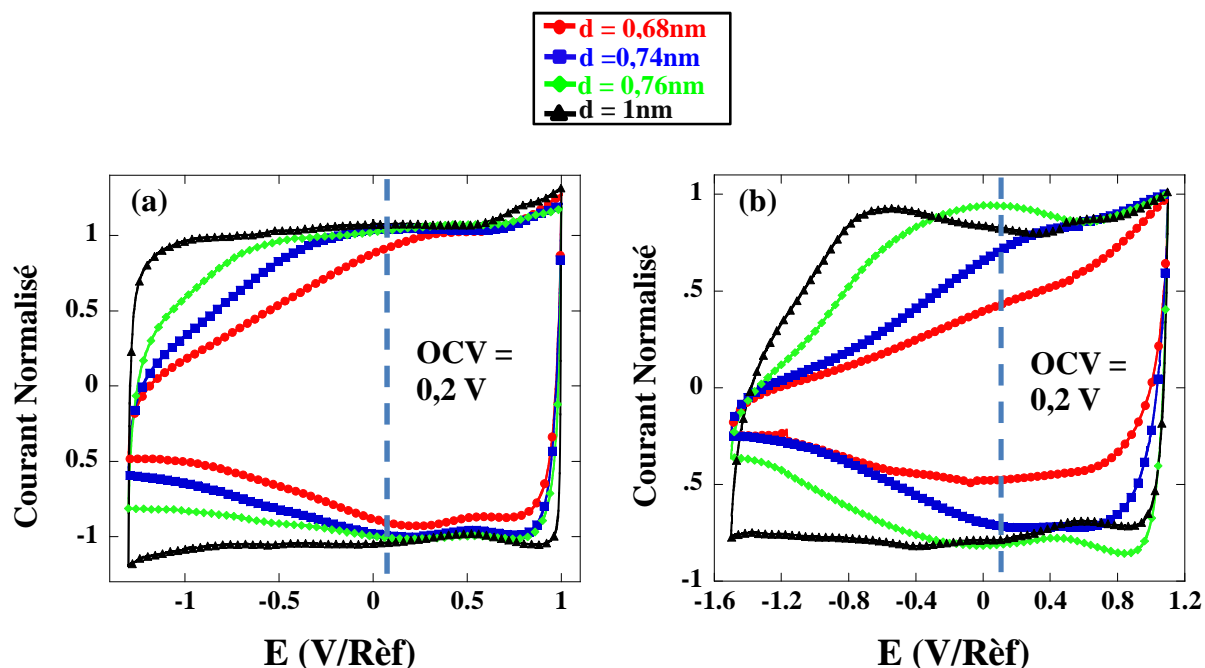

Figure 4: Voltamogrammes normalisées dans toute la gamme de potentiel à 100 mV.s^{-1} dans les électrolytes de 1.5 M NEt$_4$BF$_4$ + AN **(a)** et de 1 M NEt$_4$BF$_4$ + PC **(b)**.

Une courbe Intensité/Potentiel (CV) représentant un comportement capacitif idéal est rectangulaire. La figure 4 montre la réponse capacitive des Ti-CDCs dans des électrolytes utilisant le même sel, le NEt$_4$BF$_4$, dans différents solvants : AN et PC, respectivement (a) et (b). Les CVs de quatre échantillons Ti-CDC ont été enregistrées avec une vitesse de balayage de 100 mV.s^{-1}, dans toute la gamme de potentiel comprise entre : -1.3 V/Réf. et +1 V/Réf pour 1.5 M de Net$_4$BF$_4$ dans l'AN -1.5 V/Réf et 1 V/Réf pour 1 M de NEt$_4$BF$_4$ dans le PC. Dans ces expériences, chaque échantillon a été caractérisé dans toute la gamme de potentiel. Pour des potentiels inférieure à l'open circuit voltage (OCV), (0,2 V/Réf pour tous les échantillons) le comportement capacitif provient de l'adsorption cationique des ions Et$_4$N$^+$; au-dessus de l'OCV, l'adsorption anionique des ions BF$_4^-$. Deux zones de potentiel peuvent donc être définies comme sur la figure 4 à savoir en-dessus et au-dessous de l'OCV.

1.5 M NEt₄BF₄ dans l'acétonitrile (AN)

Dans la gamme de potentiel au-dessus de l'OCV, les courbes intensité/potentiel ont une forme rectangulaire (comportement capacitif), seuls de légers écarts entre les courbes sont observés. L'adsorption des anions n'est donc pas limitée, ce qui correspond à un comportement capacitif idéal. Cependant, pour un balayage en potentiel au-dessous de l'OCV, la forme rectangulaire des courbes I=f(E) est perdue à l'exception du 900°C qui a la plus large taille de pore (1nm). L'adsorption/désorption des anions et des cations n'est pas symétrique.

L'adsorption de BF₄⁻ - La capacité maximum est atteinte en minimisant le volume inoccupé dans la structure poreuse du carbone. Dans nos expériences, les pores de 1nm sont assez larges car l'adsorption des anions se produit sans aucune limitation même pour des tailles de pore de 0.68 nm, bien que pendant la décharge il y ait une très légère déviation du profil capacitif rectangulaire idéal. Par conséquent, il peut être déduit de ces informations que la taille réelle des ions de l'électrolyte (différent de la taille des ions nus), aussi nommée dans ce rapport "taille effective de l'ion", peut être estimée inférieure ou égale à 0.68 nm. Ceci est en accord avec un travail précédent qui mettait en évidence la capacité spécifique maximale pour une échantillon taille de pore égale à 0.68nm en utilisant un montage de 3 électrodes (4 cm²) [17]. L'hypothèse de la désolvatation partielle des ions lors de l'adsorption dans des pores subnanométriques confirme ces résultats, puisque la taille des pores est plus petite que la taille des ions solvatés (tableau 2), les ions entièrement solvatés ne seraient pas en mesure d'entrer dans les pores de Ti-CDC.

L'adsorption de Et₄N⁺ - La limitation observée pour des échantillons de faibles tailles de pores n'est ni liée à la résistance du 'bulk' de l'électrolyte, ni à la polarisation de la microélectrode à cavité qui est généralement observée pour des vitesses de balayage élevées quand la chute ohmique obtenue est trop importante [19],mais à cause du transport des ions dans le réseau de carbone poreux (déformation des ions les plus larges : Et₄N⁺ dans des pores de petites tailles). Cela a été aussi confirmé par le profil asymétrique des voltamogrammes enregistrés pour des échantillons à faibles tailles de pores.

L'effet de tamisage est facilement visible sur la figure 4a. Lorsque la taille des pores diminue jusqu'à ce qu'elles soient trop petites pour les cations (1,3 nm et 0,67 nm avec Et₄N⁺.7AN et sans couche de solvatation respectivement [17,18]), nous observons une déformation des voltamogrammes (figure 4a). Pour des tailles de pore plus petits ou égals à 0,76 nm, le comportement capacitif du carbone est détérioré. C'est l'effet stérique qui entraîne une résistivité importante, elle-même liée à la limitation du transport des cations dans les pores.

Lorsque la taille des pores est de plus de 1 nm, les pores sont accessibles aux cations comme le montre la CV rectangulaire (Figure 4a). La taille optimale des pores pour l'adsorption de l'ion Et_4N^+ solvatés par AN dans le carbone est comprise entre 0,76 nm (limitation) et 1 nm (pas de limitation). Des lors, la taille effective des cations solvatés par les molécules AN pendant la charge/décharge de double couches électrochimique peut être estimée entre 0.76 nm and 1 nm.

1 M NEt_4BF_4 dans carbonate de propylène (PC)

Concernant les pores de carbone de petites tailles (0,74 et 0,68 nm pour les échantillons de Ti-CDC à 600 °C et 500 °C respectivement), nous observons une réponse électrochimique différente avec une distorsion asymétrique de la forme du voltamogramme par rapport un comportement purement capacitif (CV rectangulaire). Des voltamogrammes avec des distorsions analogues ont été obtenus avec le même électrolyte en utilisant des électrodes en tissues de carbone, ce qui nous confirme que ces observations ne sont pas liées à l'utilisation de l'électrode à microcavité [20].

L'adsorption de BF_4^- - La distorsion observée sur les CV de la figure 4b pour le carbone de taille 0,68 nm montre que la taille effective des ions dans le PC est comprise entre 0,68 et 1 nm. Elle est donc supérieure à celle mesuré dans l'AN.

L'adsorption de Et_4N^+ - La signature électrochimique varie d'un échantillon à l'autre dans une gamme de potentiel de 0 V/Réf à -1.5 V/Réf. Tous les graphiques sont distordus et aucuns d'entre eux ne présente un comportement typiquement capacitif. Plus la taille de pore est petite, plus le courant est faible pour un potentiel donné. Etonnement, même une pore de grande taille de 1 nm, le graphe voltamogramme ne nous montre pas une signature électrochimique purement capacitive. La figure 4a nous a montré que la taille optimale des pores pour l'adsorption des cations Et_4N^+ issue de électrolyte basé sur de l'acétonitrile est entre 0,76 nm et 1 nm. Lorsque l'on remplace l'acétonitrile par le carbonate de propylène, la taille optimale des pores est alors augmentée à une valeur > 1 nm. Ces résultats sont en accord avec les tailles des ions solvatés : $BF_4^-.8PC$ = 1,40 nm et $Et_4^+N.4PC$ 1,35 nm [18] (Tableau 2).

Pour conclure, l'électrode à microcavité à été utilisée pour étudier le comportement électrochimique de carbones dérivés de carbure de titane matériaux poreux qui offre une distribution de pore étroite avec des tailles de pores de Ti-CDC comprise entre 0,68 à 1 nm. Les premiers résultats obtenus portent sur les tailles effectives des ions Et_4N^+ et BF_4^-. Ces tailles effectives varient selon les solvants utilisés (AN ou PC) ; elles ont été estimée d'après

les voltamogrammes enregistrés à une vitesse de balayage de 100 mV.s^{-1}. Elle diminue selon l'ordre suivant : Et$_4$N$^+$ dans PC > Et$_4$N$^+$ dans AN > BF$_4^-$ dans PC > BF$_4^-$ dans AN. Il apparait que les ions doivent être partiellement désolvatés pour entrer dans les sub-nanopores de petite taille (< 1 nm). Ces résultats sont en accord avec les récents résultats obtenus selon une série d'expérience utilisant des électrodes de 4 cm² dans des électrolytes à basé d'acétonitrile (AN)[16, 17].

Les études par électrode à microcavité permettent une mesure facile et rapide des corrélations entre la taille de pore et la performance de l'électrode pour une variété de carbones, d'électrolyte et de solvants. Plus important, nous avons obtenu les informations de la taille effective des ions dans les électrolytes en présence de différents solvants lors de l'adsorption/désorption des ions dans des carbones poreux de façon *in-situ*. Ces résultats montrent que différentes tailles de pores sont requises pour chaque électrode positive et négative. Cette technique qui associe des électrochimiques rapides avec des carbones Ti-CDCs avec porosité monodisperses est donc très utile en particulier pour étudier les interactions entre taille des ions et pores, Dans le prochain chapitre, nous étudierons les effets des solvants et nous présenterons l'utilisation des liquides ioniques.

Chapitre IV

Les résultats obtenus dans le chapitre III avec un électrolyte composé d'un sel et d'un solvant, ont montré que lors du stockage des charges dans la porosité d'électrodes de supercondensateurs à base de Ti-CDC, les ions étaient au minimum partiellement désolvatés. Cependant, la présence de solvant dans l'électrolyte rend difficile la détermination de la taille des pores à utiliser et pour cette raison, on ne peut pas avoir accès à la taille effective des ions adsorbés. De plus, nous n'avons pas les moyens de connaitre le degré de désolvation des ions et donc son effet sur la capacité dans les carbones. Le quatrième chapitre porte sur l'étude de la relation taille de pore / taille des ions en utilisant les Ti-CDCs présenté dans le Tableau 1 dans un électrolyte ne contenant pas de solvant. Nous avons donc utilisé une liquide ionique, le 1-Ethyl-1-MethylImidazolium bis (TriFluroSulfonyl)Imide (EMI-TFSI).

Dans un deuxième temps, l'expérience a été répétée en rajoutant un solvant l'acétonitrile (AN) pour mieux comprendre l'effet de solvatation sur la capacité dans les Ti-CDCs.

Electrolytes

Tableau 3: Parametres électrochimique des électrolytes.

Electrolytes	Fenêtre Electrochimique (V)	Température (°C)	Concentration (M)
EMITFSI	3.0	60	Neat
EMITFSI / AN	2.8	20	2

(a)   **(b)**
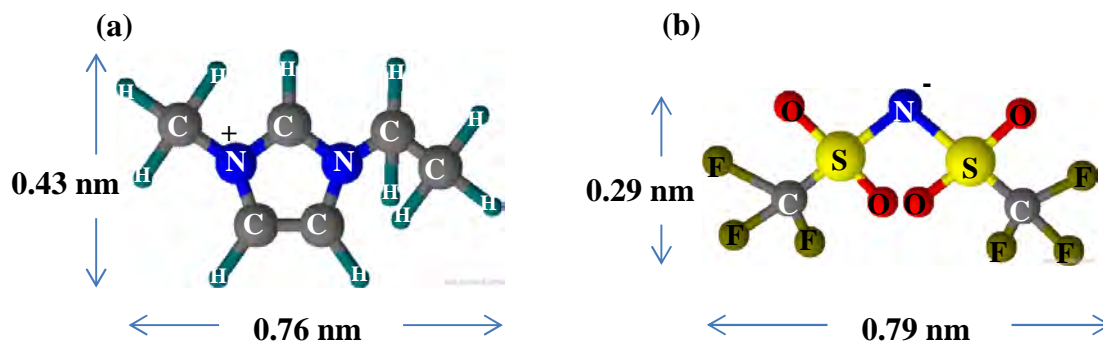
0.43 nm

0.76 nm

0.29 nm

0.79 nm

Figure 5: Illustration planaire des ions dans le liquide ionique pur: EMI$^+$ ion (a) et TFSI$^-$ ion (b).

Résultats

Un montage à trois électrodes a été utilisé pour étudier le comportement capacitif de chacune des électrodes sous polarisation. Les anions sont adsorbés à l'électrode positive, et les cations à l'électrode négative. L'étude séparé de chaque électrode d'électrode permet d'améliorer la compréhension des phénomènes d'adsorption de chacun des ions et donc du fonctionnement des supercondensateurs. Une électrode de quasi-référence constituée d'un fil d'argent dont le potentiel est constant a été utilisée afin d'enregistrer les réponses en courant ou en tension d'électrode de travail.
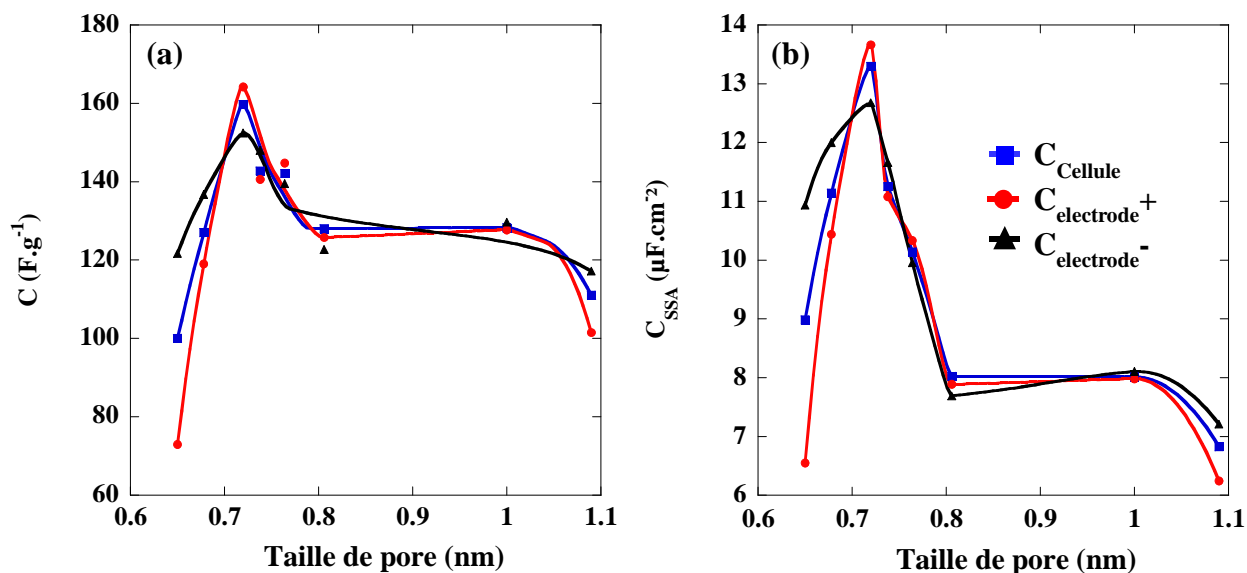
Figure 6: Capacités (F.g^{-1}) en fonction de la taille des pores **(a)** et capacités normalisées (µF.cm^{-2}) en fonction de la taille des pores **(b)** et des graphes de capacités de cellule, d'électrode de positive et négative de Ti-CDCs en fonction de la taille de pores dans l'électrolyte de EMI-TFSI pur à 60°C

La figure 6a montre les capacités de chaque électrode en fonction de la taille des pores. Les capacités sont calculées a partir de résultats du cyclage galvanostatique. Les trois capacités maximales, (pour la cellule, l'électrode positive et l'électrode négative) ont été mesurées à la même taille de pore : 0,72 nm. Cette taille, correspond à la taille des cations et anions d'électrolyte (Figure 5a et b). Ces résultats montrent une capacité maximale 160 F.g^{-1} pour une cellule possédant des électrodes de 0,72 nm de taille de pore. La capacité du positif est de 165 F.g^{-1} et la négative est de 153 F.g^{-1}, soit 50% plus élevée que la capacité obtenue dans des carbones activés commerciaux du type YP 17. De plus, ce qui est remarquable est que le capacité maximum est obtenu lorsque la taille des ion est proche de la taille des pores.

La figure 6b présente la variation de la capacité normalisé en fonction de la taille de pore. Les pics sont plus prononcés et sont visible à la même valeur de taille de pore : 0,72 nm. Les deux graphes de la figure 6 sont en accord avec le postulat que le maximum de capacité est obtenu lorsque la taille des ions est proche de celles des pores.
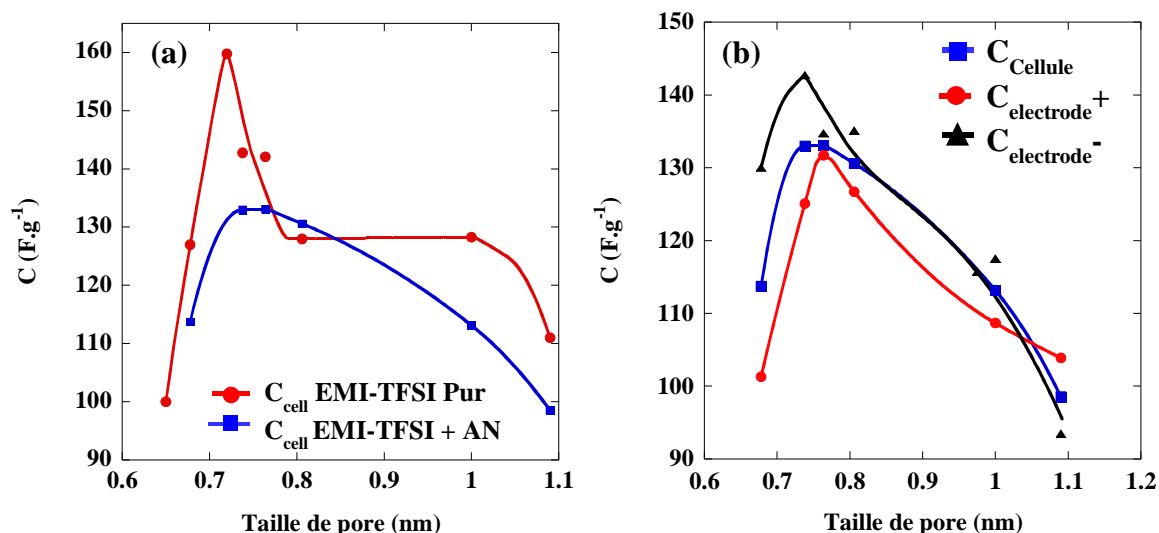
Figure 7: Capacités (F.g^{-1}) en fonction de la taille des pores dans les électrolytes EMI-TFSI pur (courbe bleue) et 2 M EMI-TFSI + AN solvaté (courbe rouge) **(a)** Capacités de cellule, d'électrode de positive et negative de Ti-CDCs en fonction de la taille de pores dans 2 M EMI-TFSI + AN solvaté **(b)**.

Capacités gravimétrique de plusieurs échantillons de Ti-CDCs dans les deux électrolytes (EMI-TFSI et 2 M EMI-TFSI + AN) sont montrées sur la figure 7a. Celle-ci montre que la maximum des capacité mesurée est plus faible pour l'électrolyte solvaté par rapport à l'électrolyte pur. Ces observations mettent en evidence l'influence du degrè de désolvatation sur la valeur de la capacité.

Les capacités de chaque électrode en fonction de la taille des pores dans l'électrolyte solvaté de 2 M EMI-TFSI + AN sont présentés en figure 7b. Les différents degrés de désolvatation peuvent être liés aux différentes tailles de pore qui correspondent aux capacités maximales. Il apparait que la taille effective des anions est légèrement grande que celles des cations dans l'électrolyte solvaté. L'électrode à microcavité a été utilisée pour confirmer ces résulatats avec : le Ti-CDCs et l'électrolyte de 2 M EMI-TFSI + AN. Les résultats obtenus sont en accord avec ce qui est présenté dans la figure 7b.

L'utilisation d'un liquide ionique en tant qu'électrolyte a permis de confirmer et d'affiner les résultats obtenus avec un électrolyte à base d'acétonitrile. Les capacités obtenues sont maximales lorsque la taille des pores de la matière active est du même ordre de grandeur que la taille des ions de l'électrolyte. En comparant les résultats obtenus dans les deux électrolytes, on peut affirmer que le stockage des charges se fait par l'adsorption d'ions au moins partiellement désolvatés. Dans l'acétonitrile, les ions conservent une partie de leur couche de solvatation : la capacité maximale est effectivement obtenue pour une taille de pore située entre la taille des ions désolvatés et celle des ions solvatés, alors que dans l'EMI-TFSI,

où la solvatation n'existe pas, la capacité maximale est obtenue pour des tailles de pores égales à la taille des ions de l'électrolyte. La taille de pores doit également être adaptée à la taille des ions afin de conserver des capacités importantes lorsque la densité de courant augmente.

Pour conclure, cette étude à démontré que la capacité est liée à l'absorption des ions dans les carbons poreux dépend de la structure poreuse des électrodes et la dimension des ions de l'électrolyte sans solvant. L'augmentation de la capacité dans les carbones qui possèdent une taille de pore inferieure à 1 nm en utilisant l'électrolyte non-solvaté (EMI-TFSI pure) est montrée et confirmé. Cette découverte montre que la vision intuitive qui voudrait que des pores substantiellement plus grands que la taille des ions de l'électrolyte solvatés soient requis pour obtenir une grande capacité n'est pas vraie [21]. Dans ce travail, nous avons étudié l'influence de la solvatation et découvert que la capacité peut être améliorée en utilisant l'électrolyte non-solvaté. Suivant, nous avons montré que lorsque la taille des pores est de l'ordre de grandeur de la taille des ions, l'augmentation de la capacité est importante. C'est donc en remise en cause du modèle jusque la décrire l'adsoprtion des ions dans les carbones poreux.

Chapitre V

Le cinquième et dernier chapitre présente la synthèse de liquides ioniques (LIs) et la formulation à base de ces mélanges de LIs. La mise en œuvre de ces électrolytes pour des applications de supercondensateurs est optimisée à travers l'interface électrolyte/électrode

Le mélange de deux LIs ayant chacune un point de fusion 6°C (PIP$_{13}$-FSI) and -18 °C (PYR$_{14}$-FSI) (Figure 8) a permis d'obtenir une solution qui ne solidifie pas au-dessus de -80 °C. L'état liquide du mélange eutectique (III) peut être maintenu plusieurs dizaines de degrés plus bas que les deux constituants pris séparément comme présenté dans la figure 8.
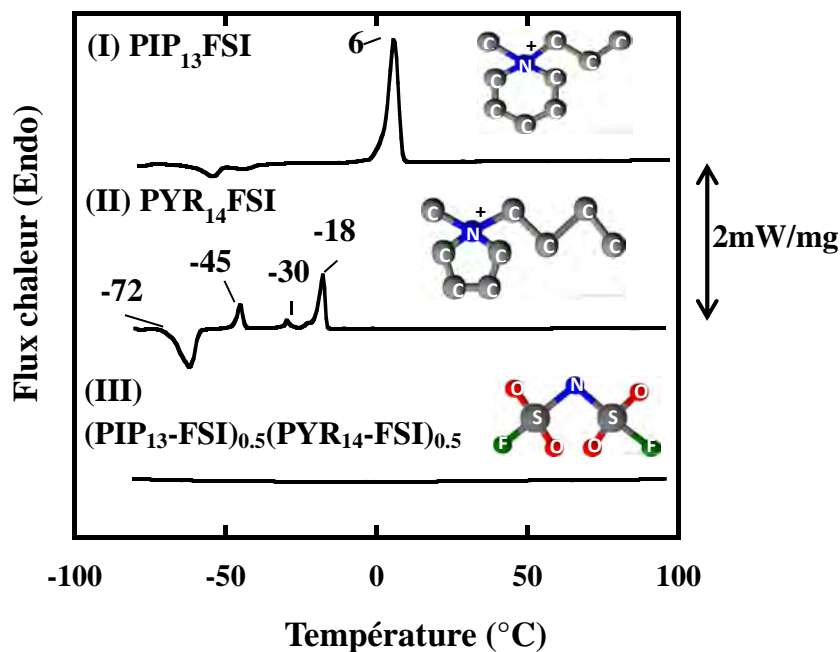
Figure 8: Profils DSC de (I) PIP$_{13}$-FSI, (II) PYR$_{14}$-FSI et (III) du mélange (PIP$_{13}$-FSI)$_{0.5}$(PYR$_{14}$-FSI)$_{0.5}$, ainsi que leur structure chimique (I) PIP$_{13}^+$, (II) PYR$_{14}^+$ et (III) FSI$^-$.

Nos résultats montrent que la sélection adéquate de deux différentes cations avec le même anion peut empêcher l'arrangement des ions à l'état liquide, inhibant ainsi la formation de structure cristalline. Dans ces mélanges, les cations ont le même nombre d'atomes et de même nature. Un comportement similaire a été observé pour un autre mélange de cations de LIs PYR$_{14}$-FSI et PYR$_{23}$-FSI selon la même approche.

Ces deux mélanges eutectique sont testés en temps qu'électrolytes dans les électrodes de carbones de differentes natures selon ses nanostructures : des oignons de carbone (OLCs) [22], Nanotubes de Carbone (NTCs) [23] et Graphène [24].
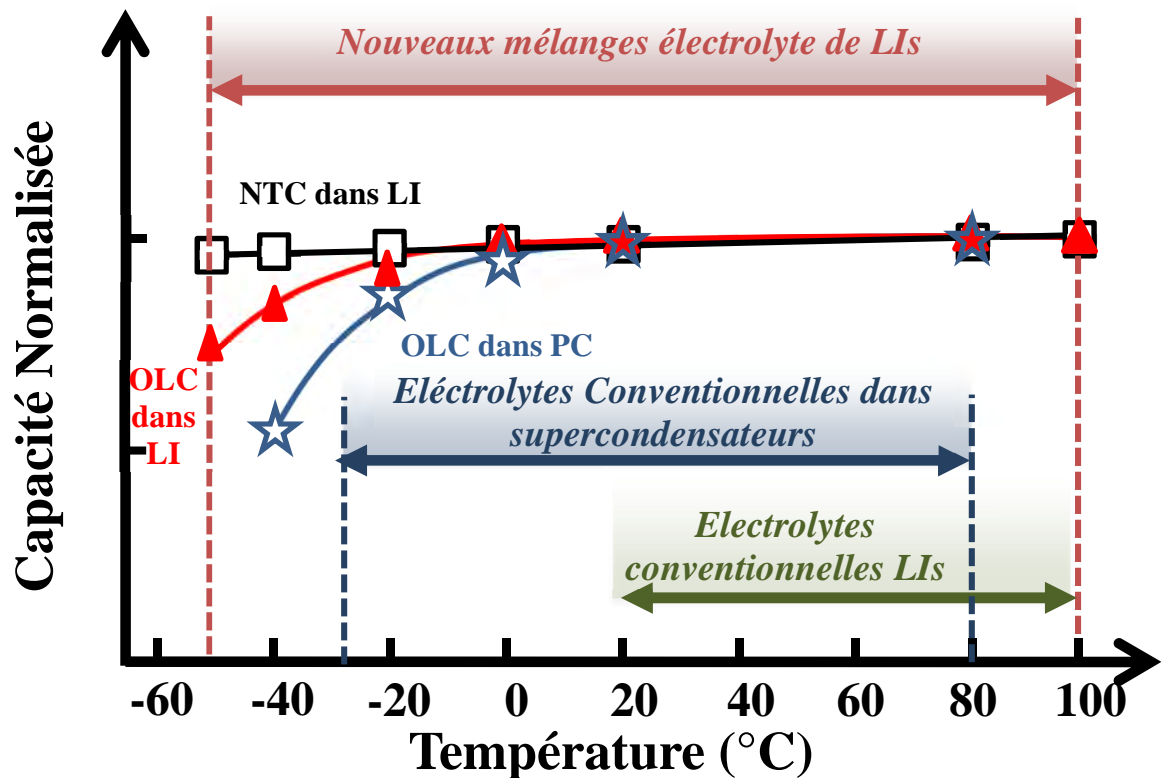
Figure 9: Capacité normalisée (C/C$_{20\ °C}$) pour les électrodes d'OLCs et de NTC dans le mélange eutectique (PIP$_{13}$-FSI)$_{0,5}$(PYR$_{14}$-FSI)$_{0,5}$ et PC + 1 M NEt$_4$BF$_4$ comme électrolytes. Les capacités sont calculées à une vitesse de balayage de100 mV.s^{-1}, sauf pour les expériences faites à -50 °C (1 mV.s^{-1}) et -40 °C (5 mV.s^{-1}). Cette figure montre que le mélange eutectique permet d'étendre la gamme de température pour les applications en supercondensateurs (-50 to 100 °C). Dans l'électrolyte qui contient un solvant comme PC, la gamme de température est limitée de -30 à 80 °C. C$_{20°C}$ = 80 mF.cm^{-2} pour cellule de OLC et C$_{20°C}$ = 4 mF.cm^{-2} pour cellule de NTC. Les cellules sont testées en voltamétrie cyclique de 0 V à 2,8 V.

La figure 9 présente l'évolution de capacité en fonction de la température dans les électrodes d'OLC (calculée à partir de voltamogrammes, avec une tension jusqu'à 3 V) et NTC (calculée à partir de voltamogrammes, avec une tension jusqu'à 2,8 V). Les capacités ont été normalisées afin de faire des comparaisons. Chaque capacité a été divisée par la capacité obtenue à 20°C pour chaque combinaison électrolyte/carbone. Pour l'électrolyte à 1 M NEt$_4$BF$_4$ dans PC utilisé dans l'électrode d'OLC, la diminution de la capacité aux basses températures et l'oxydation de l'électrolyte aux hautes températures ont restreint gamme de température entre -30 to 80 °C (110 °C d'amplitude) ainsi que la tension de la cellule à 2,5 V à 100°C (en accord avec les supercondensateurs commerciaux). Cette figure met en évidence l'élargissement de la gamme de température en utilisant le mélange eutectique de (PIP13-FSI)$_{0,5}$(PYR14-FSI)$_{0,5}$ dans des électrodes de différentes architectures (OLC et NTC). Pour ce mélange eutectique l'amplitude de température est 150 °C (-50 à 100°C). De plus, l'électrode de NTC avec le mélange eutectique montre de meilleures performances dans la même gamme

de température allant de -50 à 100 °C, grâce à une large surface accessible, un montage exempt de liant, et l'amélioration de l'interface carbone/métal liée àla synthèse dans NTC élaborée par voie CVD. Nous avons démontré que l'adaptation de l'architecture de l'électrode à l'électrolyte est importante pour l'amélioration des comportements capacitifs et leurs performances. Bien que cette approche d'optimisation de l'interface électrolyte/électrode améliore la densité de stockage de l'énergie dans cette large gamme de température, Le point faible reste la faible capacité due aux structures de carbones.

La figure 10a montre les CV 100 mV.s^{-1}, température en utilisant des électrodes de graphène dans le mélange eutectique de LIs, (PIP13-FSI)$_{0.5}$(PYR14-FSI)$_{0.5}$. La capacité gravimétrique augmente de 30 F.g^{-1} à ~160 F.g^{-1} en changeant l'électrode OLC ou NTC en électrode de graphène.

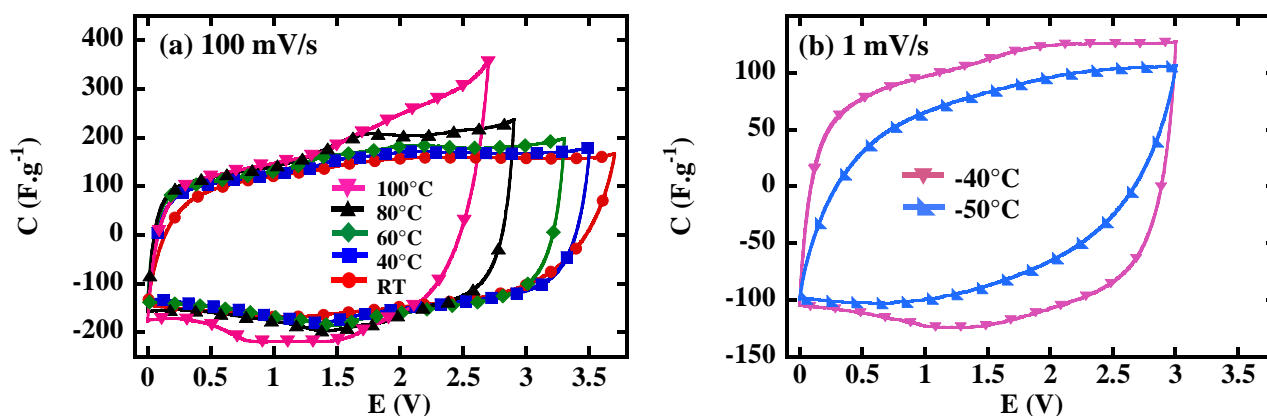**Figure 10: Caractérisation électrochimique de l'électrode de graphene dans l'électrolyte (PIP$_{13}$-FSI)$_{0.5}$(PYR$_{14}$-FSI)$_{0.5}$.** Fenêtre de potentiel maximum pour $20 \geq T \geq 80$°C à 100 mV.s^{-1}; **(a)** et pour des températures négatives (- 40 et -50°C) à 1 mV.s^{-1} avec une tension jusqu'à 3 V **(b)**. Masse volumique = 1.65 mg.cm^{-2}.

Entre 20°C et 60°C, pour une tension de 3 V, la capacité augmente graduellement (aire sous la courbe voltamétrie cyclique). Cet accroissement peut être expliqué par la forte conductivité ionique de l'électrolyte à haute température, ceci pouvant être observé dans les courbes de voltamétrie cyclique les plus rectangulaires. Une forte capacité est maintenue, variant de 160 à 180 F.g^{-1} pour des températures de 20 à 80°C.

Pour des températures négatives (-40 and -50°C), ~70% de la capacité est encore maintenue à 1 mV.s^{-1} (vitesse de balayage raisonnable pour prendre en compte la réduction de mobilité des ions à basses températures). Les voltamogrammes montrent un bon comportement capacitif à -40°C (Figure 10b). De fortes valeurs de capacités (100 to 120 F.g^{-1}) sont atteintes pour une tension de 3 V.

En résumé, dans cette étude, nous avons montré un élargissement significative de la gamme température pour le stockage de l'énergie électrique avec une bonne combinaison entre l'électrode de carbone nanostructuré (NTC et OLC) et un mélange eutectique de LIs. Les supercondensateurs sont capables de fonctionner dans températures négatives, de -50°C à 100°C dans une large fenêtre de potentiel jusqu'à 3,7 V. Ces découvertes ouvrent de nouvelles applications pour LIs en temps qu'électrolytes pour les applications en dessus de la température ambiante. Nous n'avons pas seulement observé une capacité stable aux très basses températures (~70 % à -50 °C), nous avons aussi observé un très fort taux de charge/décharge jusqu'à 20 $V.s^{-1}$ à 100 °C. Ceci montre la possibilité d'application en conditions climatiques extrêmes, qui établit la robustesse des LIs.

Une amélioration importante de la capacité a été possible grâce à utilisation de l'électrode de graphène (160 $F.g^{-1}$) avec une tension maximum de 3,7 V pour les applications de -50 à 100°C, comparativement aux électrolytes organiques conventionnels dont la température de -30°C à 80°C). Ces résultats ce qui constitue un progrès important par rapport à la littérature.

Conclusion Générale

Les résultats obtenus à l'issue de cette étude ont conduit à trois publications, dans lesquelles nous avons tout d'abord montré que la taille des pores de la matière active et la taille des ions de l'électrolyte doivent être adaptée pour augmenter la capacité, la capacité est maximale lorsque la taille des pores est proche de la taille des ions. En utilisant un liquide ionique solvaté (EMI-TFSI + acétonitrile), nous avons également montré que les ions de l'électrolyte sont partiellement désolvatés lors de leur adsorption dans les micropores inférieurs à 1 nm. En fin, des mélanges de liquides ioniques ont été préparés en sélectionnant des cations spécifiques, et des électrolytes eutectiques liquides jusqu'à -80°C. L'association de ce type de liquide ionique et de nanotubes de carbone possédant une structure ouverte permet d'utiliser une large gamme de température de -50°C jusqu'à 100°C pour le fonctionnement des supercondensateurs.

Ces recherches ont donc permis d'une part d'approfondir la compréhension de la relation taille des ions/taille de pore dans le but d'augmenter les performances de supercondensateurs ; D'autre part, la découverte de nouvelles propriétés des mélanges de liquides ioniques ont permis d'étendre la gamme de températures pour les applications des supercondensateurs.

Références

[1]   Communication from the commission to the European parliament, the council, the European economic and social committee and the committee of the regions (COM(2010) 639 of 10 November 2010)

[2]   http://energy.gov/

[3]   http://www.energy.eu/

[4]   http://energy.gov/articles/energy-matters-clean-energy-technology-markets

[5]   Article 194 of the treaty on the functioning of the European Union (TFUE)

[6]   Simon, P.; Gogotsi, Y. *Nature Materials* **7** (2008) 845.

[7]   Miller, J. R.; Simon, P. *Science* **321** (2008) 651.

[8]   Conway, B. E. *Electrochemical Supercapacitors: Scientific Fundamentals and Technological Applications* (Kluwer, 1999).

[9]   Armand, M.; Tarascon, J. M. *Nature* **451** (2008) 652.

[10]   www.solvionic.com

[11]   Béguin, F., Frackowiak, E. Carbon Materials for Electrochemical Energy Storage Systems; *Béguin, F., Frackowiak, E., Eds.*; *CRC Press/Taylor and Francis: Boca Raton, FL* (2009).

[12]   Portet, C.; Chmiola, J.; Gogotsi, Y.; Park, S; Lian, K. *Electrochimica Acta* **53** (2008) 7675.

[13]   Lin, R.; Taberna, P-L.; Fantini, S.; Presser, V.; Pérez, C.R. Malbosc, F.; Rupesinghe, N.L.; Teo, K.B. K.; Gogotsi, Y.; Simon, P. *Journal of Physical Chemistry Letters* **2** (2011) 2396.

[14]   Zhu, Y.; Murali, S.; Stoller, M. D.; Ganesh, K. J.; Cai, W. ; Ferreira, P. J. Pirkle, A. ; Wallace, R. M.; Cychosz, K.A. ; Thommes, M. ; Su, D. ; Stach, E.A.; Ruoff, R. S. *Science* **332** (2011) 1537.

[15]   Dash, R.; Chmiola, J.; Yushin, G.; Gogotsi, Y.; Laudisio, G.; Singer, J.; Fischer, J.; Kucheyev, S. *Carbon* 44 (2006) 2489.

[16]   Chmiola, J.; Yushin, G.; Gogotsi, Y.; Portet, C.; Simon, P.; Taberna, P.-L. *Science* **313** (2006) 1760.

[17]   Chmiola, J.; Largeot, C.; Taberna, P-L.; Simon, P.; Gogotsi, Y. *Angewandte Chemie International Edition* **47** (2008) 3392.

[18]   Yang, C. M. ; Kim, Y. J.; Endo, M.; Kanoh, H.; Yudasaka, M.; Iijima, S.; Kaneko, K. *Journal of the American Chemical Society* **129** (2007) 20.

[19]   Cachet-Vivier, C.; Vivier, V.; Cha, C. S.; Nedelec, J. Y.; Yu, L. T. *Electrochimica Acta* **47** (2001) 181-189.

[20]   Salitra, G.; Soffer, A.; Eliad, L.; Cohen, Y.; Aurbach, D. *Journal of the Electrochemical Society* **147** (2000) 2486.

[21]   Endo, M.; Maeda, T.; Takeda, T.; Kim, Y. J.; Koshiba, K.; Hara, H.; Dresselhaus, M. S. *Journal of the Electrochemical Society* **148** (2001) A910.

[22]   Portet, C.; Chmiola, J.; Gogotsi, Y.; Park, S; Lian, K. *Electrochimica Acta* **53** (2008) 7675.

[23]   Lin, R.; Taberna, P-L.; Fantini, S.; Presser, V.; Pérez, C.R. Malbosc, F.; Rupesinghe, N.L.; Teo, K.B. K.; Gogotsi, Y.; Simon, P. *Journal of Physical Chemistry Letters* **2** (2011) 2396.

[24]   Zhu, Y.; Murali, S.; Stoller, M. D.; Ganesh, K. J.; Cai, W. ; Ferreira, P. J. Pirkle, A. ; Wallace, R. M.; Cychosz, K.A. ; Thommes, M. ; Su, D. ; Stach, E.A.; Ruoff, R. S. *Science* **332** (2011) 1537.

Abstract

Energy storage is indispensable for the sustainability of our daily energy needs. Without the support of energy storage systems, the over production of energy would be wasted and the shortage of energy would result in consequential disruptions to our daily activities. Electrochemical energy storage (EES) systems serve as one of the distributed energy technologies and are drawing attention in research to address today's industrial and societal challenges for security and sustainability of energy that they can provide. Amongst the EES, Electrochemical capacitors (EC), also known as supercapacitors are emerging to be prospective energy storage devices with high and fast power delivery owing to the simple charge storage mechanism based on electrostatic attraction: the adsorption of the ions of an electrolyte onto the surface area of the active material of the electrodes.

The objectives of this thesis are (1) to study the capacitive behaviour of the electrochemical double layer, constituted by the ions of the electrolyte and the charges induced by the application of an external potential at the electrodes, in view to increase the capacitance and (2) to formulate electrolytes based on ionic liquids with the goal to increase the electrochemical window and hence energy density of the ECs. Ionic liquids (ILs) have in recent years emerged as a neoteric genre of electrolytes which offer great varieties of electrochemical as well as physical properties (ionic conductivity, melting points, electrochemical stability, etc.). In this context, this thesis has been effectuated by SOLVIONIC, a company which specialized in the research and development of ionic liquids and formulation of electrolytes, in collaboration with CIRIMAT in University of Paul Sabatier in Toulouse, France.

Results have provided better insights and understanding on the electrolyte/electrode interface in view of increasing the performances of supercapacitors. A new approach of optimizing the electrode/electrolyte interface that allows capacitive energy storage in a widened temperature range from -50°C to 100 °C has also been demonstrated using formulated eutectic mixtures of ionic liquids and architected electrodes.

Keywords: Supercapacitor; Electrolyte; Ionic liquid; Eutectic mixture; Carbide-derived Carbon; Graphene; Onion-like carbon; Carbon nanotube

Résumé

Le stockage de l'énergie est indispensable pour répondre aux besoins énergétiques quotidiens. Sans le recours à des systèmes de stockages, l'énergie surproduite sera gaspillée et l'énergie sous produite entraînera des interruptions des activités quotidiennes. Par conséquent, les systèmes de stockage d'énergie, parmi lesquels on trouve les supercondensateurs jouent un rôle primordial. Ceux-ci présentent un grand intérêt dans les applications de puissance puisqu'ils peuvent stocker et fournir de l'électricité rapidement (quelques secondes) grâce à un fonctionnement basé sur le stockage électrostatique des charges électriques : les ions d'un électrolyte sont adsorbés/désorbés à la surface de la matière active des électrodes.

Les objectifs de cette thèse sont (1) d'étudier la charge de la double couche électrochimique, constituée par les ions de l'électrolyte et les charges induites par l'application d'un potentiel externe au niveau des électrodes, en vue d'augmenter la capacité et (2) de formuler des électrolytes à base de liquides ioniques dans le but d'augmenter la fenêtre de potentiel d'électrochimique, et donc l'énergie. Ces travaux de recherches ont été réalisés en partenariat avec la société industrielle Solvionic, spécialisée dans le développement et la production de liquides ioniques, et le laboratoire du CIRIMAT de l'université Paul Sabatier.

Les résultats obtenus à l'issue de cette étude ont conduit à trois publications, dans lesquelles nous avons tout d'abord montré que la taille des pores de la matière active et la taille des ions de l'électrolyte doivent être adaptée pour augmenter la capacité, la capacité est maximale lorsque la taille des pores est proche de la taille des ions. En utilisant un liquide ionique solvaté (EMI-TFSI + acétonitrile), nous avons également montré que les ions de l'électrolyte sont partiellement désolvatés lors de leur adsorption dans les micropores inférieurs à 1 nm. En fin, des mélanges de liquides ioniques ont été préparés en sélectionnant des cations spécifiques, et des électrolytes eutectiques liquides jusqu'à -80°C. L'association de ce type de liquide ionique et de nanotubes de carbone possédant une structure ouverte permet d'utiliser une large gamme de température de -50°C jusqu'à 100°C pour le fonctionnement des supercondensateurs.

Ces recherches ont donc permis d'une part d'approfondir la compréhension de la relation taille des ions/taille de pore dans le but d'augmenter les performances de supercondensateurs ; D'autre part, la découverte de nouvelles propriétés des mélanges de liquides ioniques ont permis d'étendre la gamme de températures pour les applications des supercondensateurs.